Cheng Feng

Spectrum Engineering of Stimulated Brillouin Scattering in Distributed Fiber Sensing and Optical Signal Processing

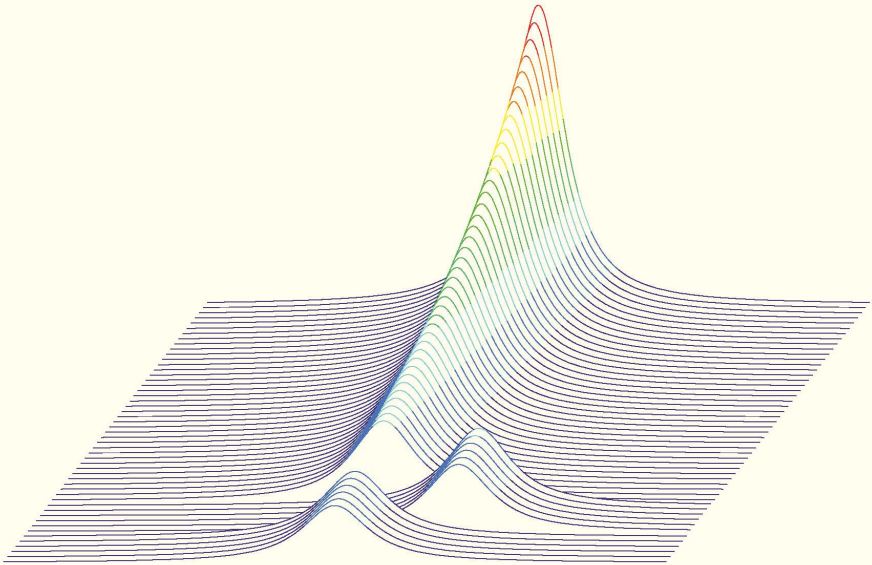

Cuvillier Verlag Göttingen
Internationaler wissenschaftlicher Fachverlag

Spectrum Engineering of Stimulated Brillouin Scattering in Distributed Fiber Sensing and Optical Signal Processing

Dieses Werk ist copyrightgeschützt und darf in keiner Form vervielfältigt werden noch an Dritte weitergegeben werden.
Es gilt nur für den persönlichen Gebrauch.

Dieses Werk ist copyrightgeschützt und darf in keiner Form vervielfältigt werden noch an Dritte weitergegeben werden.
Es gilt nur für den persönlichen Gebrauch.

Spectrum Engineering of Stimulated Brillouin Scattering in Distributed Fiber Sensing and Optical Signal Processing

Von der Fakultät für Elektrotechnik, Informationstechnik, Physik
der Technischen Universität Carolo-Wilhelmina zu Braunschweig

zur Erlangung des Grades eines Doktors
der Ingenieurwissenschaften (Dr.-Ing.)

genehmigte Dissertation

von Cheng Feng

aus Shanghai

eingereicht am: 16.09.2020

mündliche Prüfung am: 16.11.2020

1. Referent: Prof. Dr. rer. nat. Thomas Schneider
2. Referent: Prof. Dr. Alayn Loayssa

Druckjahr: 2020

Dieses Werk ist copyrightgeschützt und darf in keiner Form vervielfältigt werden noch an Dritte weitergegeben werden.
Es gilt nur für den persönlichen Gebrauch.

Bibliografische Information der Deutschen Nationalbibliothek
Die Deutsche Nationalbibliothek verzeichnet diese Publikation in der Deutschen Nationalbibliografie; detaillierte bibliografische Daten sind im Internet über http://dnb.d-nb.de abrufbar.
1. Aufl. - Göttingen: Cuvillier, 2020
Zugl.: (TU)Braunschweig, Diss., 2020

Dissertation an der Technischen Universität Braunschweig,
Fakultät für Elektrotechnik, Informationstechnik, Physik

© CUVILLIER VERLAG, Göttingen 2020
Nonnenstieg 8, 37075 Göttingen
Telefon: 0551-54724-0
Telefax: 0551-54724-21
www.cuvillier.de

Alle Rechte vorbehalten. Ohne ausdrückliche Genehmigung des Verlages ist es nicht gestattet, das Buch oder Teile daraus auf fotomechanischem Weg (Fotokopie, Mikrokopie) zu vervielfältigen.
1. Auflage, 2020
Gedruckt auf umweltfreundlichem, säurefreiem Papier aus nachhaltiger Forstwirtschaft.

ISBN 978-3-7369-7329-9
eISBN 978-3-7369-6329-0

Dieses Werk ist copyrightgeschützt und darf in keiner Form vervielfältigt werden noch an Dritte weitergegeben werden.
Es gilt nur für den persönlichen Gebrauch.

Kurzfassung

Aufgrund des niedrigen Schwellwertes ist die stimulierte Brillouin Streuung der dominanteste nichtlineare Effekt in optischen Einmodenfasern. Das einzigartige Lorentz förmige Gewinnspektrum mit einer Linienbreite von 20 bis 30 MHz hat umfangreiche Anwendungen ermöglicht, wie z.B. optische Signalverarbeitung, Verzögerung und Speicherung von optischen Datensignalen, optische Spektrumanalyse und verteilte Sensoren. Alle diese Anwendungen würden von einem beliebig konstruier- und konfigurierbaren bzw. willkürlich manipulierbaren Verstärkungsspektrum profitieren. In dieser Arbeit wird die Manipulation des Brillouin-Gewinnspektrums durch die Überlagerung mit Brillouin-Verlusten vorgestellt, sowie Anwendungen im Bereich der verteilten Sensoren sowie der optischen Signalverarbeitung untersucht.

Bei herkömmlichen statisch verteilten Brillouin-Sensoren ist die Auflösung der Messgröße (Temperatur und/oder Dehnung) sehr rauschempfindlich. Die Ermittlung der Spitze des Spektrums, welche die Messgröße symbolisiert, wird durch verschiedenste Rauschweinflüsse während der Detektion stark erschwert. Die Überlagerung des Brillouin-Gewinns mit Verlusten führt zu einem schärfen konstruierten Verstärkungsspektrum, welches wesentlich robuster gegenüber Rauscheinflüssen ist. Dies trägt dazu bei, dass die Spitze des Spektrums genauer bestimmt werden kann und resultiert in einer doppelt so hohen Auflösung, sowie einer Erhöhung der möglichen Messentfernung um bis zu 60%.

In dynamischen verteilten Brillouin-Sensoren wird im Wesentlichen die Untersuchung der Steigung des Gewinnspektrums als Messmethode eingesetzt. Jedoch ist der verwendbare lineare Frequenzbereich des Gewinnspektrums gewöhnlich sehr schmal. Eine dynamische Messung außerhalb des linearen Bereichs führt zu schwerwiegenden Fehlern. Ein präzise konstruiertes Gewinnspektrum kann den linearen Bereich weitgehend erweitern, ohne die Steigung zu beeinträchtigen. In dieser Arbeit wird eine praktische und quantifizierte Definition vorgeschlagen, sowie eine quantitative Erweiterung von 70% nachgewiesen.

Darüber hinaus wird das beliebig konstruierbare Gewinnspektrum im Bereich der optischen Signalverarbeitung eingesetzt, insbesondere als optischer Filter sowie als photonischer Filter für Mikrowellen-Signale. Der Nachteil herkömmlicher Filter auf Basis der Brillouin Streuung ist das unvermeidliche Brillouin-Rauschen. Der in dieser Arbeit vorgeschlagene neuartige optische Filter blockiert die unerwünschten Signale durch Brillouin-Verluste, während das Durchlassband transparent und rauschfrei bleibt. Die ursprünglichen Vorteile von Brillouin-

Dieses Werk ist copyrightgeschützt und darf in keiner Form vervielfältigt werden noch an Dritte weitergegeben werden.
Es gilt nur für den persönlichen Gebrauch.

Filter, wie sehr steile Flanken und eine durchstimmbare Bandbreite bleiben dabei erhalten. Dies stellt einen großen Schritt in Richtung eines idealen optischen Filters dar.

Zusätzlich wurde ein photonischer Mikrowellen-Notchfilter auf Basis der Wechselwirkung zwischen Brillouin-Verlusten untersucht. Besonders hervorzuheben ist dabei die genaue Steuerung der Amplitude und Phase der Modulationsseitenbänder. Die Ergebnisse zeigen eine Filterleistung, einschließlich einer Reduzierung der Notchtiefe sowie einer Verschiebung der Mittenfrequenz des Filters, die sehr stark von der Dispersion in der Faser abhängt. Dies ist einerseits nachteilig, biete andererseits jedoch einen neuen Weg zur Dispersionsmessung.

Abschließend wird eine vorläufige Idee präsentiert, bei der die Mikrowellenphotonik, insbesondere die phasenverschobene Aufhebung, im Bereich der verteilten Brillouin-Sensoren angewendet werden soll. Die theoretische Untersuchung zeigt, dass das konstruierte Gewinnspektrum für die hochfrequenten Signale einen wesentlich höheren Signal-zu-Rausch Abstand sowie einen erweiterten linearen Bereich an den Flanken aufweist. Daraus ergeben sich wesentliche Vorteile für dynamische Brillouin-Sensoren auf Basis der Steigungsanalyse.

Dieses Werk ist copyrightgeschützt und darf in keiner Form vervielfältigt werden noch an Dritte weitergegeben werden.
Es gilt nur für den persönlichen Gebrauch.

Abstract

Due to the low threshold, stimulated Brillouin scattering is one of the dominant nonlinear effects in single mode optical fibers. Its unique Lorentzian gain spectrum characteristic with the narrow linewidth of 20-30 MHz has enabled a variety of applications, such as optical signal processing, delay and light storage, optical spectrum analysis and distributed sensing. Most of them will further benefit from an engineered, reconfigurable or arbitrary manipulated gain spectrum. This work will introduce the basic method for Brillouin gain spectrum engineering by the superposition with Brillouin loss(es) and its applications in the field of distributed sensing and optical signal processing.

In static distributed Brillouin sensing, the measurand resolution (temperature and/or strain) is highly noise sensitive. A noisy detection makes the estimation of the spectrum peak, which symbolizes the measurand, very hard. By superimposing the Brillouin gain with losses, the engineered gain spectrum could be sharper and more robust to the noise. This could help to determine the spectrum peak more accurately and leads to a doubled resolution and a sensing range extension up to 60%.

In dynamic distributed Brillouin sensing, slope-assisted Brillouin sensing is a very practical technique. However, the useful linear frequency span of a conventional Brillouin gain spectrum is usually narrow. A dynamic measurement working outside the linear range leads to severe errors. A well engineered gain spectrum is able to largely extend this linear range without compromise to the slope. A practical and quantified definition has been proposed in this work and a quantitative extension of more than 70% has been demonstrated.

Furthermore, the engineered gain spectrum has been applied to optical signal processing, especially to the optical and microwave photonic filters. The bottleneck of the conventional Brillouin gain based optical filters is the inevitable Brillouin noise. The novel optical filter proposed in this work blocks the undesired signals by Brillouin losses, while leaving the passband transparent and noise-free. The original striking advantages of Brillouin filters, such as sharp roll-off and flexible bandwidth tunability are well maintained, giving a giant step towards an ideal optical filter.

In addition, the microwave photonic notch filter based on Brillouin loss interaction has been investigated. The highlight of this technique is the precise control of the amplitude and phase of the modulation sidebands. The results indicate a highly fiber dispersion sensitive

Dieses Werk ist copyrightgeschützt und darf in keiner Form vervielfältigt werden noch an Dritte weitergegeben werden.
Es gilt nur für den persönlichen Gebrauch.

filter performance, including notch rejection reduction and notch frequency shift. This is on one hand detrimental, however, on the other hand provides a novel way for dispersion measurement.

Finally, a tentative idea to apply the microwave photonic technique, *i.e.*, the out-of-phase cancellation, on distributed Brillouin sensing is proposed. According to the theoretical investigation, the engineered radio frequency gain spectrum depicts a much higher signal-to-noise ratio and an extended linear range at the edge, providing an attractive advantage for slope-assisted dynamic sensing.

Dieses Werk ist copyrightgeschützt und darf in keiner Form vervielfältigt werden noch an Dritte weitergegeben werden.
Es gilt nur für den persönlichen Gebrauch.

Acknowledgments

It is my pleasure to thank everyone who have supported me and made this thesis possible.

First of all, I wish to express my sincere appreciation to my supervisor, Prof. Dr. Thomas Schneider. His wisdom and inspiration guided me to be professional. His encouragement and support helped me to do the right things even when the road got tough. He taught me how to analyze problems scientifically and solve them both as a researcher and a well-trained engineer. Under his patient guidance and the numerous fruitful discussions in the past years, the theories were established, the experimental setup was built up and new ideas came up. This thesis and my whole Ph.D. study would not have been accomplished without his assistance.

Moreover, I would also like to express my profound gratitude to Prof. Dr. Alayn Loayssa from Public University of Navarre in Spain, and Prof. Dr. Moshe Tur from Tel-Aviv University in Israel. They have not only provided me precious visiting chances to cooperate with their group members in their laboratories, but also significantly widened my view and inspired me with new ideas and skills. It was my honor to work with them during my Ph.D. study. I am deeply moved by their enthusiasms on research and enjoy every valuable discussion with them.

Furthermore, I would like to acknowledge my lovely colleagues who are always supportive for different research topics and also in building up a relax working environment. In particular, my thanks go to Dr. Stefan Preußler and Dr. Hassanain Al-Taiy for their introduction to the laboratory and the technical support in challenging tasks, Mr. Arijit Misra, Mr. Janosch Meier, Mr. Karanveer Singh, and Dr. Xin Lu from Federal Institute for Materials Research and Testing (BAM) in Berlin, for their fruitful and enlightening discussions on methodology and results. I also would like to say a special thank you to Dr. Haritz Iribas, Dr. Jon Mariñelarena, Dr. Javier Urricelqui, Dr. Juan José Mompo in Pamplona, Spain, and Mr. Hari Datta Bhatta, Mr. Jonathan Bohbot, Mr. Roy Davidi in Tel-Aviv, Israel, for their cooperation, active technical support and the wonderful moment we have spent together during my visits.

Finally, nobody is more important to me in the pursuit of this study than the members of my family. My deep gratefulness goes to my beloved parents for their consistent trust and endless love. My special grateful thank goes to my wife, Dr. Weihong Liang, for her unfailing support, continuous encouragement and unconditional belief in me throughout my years of study, the process of researching and writing this thesis. This work is also dedicated to my little daughter, Norah Xiangyi Feng, who is coming to the world at the end of this year and may not be able to join my graduation personally.

Dieses Werk ist copyrightgeschützt und darf in keiner Form vervielfältigt werden noch an Dritte weitergegeben werden.
Es gilt nur für den persönlichen Gebrauch.

Dieses Werk ist copyrightgeschützt und darf in keiner Form vervielfältigt werden noch an Dritte weitergegeben werden.
Es gilt nur für den persönlichen Gebrauch.

Acronyms

ASE	amplified spontaneous emission
AWG	arbitrary waveform generator
AWGN	additive white Gaussian noise
BFS	Brillouin frequency shift
BGS	Brillouin gain spectrum
BLS	Brillouin loss spectrum
BOCDA	Brillouin optical correlation-domain analzyer
BOFDR	Brillouin optical frequency-domain reflectometry
BOTDA	Brillouin optical time-domain analyzer
BOTDR	Brillouin optical time-domain reflectometry
BPF	band-pass filter
BPS	Brillouin phase spectrum
Cir	circulator
CW	continuous wave
DDMZM	dual-drive Mach-Zehnder modulator
DFB	distributed feedback
DPMZM	dual-parallel Mach-Zehnder modulator
EDFA	Erbium-doped fiber amplifier
ER	extinction ratio
ESA	electrical spectrum analyzer
FBG	fiber Bragg grating
FM	frequency modulation
FUT	fiber under test
FWHM	full width at half maximum
FWM	four wave mixing
ISO	isolator
LD	laser diode
LDC	laser diode current controller
$LiNbO_3$	lithium niobate

Dieses Werk ist copyrightgeschützt und darf in keiner Form vervielfältigt werden noch an Dritte weitergegeben werden.
Es gilt nur für den persönlichen Gebrauch.

LSB	lower frequency sideband
MI	modulation instability
MPF	microwave photonic filter
MPNF	microwave photonic notch filter
MZM	Mach-Zehnder modulator
NLE	non-local effect
O-BPF	optical band-pass filter
OC	optical coupler
OFDR	optical frequenc-domain reflectometry
OS	optical switch
OSA	optical spectrum analyzer
OTDR	optical time-domain reflectometry
PBS	polarization beam splitter
PC	polarization controller
PD	photodiode
PM	phase modulator
RF	radio frequency
RFG	radio frequency generator
SA-BOTDA	slope-assisted Brillouin optical time-domain analyzer
SBS	stimulated Brillouin scattering
SG	signal generator
SMF	single mode fiber
SNR	signal-to-noise ratio
SOA	semiconductor optical amplifier
SOP	state of polarization
SpBS	spontaneous Brillouin scattering
SPM	self-phase modulation
TDCM	tunable dispersion compensation module
USB	upper frequency sideband
VOA	variable optical attenuator
XPM	cross-phase modulation

Dieses Werk ist copyrightgeschützt und darf in keiner Form vervielfältigt werden noch an Dritte weitergegeben werden.
Es gilt nur für den persönlichen Gebrauch.

Contents

Dieses Werk ist copyrightgeschützt und darf in keiner Form vervielfältigt werden noch an Dritte weitergegeben werden.
Es gilt nur für den persönlichen Gebrauch.

Dieses Werk ist copyrightgeschützt und darf in keiner Form vervielfältigt werden noch an Dritte weitergegeben werden.
Es gilt nur für den persönlichen Gebrauch.

Dieses Werk ist copyrightgeschützt und darf in keiner Form vervielfältigt werden noch an Dritte weitergegeben werden.
Es gilt nur für den persönlichen Gebrauch.

Dieses Werk ist copyrightgeschützt und darf in keiner Form vervielfältigt werden noch an Dritte weitergegeben werden.
Es gilt nur für den persönlichen Gebrauch.

1 Introduction

The field of optics and photonics has a long history. It starts with the development of lenses by the ancient Egyptians and Mesopotamians, followed by theories on light and vision developed by ancient Greek philosophers, and the development of geometrical optics in the Greco-Roman world. In between, the ancient Greek mathematician Euclid described the law of reflection at about 300 B.C., the Roman astronomer Ptolemy tried to experimentally derive the law of refraction in the 2nd century and the Persian mathematician and physicist Ibn Sahl discovered the full law of refraction in 984 B.C., which is later well-known as the Snell's law. Based on these behaviors, light is first treated as discrete particles which travel in a straight line with a finite velocity in Newton's corpuscular theory of light. Until Thomas Young and Augustin Fresnel demonstrated the interference and diffraction of light in 1801 and 1818, respectively, the wave theory of light proposed by the Dutch physicist Christiaan Huygens in 1678 has been accepted. Later on in 1865, the Scottish scientist James Clerk Maxwell deduced further that light is an electromagnetic wave, and can be well described by electromagnetic wave theory.

1.1. Basics of Electromagnetic Wave Theory

Like all forms of electromagnetic radiations, the optical wave also follows Maxwell's equations. Its well known mathematical expressions are as follows: [1, 2]

$$\nabla \times \mathbf{E} = -\frac{\partial \mathbf{B}}{\partial t} \tag{1.1.1a}$$

$$\nabla \times \mathbf{H} = \mathbf{J} + \frac{\partial \mathbf{D}}{\partial t} \tag{1.1.1b}$$

$$\nabla \cdot \mathbf{D} = \rho_f \tag{1.1.1c}$$

$$\nabla \cdot \mathbf{B} = 0 \tag{1.1.1d}$$

Dieses Werk ist copyrightgeschützt und darf in keiner Form vervielfältigt werden noch an Dritte weitergegeben werden.
Es gilt nur für den persönlichen Gebrauch.

where $\mathbf{E}$ and $\mathbf{H}$ are the electric and magnetic field vectors, respectively, with $\mathbf{D}$ and $\mathbf{B}$ as the corresponding electric and magnetic flux densities. The current density $\mathbf{J}$ and the carrier density ρ_f symbolize the sources of the electromagnetic field. For a light wave propagation in a dielectric medium without free electronic charges or currents, we have $\mathbf{J} = 0$ and $\rho_f = 0$. $\nabla\times$ and $\nabla\cdot$ represent the curl and divergence vector operators, respectively.

The relationship between the electric flux density $\mathbf{D}$ and the electric field $\mathbf{E}$ depends on the electrical properties of the medium, described by the dielectric polarization $\mathbf{P}$. The dielectric polarization is the electric dipole moment per unit volume of the dielectric material induced by an external electric field. In analog to this, the relationship between magnetic flux density $\mathbf{B}$ and the magnetic field strength $\mathbf{H}$ depends on the magnetic properties of the material described by the magnetization $\mathbf{M}$, which is defined similarly to the dielectric polarization. The relations between the flux densities and the field strengths are given by: [1]

$$\mathbf{D} = \varepsilon_0\mathbf{E} + \mathbf{P} \tag{1.1.2a}$$

$$\mathbf{B} = \mu_0(\mathbf{H} + \mathbf{M}) \tag{1.1.2b}$$

where ε_0 and μ_0 are the permittivity and permeability of vacuum. For a non-magnetic medium, such as optical fibers, $\mathbf{M} = 0$. In a homogeneous, linear, non-dispersive and isotropic dielectric medium, the polarization $\mathbf{P}$ is aligned to and proportional to the electric field $\mathbf{E}$, that is:

$$\mathbf{P} = \chi\varepsilon_0\mathbf{E} \tag{1.1.3}$$

where the constant χ is the dielectric susceptibility. The substitution of Eq. (1.1.3) in Eq. (1.1.2a) yields:

$$\mathbf{D} = \varepsilon_0(1+\chi)\mathbf{E} = \varepsilon\mathbf{E} \tag{1.1.4}$$

showing that, $\mathbf{D}$ and $\mathbf{E}$ are also parallel and proportional. Here $\varepsilon/\varepsilon_0 = 1 + \chi$ is the relative permittivity of the medium.

The wave equation for the optical wave propagation can be derive with the elimination of $\mathbf{B}$ and $\mathbf{D}$ by taking the curl of Eq. (1.1.1a) and using Eqs. (1.1.1b), (1.1.2a) and (1.1.2b), leading to: [1]

$$\nabla\times\nabla\times\mathbf{E} = -\frac{1}{c^2}\frac{\partial^2\mathbf{E}}{\partial t^2} - \mu_0\frac{\partial^2\mathbf{P}}{\partial t^2} \tag{1.1.5}$$

where $c = 1/\sqrt{\mu_0\varepsilon_0}$ is the speed of light in vacuum. By applying a Fourier transform, we can get the wave equation in the frequency domain as: [1]

$$\nabla\times\nabla\times\tilde{\mathbf{E}} = \tilde{\varepsilon}(\omega)\frac{\omega^2}{c^2}\tilde{\mathbf{E}} \tag{1.1.6}$$

Dieses Werk ist copyrightgeschützt und darf in keiner Form vervielfältigt werden noch an Dritte weitergegeben werden.
Es gilt nur für den persönlichen Gebrauch.

where $\tilde{\mathbf{E}}$ is the Fourier transform of $\mathbf{E}$, defined as

$$\tilde{\mathbf{E}} = \int_{-\infty}^{\infty} \mathbf{E} \exp(j\omega t) \mathrm{d}t \tag{1.1.7}$$

and $\tilde{\varepsilon}(\omega) = 1 + \tilde{\chi}(\omega)$ is the frequency-dependent relative dielectric constant, where $\tilde{\chi}(\omega)$ is the Fourier transform of χ. As $\tilde{\chi}(\omega)$ is in general complex, so is $\tilde{\varepsilon}(\omega)$. Its real and imaginary part represent the refractive index $n(\omega)$ and the absorption coefficient $\alpha(\omega)$ with the following definition: [1]

$$\varepsilon = (n + j\alpha c/2\omega)^2 . \tag{1.1.8}$$

Based on this definition, the refractive index and fiber attenuation can be derived as: [1]

$$n(\omega) = 1 + \frac{1}{2}\mathrm{Re}\left[\tilde{\chi}(\omega)\right] \tag{1.1.9a}$$

$$\alpha(\omega) = \frac{\omega}{nc}\mathrm{Im}\left[\tilde{\chi}(\omega)\right] \tag{1.1.9b}$$

where Re and Im denote the real and imaginary part, respectively.

If we assume the loss of the medium is low in the wavelength range of interest, the imaginary part of $\tilde{\varepsilon}(\omega)$ is small in comparison to the real part. Therefore, $n^2(\omega)$ can be used to replace $\tilde{\varepsilon}(\omega)$ for further simplifications to Eq. (1.1.6). Additionally, provided that the refractive index $n(\omega)$ is independent of the spatial coordinate, the vector identity $\nabla \times \nabla \times \mathbf{E} \equiv \nabla(\nabla \cdot \mathbf{E}) - \nabla^2\mathbf{E} = -\nabla^2\mathbf{E}$ with $\nabla \cdot \mathbf{D} = \varepsilon(\nabla \cdot \mathbf{E}) = 0$ can be utilized, leading to the following expression in form of the Helmholtz equation: [1]

$$\nabla^2\tilde{\mathbf{E}} + n^2(\omega)\frac{\omega^2}{c^2}\tilde{\mathbf{E}} = 0. \tag{1.1.10}$$

1.2. Basics of Nonlinear Optics

If the external electric field to an atom is not too high, the shift of the internal carrier acts as a field-induced dipole moment that is parallel and proportional to the external field, as indicated by Eq. (1.1.3). However, with a strong external field strength, the electrons of the dipole move in nonlinear oscillations in the Coulomb potential, whose nonlinearity can no longer be neglected [2]. The invention of the laser in 1960 enables such a high intensity and thus discovers the variety of optical nonlinear effects.

The optical nonlinear effects can be both useful attributes and characteristics to be avoided. For electromagnetic fields with high intensities, the material polarization $\mathbf{P}$ of a homogeneous material is no longer proportional to the electric field $\mathbf{E}$ and can be extended by a Taylor

Dieses Werk ist copyrightgeschützt und darf in keiner Form vervielfältigt werden noch an Dritte weitergegeben werden.
Es gilt nur für den persönlichen Gebrauch.

series as: [2, 3]

$$\mathbf{P} = \varepsilon_0 \chi^{(1)} \mathbf{E} + \varepsilon_0 \chi^{(2)} \mathbf{EE} + \varepsilon_0 \chi^{(3)} \mathbf{EEE} + \ldots = \mathbf{P_L} + \mathbf{P_{NL}} \tag{1.2.1}$$

where $\chi^{(k)}$ is the k-th order susceptibility. The dominant contribution to $\mathbf{P}$ is the linear susceptibility $\chi^{(1)}$, as described in Sec. 1.1. The second order susceptibility $\chi^{(2)}$ is responsible for the second order harmonic and sum-frequency generation. Another important effect related to $\chi^{(2)}$ is:

- Pockels effect: this linear electro-optic effect induces a refractive index change that linearly depends on the strength of the applied electric field [3]. It occurs in a medium (or crystal), whose molecule lacks inversion symmetry, such as lithium niobate ($LiNbO_3$) as the main material for electro-optic modulators [4]. Based on this principle, the modulator shifts the optical phase linearly by the external bias voltage (see Appendix B.1 for details).

For a medium with symmetric molecule, like silica as in the optical fiber, $\chi^{(2)}$ is degraded to zero. Therefore, optical fibers do not exhibit second order nonlinear effects, and the third order susceptibility $\chi^{(3)}$ is responsible for the third (also the lowest) order nonlinear effects in fibers [1]. The refractive index with the absence of the second order nonlinearity can be represented as [3]:

$$n = n_0 + n_2 I \tag{1.2.2}$$

where I is the intensity of the optical wave, defined as,

$$I = \frac{1}{2} c \varepsilon_0 n_0 |E_0|^2 \tag{1.2.3}$$

and n_0 is the linear (or low-intensity) refractive index. The nonlinear Kerr constant n_2 characterizes the strength of the nonlinear effects and can be expressed as: [3]

$$n_2 = \frac{3}{2} \frac{\chi^{(3)}}{c \varepsilon_0 n_0} \tag{1.2.4}$$

The power dependence of the refractive index leads to the Kerr effect, which includes:

- Self-phase modulation (SPM): indicates that the phase modulation can be self-induced. It occurs particularly when the intensity of the optical wave is not equally distributed in the time domain, such as a pulse. The higher intensity period of the optical wave faces a higher refractive index, while the lower intensity part encounters a lower one. Specifically for a pulse, the rising edge experiences a positive, and the falling edge a

Dieses Werk ist copyrightgeschützt und darf in keiner Form vervielfältigt werden noch an Dritte weitergegeben werden.
Es gilt nur für den persönlichen Gebrauch.

negative refractive index gradient. This time varying refractive index leads to a phase change of different parts of the pulse, also called frequency chirping. In frequency domain, this results in the rising edge shifting towards the higher frequency while the falling edge to the lower one. Whereas, the spectrum broadening will not change the original shape of the pulse in time domain.

- Cross-phase modulation (XPM): is a similar effect to SPM, but involves two or more optical waves, for instance in different frequencies, with time varying intensities. These waves interact with each other via changing the intensity dependent refractive index. Therefore, XPM is always accompanied with SPM and corporately results in a temporal phase shift that not only depends on the intensity of the optical wave itself, but also on the intensities of optical waves in other co-propagating channels. Specifically for a pulse signal, XPM will lead to an asymmetric spectrum broadening for the rising and falling edge, and a distortion on the pulse shape.

- Four wave mixing (FWM): generates a new light wave with frequency $\omega_4 = \omega_1 \pm \omega_2 \pm \omega_3$ when three light waves with frequencies ω_1, ω_2, ω_3 are simultaneously co-propagating inside the nonlinear medium. In principle, all frequencies corresponding to different plus and minus sign combinations are possible. However, most of these combinations do not practically build up because of a phase-matching requirement [5]. A narrow channel spacing, a close-to-zero dispersion and other contributions to the phase matching [6, 7] will help to fulfill the requirement and thus significantly increase the FWM efficiency.

1.3. Scattering Effects in Optical Fibers

At the end of the 19th century, the first guidance of light through bent glass rods came into life. Although uncladded glass fibers were fabricated in the 1920s, the field of fiber optics was not born until the 1950s, due to the significant benefit of using the cladding layer brought to the fiber characteristics. These early fibers suffered an extreme loss of over 1000 dB/km. After intensive and continuous engineering in purity of the glass and the fiber properties, the fiber loss was finally dropped to only 0.2 dB/km in the 1550 nm wavelength region in 1979 [8]. The residual loss comes mainly from the phenomenon of Rayleigh scattering due to the inevitable impurity of the fiber.

The nonlinear effects in optical fibers result not only from the intensity dependence of the refractive index of the medium, as discussed in Sec. 1.2 , but also due to scattering phenomena. The scattering effects occur when the light is interacting with the medium due to thermal vibrations, impurity, etc. According to the scattered wave frequency, they can be categorized

Dieses Werk ist copyrightgeschützt und darf in keiner Form vervielfältigt werden noch an Dritte weitergegeben werden.
Es gilt nur für den persönlichen Gebrauch.

into elastic and inelastic scatterings. The scattered wave frequency in an elastic scattering is identical to that of the incident wave, while an inelastic scattering shifts the scattered wave frequency, due to an interaction with the medium usually with an energy and momentum conversion. Considering the most general scenario when an incident pump wave with the frequency ν_p is coupled into a standard single mode fiber (SMF), the scattered wave would form a spectrum as depicted in Fig. 1.3.1 [3]. Based on the definition, the frequency down- and up-shifted scattered waves are called Stokes and anti-Stokes waves, respectively. According to the energy conservation, the energy flows from the pump to the Stokes wave, while the anti-Stokes wave transfer energy to compensate the depletion of the pump.

The common types of scatterings are listed as follows according to their threshold in SMF:

- Rayleigh scattering: is the scattering of light due to the steady density fluctuations. It occurs when there is impurity in solid medium, and in liquid and gas even it is a pure media. It is known as the quasi-elastic scattering owing to the zero frequency shift. Since the medium molecular re-orientation process is very rapid, the Rayleigh spectrum is usually very broad, called Rayleigh-wing [3]. Rayleigh scattering is not directional and therefore can be observed almost in every direction. Rayleigh scattering determines the limit of the optical fiber loss. Due to the high sensitivity of the phase of the Rayleigh back scattering on the external strain and temperature, phase sensitive and coherent optical time-domain reflectometry (Φ-OTDR and COTDR) are widely used for distributed fiber sensing [9].

- Brillouin scattering: is the scattering of light from sound wave, *i.e.*, propagating density (or pressure) waves. From a quantum point of view, Brillouin scattering can also be

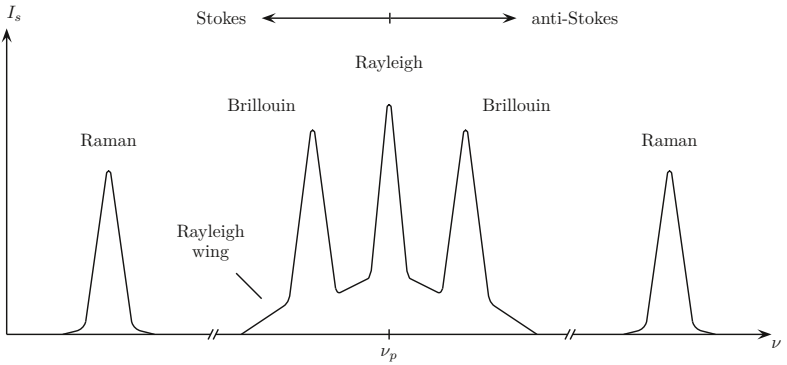

Figure 1.3.1.: Schematic of a typical spectrum of the scattering effects [3].

Dieses Werk ist copyrightgeschützt und darf in keiner Form vervielfältigt werden noch an Dritte weitergegeben werden.
Es gilt nur für den persönlichen Gebrauch.

considered as a scattering of light by acoustic phonons. In the telecommunication wavelength range, the Brillouin scattering causes a frequency shift of around 11 GHz and has a linewidth of around 30 MHz. Its wide range of applications in the field of photonics will be introduced in the rest of this thesis.

- Raman scattering: results from the interaction of light with the vibrational modes of the medium molecules. It can also be equivalently described as a scattering of light by optical phonons. Since the vibrational modes of a molecule and their Raman spectral shifts are unique, the Raman scattering are widely used for spectroscopy. For optical fibers with the incident wave in the telecommunication wavelength range, the Raman scattering shifts the scattered wave frequency by tens of THz from the incidence wave frequency and has a linewidth of tens of THz. Due to the gain mechanism on the scattered waves, Raman amplifiers are widely used in the filed of laser physics and telecommunications [10]. The Raman gain dependence on the temperature enables the Raman scattering based OTDR and optical frequency-domain reflectometry (OFDR) technique to be one of the most popular options for distributed temperature sensing [11, 12].

1.4. Structure of the Thesis

After a general introduction of the fundamental knowledge in fiber optics, the specifications about Brillouin scattering and its applications will be explained in the following chapters of this dissertation. The following content is divided into 8 chapters:

In chapter 2, a detailed theory of Brillouin scattering specifically in optical fibers will be introduced. It starts with the process from spontaneous (SpBS) to stimulated Brillouin scattering (SBS), and lies an emphasis on its theoretical model and the gain spectrum characteristics. As will also be described in the following chapters, an engineered gain spectrum would benefit a variety of applications based on SBS.

Chapter 3 is devoted to one of the popular applications of SBS, namely the distributed fiber sensing. After the introduction of common configurations of distributed Brillouin sensors, we will mainly focus on the most consolidated technique, Brillouin optical time-domain analysis (BOTDA). An improved theoretical model based on the fundamental model of SBS in chapter 2 is proposed to this technique with a generalized solution. An overview on the updates and limitations of the technique is also provided.

In chapter 4 and chapter 5, the basic idea of gain spectrum engineering by exploiting the superposition of gain and loss(es) is applied on the static and dynamic BOTDA, respectively. In the proposed static technique, the gain spectrum is engineered to have sharper shape with higher contrast than the conventional one. In this way, the peak of the spectrum is more

Dieses Werk ist copyrightgeschützt und darf in keiner Form vervielfältigt werden noch an Dritte weitergegeben werden.
Es gilt nur für den persönlichen Gebrauch.

accurate to be estimated and more robust to the inevitable noise. In the proposed dynamic technique, the proposed gain spectrum is engineered so that the linear range of the spectrum is extended. This will benefit to slope-assisted sensing for a more accurate dynamic measurement with higher strain amplitude.

In chapter 6, a general picture of another popular application of SBS, namely the microwave photonic filter (MPF) is presented. The advantages and limitations of a conventional Brillouin based MPF regarding the key performances are reviewed. In chapter 7 and chapter 8, instead of the conventional Brillouin gain interaction, novel techniques based on Brillouin loss will be proposed for optical filtering and microwave photonic notch filtering (MPNF), respectively. The proposed optical filter blocks the undesired signal with Brillouin losses and leaves the passband signal transparent. The technique has successfully circumvented the Brillouin noise and proposes a solution to this bottleneck problem of the conventional Brillouin gain based filter. The investigation on the Brillouin loss based MPNF focuses on the impairments induced by the fiber dispersion on the filter performances. It is demonstrated that, any dispersion misalignment will drastically degrade the filter performance in terms of an undesired notch frequency shift and significant lower rejection.

In chapter 9, the summary of the works in the previous chapters is presented. As a perspective and future work, an idea to apply the out-of-phase signal cancellation on the BOTDA setup is proposed. According to the theoretical investigation, the proposed method would significantly improved the signal-to-noise ratio of the gain spectrum, bringing attractive benefits for slope-assisted dynamic measurements.

Dieses Werk ist copyrightgeschützt und darf in keiner Form vervielfältigt werden noch an Dritte weitergegeben werden.
Es gilt nur für den persönlichen Gebrauch.

2 Brillouin Scattering

Brillouin scattering is named after the French physicist Léon Brillouin, who theoretically predicted the light scattering by a thermally excited acoustic wave in 1922 [13]. However, Soviet physicist Leonid Mandelstam is believed to have recognized the possibility of such scattering as early as 1918, but he published his idea only in 1926 [14]. In order to credit Mandelstam, the effect is also called Brillouin-Mandelstam scattering. The first experimental validation of this phenomenon was carried out in 1930 by Gross in crystals and liquids [15]. Limited by the available maximum optical intensity, only spontaneous process was observed at that time. Thanks to the invention of the laser, the process of stimulated Brillouin scattering (SBS) was first observed in 1964 [16]. As a popular telecommunication and nonlinear waveguide, the SBS effect in optical fibers has also been intensively studied. Its first successful experimental demonstration could date back to 1972 [17]. In the same year, the ultra-low threshold of SBS in the optical fibers was quantitatively determined [18], which makes it one of the most prominent nonlinear effects in optical fibers [19].

The investigations on the SBS in optical fibers have been split into different directions since its discovery. On one hand, the easy occurrence of SBS drastically limits the maximum incidence power and becomes a bottleneck of optical fiber communication. Several approaches have been proposed to overcome this detrimental effect, such as artificially broadening the pump spectrum [20]. On the other hand, besides microwave photonics filter and distributed sensing, which will be discussed in details in the following chapters, SBS can also be utilized in numerous applications in the filed of optics and photonics, such as fast/slow light [21–23], spectroscopy [24] and laser physics [25].

In this chapter, an overview of the physical procedures of SBS will be presented. From a simplified theoretical model and its steady-state solution, a general picture of the SBS will be provided and key issues, such as threshold and polarization dependence, will be discussed. Finally, different ways to engineer the spectral property of the Brillouin gain will be presented.

Dieses Werk ist copyrightgeschützt und darf in keiner Form vervielfältigt werden noch an Dritte weitergegeben werden.
Es gilt nur für den persönlichen Gebrauch.

2.1. Bragg Scattering of Optical Waves by Sound Waves

The Brillouin scattering is the result of the deviation of an optical wave in a density modulated material. It can be well modeled by the interaction in a Bragg scattering cell schematically shown in Fig. 2.1.1 [3]. Provided that a traveling acoustic wave of frequency ν_A is established in a scattering medium and propagates with the velocity of v_A, its wavelength can be derived as $\Lambda = v_A/\nu_A$. The density modulation of the material leads to the periodical variation of the refractive index, and thus the incident optical wave is scattered as specified by Fig. 2.1.1. Due to the phase mismatch, the scattered wave intensity is usually weak. However, the total scattered field may become strong with the help of a constructive interference when the phase match condition given by,

$$\lambda_E = 2\Lambda \sin\theta \tag{2.1.1}$$

is satisfied, where λ_E is the wavelength of the incident light and θ is the incidence angle. This condition is also known as the Bragg condition and determines the maximum wavelength that can form a constructive interference in a specific structure.

We first consider the situation when the acoustic wave is propagating in the direction of the solid arrow of v_A in Fig. 2.1.1. Taking the conservation of energy and momentum, and the wave vector diagram into consideration, we may have,

$$\nu_S = \nu_E - \nu_A \tag{2.1.2a}$$

$$\boldsymbol{k_S} = \boldsymbol{k_E} - \boldsymbol{k_A} \tag{2.1.2b}$$

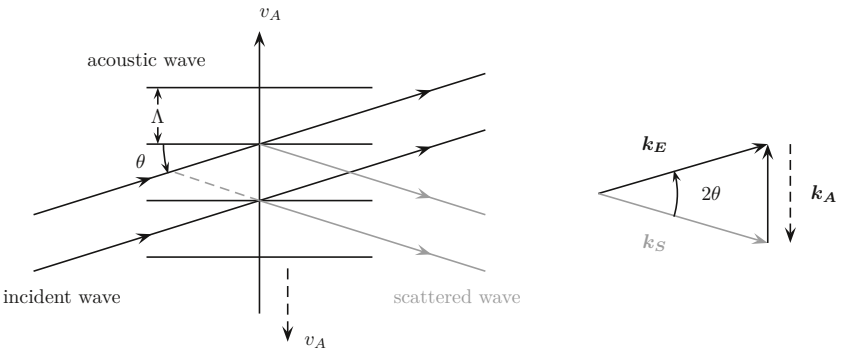

Figure 2.1.1.: Schematic of the Bragg scattering of an optical wave by an acoustic wave (left) and its wave vector diagram (right). The constructive interference will be formed when the optical path length difference between the scattered and incidence wave (dashed gray line) equals to the incidence wavelength.

Dieses Werk ist copyrightgeschützt und darf in keiner Form vervielfältigt werden noch an Dritte weitergegeben werden.
Es gilt nur für den persönlichen Gebrauch.

where $\boldsymbol{k_A}$, $\boldsymbol{k_E}$, $\boldsymbol{k_s}$ are the wave vectors of acoustic, incident and scattered wave, and ν_A, ν_E, ν_S are their corresponding frequencies. As expected from the Doppler effect, the scattered wave frequency is down-shifted in the situation when the modulated density moves away. Since ν_A is much smaller than ν_E and ν_S, we may regard $\nu_E \approx \nu_S$ and hence $|\boldsymbol{k_E}| \approx |\boldsymbol{k_S}|$. The absolute value of the wave vector of the acoustic wave can be calculated as,

$$|\boldsymbol{k_A}| = 2\,|\boldsymbol{k_E}| \sin\theta \tag{2.1.3}$$

Considering the dispersion relation of the acoustic wave $|\boldsymbol{k_A}| = 2\pi\nu_A/v_A$ and that of the incident optical wave $|\boldsymbol{k_E}| = 2\pi n/\lambda_E$, where n is the refractive index of the medium, the frequency down-shift of the scattered wave ν_A is given by [2],

$$\nu_A = \frac{2v_A n}{\lambda_E}\sin\theta \tag{2.1.4}$$

The frequency down-shifted scattered wave is defined in Sec. 1.3 as Stokes wave.

Then we consider the situation when the acoustic wave is propagating in the direction of the dashed arrow in Fig. 2.1.1. The conservation of energy and momentum are written as,

$$\nu_S = \nu_E + \nu_A \tag{2.1.5a}$$

$$\boldsymbol{k_S} = \boldsymbol{k_E} + \boldsymbol{k_A} \tag{2.1.5b}$$

After the same assumptions, it is easy to derive that the relation of Eq. (2.1.3) still holds in this situation, leading to the same frequency shift of the scattered wave as in Eq. (2.1.4). However, the scattered wave is frequency up-shifted to the incidence wave and is called anti-Stokes wave.

2.2. Spontaneous and Stimulated Brillouin Scattering

Spontaneous Brillouin scattering

Spontaneous Brillouin scattering (SpBS) occurs when an incident photon (pump wave) is transformed into a scattered photon and a phonon (acoustic wave). This initial acoustic wave could be arbitrary in the medium, such as the thermally excited motions of the material molecules, as indicated by Fig. 2.2.1 [2]. These motions act as a superposition of a large number of arbitrary acoustic waves in different directions. Only those who fulfill the geometrical requirements of the medium and follow the conservation of energy and momentum will contribute to the SpBS. Therefore, SpBS is generally weak. Depending on the structure of the fiber and the doping concentration, several guided acoustic modes may co-exist in the

Dieses Werk ist copyrightgeschützt und darf in keiner Form vervielfältigt werden noch an Dritte weitergegeben werden.
Es gilt nur für den persönlichen Gebrauch.

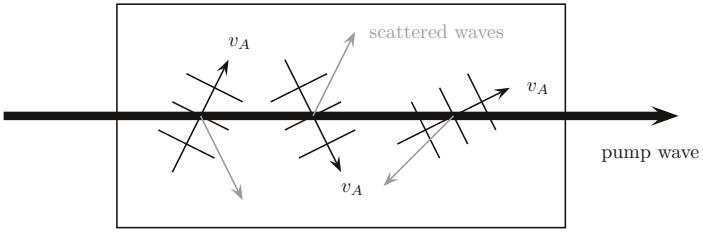

Figure 2.2.1.: Schematic process of the spontaneous Brillouin scattering.

spontaneous process, leading to multiple peaks in the spectrum of SpBS with different damping and intensity [26]. With the increase of pump power, the resonances compete with each other for the pump energy and hence, only one phonon frequency with the lowest damping and highest intensity survives, eventually leading to the SBS spectrum with a single peak [26].

Specifically for SMF, light waves could only be guided either in the forward or backward propagation direction. Therefore, the angle between the scattered wave and incident wave 2θ shall be either 0 or π. According to Eq. (2.1.4), SpBS is minimized in forward direction and occurs only in backward direction. For typical situations in SMF and a pump wavelength in the C-Band of optical telecommunications, v_A=5.96 km/s, n=1.45, λ_E=1.55 μm, the Brillouin frequency shift (BFS), here after denoted as ν_B, approximates to 11.1 GHz [1]. The general picture of SpBS in SMF is: for an incident pump wave propagating in the $+z$ direction with the frequency ν_p, a thermally excited co-propagating acoustic wave scatters a part of the pump wave into the $-z$ direction as the Stokes wave with a frequency of ν_S, while another thermally excited counter-propagating (in $-z$ direction) acoustic wave scatters part of the pump wave into the $-z$ direction as the anti-Stokes wave with a frequency of ν_{aS}. The expression of ν_S and ν_{aS} are given by,

$$\nu_S = \nu_p - \nu_B \tag{2.2.1a}$$

$$\nu_{aS} = \nu_p + \nu_B \tag{2.2.1b}$$

Nevertheless, the co-existence of Stokes and anti-Stokes wave in the SpBS [27] is no longer supported with an intense pump wave due to its transfer into the stimulated process.

Stimulated Brillouin Scattering

As described, the SpBS is raised with an incident pump wave scattered by the thermally excited acoustic waves. However, the energy transfer from the pump to the Stokes wave is very

Dieses Werk ist copyrightgeschützt und darf in keiner Form vervielfältigt werden noch an Dritte weitergegeben werden.
Es gilt nur für den persönlichen Gebrauch.

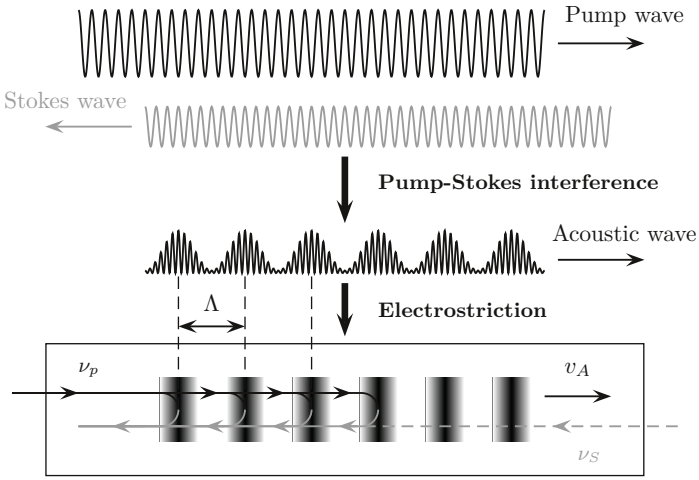

Figure 2.2.2.: Schematic process from the spontaneous Brillouin scattering (bottom solid gray curve) to stimulated Brillouin scattering with a counter-propagating optical wave (bottom dahsed gray line) via electrostriction [28].

inefficient. With a more intense pump wave, more energy is flowed towards the Stokes wave, leading to a Brillouin gain, while also more energy is transferred from the anti-Stokes to pump, resulting in a Brillouin loss and the anti-Stokes wave fading into the noise. The interference of the pump and the back scattered Stokes wave builds up a more strengthened acoustic wave, which reflects a stronger Stokes wave and stronger interference is formed, as illustrated in Fig. 2.2.2 [19]. In this way, a feedback loop is established and the SpBS is transferred to a stimulated process, *i.e.,* SBS. In comparison to SpBS, the energy transfer is much more efficient with SBS.

There are several physical mechanisms that explain the generation of the acoustic wave by the interference of the pump and Stokes wave. The most common one is the electrostriction, which describes the material characteristic of becoming more compressed in the presence of an electric field. It can be physically explained as the re-orientation of the medium molecules so that the potential energy of the medium is minimized under the external electric field [3]. Therefore, the superposition of the pump and Stokes wave periodically modulates the density. With this mechanical deformation, the refractive index of the material is also modulated correspondingly, as depicted in Fig. 2.2.2, leading to a Bragg grating structure co-propagating with the pump wave in the velocity of sound.

Despite the same origin of SBS from the electrostriction, there are two conceptually different

Dieses Werk ist copyrightgeschützt und darf in keiner Form vervielfältigt werden noch an Dritte weitergegeben werden.
Es gilt nur für den persönlichen Gebrauch.

configurations of SBS. The solid black and gray curves with arrows at the bottom of Fig. 2.2.2 show the first configuration, where only an intense pump wave with frequency ν_p is launched into the fiber. A variety of weak back scattered waves are generated by the partially scattering of the pump wave by the thermally excited acoustic waves. However, only those who satisfy the requirements of medium geometry and conservation of energy and momentum survive, and the output scattered wave frequency coincides Eq. (2.2.1a). Since the Stokes wave rises from the thermal noise in this case, this configuration is called *SBS generator* [3].

On the other hand, the second SBS configuration is demonstrated by the solid black and dashed gray curves with arrows at the bottom of Fig. 2.2.2, in which not only the pump wave but also a counter-propagating wave at frequency ν_S are involved. In the case of ν_S satisfying Eq. (2.2.1a), the envelope of the interference of the pump and the counter-propagating wave coincides the frequency difference between the two waves and co-propagates with the pump. Therefore, once the interference pattern is inscribed on the refractive index of the optical fiber via electrostriction, the back scattered wave frequency equals also to ν_S according to Eq. (2.1.1), In this way, the counter-propagating wave gets strengthened and amplified. Since the Stokes wave rises in the presence of and gets amplified from an external counter-propagating electric field in this scenario, this configuration is called *SBS amplifier* [3].

2.3. Theoretical Model and Steady-State Solution

Theoretical Model

The wave equation of an electric field in an optical fiber can be further derived from Eq. (1.1.5) with the consideration of the vector identity $\nabla \times \nabla \times \mathbf{E} \equiv \nabla (\nabla \cdot \mathbf{E}) - \nabla^2 \mathbf{E} = -\nabla^2 \mathbf{E}$ and fiber attenuation as,

$$\nabla^2 \mathbf{E}_i - \frac{n^2}{c^2}\frac{\partial^2 \mathbf{E}_i}{\partial t^2} - \frac{\alpha n}{c}\frac{\partial \mathbf{E}_i}{\partial t} = \mu_0 \frac{\partial^2 \mathbf{P}^{\mathbf{i}}_{\mathbf{NL}}}{\partial t^2} \tag{2.3.1}$$

Here α is the fiber attenuation coefficient, the polarization $\mathbf{P}$ is expanded according to Eq. (1.2.1) and only the SBS related third order term is taken into consideration as $\mathbf{P_{NL}}$. Considering the geometrical requirement in the optical fiber, the vectors can be simplified into scalars in the direction of propagation. Equation (2.3.1) is valid for both pump ($i = p$) and Stokes wave ($i = s$) in an one-dimensional SBS interaction that are given by,

$$\tilde{E_p}(z,t) = \frac{1}{2} E_p(z,t) \exp[j(\omega_p t - k_p z)] + c.c \tag{2.3.2a}$$

$$\tilde{E_s}(z,t) = \frac{1}{2} E_s(z,t) \exp[j(\omega_s t + k_s z)] + c.c \tag{2.3.2b}$$

Dieses Werk ist copyrightgeschützt und darf in keiner Form vervielfältigt werden noch an Dritte weitergegeben werden.
Es gilt nur für den persönlichen Gebrauch.

where ω_p and ω_s are the angular frequency of the pump and Stokes wave, respectively, k_p and k_s are their corresponding wave vectors that indicate the counter-propagation, and $E_p(z,t)$ and $E_s(z,t)$ are the corresponding slow-varying envelopes.

Since the back scattering of the Stokes wave is strengthened by the acoustic wave, we may safely assume that the acoustic field has the similar sinusoidal expression given by,

$$\tilde{\rho}(z,t) = \rho_0 + \frac{1}{2}\Delta\rho(z,t)\exp[j(\Omega t - Kz)] + c.c \tag{2.3.3}$$

where ρ_0 is the average density of the fiber, $\Omega = \omega_p - \omega_s$ and $\Delta\rho$ are the angular frequency and the amplitude of the acoustic wave, respectively, the acoustic wave vector $K = k_p + k_s \approx 2k_p$. Since the acoustic wave is generated due to the electrostriction, it can be described by the equation of motion for a pressure wave given by [3],

$$\frac{\partial^2\tilde{\rho}}{\partial t^2} - \Gamma\nabla^2\frac{\partial\tilde{\rho}}{\partial t} - v_a^2\nabla^2\tilde{\rho} = \nabla\cdot\mathbf{f} \tag{2.3.4}$$

where v_a is the velocity of sound, Γ is the acoustic damping parameter [3], $\mathbf{f}$ refers to the electrostrictive force per unit volume and is related to electrostrictive pressure p_{st} by $\mathbf{f} = \nabla p_{st}$ and $p_{st} = -\frac{1}{2}\varepsilon_0\gamma_e\left\langle\tilde{E}^2\right\rangle$, where γ_e is the electrostrictive coefficient and $\tilde{E}(z,t) = \tilde{E}_p(z,t) + \tilde{E}_s(z,t)$. The source term on the right side of the equation is explicitly given by,

$$\nabla\cdot\mathbf{f} = \varepsilon_0\gamma_e K^2 E_p E_s^* \exp\left[j(\Omega t - Kz)\right] \tag{2.3.5}$$

For an electrostrictive material, the nonlinear polarization in Eq. (2.3.1) can be expressed by [3],

$$P_{NL} = \frac{\varepsilon_0\gamma_e}{\rho_0}\tilde{\rho}\tilde{E} = P_{NL}^p + P_{NL}^s \tag{2.3.6}$$

with the contributions from the pump and Stokes wave written as,

$$P_{NL}^p = \frac{1}{2}\frac{\gamma_e}{\rho_0}\Delta\rho(z,t)E_s(z,t)\exp[j(\omega_p t - k_p z)] + c.c \tag{2.3.7a}$$

$$P_{NL}^s = \frac{1}{2}\frac{\gamma_e}{\rho_0}\Delta\rho^*(z,t)E_p(z,t)\exp[j(\omega_s t + k_s z)] + c.c \tag{2.3.7b}$$

The complete description of the coupling of pump, Stokes and acoustic wave can be derived by introducing Eqs. (2.3.2a) and (2.3.2b) into Eq. (2.3.1) along with Eqs. (2.3.7a) and (2.3.7b), respectively, and Eq. (2.3.3) into Eq. (2.3.4) along with Eq. (2.3.5). The coupled equations

Dieses Werk ist copyrightgeschützt und darf in keiner Form vervielfältigt werden noch an Dritte weitergegeben werden.
Es gilt nur für den persönlichen Gebrauch.

under slow-varying envelope approximation can be expressed as [29],

$$\left[\frac{\partial}{\partial z}+\frac{n}{c}\frac{\partial}{\partial t}+\frac{\alpha}{2}\right]E_p(z,t)=\frac{j\omega_p\gamma_e}{4nc\rho_0}\Delta\rho E_s(z,t) \tag{2.3.8a}$$

$$\left[-\frac{\partial}{\partial z}+\frac{n}{c}\frac{\partial}{\partial t}+\frac{\alpha}{2}\right]E_s(z,t)=\frac{j\omega_s\gamma_e}{4nc\rho_0}\Delta\rho^* E_p(z,t) \tag{2.3.8b}$$

$$\left[-2jKv_a^2\frac{\partial}{\partial z}-2j\Omega\frac{\partial}{\partial t}+\left(\Omega_B^2-\Omega^2-j\Omega\Gamma_B\right)\right]\Delta\rho=\frac{\varepsilon_0\gamma_e K^2}{2}E_p(z,t)E_s^*(z,t) \tag{2.3.8c}$$

where $\Omega_B=2\pi\nu_B$ is the angular frequency of BFS. It is also indicated from the equations that, the interaction takes place not only when the pump and probe frequency offset equals to the BFS, but also around a specific frequency range in the vicinity of the BFS. The full width at half maximum (FWHM) of the spectrum, *i.e.*, Brillouin linewidth, is defined as $\gamma_B=\frac{\Gamma_B}{2\pi}=\frac{1}{2\pi}k_B^2\Gamma$ and the phonon lifetime is given by $\tau_p=\Gamma_B^{-1}$ [3].

Steady-State Solution

The coupled wave equations are generally solved numerically. However, analytical solutions are also possible with some preliminary simplifications. For instance, if the interaction takes longer than the phonon lifetime τ_p, the evolution of three waves have reached a steady state, so that an analytical *steady state solution* can be given. Under this scenario, all time derivatives can be neglected. Besides, the spatial derivatives of the acoustic wave can also be neglected as the sound velocity is much smaller than that of the light. In this way, the acoustic wave is treated as static and does not propagate [29] in the small time period of interest. Under the consideration of these approximations, Eq. (2.3.8c) can be solved, yielding

$$\Delta\rho(z)=\frac{\varepsilon_0\gamma_e K^2}{2}\frac{E_p(z)E_s^*(z)}{\Omega_B^2-\Omega^2-j\Omega\Gamma_B} \tag{2.3.9}$$

If only a small detuning from the resonance is considered, *i.e.*, we may approximate $\Omega^2-\Omega_B^2\approx 2\Omega_B(\Omega-\Omega_B)=2\Omega_B\Delta\omega$, the expression of the acoustic field may be further simplified to a form given by,

$$\Delta\rho(z)=\frac{j\varepsilon_0\gamma_e K}{4v_a}\cdot\frac{E_p(z)E_s^*(z)}{1-2j\Delta\omega/\Gamma_B}=\frac{j\varepsilon_0\gamma_e K}{4v_a}\cdot\frac{E_p(z)E_s^*(z)}{1-2j\Delta\nu/\gamma_B} \tag{2.3.10}$$

Here the relation of $K=\Omega/v_a$ is used and $\Delta\nu=\frac{1}{2\pi}\Omega=\nu-\nu_B$ is the frequency offset to the BFS. The further substitution of Eq. (2.3.9) into Eqs. (2.3.8a) and (2.3.8b) yields to coupled

Dieses Werk ist copyrightgeschützt und darf in keiner Form vervielfältigt werden noch an Dritte weitergegeben werden.
Es gilt nur für den persönlichen Gebrauch.

wave equations in the form of:

$$\frac{d}{dz}E_p(z) = -\frac{\omega_p \gamma_e^2 \varepsilon_0 K}{16nc\rho_0 v_a} \cdot \frac{|E_s(z)|^2 E_p(z)}{1 - 2j\Delta\nu/\gamma_B} - \frac{\alpha}{2}E_p \tag{2.3.11a}$$

$$\frac{d}{dz}E_s(z) = -\frac{\omega_p \gamma_e^2 \varepsilon_0 K}{16nc\rho_0 v_a} \cdot \frac{|E_p(z)|^2 E_s(z)}{1 + 2j\Delta\nu/\gamma_B} + \frac{\alpha}{2}E_s \tag{2.3.11b}$$

Here we denote $\omega_p \approx \omega_s$. After the derivation of the conjugate expressions of Eqs. (2.3.11a) and (2.3.11b), a coupled intensity equation can be introduced with the optical intensity definition in Eq. (1.2.3) as,

$$\frac{d}{dz}I_p(z) = -g_B(\Delta\nu)I_p(z)I_s(z) - \alpha I_p(z) \tag{2.3.12a}$$

$$\frac{d}{dz}I_s(z) = -g_B(\Delta\nu)I_p(z)I_s(z) + \alpha I_s(z) \tag{2.3.12b}$$

where $g_B(\Delta\nu)$ is the inherent material SBS gain coefficient. It peaks when $\Delta\nu = 0$ with the maximum value expression of [1]

$$g_p \equiv g_B(\Delta\nu = 0) = \frac{4\pi\gamma_e^2}{n_p\lambda_p^2\rho_0 c v_A \gamma_B} \tag{2.3.13}$$

The typical value of g_p can be estimated with the electrostrictive constant $\gamma_e \approx 0.902$, the density $\rho \approx 2210$ kg/m^3, v_A=5.96 km/s in silicon fiber and the pump wave refractive index $n_p = 1.45$, pump wavelength λ_p=1550 nm, the typical FWHM of the gain spectrum γ_B=30 MHz, leading to $g_p \approx 5\times10^{-11}$ m/W.

The coupled intensity equations are also generally solved numerically. However, an analytical solution is available with further approximations, such as when the Stokes wave power is weak enough so that the pump depletion is negligible. Under this situation, we may substitute the expression of $I_p(z) = I_p(0)\exp(-\alpha z)$ in Eq. (2.3.12b), make integration over the fiber length L and get the exponential expression of the Stokes wave intensity as: [1]

$$I_s(0) = I_s(L)\exp\left(\frac{g_B P_{p0} L_{eff}}{A_{eff}} - \alpha L\right) \tag{2.3.14}$$

where $P_{p0} = I_p(0)A_{eff}$ is the input pump power, A_{eff} is the effective mode area of the fiber, L_{eff} refers to the fiber effective length and it is in relation with the physical fiber length L by:

$$L_{eff} \equiv \frac{1 - \exp(-\alpha L)}{\alpha} \overset{L\to+\infty}{=} \alpha^{-1} \tag{2.3.15}$$

Dieses Werk ist copyrightgeschützt und darf in keiner Form vervielfältigt werden noch an Dritte weitergegeben werden.
Es gilt nur für den persönlichen Gebrauch.

2.4. The Brillouin Gain

The consequence of the Brillouin interaction on the probe wave is not only a literally gain on the amplitude (intensity), but also a gain dependent phase modulation, as indicated from Eq. (2.3.11b). In this section, both amplitude and phase modulation due to SBS, *i.e.*, a complex Brillouin gain, will be introduced.

The complex SBS gain coefficient is written as [22, 23]:

$$g(\nu) = \frac{\pm \frac{1}{2} g_0 P_{p0}}{1 - j \cdot 2(\nu - \nu_B)/\gamma_B} \tag{2.4.1}$$

where ν=$|\nu_s - \nu_p|$ is the frequency offset between pump and probe wave, the positive and negative signs refer to the Brillouin gain and loss respectively, g_0 is the center SBS gain coefficient and related to the inherent material SBS gain coefficient $g_B(\nu)$ in Eqs. (2.3.12a) and (2.3.12b) with

$$g_0 = \frac{g_B(\nu_B)}{A_{eff}} = \frac{g_p}{A_{eff}} \tag{2.4.2}$$

In standard SMF at 1550 nm, ν_B is in the range of 11 GHz, γ_B approximates 30 MHz, the typical value of $g_B(\nu_B)$=5×10^{-11} m/W, A_{eff}=90 μm^2, which leads to g_0 in the magnitude of 0.2 (W·m)$^{-1}$. Under the assumption of a sufficiently high pump power so that its depletion is negligible, the probe signal at the fiber output with a length of L can be expressed as: [23]

$$\begin{aligned} E_s(L) &= E_{s0} \cdot \exp\left[g(\nu) L_{eff}\right] \cdot \exp\left(-\frac{1}{2}\alpha L\right) \\ &= E_{s0} \cdot \exp\left[G_{SBS}(\nu) L_{eff} - \frac{1}{2}\alpha L\right] \cdot \exp\left[j\Phi_{SBS}(\nu)\right] \end{aligned} \tag{2.4.3}$$

where E_{s0} is the incidence probe electric field. It is more clearly indicated from this equation that, besides the intrinsic fiber loss, the probe signal experiences both gain and dispersion from the Brillouin interaction induced via the pump wave.

- Brillouin gain (loss) spectrum

The real part of $g(\nu)$ in Eq. (2.4.1) determines the frequency dependent Brillouin gain or loss of the amplitude of the probe signal, *i.e.*, Brillouin gain spectrum (BGS) or Brillouin loss spectrum (BLS). It shows a Lorentzian shape in the frequency domain with the FWHM value of γ_B and can be written as:

$$G_{SBS}(\nu) = \frac{\pm \frac{1}{2} g_0 P_p}{1 + 4(\nu - \nu_B)^2/{\gamma_B}^2} \tag{2.4.4}$$

Dieses Werk ist copyrightgeschützt und darf in keiner Form vervielfältigt werden noch an Dritte weitergegeben werden.
Es gilt nur für den persönlichen Gebrauch.

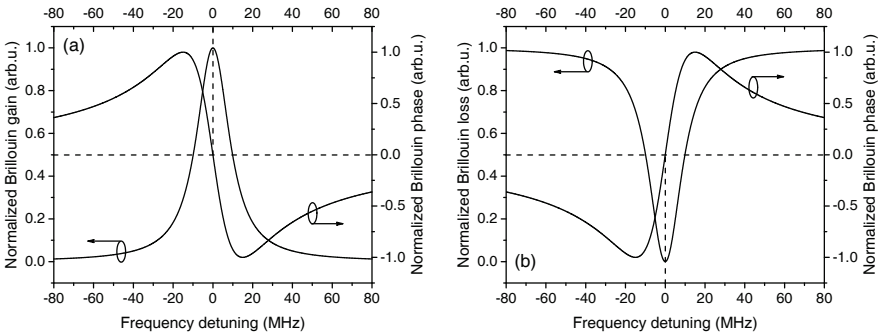

Figure 2.4.1.: Normalized (a) Brillouin gain spectrum and (b) Brillouin loss spectrum and their corresponding Brillouin phase.

- Brillouin phase spectrum

The imaginary part of $g(\nu)$ in Eq. (2.4.1) governs the phase change of the probe signal due to the Brillouin interaction. This accompanied phase change, also called *Brillouin phase spectrum* (BPS), can be physically explained by the Kramers-Kronig relations that connect the real and imaginary part of the susceptibility of a medium. Its explicit expression is given by:

$$\Phi_{SBS}(\nu) = \frac{\pm\, g_0 P_p(\nu - \nu_B)/\gamma_B}{1 + 4(\nu - \nu_B)^2/{\gamma_B}^2} \tag{2.4.5}$$

The normalized BGS and BPS are depicted in Fig. 2.4.1(a). As we can see, the BPS maximizes at the frequency, with which the BGS has the highest first-order derivative (inflection point). It is also clearly indicated that, no phase changes due to the Brillouin interaction will be introduced at the peak Brillouin gain. Both these characteristics are the direct result of the Kramers-Kronig relations and important to some of the applications, which will be introduced in the following chapters of this thesis. As discussed in Sec. 2.2, a counter-propagating probe wave frequency that satisfies Eq. (2.2.1b) will suffer from Brillouin loss by the interaction. In Fig. 2.4.1(b), the corresponding BLS and its phase change are illustrated.

2.5. Polarization Dependence

The SBS is originated from the interference between pump and probe wave. Therefore, the relative state of polarization (SOP) between the two waves plays an important role in the efficiency of the interference. However, since the SOP of both waves hover randomly in the

Dieses Werk ist copyrightgeschützt und darf in keiner Form vervielfältigt werden noch an Dritte weitergegeben werden.
Es gilt nur für den persönlichen Gebrauch.

fiber due to the weak birefringence of SMF and only an averaged interaction can be detected at the output, the dependence of the SBS gain on the SOP has been neglected for long. With the rise of the polarization maintaining technique, the polarization effect of SBS has been investigated [30] and a complete theory has been developed [31].

The SOP of pump and probe waves can be denoted by the normalized Stokes representations in the following form:

$$\mathbf{e_p} = (1, s_{1p}, s_{2p}, s_{3p}) \tag{2.5.1a}$$

$$\mathbf{e_s} = (1, s_{1s}, s_{2s}, s_{3s}) \tag{2.5.1b}$$

where (1,s_{1i},s_{2i},s_{3i}) represents the unit vector of the pump ($i = p$) and Stokes wave ($i = s$) in the Poincaré sphere, respectively, and $s_{1i}^2 + s_{2i}^2 + s_{3i}^2 = 1$. The efficiency of coherent mixing (for instance, at a receiver) of two signals with polarization $\mathbf{e_p}$ and $\mathbf{e_s}$ is given by,

$$\eta_s = \frac{1}{2}(\mathbf{e_p} \cdot \mathbf{e_s}) = \frac{1}{2}(1 + s_{1p}s_{1s} + s_{2p}s_{2s} + s_{3p}s_{3s}) \tag{2.5.2}$$

Considering the counter-propagation of the pump and probe wave, we may denote $s_3 = s_{3s} = -s_{3p}$. For a co-aligned (identically) polarization between pump and probe wave, we may note $s_1 = s_{1p} = s_{1s}$, $s_2 = s_{2p} = s_{2s}$, while for orthogonally polarized pump and probe wave, $s_1 = s_{1p} = -s_{1s}$, $s_2 = s_{2p} = -s_{2s}$, leading to:

$$\eta_{s\parallel} = \frac{1}{2}(1 + s_1^2 + s_2^2 - s_3^2) = 1 - s_3^2 \tag{2.5.3a}$$

$$\eta_{s\perp} = \frac{1}{2}(1 - s_1^2 - s_2^2 + s_3^2) = s_3^2 \tag{2.5.3b}$$

Therefore, for a fiber without birefringence (polarization maintaining fiber) and linear pump polarization, s_3=0 yields,

$$\eta_{s\parallel} = 1 \quad \eta_{s\perp} = 0 \tag{2.5.4}$$

It indicates that, by aligning the input SOP of pump and probe wave in polarization maintaining fibers, we could achieve a full gain or completely suppression of SBS interaction. For fibers with linear birefringence (SMF), $s_3 = \cos\phi$ where ϕ is the optical phase difference between the fast and the slow axis [31]. Due to the uniform distribution of ϕ, the mean value of s_3^2 is $\frac{1}{2}$, yielding:

$$\eta_{s\parallel} = \frac{1}{2} \quad \eta_{s\perp} = \frac{1}{2} \tag{2.5.5}$$

In a similar way, the mean value of s_1^2, s_2^2 and s_3^2 are equally $\frac{1}{3}$ for a scrambled relative

Dieses Werk ist copyrightgeschützt und darf in keiner Form vervielfältigt werden noch an Dritte weitergegeben werden.
Es gilt nur für den persönlichen Gebrauch.

polarization input. Therefore, the resulted mixing efficiencies are given by,

$$\eta_{s\parallel} = \frac{2}{3} \quad \eta_{s\perp} = \frac{1}{3} \tag{2.5.6}$$

With the introduction of the polarization mixing efficiency factor η_s, the coupled intensity equations in Eqs. (2.3.12a) and (2.3.12b) can be re-written as:

$$\frac{d}{dz}I_p(z) = -\eta_s g_B(\Delta\nu) I_p(z) I_s(z) - \alpha I_p(z) \tag{2.5.7a}$$

$$\frac{d}{dz}I_s(z) = -\eta_s g_B(\Delta\nu) I_p(z) I_s(z) + \alpha I_s(z) \tag{2.5.7b}$$

2.6. Threshold

One of the important parameters that describe the SBS interaction is the threshold, from where the reflected power starts to rapidly increase. Figure 2.6.1 shows a typical measurement of the input (pump) and output (transmission and reflection) power of an SBS interaction in a 20 km SMF with a distributed feedback (DFB) laser. As it is clearly indicated, the transmission output curve can be divided into 3 different stages:

- stage I - input power smaller than 7 dBm: the reflection power is weak and grows with almost the same slope as the transmission power when the input power increases. The reflection power at this stage consists mainly of SpBS and Rayleigh back scattering.

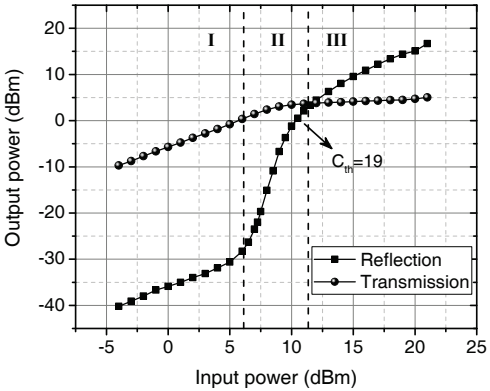

Figure 2.6.1.: Measurement of the transmitted and reflected power with respect to the input power for a 20 km SMF. The SBS threshold with C_{th}=19 is highlighted.

Dieses Werk ist copyrightgeschützt und darf in keiner Form vervielfältigt werden noch an Dritte weitergegeben werden.
Es gilt nur für den persönlichen Gebrauch.

- stage II - input power range from 7 dBm to 11 dBm: the reflection power increases rapidly and significantly, while the growth rate of the transmission power decreases. In this stage, the acoustic wave is gradually strengthened due to the intensified interference between pump and SpBS via electrostriction.

- stage III - input power higher than 11 dBm: the reflection power keeps growing with the same slope as in stage I, while the transmission power remains almost constant. In this stage, the acoustic wave is completely established and the SBS process is fully formed. All the further launched input power is totally reflected.

As implied from the above analysis, the formation of SBS, or to be more specified, the generation of the acoustic wave, is a gradual process instead of an instantaneous turning point. Therefore, there are a variety of definitions on the threshold of SBS and almost all of them are within stage II. The typical definitions are: [32]

- the input power that is equal to the reflection power;

- the input power that makes the reflection power equal to the transmitted power;

- the input power that is required for a strong increase of the reflection power or a strong decay of the pump power;

- the input power at which the reflection power at the fiber input equals to 1% of the input power;

Under the assumption of a negligible pump depletion, the expression of the above mentioned threshold definitions can be concluded along with Eq. (2.3.14) in a form given by,

$$P_{th} \equiv C_{th} \frac{K_B A_{eff}}{g_p L_{eff}} \tag{2.6.1}$$

where $K_B = \eta_s^{-1}$ is a polarization factor between 1 and 2 [31]. Similar to the case of η_s in Sec. 2.5, K_B is minimized with K_B=1 when the pump and probe wave are co-polarized along the whole fiber, for instance in a polarization maintaining fiber. If pump and probe wave have completely random polarization, K_B=1.5. The conventional SMF show a value of K_B=2 [31, 32]. The value of C_{th} depends on the specific definition. Smith proposed the first model and defined $C_{th} \approx$21 [18]. Later on, it was revised and improved with different models and theories, leading to different values of C_{th} [33, 34]. For the time being, the most acceptable value recommended by ITU to adapt is C_{th}=19 [32]. As it is clearly indicated in Eq. (2.6.1), the threshold decreases with the fiber length. However, with an increasing physical fiber

Dieses Werk ist copyrightgeschützt und darf in keiner Form vervielfältigt werden noch an Dritte weitergegeben werden.
Es gilt nur für den persönlichen Gebrauch.

length L, the convergence of the effective length in Eq. (2.3.15) leads to a convergent value of the threshold [2]. In standard SMF, g_p=2×10^{-11} m/W, A_{eff}=80 μm^2, K_B=2, α=0.2 dB/km, if we take C_{th}=19, the estimated threshold for 5 km, 20 km and 50 km fiber are 34.03 mW (15.32 dBm), 11.63 mW (10.66 dBm) and 6.55 mW (8.16 dBm), respectively.

2.7. Gain Spectrum Engineering

The low threshold of SBS enables a variety of applications. However, the performance of almost all the SBS related applications rely on the spectrum characteristics of the Brillouin gain, such as the filter profile of the SBS based microwave photonics filter [35] and the measurand resolution of the distributed Brillouin sensors [36]. Numerous efforts have been made to manipulate the BGS profile, which includes linewidth control and shape engineering, to meet the requirements of a variety of applications. In this section, the most popular BGS controlling methods together with pros and contras will be introduced.

Pump Modulation

Modulation on the pump wave is one of the most common ways for BGS manipulation. If the pump power spectrum is polychromatic, it can be decomposed as a summation of multiple monochromatic waves. Since each wave has its individual SBS spectral response, an overall spectrum response is the result of the summation of all the separate contributions. This principle can be mathematically written as: [21]

$$G_{SBS}^{eff}(\nu) = G_{SBS}(\nu) * \frac{P_p(\nu)}{P_p^{tot}} \tag{2.7.1}$$

where $*$ denotes the convolution operator, $P_p(\nu)$ is the pump spectral density, P_p^{tot} is the total pump power given by the integral of the spectral density over the full frequency range as $P_p^{tot} = \int_0^\infty P_p(\nu)d\nu$, G_{SBS} is defined in Eq. (2.4.4) as the response of a monochromatic wave and $G_{SBS}^{eff}(\nu)$ is the overall SBS spectral response of the polychromatic pump wave.

Specifically for internal modulation, the pump wave spectrum is controlled by the time-varying laser diode operating current [37]. A change in the injection current is originally for pump intensity modulation. However, the carrier density change will inevitably lead to a corresponding change in the refractive index, which in turn modifies the lasing frequency. This phenomenon is called chirp [38–40]. The simultaneous modulation of frequency and intensity is one of the disadvantages of internal modulation. A further problem of this technique is the limited bandwidth. The maximum internal modulation bandwidth is several GHz.

Dieses Werk ist copyrightgeschützt und darf in keiner Form vervielfältigt werden noch an Dritte weitergegeben werden.
Es gilt nur für den persönlichen Gebrauch.

For external modulation, the pump wave spectrum is determined by the radio frequency (RF) signal from the RF generator (RFG) via an electrical optical modulator. One of the most commonly used modulators is the Mach-Zehnder modulator (MZM), which transfers the RF signal into an optical intensity modulation in time domain [37]. The frequency response of the modulation is the generation of symmetric sidebands centered at the carrier frequency (see Appendix B.2 for derivations). The sideband can be precisely controlled by a time-varying amplitude and frequency of the RF signal, and hence the excited BGS by the sideband as the pump wave. In comparison to internal modulation, the intensity and frequency modulation from the external modulation are independent to each other and thus more controllable. Furthermore, the modulation bandwidth can be extended to several tens of GHz.

Pump modulation could theoretically achieve any arbitrary BGS profiles when necessary feedback loop and controlling software is supplemented [41, 42]. However, due to the mathematical characteristic of the convolution operation, the overall SBS spectral response of a modulated pump wave cannot be narrower than the intrinsic Brillouin linewidth γ_B. In order to achieve a narrower BGS, several other techniques must be exploited.

Superposition

The BGS linewidth can be effectively narrowed by superimposing the Brillouin gain with two symmetric Brillouin losses with a frequency offset [43]. The superimposed BGS can be well modeled by [36, 43]

$$g_s(\nu) = g(\nu) - m \cdot g(\nu + d \cdot \gamma_B) - m \cdot g(\nu - d \cdot \gamma_B) \tag{2.7.2}$$

where $g(\nu)$ is the conventional BGS that shares the same definition in Eq. (2.4.1), m is the ratio of the maximum Brillouin loss and gain, $d = \Delta/\gamma_B$, where Δ is the frequency offset between the center of Brillouin loss and gain, γ_B is the FWHM of the conventional BGS. In Fig. 2.7.1(a), some typical superimposed gain spectra with different m and d values are depicted together with the conventional BGS.

One of the advantages of the technique is the ability to further shrink the Brillouin linewidth from the intrinsic one. However, the simultaneous decreased peak gain with the narrowed linewidth, as depicted in Fig 2.7.1(a), is also a disadvantage of the technique. This disadvantage can be mitigated when the pump modulation technique is supplemented. In comparison with the conventional BGS, the superimposed BGS with narrowed linewidth is sharper in the vicinity of the peak gain, leading to an easier determination of the peak position in a noise environment. This character is important for distributed Brillouin sensing [36] and Brillouin based spectroscopy [44].

Dieses Werk ist copyrightgeschützt und darf in keiner Form vervielfältigt werden noch an Dritte weitergegeben werden.
Es gilt nur für den persönlichen Gebrauch.

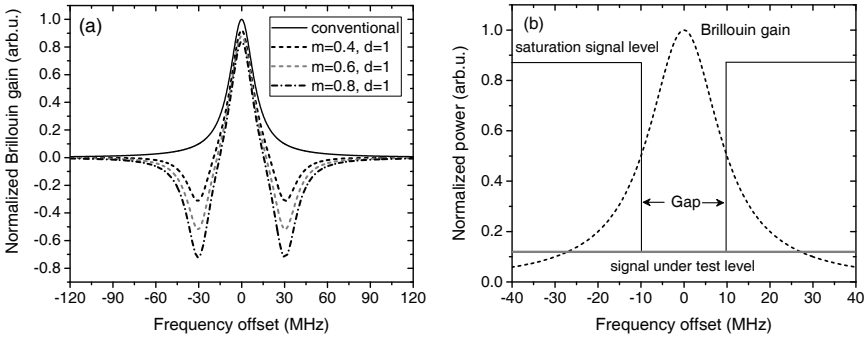

Figure 2.7.1.: (a) Conventional (solid) and typical superimposed BGS; (b) schematic principle of the frequency domain aperture.

Frequency Domain Aperture

Another possibility to engineer the BGS is to utilize the frequency domain aperture. It takes the advantage of the characteristic of inhomogeneous Brillouin gain saturation [45]. The key factor of this technique is the dependence of the Brillouin amplification on the probe wave signal, when the probe power is high. It is approximated that the pump wave transfers energy to the probe signal in an SBS interaction with a negligible depletion if the probe signal is weak. However, this approximation is no longer valid when the probe intensity grows significantly to the same magnitude as the pump. The pump is strongly depleted in this scenario, yielding to a gain saturation of the probe intensity and making the further amplification of the probe signal impossible [3]. A deeper investigation on the saturation effect can be found in [46, 47].

The inhomogeneous gain saturation characteristic enables the saturation effect to occur only at the specific probe frequency without interferences to the gain processes in other frequencies of the BGS. This phenomenon is also called spectral hole-burning [48]. The principle of the frequency domain aperture can be schematically explained in Fig 2.7.1(b). Two spectrum broadened saturation signals with high intensity (black solid line level) is utilized to saturate both edges of the BGS (dashed curve), creating an aperture structure in the frequency domain. Only the probe wave whose frequency is located in the gap and with an intensity lower than the signal under test level (gray solid line level) could be amplified by Brillouin interaction. The Brillouin linewidth to be achieved approximates the gap span, and can be precisely tuned by the frequency separation between the saturation signals. An experimental linewidth reduction from 16 MHz to 3 MHz has been demonstrated in [49]. In contrast to the pump modulation, the frequency domain aperture could only narrow the BGS linewidth.

Dieses Werk ist copyrightgeschützt und darf in keiner Form vervielfältigt werden noch an Dritte weitergegeben werden.
Es gilt nur für den persönlichen Gebrauch.

Dieses Werk ist copyrightgeschützt und darf in keiner Form vervielfältigt werden noch an Dritte weitergegeben werden.
Es gilt nur für den persönlichen Gebrauch.

3 Distributed Brillouin Fiber Sensing

Distributed fiber sensing is different from the traditional point sensing, *e.g.*, fiber Bragg grating [50], in that, a spatial-resolved measurement along the entire fiber length is carried out. This characteristic enables the measurement of the distribution of the measurand instead of only at discrete points. Generally speaking, the detectable range of the distributed fiber sensors is continuous and relatively large (usually the fiber length itself). However, in comparison with point sensors, the moderate spatial resolution and measurand sensitivity are the disadvantages of almost every kind of distributed fiber sensors, and a great number of efforts have been spent to avoid them. As a more cost-effective solution than applying nuermous point sensors, distributed sensors are widely used for large scale sensing applications, such as homeland security, railway surveillance, and oil and gas pipelines leakage monitoring.

Currently, almost all kinds of scattering effects in optical fibers, *i.e.*, Rayleigh [9], Brillouin [51], and Raman [11], can be utilized for distributed sensing. Among them, distributed Brillouin sensing owns the most versatile sensing system due to its sensitivity to both temperature and strain, whereas Raman scattering-based distributed sensors are only sensitive to temperature [52]. In addition, Brillouin sensors provide the absolute measurement result, but the Rayleigh scattering-based sensors can only offer a relative value between two measurements [53]. Besides, the low Brillouin threshold and high Brillouin gain make the detection of the sensing response also much easier. As a result, distributed Brillouin sensing draws the most attention and develops rapidly since its first demonstration three decades ago [54, 55].

The conventional SBS interaction happens between two continuous waves (CW). According to the coupled intensity equation in Eqs. (2.3.12a) and (2.3.12b), the Brillouin gain between the two waves at each fiber section is accumulated along the fiber, leading to a relative high gain detected by a receiver. Nevertheless, this accumulation is not a benefit for a spatial-resolved measurement, since this accumulation makes it difficult to distinguish the information of local interaction from each fiber section. Some changes and also advanced techniques need

Dieses Werk ist copyrightgeschützt und darf in keiner Form vervielfältigt werden noch an Dritte weitergegeben werden.
Es gilt nur für den persönlichen Gebrauch.

to be adapted for distributed Brillouin fiber sensing. In this chapter, an overview of various distributed Brillouin sensing techniques will be classified and presented, with the emphasis on the time-domain technique and its state-of-the-art performance enhancements.

3.1. Sensing Principle

The sensing principle of distributed Brillouin sensors is originated from the measurand (temperature and strain) dependent acoustic wave velocity given by, [55, 56]

$$v_a = \sqrt{\frac{Y(1-\kappa)}{(1+\kappa)(1-2\kappa)\rho}} \tag{3.1.1}$$

where Y is the Young's modulus, κ is the Poisson's ratio and ρ is the fiber density. Due to the close relation between the BFS ν_B and the acoustic wave velocity v_a via Eq. (2.1.4), the temperature [54] and strain dependence of the BFS [55] can be mathematically expressed as: [57]

$$\nu_B(T,\varepsilon) = C_T\Delta T + C_\varepsilon\Delta\varepsilon + \nu_B(T_0,\varepsilon_0) \tag{3.1.2}$$

where T_0 and ε_0 are called the reference temperature and strain, ΔT and $\Delta\varepsilon$ are the change of temperature and strain, respectively. Considering the rigidity of the optical fiber, the strain value is often expressed in microstrain ($\mu\varepsilon = \varepsilon \times 10^{-6} = \frac{\Delta L}{L} \times 10^{-6}$, where ΔL and L are the length variation and the original length, respectively). C_T and C_ε are the temperature and strain coefficient, which are dependent on the fiber doping, pump wavelength, fiber coating and jackets [57]. A good approximation of C_T and C_ε in standard SMF with a pump wavelength at 1550 nm around the near-room-temperature are 1 MHz/°C and 50 kHz/$\mu\varepsilon$, respectively [28], as the typical experimental data in Fig. 3.1.1 demonstrates [58]. Therefore, the measurand distribution can be determined by measuring the local BFS at each fiber section.

Depending on the specific configuration of the distributed Brillouin sensor, there are several ways to localize the Brillouin interaction in each fiber section (see Sec. 3.3). However, no matter what kind of configuration, BGS measurement at each fiber section has to be carried out before the BFS determination by scanning the pump-probe frequency offset typically in a range of a few hundred MHz in the vicinity of the estimated BFS [51, 59]. Additionally, the scanning range must cover the frequency shift induced by the estimated temperature (strain) variation. The local BFS is determined by the peak frequency of the local BGS. Practically, a proper fitting algorithm will be applied on the measured BGS to overcome the inevitable system noise in peak frequency determination [59, 60]. In principle, all the above mentioned techniques are valid not only for distributed fiber sensing based on Brillouin gain, but also

Dieses Werk ist copyrightgeschützt und darf in keiner Form vervielfältigt werden noch an Dritte weitergegeben werden.
Es gilt nur für den persönlichen Gebrauch.

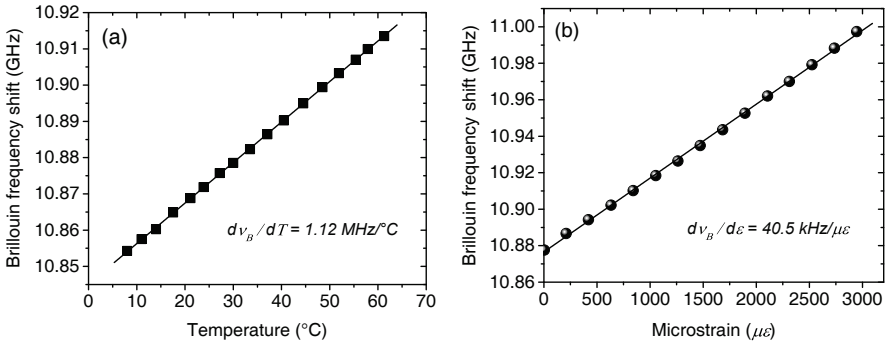

Figure 3.1.1.: BFS dependence on (a) temperature and (b) strain in a standard SMF with a pump wavelength at 1550 nm [58].

for Brillouin loss-based one. In fact, Brillouin loss based sensing techniques demonstrate an overall better performance than the Brillouin gain based one regarding long range sensing [61] and are more favorable for commercialization. For simplicity, the discussions in the following contexts will only focus on Brillouin gain based distributed fiber sensing.

3.2. Key Performances

Depending on the application, configuration and supplement techniques, the performance of a distributed Brillouin sensor can be specifically evaluated by a variety of criteria [62]. In this section, the most general performance evaluation for a distributed Brillouin sensor will be introduced. Due the intrinsic physical relations, some of the key performances are closely correlated.

- Spatial Resolution

The spatial resolution symbolizes how localize the SBS interaction is. It can also be characterized by the number of resolved points evenly distributed in the entire length of the fiber and describes the accuracy of the sensor in the spatial domain. A distributed Brillouin sensor with a high spatial resolution is able to measure the location of the measurand change more accurately and could identify the measurand change in a very small scale, such as a crack in a building. However, the higher spatial resolution is usually at the cost of a shorter interaction length in most of the configurations, leading to a lower gain and lower detected probe signal level at the receiver.

Dieses Werk ist copyrightgeschützt und darf in keiner Form vervielfältigt werden noch an Dritte weitergegeben werden.
Es gilt nur für den persönlichen Gebrauch.

- Measurand Resolution

Due to the inevitable system noise, the determination of the local BFS is not always accurate. Even with the assistance of a fitting algorithm, multiple times of measurements on the same fiber section under the same environment condition show still a deviation of the BFS value [62, 63]. The measurand resolution is characterized by the standard deviation of the BFS value after a sufficient large number of measurements (usually larger than 20 times). It symbolizes how precise the distributed Brillouin sensor could determine the measurand. A high Brillouin gain, low noise level [63] (or an overall enhanced signal-to-noise ratio (SNR) [64]) and an engineered, particularly sharp spectrum profile [36] could contribute to a higher measurand resolution. Due to this characteristic, the measurand resolution is not a constant in the entire fiber length, but higher at the pump launching end and lower at the probe launching end of the fiber, respectively. As a supplement to the spatial resolution, the measurand resolution describes the precision of the sensor in the frequency domain.

- Sensing Range

The sensing range of distributed Brillouin sensors is normally the fiber length itself. However, this is no longer valid if the probe signal is significantly attenuated and eventually faded into the system noise. This scenario occurs particularly with low (pump and probe) power, ultra-long fiber length (>100 km) [28] and high system noise. Therefore, a low system noise level, high probe power and intensive Brillouin interaction, *i.e.*, high Brillouin gain or longer interaction length, would effectively extend the sensing range.

- Measurement Time

The measurement time of a distributed Brillouin sensor is usually long (several minutes) due to several reasons. The first one is the pump-probe frequency scanning for the BGS reconstruction in most of the conventional configurations. Besides, owing to the requirement on the spatial resolution, the Brillouin interaction efficiency in sensing is not as high as the conventional CW-interaction. Therefore, a large number of averaging at each pump-probe frequency offset must be applied for noise reduction [28]. A detailed discussion about the optimization of the measurement time will be presented in Sec. 3.5.6.

- Signal-to-noise Ratio

In order to acquire environmental information in a more precise location, a higher spatial resolution is required at the cost of a shorter Brillouin interaction length in most of the scenarios, leading to a lower SNR. The sensing range is restricted at the fiber far end when

Dieses Werk ist copyrightgeschützt und darf in keiner Form vervielfältigt werden noch an Dritte weitergegeben werden.
Es gilt nur für den persönlichen Gebrauch.

the probe signal level is ambiguous to the noise after the accumulation of fiber loss. A low SNR also makes the BFS determination from the measured BGS susceptible to the noise. In order to maintain the measurand resolution, a larger number of averaging has to be carried out, leading to a more time-consuming measurement. Therefore, all the above mentioned parameters are eventually related to each other by the SNR of the system. Just like the measurand resolution, the SNR of a distributed Brillouin sensing system is also not a constant, but is decreasing with the propagation distance due to the influence of fiber loss on both the pump and probe wave.

3.3. Configurations of Distributed Brillouin Sensors

Depending on the principle used to reconstruct the local BGS, the distributed Brillouin sensors can be classified into several configurations. Basically, there are interrogation techniques in the correlation domain, denominated *Brillouin optical correlation-domian analysis* (BOCDA); in frequency domain, named as *Brillouin optical frequency-domain analysis* (BOFDA); and in time domain, called *Brillouin optical time-domain analysis* (BOTDA). Some of the interrogation techniques have the option to utilize only one end of the fiber, called *reflectometry* in the specific domain. Generally speaking, interrogation techniques based on reflectometry are more appropriate for applications, which have a strong requirement on the setup simplicity instead of measurement accuracy.

BOCDA

BOCDA is one of the most recently developed distributed Brillouin sensing technqiues [65]. In comparison to other configurations, it has an absolute advantage in its spatial resolution down to several millimeters [66] and hence, a wide range of applications on tiny crack detections in structural health monitoring [67]. This ultra-high spatial resolution is attributed to its principle based on the interaction of two identically sinusoidally frequency modulated quasi-CW pump and probe waves. Correlation peaks will be generated when the counter-propagating pump and probe meet and the frequency difference at specific sections of the fiber remains constant, similar to the principle of a standing wave depicted in Fig. 3.3.1 [68]. Brillouin interactions will take place at these correlation peaks when the frequency difference is properly set in the vicinity of the BFS of the fiber section. A scanning of the frequency difference reconstructs the BGS at the correlation peaks and by changing the modulation frequency, the BGS can be obtained along the entire length of the fiber [65].

Since the frequency difference varies (with the same period as the frequency modulation) much faster than the time required to excite an acoustic wave, the Brillouin interactions at the

Dieses Werk ist copyrightgeschützt und darf in keiner Form vervielfältigt werden noch an Dritte weitergegeben werden.
Es gilt nur für den persönlichen Gebrauch.

positions other than the correlation peaks are negligible. Therefore the spatial resolution of the BOCDA is usually high and given by the parameters of the frequency modulation as, [68]

$$\Delta z = \frac{v_g \cdot \gamma_B}{2\pi f_m \cdot \Delta f} \tag{3.3.1}$$

where v_g is the light speed in optical fibers, γ_B is the intrinsic Brillouin linewidth, f_m and Δf represent the frequency and the amplitude of the frequency modulation, respectively, as depicted in Fig. 3.3.1.

Since it is impossible for the receiver to distinguish the contributions of the Brillouin interaction from multiple correlation peaks of the fiber simultaneously, parameters of the frequency modulation should be carefully designed so that there is only one correlation peak within the fiber under test (FUT) [65]. The upper limit of the sensing range is given by the distance between the adjacent correlation peaks, expressed as: [65]

$$z_{max} = \frac{v_g}{2f_m} \tag{3.3.2}$$

Therefore, as a cost of the ultra-high spatial resolution, the sensing range of a BOCDA system is usually short with a typical value of tens of meters. Due to the scanning in both frequency and spatial domain, it is usually time-consuming to carry out a measurement with a conventional BOCDA setup.

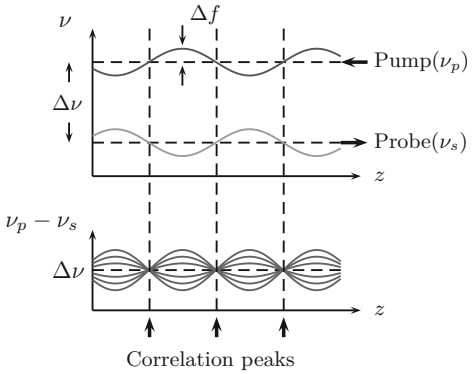

Figure 3.3.1.: Schemtaic principle of BOCDA with the Δf as the amplitude of the frequency modulation [68]. ν_p and ν_s are the pump and probe wave frequency, respectively, with $\Delta\nu = \nu_p - \nu_s$. The arrows at the bottom show the correlation peaks where the frequency difference between pump and probe wave remains constant

Dieses Werk ist copyrightgeschützt und darf in keiner Form vervielfältigt werden noch an Dritte weitergegeben werden.
Es gilt nur für den persönlichen Gebrauch.

BOFDA

The technique of BOFDA was firstly demonstrated in 1996. It relies on the measurement of the complex transfer function between the amplitude of the pump and probe waves [69]. A conventional BOFDA setup utilizes a CW pump wave counter-propagating a sinusoidally amplitude modulated quasi-CW probe wave frequency down-shifted by the BFS to the pump wave. The intensity of both waves after the interaction are recorded by two separate receivers and fed to a network analyzer. Once the frequency of the amplitude modulation has finished a scanning over a certain range, the network analyzer could provide the baseband transfer function of the FUT, whose inverse Fourier transformation is a good approximation of the response of the Brillouin interaction in each fiber section and represents the measurand distribution along the fiber [70].

Due to the characteristic of the Fourier transform, the spatial resolution and the sensing range are limited and closely link to the parameters of the amplitude modulation [69]. The spatial resolution is given by:

$$\Delta z = \frac{c}{2n} \frac{1}{f_{m.max} - f_{m,min}} \tag{3.3.3}$$

where n is the refractive index of the fiber, $f_{m.max}$ and $f_{m,min}$ are the maximum and minimum modulation frequencies, respectively. The sensing range is denoted as:

$$z_{max} = \frac{c}{2n} \frac{1}{\Delta f_m} \tag{3.3.4}$$

where Δf_m is the frequency step of the scanning. It is clearly indicated that, a wide range of frequency scanning with a small step could achieve both high spatial resolution and long sensing range, though at a tremendous cost of the measurement time.

BOTDA

The technique of BOTDA is the first demonstrated [54, 55] and also one of the most well-developed interrogation techniques of distributed Brillouin sensing. The schematic principle of the BOTDA is illustrated in Fig. 3.3.2(a). The Brillouin interaction is localized in time domain by exploiting a pulsed pump (or probe) wave. An acoustic wave is generated locally at the point where the pulsed pump and the probe CW meet and interact. The spatial interaction confinement determined by the pulse duration τ defines the spatial resolution of the sensor as:

$$\Delta z = \frac{1}{2} v_g \tau \tag{3.3.5}$$

Dieses Werk ist copyrightgeschützt und darf in keiner Form vervielfältigt werden noch an Dritte weitergegeben werden.
Es gilt nur für den persönlichen Gebrauch.

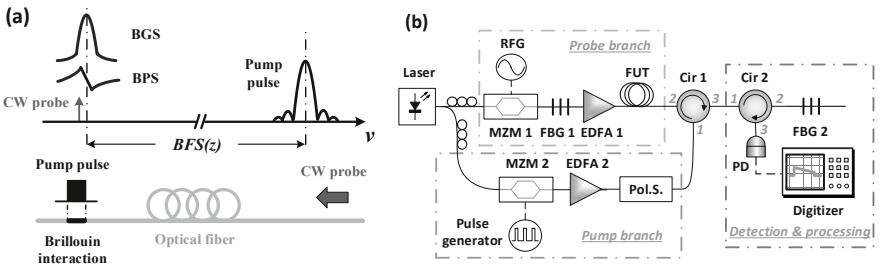

Figure 3.3.2.: (a) Schematic principle of BOTDA in frequency domain (top) and time domain (bottom); (b) typical conventional BOTDA setup [59]. RFG: radio frequency generator, MZM: Mach-Zehnder modulator, EDFA: Erbium-doped fiber amplifier, Pol.S.: polarization scrambler, FUT: fiber under test, PD: photodiode, Cir: circulator, FBG: fiber Bragg grating.

where v_g is the speed of light in the fiber and the factor 2 represents the round-trip propagation. The Brillouin interaction efficiency depends on the pump-probe frequency offset to the local BFS of the fiber section. The amplified probe wave propagates back to the photodector placed at the end of the fiber, where the time evolution of the intensity is detected. The time-dependent probe wave power, also commonly called *BOTDA trace*, can be straightforwardly converted into the distance-dependent information via $z = v_g t/2$. This round-trip relation also regulates the minimum pump pulse launching period to avoid trace overlapping. The local BGS at each fiber section can be reconstructed by scanning the pump-probe frequency offset in the vicinity of the estimated BFS and the local BFS is determined by applying a fitting algorithm to the measured local BGS at each fiber section.

As illustrated in Fig. 3.3.2(b), a typical conventional BOTDA setup is comprised of three parts. The output from a highly coherent laser source is split via a coupler into two branches. In the upper probe branch, the Mach-Zehnder modulator (MZM 1) operated in the carrier suppression regime is modulated by an RF signal from an RF generator (RFG), which scans the RF signal in the vicinity of the BFS (≈11 GHz) over a range of several hundreds of MHz. A fiber Bragg grating (FBG 1) works as a narrow band-pass filter to block the generated upper frequency sideband and the lower one serves as the probe wave. Before launching into the FUT, the probe power is controlled and amplified by an Erbium-doped fiber amplifier (EDFA 1). In the upper pump branch, the pump wave is pulsed to a required duration by another MZM (MZM 2) operated by a pulse generator. The pump power is also amplified and controlled by an EDFA before launching into the FUT via the circulator (Cir 1). The polarization scrambler (Pol.S.) has to be used to randomize the polarization of either pump or probe wave to mitigate the influence of the SBS polarization effect [71], as generally introduced

Dieses Werk ist copyrightgeschützt und darf in keiner Form vervielfältigt werden noch an Dritte weitergegeben werden.
Es gilt nur für den persönlichen Gebrauch.

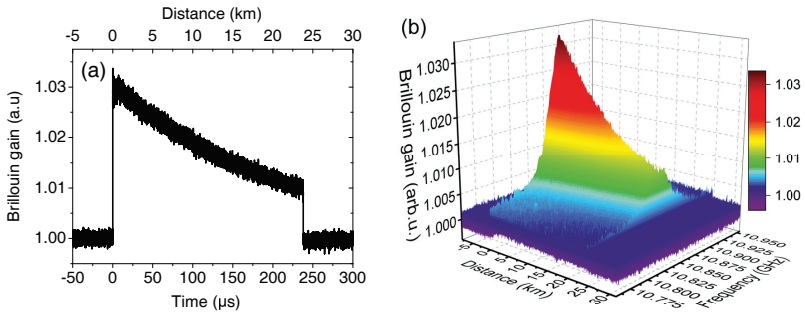

Figure 3.3.3.: A typical (a) BOTDA trace of a 25 km SMF at a specific pump-probe frequency offset and (b) the reconstructed 3D BGS along the fiber [59].

in Sec. 2.5.

In the detection and processing part, the time evolution of the amplified probe wave is detected by a photodiode (PD). In order to avoid any trace distortions, the relation between the pulse duration τ and the minimum bandwidth of the PD should follow $BW_{min} = 1.5/\tau$ [72]. This is only valid for the pulses with an optimized rising/falling time of $\tau/3$ [73]. For pulses with sharper rising edge and shorter rising time t_r, the bandwidth follows $t_r \cdot BW_{min} \approx 0.35$ [63, 74]. Another narrow band-pass filter (FBG 2) is usually utilized to block the residual reflected and Rayleigh scattered pump wave before the detection. The electric output from the PD is digitally processed by a digitizer with a large number of averaging. As a typical BOTDA trace

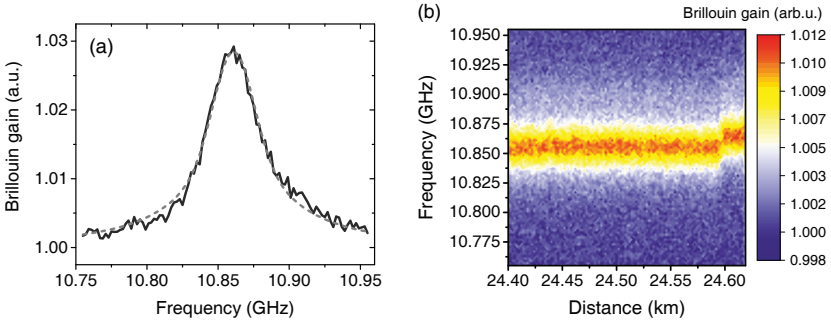

Figure 3.3.4.: A measured BGS (solid) at a specific fiber section fitted by a Lorentzian function (dashed); (b) a top view of the reconstructed Brillouin gain with a 20 m hot spot at the fiber end [59].

Dieses Werk ist copyrightgeschützt und darf in keiner Form vervielfältigt werden noch an Dritte weitergegeben werden.
Es gilt nur für den persönlichen Gebrauch.

in Fig. 3.3.3(a) depicts, the local Brillouin gain can be derived by dividing the electrical signal at each fiber section (with Brillouin interaction) by the signal before the pump pulse is launched into the fiber (without Brillouin interaction) [28]. Figure 3.3.3(b) illustrates the reconstructed BGS along the fiber. A proper fitting algorithm has to be applied on the measured BGS to determine the local BFS at each fiber section [60, 75]. Figure 3.3.4(a) demonstrates an example of a Lorentzian fitting and Fig. 3.3.4(b) depicts a measured hot spot at the end of the 25 km FUT.

BOTDR

Optical time-domain reflectometry (OTDR) utilizes the localized Rayleigh back scattering under a pulsed pump wave to achieve a spatial resolved interrogation [76]. One of the advantages of this reflectometry is that, it is necessary to get access to only one end of the fiber for pump launching. The principle of Brillouin optical time-domain reflectometry (BOTDR) is the OTDR technique based on SpBS. Different from BOTDA, no probe wave is required to be launched into the fiber from the other end of fiber, which makes BOTDR advantageous for some certain practical applications. The spatial resolution in BOTDR is also confined by the pump pulse duration, sharing the same expression with Eq. (3.3.5). Since the efficiency of SpBS is not as high as SBS, the back scattered signal power is much weaker than with BOTDA. Thus, it is of great significance to employ the coherent detection with a strong optical and electrical local oscillator [51, 77]. Unlike the case of BOTDA, the pump-probe scanning for BGS reconstruction is conducted in the electrical domain with the scanning of the electrical local oscillator [51, 77]. The disadvantages due to the weak signal are the inevitable but undesired Rayleigh back scattering and the Fresnel reflection from the connectors and at the end of the fiber, from which almost all the OTDR techniques are suffering [76]. The solution for an effective mitigation is a band-pass filter, such as FBG. Nevertheless, the filter passband profile must be as rectangular as possible, so that the weak SpBS signal remains undistorted.

3.4. Theoretical Model of BOTDA

In this section, a simplified theoretical model especially for the well-developed BOTDA will be derived step by step. The pump pulse extinction ratio (ER) in this model is regarded as infinite high, so that the Brillouin interaction between the probe wave and the pulse leakage is negligible. More details about the influence of the pump pulse ER on the sensing performance will be given in Sec. 3.5.2.

The foundation of this model lies in the coupled wave equation introduced in Sec. 2.3.

Dieses Werk ist copyrightgeschützt und darf in keiner Form vervielfältigt werden noch an Dritte weitergegeben werden.
Es gilt nur für den persönlichen Gebrauch.

Considering the expression of the maximum inherent SBS gain coefficient g_p in Eq. (2.3.13), the coupled wave equations Eqs. (2.3.11a) and (2.3.11b) can be re-written as:

$$\frac{d}{dz}E_p = \left[-\frac{g_p}{2}\frac{\gamma_B}{\gamma_B - j\cdot 2\Delta\nu}|E_s|^2 - \frac{\alpha}{2}\right]E_p \tag{3.4.1a}$$

$$\frac{d}{dz}E_s = \left[-\frac{g_p}{2}\frac{\gamma_B}{\gamma_B + j\cdot 2\Delta\nu}|E_p|^2 + \frac{\alpha}{2}\right]E_s \tag{3.4.1b}$$

where $\Delta\nu = \nu_p - \nu_s - \nu_B$ is the probe wave frequency detuning from the BFS. The pump pulse is launched into the fiber from $z = 0$ and propagates in $+z$ direction, while the probe wave is launched from $z = L$ where L is the fiber length, and propagates in $-z$ direction. Provided that the pump power at the location z remains constant in a short distance of Δz, where Δz is the spatial resolution defined in Eq. (3.3.5), the integral over Δz in Eq. (3.4.1b) yields:

$$E_s(z-\Delta z) = E_s(z)\cdot\exp\left[\frac{g_p}{2}\frac{\gamma_B^2 - j\cdot 2\gamma_B\Delta\nu}{\gamma_B^2 + 4\Delta\nu^2}|E_p(z)|^2\Delta z\right]\cdot\exp\left(-\frac{\alpha}{2}\Delta z\right) \tag{3.4.2}$$

As described in Sec. 2.4, both amplitude and phase change due to the interaction have been imposed on the probe electrical field. Due to the assumption of a negligible probe-pulse leakage interaction, the probe wave suffers only from the fiber attenuation in the rest of the fiber locations, leading to the expression of the probe electrical field at the receiver as:

$$E_s(z)\Big|_{rx} = E_{s0}\cdot\exp\left[\frac{g_p}{2}\frac{\gamma_B^2 - j\cdot 2\gamma_B\Delta\nu}{\gamma_B^2 + 4\Delta\nu^2}|E_p(z)|^2\Delta z\right]\cdot\exp\left(-\frac{\alpha}{2}L\right) \tag{3.4.3}$$

where E_{s0} is the input probe electrical field, $E_s(z)|_{rx}$ represents the probe electrical field detected at the receiver after the Brillouin interaction occurred at the fiber location z. Assuming that the pump power is only affected by the fiber attenuation, *i.e.*, pump depletion is negligible, we may write the spatial evolution of the pump wave as:

$$E_p(z) = E_{p0}\exp\left(\frac{1}{2}\alpha z\right) \tag{3.4.4}$$

where E_{p0} is the input pump electrical field. The substitution of the pump power at the location z in Eq. (3.4.3) with Eq. (3.4.4) leads to the detected optical power at the receiver, given by:

$$P_s(z)\Big|_{rx} = P_{s0}\cdot\exp\left[\frac{g_0\gamma_B^2}{\gamma_B^2 + 4\Delta\nu^2}P_{p0}\exp(-\alpha z)\Delta z\right]\cdot\exp(-\alpha L) \tag{3.4.5}$$

Dieses Werk ist copyrightgeschützt und darf in keiner Form vervielfältigt werden noch an Dritte weitergegeben werden.
Es gilt nur für den persönlichen Gebrauch.

where P_{p0} and P_{s0} are the launched pump and probe wave power. Here the relation of Eq. (2.4.2) is used. This result shows a good agreements with Eq. (2.4.3) with a localized pump expression.

Due to the small Brillouin gain in most of the sensing scenarios, small gain approximation may be applied to Eq. (3.4.5), leading to,

$$P_s(z)\Big|_{rx} = P_{s0} \cdot \exp(-\alpha L)\left[1 + \frac{g_0\gamma_B^2}{\gamma_B^2 + 4\Delta\nu^2} P_{p0}\exp(-\alpha z)\Delta z\right] \tag{3.4.6}$$

where the first term is the probe wave power influence only by the fiber attenuation and the second term represents the result of the Brillouin interaction at the position z. As it is clearly indicated, a high local pump power, a longer pulse duration and a higher gain coefficient would contribute to a more efficient Brillouin interaction. The linear local Brillouin gain (on the probe power) at the fiber section z can be calculated as:

$$G_{local}(z) = \frac{P_s(z)\Big|_{rx}}{P_{s0} \cdot \exp(-\alpha L)} = 1 + \frac{g_0\gamma_B^2}{\gamma_B^2 + 4\Delta\nu^2} P_{p0}\exp(-\alpha z)\Delta z \tag{3.4.7}$$

showing an exponential decay with the fiber length. Similarly, the logarithmic local Brillouin gain shows a linear relation with the fiber length with the slope having a Lorentzian distribution to the frequency. The lowest received power is the back scattered wave from the far end of the fiber $z = L$, given by:

$$P_s(L)\Big|_{rx} = P_{s0} \cdot \exp(-\alpha L) + \frac{g_0\gamma_B^2}{\gamma_B^2 + 4\Delta\nu^2} P_{p0}P_{s0}\exp(-2\alpha L)\Delta z \tag{3.4.8}$$

where the factor of 2 in the second term indicates the round-trip relation, *i.e.*, the fiber section at $z = z_i$ will only be interrogated when the pump pulse propagates a distance of z_i to the fiber section and the amplified probe wave is back scattered to the detector with the same propagation distance, suffering a doubled fiber attenuation. In a conventional BOTDA setup, the worst sensing performance usually happens at the far end of the fiber owing to the lowest signal level [62]. As mentioned in Sec. 3.2, the sensing range of the BOTDA is no longer the fiber length if the second term of Eq. (3.4.8) is comparable to or lower than the system noise.

3.5. State-of-the-art and Limitations of BOTDA

The overall objective of the distributed Brillouin sensing is to retrieve the temperature and strain profile of the fiber with a high precision, with a large number of spatial resolved points,

Dieses Werk ist copyrightgeschützt und darf in keiner Form vervielfältigt werden noch an Dritte weitergegeben werden.
Es gilt nur für den persönlichen Gebrauch.

in a very wide spatial range. However, due to the intrinsic physical relations and limitations, a conventional BOTDA system is not able to achieve these criteria. Numerous investigations have been carried out to propose a state-of-the-art setup towards this ultimate aim. A figure of merit (FoM) [62] given by:

$$FoM = \frac{(\alpha L_{eff})^2 \exp\left[(2+f_l)\alpha L\right]}{\Delta z \sqrt{N_{Tr} N_{AV}}} \cdot \frac{\sqrt{\delta \gamma_B}}{\sigma_v} \tag{3.5.1}$$

is utilized to quantify the overall performance of a BOTDA system. A bigger value of the FoM symbolizes an overall better performance of the sensing system. L_{eff} is the effective nonlinear length of the fiber defined in Eq. (2.3.15), L is the sensing fiber length, Δz is the spatial resolution determined by the pump pulse duration in Eq. (3.3.5), N_{Tr} is the number of different traces required per frequency step, N_{AV} is the number of time-averaged traces, δ is the scanning frequency step, γ_B is the FWHM of the gain spectrum, σ_v is the standard deviation of the BFS determination. f_l is a parameter related to the setup configuration. $f_l = 1$ for loop configuration, if only half of the total fiber length is used for sensing, while $f_l = 0$ for the standard configuration, where all the fiber length is used for sensing [62]. The analytical expression of the BFS error σ_v is found with a quadrature fitting of the measured BGS as:

$$\sigma_v(z) = \frac{1}{SNR(z)} \sqrt{\frac{3\delta\gamma_B}{8\sqrt{2}(1-\eta)^{3/2}}} \quad \overset{\eta=0{,}5}{\Longrightarrow} \quad \sigma_v(z) = \frac{1}{SNR(z)} \sqrt{\frac{3}{4}\delta\gamma_B} \tag{3.5.2}$$

where $SNR(z) = \sigma(z)^{-1}$ with $\sigma(z)$ as the root-mean-square (RMS) value of the noise of the BGS measured at the fiber location z, η is the fraction of the peak value, above which all the points on the measured BGS are involved in the quadrature fitting, as illustrate in Fig. 3.5.1. For a particular case when the data points in the range of the FWHM are centered at the peak value of BGS ($\eta = 0.5$), the expression of the BFS error can be simplified. With Eqs. (3.5.1) and (3.5.2), the performance of any arbitrary BOTDA configuration can be evaluated, and it also provides a guideline for sensing performance enhancement. In this section, the most important works in the performance enhancement and intrinsic physical limitations that blocks the ultimate criteria to be achieved will be introduced.

3.5.1. Power Limits

A more intensive power of the probe and pump wave leads to a higher Brillouin gain, higher SNR, and thus an overall better sensing performance. However, considering the intrinsic physical limitations, there are several reasons to restrict the power levels.

Dieses Werk ist copyrightgeschützt und darf in keiner Form vervielfältigt werden noch an Dritte weitergegeben werden.
Es gilt nur für den persönlichen Gebrauch.

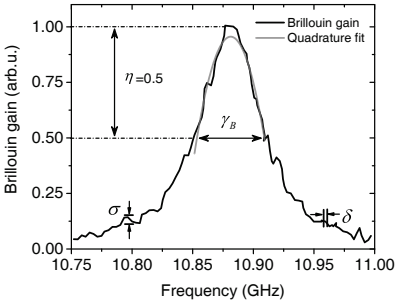

Figure 3.5.1.: Typical measured local BGS (black) and the corresponding quadrature fitting (gray) with η=0.5 [59]. An uncertainty of the BFS estimation is influenced by δ as the frequency step of the scanning, σ as the spectrum noise level and γ_B as the Brillouin linewidth [62].

Pump Wave Power

The pump power in a BOTDA system is normally referred to the pump pulse peak power P_0. It is related to the pump average power P_{avg} measured by an optical power meter and the pulse ER with the conservation of energy, given by: [78]

$$P_{avg} \cdot \frac{1}{f_{rep}} = \frac{P_0}{ER} \cdot \frac{1}{f_{rep}} + P_0 \cdot \tau \tag{3.5.3}$$

where f_{rep} is the repetition rate of the pulse sequence, τ is the pulse width. Modulation instability (MI) is one of the factors that rises when the pump pulse power is beyond a certain threshold [79]. The distortion-free propagation of an optical pulse in the optical fiber requires a good balance between Kerr effect and the anomalous dispersion [1]. However, a higher pulse power strengthens the Kerr effect and breaks the balance, so that a periodic train of localized wave packets rise from the noise. In frequency domain, this process can be interpreted as the energy transfer between the fundamental mode that constitutes the initial continuous wave and high-order Fourier modes [79], leading to the creation of symmetric side lobes centered at the pulse frequency [80]. By solving the nonlinear Schrödinger equation, the energy spread over different frequencies eventually returns to the initial mode after a definite propagation length. This reversible phenomenon is known as Fermi-Pasta-Ulam recurrence [79, 81].

Specifically for BOTDA, the FPU recurrence give rise to the oscillatory evolution of the pump power along the fiber length, leading to a strong MI-induced pump depletion and a distorted BOTDA trace when the pump power is high. As depicted in Fig. 3.5.2, some of the fiber sections are not correctly interrogated due to the strong pump depletion. The MI critical power for a conventional BOTDA with 25 km SMF is estimated to be only 135 mW [82]. Due

Dieses Werk ist copyrightgeschützt und darf in keiner Form vervielfältigt werden noch an Dritte weitergegeben werden.
Es gilt nur für den persönlichen Gebrauch.

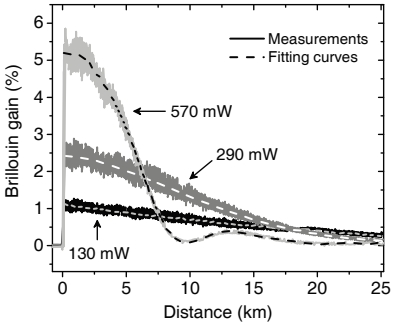

Figure 3.5.2.: BOTDA traces with distortion due to MI with various input pump powers and fitting curves [82].

to the low threshold of MI and the rapid pump depletion because of that, MI severely limits the sensing range and the overall performance of the sensing system.

Another factor that prevents the pump power from being higher is the SPM. Particular at the rising and falling edge of the pulse when the pulse shape is not perfectly rectangular, the spectral broadening effect induced by SPM is severe due to the short rising and falling time of the pulse. The detrimental outcome is the corresponding broadening of the measured BGS and thus the reduction of the measurand precision.

There are several ways for MI mitigation and further increasing the pump power, which includes:

- Noise filtering: employs a narrow band-pass optical filter to block the amplified spontaneous emission (ASE) from the EDFA for pump pulse amplification. Since the MI gain spectrum expands over a frequency range up to 60 GHz, any filters whose bandwidth are below this level would contribute to the MI mitigation. An enhanced MI mitigation performance is expected with a narrower filter [83].

- Multi-frequency pump-probe interaction: spreads the intensive total pump power beyond the MI threshold over multi-wavelengths with each single channel power below the MI threshold [84]. Consecutive FBGs separated by a certain length of fiber are utilized to solve the FWM induced by co-propagation of pump pulses in time domain. Therefore, the pump-probe interaction happens one after another instead of simultaneously. An inverse sequence of the consecutive FBGs offers a reversed delay and combines the trace back in time domain, so that a simultaneous detection can be achieved. SNR is theoretically expected to be enhanced by N times with N pump wavelengths.

Dieses Werk ist copyrightgeschützt und darf in keiner Form vervielfältigt werden noch an Dritte weitergegeben werden.
Es gilt nur für den persönlichen Gebrauch.

- Orthogonal-polarized pump pulses: circumvent the problem of FWM induced by the pulse co-propagation due to the highly polarization dependence of the FWM [1]. Owing to the unitary nature of the fiber, the orthogonality of the pulses SOP will remain the same, even though each SOP hovers in the fiber due to the slight birefringence [85]. As a consequence, the overall efficiency of the Brillouin interaction is doubled [86] with a negligible orthogonalization error induced by the polarization dependent loss [87].

Probe Wave Power

The restriction of the probe wave power is mainly due to the non-local effects (NLE) and SpBS. It is straightforward that the probe wave may excite its own acoustic wave when the probe wave power is strong enough to reach the threshold. The NLE generally refers to the fact that a local Brillouin interaction in a fiber section is influenced by the interactions in other sections. The result of this cross-interference is usually a distorted gain spectrum with more than one peak and thus, an extra error on the BFS determination of the fiber section. Please note that, not only a high probe wave power could lead to the NLE effect. A detailed discussion about the NLE caused by an imperfect pulse will be given in Sec. 3.5.2.

The NLE due to a high probe power is also called the *first-order NLE*. The pump depletion, as its origin, is usually regarded as negligible in the general model of SBS in Sec. 2.3 and in the model for BOTDA in Sec. 3.4. The magnitude of the pump depletion can be estimated in a similar way by assuming that, the probe signal is only attenuated by the fiber loss, that is, $E_s(z) = E_{s0} \exp\left[-\frac{1}{2}\alpha(L-z)\right]$ in Eq. (3.4.1a). The integral over the entire fiber length L yields the solution of the pump wave optical field as:

$$E_p(L) = E_{p0} \cdot \exp\left(-\frac{\alpha}{2}L\right) \cdot \exp\left[-\frac{g_p}{2}\frac{\gamma_B^2 + j \cdot 4\gamma_B \Delta\nu}{\gamma_B^2 + \Delta\nu^2}|E_{s0}|^2 L_{eff}\right] \tag{3.5.4}$$

where L_{eff} is the effective nonlinear length of the fiber defined in Eq. (2.3.15). The corresponding pump wave power can be written as:

$$P_p(L) = P_{p0} \cdot \exp(-\alpha L) \cdot \exp\left[-\frac{g_0\gamma_B^2}{\gamma_B^2 + \Delta\nu^2}P_{s0}L_{eff}\right] \tag{3.5.5}$$

As it is clearly indicated both from Eqs. (3.5.4) and (3.5.5) that, besides the intrinsic fiber loss, the pump wave suffers from an extra probe wave and Brillouin interaction related term, *i.e.*, pump depletion.

The influence of the pump depletion on the BGS measurement is schematically illustrated in Fig. 3.5.3(a). Since the probe wave is continuous and interacts with the pump pulse only once

Dieses Werk ist copyrightgeschützt und darf in keiner Form vervielfältigt werden noch an Dritte weitergegeben werden.
Es gilt nur für den persönlichen Gebrauch.

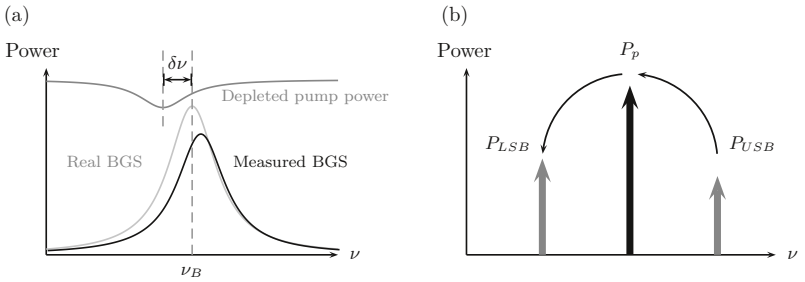

Figure 3.5.3.: (a) The schematic principle of the first-order NLE and (b) the spectral arrangement of the dual-probe regime [88].

for each time interval, the impact of the depletion is generally much higher on the pump pulse than on the probe CW. This effect of accumulation makes the pump depletion particularly severe if the sensing fiber has a uniform BFS distribution for a long distance and a short non-uniformity at the end from the probe wave launching point. Significant depletion will be generated due to the previous Brillouin interactions at the fiber sections with uniform BFS. The pump spectrum density will be no longer equally distributed in frequency domain and independent of the interaction the pump pulse has experienced before reaching the fiber section with non-uniform BFS. The first-order NLE generally leads to a biasing effect on the BGS and thus an error on the BFS. Results in Fig. 3.5.4 compare the influence of the first-order NLE on a hot spot measurement at the far and near end of the fiber.

In order to quantify this influence, a pump-probe frequency offset dependent and dimensionless depletion factor d is defined as: [88]

$$d(z) = \frac{\tilde{P}_p(z) - P_p(z)}{P_{p0}(z)} \tag{3.5.6}$$

where $\tilde{P}_p(z) = P_{p0}\exp(-\alpha z)$ is the pump power at the location z in the absence of the Brillouin interaction and its value should be independent to the pump-probe frequency offset. We may derive the expression of the depletion factor at the BFS at the output of the fiber (the launching end of the probe wave) as:

$$d(L) = 1 - e^{-g_0 P_{s0} L_{eff}} \Longrightarrow P_{s0} = -\ln\left[1 - d(L)\right]\frac{A_{eff}}{g_p L_{eff}} \approx -\ln\left[1 - d(L)\right]\frac{A_{eff}}{g_p}\alpha \tag{3.5.7}$$

The last approximation in Eq. (3.5.7) has taken the expression of Eq. (2.3.15) into consideration. For a 1 MHz tolerable error in the BFS value, the depletion factor must be smaller than

Dieses Werk ist copyrightgeschützt und darf in keiner Form vervielfältigt werden noch an Dritte weitergegeben werden.
Es gilt nur für den persönlichen Gebrauch.

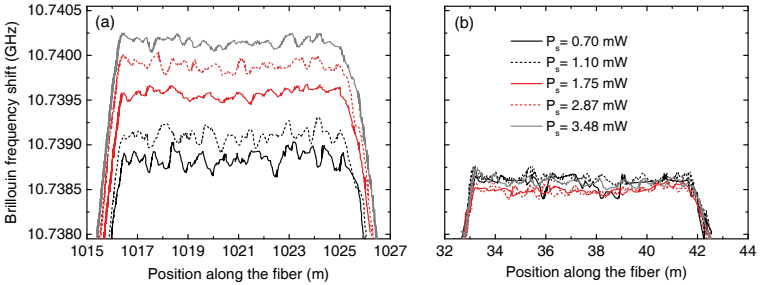

Figure 3.5.4.: BFS distribution at a 10°C warmer hot spot with different input probe power P_s when the hot spot is located at the (a) far and (b) near end of the fiber with 69 mW pump peak power [88].

0.2 [88]. This indicates a maximum input probe power of 40 μW (−14 dBm) for long sensing fibers with $L > L_{eff}$=22 km [88]. To avoid the NLE, there are the following strategies:

- Pulsed probe wave: is the most straightforward solution to avoid interrogation in undesired fiber sections [89]. The location of the fiber section under investigation, *i.e.*, the location the pump and probe pulses meet, can be controlled by the time delay between the pulses. However, besides the frequency scanning for BGS reconstruction, an extra scanning over the fiber length significantly increases the measurement time.

- Dual-probe waves: is one of the most simple solutions for first-order NLE mitigation. Instead of the single frequency probe wave in a conventional BOTDA setup, balanced dual probe waves are injected as Stokes and anti-Stokes waves with a frequency down- and up-shift by the BFS to the pump frequency, respectively. As shown in Fig. 3.5.3(b), the sidebands inevitably become unbalanced at the detector, even they are aligned balanced at the input. The reason for this behavior is that, the energy transfer from the high power (pump) to the low power (probe) is more efficient than its reverse process. Dual-probe regime could drastically rises the maximum probe wave power [88] from 40 μW (−14 dBm) to 0.5 mW (−3 dBm) for each sideband power under the same tolerable BFS error [90] with the maximum value limited by the second-order NLE. Unbalanced dual-probe wave with a higher Stokes wave reduces the compensation of the pump depletion. Considering this fact, an optimal dual-probe regime with a stronger anti-Stokes input power is proposed [91].

- Frequency-modulated probe wave: as depicted in Fig. 3.5.5(a), the *second-order NLE* is originated from the frequency-dependent spectral deformation of the pump pulse

Dieses Werk ist copyrightgeschützt und darf in keiner Form vervielfältigt werden noch an Dritte weitergegeben werden.
Es gilt nur für den persönlichen Gebrauch.

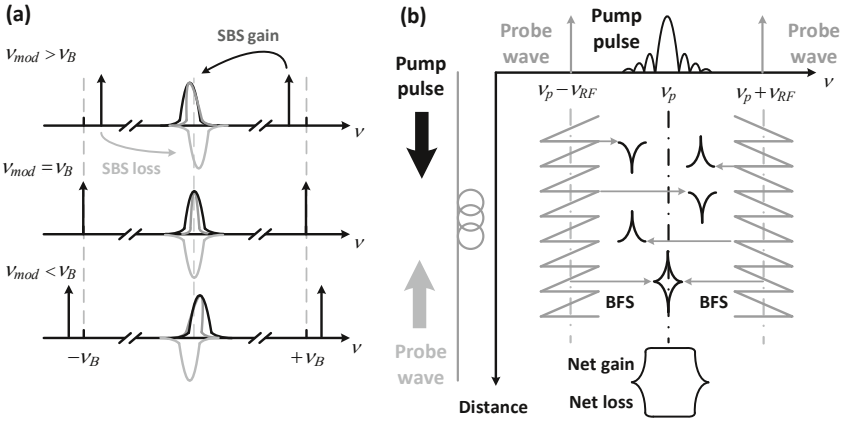

Figure 3.5.5.: (a) The schematic illustration of second-order NLE [90] and (b) the proposed dual-probe regime with additional FM to solve it [92, 93].

spectrum that affects the interaction in the gain and loss configuration differently [90]. This means that, the second-order NLE exists even with a dual-probe regime. The overall outcome of the second-order NLE is a narrowed BGS and a broadened, distorted BLS. Dual-probe sidebands with frequency modulation (FM) in saw-tooth profile provide a solution not only for first-order but also for second-order NLE mitigation [92, 93]. Provided that the FM is synchronized to the pump pulses, as illustrated in Fig. 3.5.5, a series of pulses interacts always with the same probe frequency at a specific fiber position. In turn, every single pulse experiences interactions with probe waves that have different frequency offsets during their propagation along the fiber. By interacting with different frequencies within the BGS, the pulse depletion is not accumulated and a decreased distortion on the pulse spectrum can be achieved. The mitigation of both first- and second-order NLE pushes the maximum probe power limit to 8 dBm, approaching the ultimate probe power limited by amplified SpBS in ∼20 km SMF [92]. A higher launching probe power is believed to be able to excite its own SBS process.

3.5.2. Pump Pulse Extinction Ratio

A finite pulse ER generates a leading and trailing pedestal with the same frequency as the pulse itself. Despite the lower power of the pedestal than the pulse peak, Brillouin interaction still takes place between the probe wave and pedestal before and after the main pulse-probe interaction, leading to an interference to the local interrogation from other fiber sections.

Dieses Werk ist copyrightgeschützt und darf in keiner Form vervielfältigt werden noch an Dritte weitergegeben werden.
Es gilt nur für den persönlichen Gebrauch.

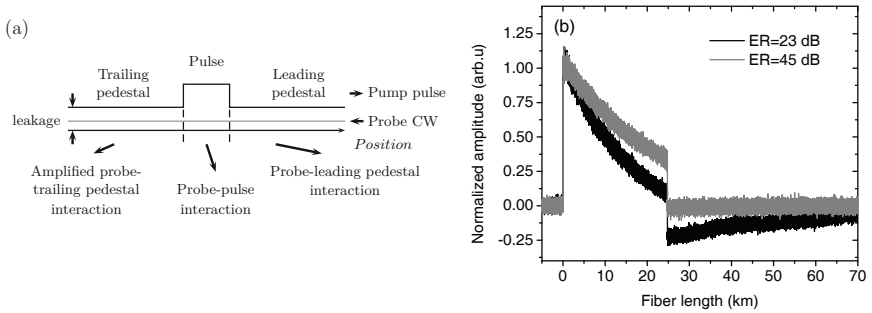

Figure 3.5.6.: (a) Scheme of pump pulse-probe interaction with limited ER and (b) the resulted distortions on the BOTDA trace [94, 95].

Therefore, the influence of a finite pulse ER can also be categorized as NLE. Since the pump pedestal has a much lower power than the pump pulse, the pedestal-probe interaction is usually spontaneous instead of stimulated, strengthening the ASE noise from the Brillouin interaction at the final detection.

The interaction between the probe wave and a pump pulse with a finite ER can be separated into three parts, as shown in Fig. 3.5.6(a). The additional pedestal-probe interaction leads to an additional amplification of the probe wave. However, these non-local amplifications bring interference to the local interrogation. In case of a strong probe wave, the pulse and pedestals, especially the trailing pedestal, will suffer from extra depletion, leading to a trace distortion in Fig. 3.5.6(b). Furthermore, the over-amplified probe wave provides interfering the BFS

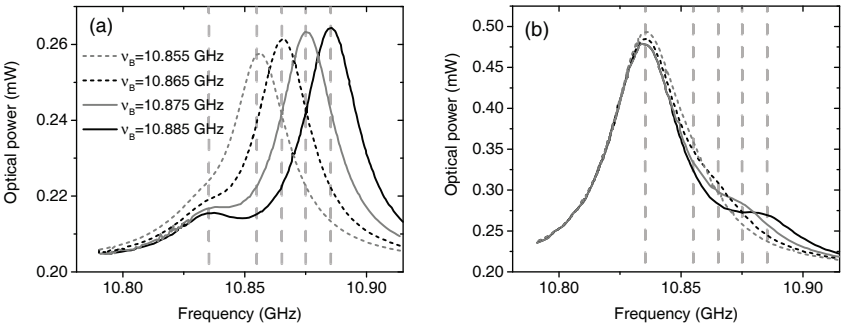

Figure 3.5.7.: The simulated BGS at the hot spots with different BFSs interrogate with pump pulse ER of (a) 40 dB and (b) 26 dB. The uniform BFS of the rest of the fiber is 10.835 GHz [96].

Dieses Werk ist copyrightgeschützt und darf in keiner Form vervielfältigt werden noch an Dritte weitergegeben werden.
Es gilt nur für den persönlichen Gebrauch.

information from other fiber sections, leading to an ambiguity in BFS determination of the local section. As demonstrated in Fig. 3.5.7, the probe-pedestal interaction may be dominant under a low ER and due to a longer interaction length than the pulse-probe interaction.

The most straight forward solution to this NLE is the enhancement of the pulse ER. A conventional MZM could only generate pulse ERs up to 20 dB. MZM with special designs could enhance this value to 30 dB. A switching type semiconductor optical amplifier (SOA) could usually suppress the pedestal by more than 40 dB. Advanced RF switch techniques offer more than 60 dB suppression of the pedestal, however, at the cost of a more complex setup [96].

3.5.3. Spatial Resolution

The round-trip relation gives the definition of the spatial resolution in Eq. (3.3.5), leading to the most straightforward way to enhance the spatial resolution with shorter pulses. However, several factors limit the spatial resolution to only 1 m.

First of all, a shorter pulse duration indicates a shorter Brillouin interaction length, and hence a lower Brillouin gain and consequently a lower SNR. Furthermore, considering the Fourier transform, the pump power spectrum for a shorter pulse will be severely broadened, leading to the correspondingly broadened effective BGS given by,

$$G_{SBS}^{eff}(\nu) = G_{SBS}(\nu) * P_p(\nu) \tag{3.5.8}$$

where $*$ denotes the convolution operator, $P_p(\nu)$ is the pump spectral density. Normally a Voigt function (a convolution of a Gaussian and Lorentzian function) is utilized to model a broadened BGS excited by short pump pulses [97]. For a quasi-monochromatic pump wave and pump pulse widths exceeding the phonon lifetime of $\sim$40 ns, the effective BGS is dominated by the intrinsic BGS with an FWHM of around 30 MHz. For shorter pump pulses with $\tau \leq$20 ns, the BGS flattens, the peak gain decreases with the FWHM of the resulted BGS approaching $1/\tau$ [28]. Moreover, it also indicates that the probe wave will be amplified only after the acoustic field is excited by the pump-probe interaction, which takes 10–30 ns. Due to the tradeoffs from the above mentioned reasons, the spatial resolution could be only enhanced to around 1 m with a shortened pulse, which corresponds to a pulse width of 10 ns. Common advanced techniques to break this limitation include:

- Differential pulse pair (DPP): utilizes two consecutive measurements with two pump pulses in the same peak power but slightly different durations [100]. The pulse widths τ and $\tau + \Delta\tau$ are both longer than the phonon lifetime, while $\Delta\tau$ is short. In this way, the acoustic fields in both measurements are fully excited. Since the amplifications to the

Dieses Werk ist copyrightgeschützt und darf in keiner Form vervielfältigt werden noch an Dritte weitergegeben werden.
Es gilt nur für den persönlichen Gebrauch.

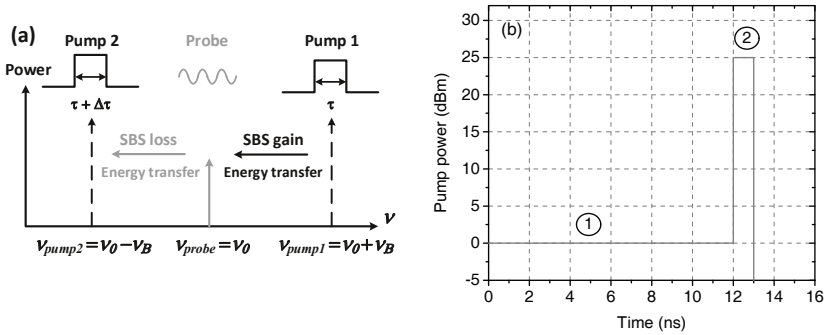

Figure 3.5.8.: Scheme of (a) simultaneous DPP-BOTDA in frequency domain [98] and (b) the time domain pulse profile in PPP-BOTDA [99]. Pulse one is utilized for acoustic wave excitation and pulse two is used for interrogation.

probe wave in both measurements from the pulse period τ is the same, the subtraction of the BOTDA traces of the two measurements yields the response of the pulse width difference $\Delta\tau$. However, two times of measurement increases the measurement time and the trace subtraction also rises the noise level by $\sqrt{2}$, leading to an additional requirement on averaging. Later on, by separating the two pump pulses in different frequencies, the DPP-BOTDA has been improved into a simultaneous measurement [98]. As the scheme principle in Fig. 3.5.8(a) illustrates, the pump pulse 1 with the duration τ transfers energy to the probe wave via Brillouin gain interaction, while the probe wave interacts with pump pulse 2 with the duration $\tau + \Delta\tau$ via Brillouin loss, leading to an automatic trace subtraction without any necessary post-processing. Despite the circumvention of the noise penalty from trace subtraction, the amplitude of the resulted trace equivalent to the short pulse response is still low. Therefore, a massive number of averaging is required in DPP-BOTDA.

- Pulse pre-pump (PPP): provides the solution to the origin of the spatial resolution limit, *i.e.*, the limited time for acoustic wave excitation. In this technique, a weak pulse with long duration (longer than the acoustic field excitation time), also called pre-pump pulse, is launched into the sensing fiber first for phonon excitation. As shown by the typical pulse shape for PPP-BOTDA in Fig. 3.5.8(b), a short pulse with high power (e.g. 25 dBm as pulse 2) and the required spatial resolution follows directly after the long pre-pump pulse (with 0 dBm power as pulse 1) for fiber section interrogation [99]. The typical effective BGS from PPP-BOTDA can be characterized as the superposition of a

Dieses Werk ist copyrightgeschützt und darf in keiner Form vervielfältigt werden noch an Dritte weitergegeben werden.
Es gilt nur für den persönlichen Gebrauch.

broadened spectrum with low amplitude and a narrow cap, whose FWHM are determined by the interrogation pulse and the pre-pump pulse, respectively. In comparison to DPP-BOTDA, the high spatial resolution by PPP-BOTDA does not come at the expense of a decreased SNR and therefore, it is more favorable for commercial use.

- Brillouin echoes: is especially designed to achieve a spatial resolution below the phonon lifetime. It employs both CW pump and probe frequencies, separated by the BFS but the phase of the pump wave is abruptly shifted by π in a small time window shorter than the phonon lifetime. During this very short time, the steady acoustic field does not have sufficient time to give reaction on the changing phase and amplitude, so that the pump will be completely reflected. The resulted destructive interference on the probe signal can be observed as a small apparent loss on the waveform [101]. Due to the existence of the pre-excited acoustic field, the BGS is normally not severely broadened, ensuring a high spatial resolution of this technique without penalty on the measurand resolution.

3.5.4. Sensing Range

Under the limit of pump and probe power of about 130 mW and 40 μW, respectively [82, 88], and a certain requirement on measurand resolution and spatial resolution, the sensing range limit of a conventional BOTDA configuration is only $\sim$60 km. This value fails to meet requirements of many applications, particularly in large scale. Common ways to extend the sensing range include: [102]

- Raman-assistance: is based on the principle of distributed gain amplification by stimulated Raman scattering [103]. An extra Raman pump at 1455 nm distributively transfers energy to the Brillouin pump, providing a good way of maintaining the pump pulse power level, and hence the Brillouin interrogation response. Despite the disadvantage of an extra noise transfer from the Raman pump source, an extension of the sensing range to above 100 km with high spatial resolution is available with Raman-assisted BOTDA.

- Coding: is a novel method that breaks the round-trip relation and enables a trace-distortion free multi-pulse propagation in the sensing fiber. In this method, the pump pulse sequence is launched into the fiber with some particular properties from an algorithm, which allow to retrieve the impulse response of the fiber sections with a corresponding decoding process. The first and the most simple form is demonstrated with the simplex coding [104]. The superimposed traces in the fiber increases the energy level received by the detector, and hence avoid the ambiguity of the sensing response from the fiber end [102]. The most advantage of this technique is its embedability to other

Dieses Werk ist copyrightgeschützt und darf in keiner Form vervielfältigt werden noch an Dritte weitergegeben werden.
Es gilt nur für den persönlichen Gebrauch.

techniques, such as pre-amplification before detection [105] and DPP technique [106] to achieve long range sensing without penalty on the spatial resolution [107]. Therefore, this algorithm based technique is particularly favorable for commercial use.

3.5.5. Signal-to-noise Ratio

The most straight forward way to enhance the SNR is either signal amplification or noise reduction. Generally, the main noise source of a BOTDA system is the detector, that is, the sensing system noise is mainly composed of thermal noise, shot noise, and the relative intensity noise (RIN) coming from the laser source [108, 109]. Comparatively speaking, the ASE noise from the Brillouin interaction is negligible due to the limited interaction length [110]. When pre-amplification before the detection is applied [105], ASE noise from the EDFA must also be taken into consideration. This will lead to a photocurrent affected by signal-ASE σ^2_{s-sp} and ASE-ASE beating noises σ^2_{sp-sp} [102, 111]. In most of the standard BOTDA configurations, the latter contribution σ^2_{sp-sp} is negligible due to the drastic bandwidth reduction when a narrowband optical filter is placed after the pre-amplifier [112]. Hence, the noise in the sensing system can be written as: [108, 111, 112]

$$\begin{aligned}\sigma^2 &= \sigma^2_{th} + \sigma^2_{sh} + \sigma^2_{RIN} + \sigma^2_{s-sp} \\ &= \frac{4k_BT}{R_L} \cdot B + 2q(\Re P_s + I_d) \cdot B + \mathrm{RIN} \cdot (\Re P_s)^2 \cdot B + 2F_N q(\Gamma - 1)\Re P_s \cdot B\end{aligned} \tag{3.5.9}$$

where σ^2_{th}, σ^2_{sh} and σ^2_{RIN} are the contributions from thermal noise, shot noise and RIN noise, respectively. K_B is the Boltzmann constant, T is the operating temperature of the detector, R_L the output resistance, $\Re$ is the detector responsivity, B is the detector bandwidth, q is the unit electron charge, I_d is the detector dark current, P_s is the input optical power, F_N is the noise figure of the EDFA (ideally F_N=2) [102] and Γ is the amplification of the detected optical signal from the pre-amplifier. Under a small input optical power, such as $P_s < -14$ dBm to circumvent the first-order NLE [88], the detector noise is generally regarded as thermal noise dominant. Besides a stable optical source to overcome the RIN noise, there are the following solutions for an SNR enhancement:

- Self-heterodyne detection: shares the same principle regarding SNR enhancement with coherent detection and balanced detection in general [113]. A strong local oscillator amplifies considerably the detected signal at the heterodyne frequency, *i.e.*, the intermediate frequency between the probe and local oscillator [108]. However, too much power from the local oscillator may bring the detector to the shot noise limit [108], leading to an SNR enhancement penalty with a rising shot noise. Therefore, it is recommended

Dieses Werk ist copyrightgeschützt und darf in keiner Form vervielfältigt werden noch an Dritte weitergegeben werden.
Es gilt nur für den persönlichen Gebrauch.

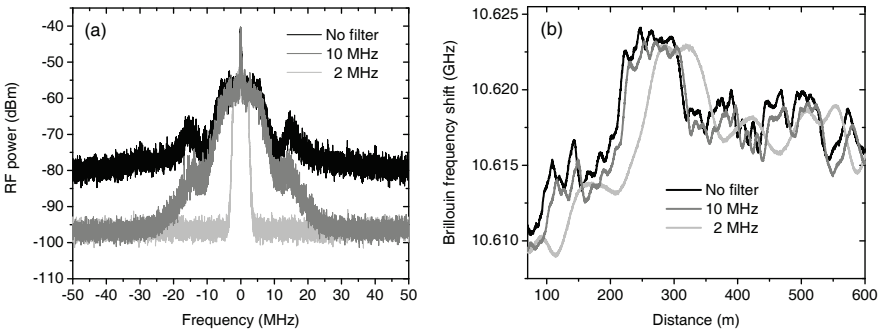

Figure 3.5.9.: Experimental results with 10 MHz and 2 MHz RF low pass filtering: (a) RF spectrum of the detected probe signal and (b) the detection of the stretched strain spot [63]. The group delay at the filter edge is observed with 2 MHz low pass filtering.

to utilize only a local oscillator with intermediate power level and keep the detector in a thermal noise dominant regime. This tradeoff is also valid for other techniques of signal amplification, such as a pre-amplification before detection [105]. In this way, it is possible to ensure a high measurand resolution while maintain the probe wave power under the limit of NLE.

- RF filtering: provides a solution for the SNR enhancement based on the bandwidth dependent detector noise [63, 114], as shown in Eq. (3.5.9). It shares the same principle as digital post-processing techniques [115]. Theoretically, the RF low-pass filtering after the photodetection could suppress the system noise by a factor of $\sqrt{B_{sys}/B_f}$, where B_{sys} is the system bandwidth and B_f is the filter bandwidth. However, two main factors prevent the noise level to be infinitely low. The first restriction factor comes from the group delay at the edge of the RF filter due to the Kramers-Kronig relations. The detrimental trace shift by the group delay may occur once the B_f is identical to the pump spectrum width, as an experimental measurement of a stretched strain spot in Fig. 3.5.9 depicts. An optimized distortion free filter bandwidth can be approximated by $t_r \cdot B_f \approx 0.35$, where t_r represents the rising time for the filter [63, 73, 74]. In this regard, for a 1 m spatial resolution BOTDA system, the optimal detector bandwidth is approximately 125 MHz [72]. The second restriction is attributed to the excess noise coming from the Brillouin interaction [63]. Its gain dependent and non-uniform frequency distribution [116] shrinks the suppression rate of the noise level from $\sqrt{B_{sys}/B_f}$.

Dieses Werk ist copyrightgeschützt und darf in keiner Form vervielfältigt werden noch an Dritte weitergegeben werden.
Es gilt nur für den persönlichen Gebrauch.

3.5.6. Measurement Time and Dynamic Sensing

The measurement time of a conventional BOTDA setup is generally in the magnitude of several minutes. Such a long duration fails to meet the requirements of numerous dynamic sensing tasks, such as a vibration monitoring of airplane wings. There are four main factors that limit the measurement speed [117], namely: (a) the time of flight, also regarded as round-trip relation with $T_{round} = 2nL/c$; (b) number of averaging N_{avg} to ensure the required SNR; (c) scanning granularity M_{freq} or also referred as scanning step; and (d) the RF frequency switching speed. The last term is usually negligible and closely related to the generation mechanism of the RF frequency. The overall time required for a complete BGS scan is given by: [117]

$$T_{scan} = N_{avg} N_{freq} T_{round} \tag{3.5.10}$$

where N_{freq} is the total number of steps of the BGS scanning. An enhancement of the SNR could reduce the requirement on the number of averaging and indirectly contribute to the shrink of the measurement time. However, the most efficient solution to reduce the measurement time is either to speed up the BGS scanning or to totally abandon it. For the latter option, a conversion from the BFS shift due to the measurand change to other physical measurands is required. Based on this analysis, the common strategies for the measurement time enhancement include:

- Fast BOTDA: provides the least required time duration for a BGS scan regulated by Eq. (3.5.10). Based on the fast switching provided by an arbitrary waveform generator (AWG) in comparison to a synthesizer based electronic sweeping mechanism, the probe waves with the scanning frequencies are launched into the sensing fiber one after another separated by the round-trip time [117]. Considering the limited fiber length for dynamic sensing tasks, the required time for single BGS scanning could be reduced to the magnitude of $\sim$100 μs. The disadvantage of this technique is the high requirement on devices memory [117]. Long length of sensing fiber and small scanning granularity requires significant amount of memory for probe waveform writing.

- Sweep-free BOTDA (SF-BOTDA): is based on the Brillouin interaction between a comb of probe and another comb of pump waves. Instead of sequential scanning, multi-tone probe waves simultaneously interrogate the fiber section with an equal number of pump pulses of matching frequencies, so that each pair of probe and pump waves scan at a different point of the Brillouin spectrum [118], as schematically depicted in Fig. 3.5.10(a). In this way, the acquisition of the BGS is sweep free and instantaneously achieved. The round-trip time and the required number of averaging are the only limit of the

Dieses Werk ist copyrightgeschützt und darf in keiner Form vervielfältigt werden noch an Dritte weitergegeben werden.
Es gilt nur für den persönlichen Gebrauch.

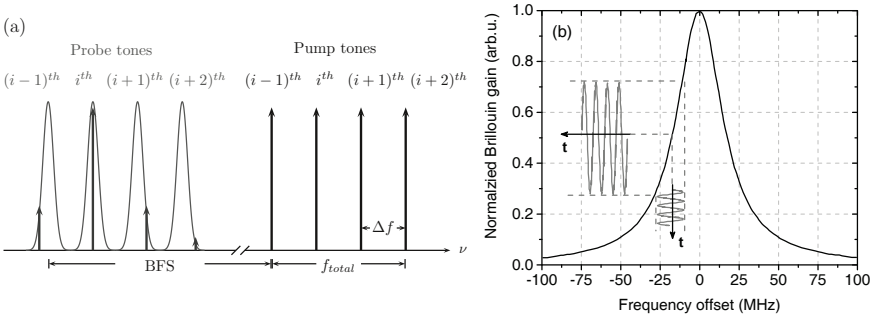

Figure 3.5.10.: Schematic principle of (a) SF-BOTDA [118] and (b) SA-BOTDA [119].

measurement time with this technique. In order to circumvent the FWM due to the pulse co-propagation [84], the pump pulses in this technique are sequentially launched, leading to a time-shift in the detected trace. Therefore, extra post temporal correction of the traces is required [118]. Very similar interrogations can also be achieved by utilizing digital optical frequency combs as probe signals [120].

- Slope-assisted BOTDA (SA-BOTDA): completely skips the BGS scanning process by taking the advantage of the linearity at the edge of the BFS to convert the BFS shift due to the measurand change to the amplitude variation, as schematically illustrate in Fig. 3.5.10(b). Considering the non-uniform BFS distribution of a practical sensing fiber, the single frequency probe wave is not able to align at the same working point of the BGS for every fiber section to carry out a real-distributed sensing [119]. To solve this problem, a frequency tailored probe wave is utilized, extending the validity of this technique to an arbitrary BFS profile. The time evolution of the probe frequency is designed in such a way, that the probe wave is always aligned at the same point of the BGS in every fiber section in the static case [121]. Currently, SA-BOTDA is one of the most practical and cost-effective BOTDA techniques for dynamic sensing with the most simple setup. A detailed discussion about this technique will be given in Sec. 5.1.

- Double slope-assisted BOTDA (DSA-BOTDA): gives the solution to the SA-BOTDA in the situations when the amplitude changes are not related to the BFS shift. A typical example is the change of the fiber attenuation due to a deformation of the monitored structure, then the pulse power and the detected Brillouin gain is modified and misinterpreted as a BFS variation. DSA-BOTDA utilizes the SA-BOTDA measurement

Dieses Werk ist copyrightgeschützt und darf in keiner Form vervielfältigt werden noch an Dritte weitergegeben werden.
Es gilt nur für den persönlichen Gebrauch.

results from both the positive and the negative slope of the BGS, so that the difference between the two measurements divided by their summation is immune to variations of the detected amplitude and hence also pump power independent [122].

- Phase slope-assisted BOTDA: employs the detection of the RF phase, circumventing the pump power dependent amplitude detection. In this technique, the probe wave is phase modulated, and the Brillouin gain interaction takes place on one of the sidebands of the phase modulation, leading to the probe electrical field as: [123]

$$\begin{aligned} E(t) = &- E_{SB}\exp[j\cdot 2\pi(\nu_0 - f_{RF})t] + E_0\exp(j\cdot 2\pi\nu_0 t) \\ &+ E_{SB}\exp[j\cdot 2\pi(\nu_0 + f_{RF})t]\cdot\exp[g(\nu_0 + f_{RF}, z)\Delta z] \end{aligned} \tag{3.5.11}$$

where g is the complex Brillouin gain at position z described in Eq. (2.4.1), E_{SB} and E_0 are the electric field of the sideband and carrier, respectively, ν_0 and f_{RF} are the carrier frequency and phase modulation frequency, respectively. The detected optical power signal at f_{RF} can be expressed as:

$$\begin{aligned} P(t) &= E_0 E_{SB}[(1+G_{SBS})\cos(2\pi f_{RF}t + \phi_{SBS}) - \cos(2\pi f_{RF}t)] \\ &\approx \frac{4E_0 E_{SB} g_0 P_p \gamma_B}{\sqrt{\gamma_B^2 + (2\Delta\nu)^2}}\cos\left[2\pi f_{RF}t - \arctan\left(\frac{2\Delta\nu}{\gamma_B}\right)\right] \end{aligned} \tag{3.5.12}$$

where P_p is the pump power at the position z, G_{SBS} and ϕ_{SBS} are defined in Eqs (2.4.4) and (2.4.4), respectively. The approximation is achieved under the assumption of a small gain, indicating the independence of the RF phase of the probe power and Brillouin gain as well as its proportionality to the BFS shift.

Dieses Werk ist copyrightgeschützt und darf in keiner Form vervielfältigt werden noch an Dritte weitergegeben werden.
Es gilt nur für den persönlichen Gebrauch.

4 Gain Spectrum Engineering in Static BOTDA

Since the first demonstration of the BOTDA technique three decades ago [54, 55], its performance has been significantly improved in almost every aspect. The sensing range has been extended from ∼60 km to over 100 km with Raman assistance [103]. With the pre-pump pulse technique, the spatial resolution could be enhanced from 1 m to several centimeters without penalty to the SNR due to the short interaction length [99]. The measurement time with a sufficient SNR is reduced to 100 microseconds with a fully optimized scanning mechanism [117]. However, the possibility to enhance the measurand resolution has not been fully studied. The bottleneck lies in the quantification of the measurand resolution. The first proposed quantified expression of the measurand resolution in a conventional BOTDA setup given by Eq. (3.5.2) only applies with a quadrature fitting of the gain spectrum [62]. Its theory will not hold with other fitting algorithms, for instance, a Lorentzian fitting, or the gain spectrum deviates from its intrinsic shape. In this chapter, a discussion about the practical definition of the measurand resolution will be presented. Based on this criteria, a novel method to enhance the measurand resolution with gain spectrum engineering is proposed.

4.1. Schematic Operation Principle

As discussed in Sec. 3.5.5, the SNR enhancement is of significant importance for the overall sensing performance. Nevertheless, the traditional de-noise and signal amplification methods cannot effectively improve the SNR of a conventional BOTDA setup. This limited space for SNR improvement is mainly attributed to the consideration of Brillouin gain interaction only. Extra space of SNR improvement will be given if the superposition of the BLS as mentioned in Sec. 2.7 is considered.

The SNR enhancement of the engineered BGS lies in the increased signal level from the maximum gain to the maximum loss. An illustration of a normalized conventional BGS (black)

Dieses Werk ist copyrightgeschützt und darf in keiner Form vervielfältigt werden noch an Dritte weitergegeben werden.
Es gilt nur für den persönlichen Gebrauch.

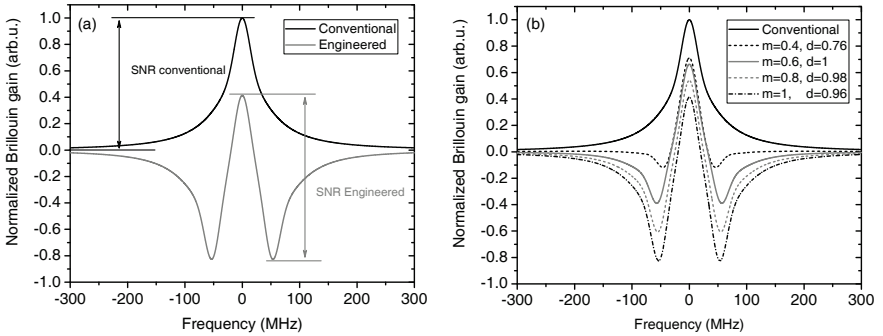

Figure 4.1.1.: (a) The demonstration of enhanced SNR with engineered BGS (gray) to the conventional BGS (black); (b) the SNR of the engineered BGS with various parameters.

excited by a 100 ns pump pulse in Fig. 4.1.1(a) shows a spectrum FWHM of 54 MHz. An example of a well engineered superposition of Brillouin losses with a frequency offset (gray) depicts a signal level higher than the conventional BGS.

The engineered BGS with the superposition of two symmetric Brillouin loss spectra with a frequency offset can be generally modeled by the superimposed complex gain coefficient in Eq. (2.7.2) with the definition of m, d, Δ and γ_B. The validation of Eq. (2.7.2) can also be extended for the broadened BGS excited by short pulses with the replacement of the Lorentzian function of the conventional BGS to the Voigt function in the form of: [97]

$$g(\nu) = G\left\{ c\frac{{\gamma_L}^2}{4(\nu-\nu_B)^2+\gamma_L^2} + (1-c)\exp\left[-4\ln 2\frac{(\nu-\nu_B)^2}{{\gamma_G}^2}\right]\right\}, \tag{4.1.1}$$

where γ_G and γ_L are the widths of the Gaussian and Lorentzian functions, respectively, c is a constant controlling the relative weights of the two spectra, G is the maximum Brillouin gain. Figure 4.1.1(b) depicts more examples of engineered BGS with different parameters based on the conventional spectrum in Fig. 4.1.1(a). It is clearly indicated that, the signal of the engineered BGS is higher than the conventional one in most of the scenarios, especially with a big m value, *i.e.* strong loss. As a proof-of-concept, this chapter concerns only the case when the conventional Brillouin gain profile remains intrinsic Lorentzian.

4.2. Simulation Prediction

According to the analysis in Sec. 3.2, the SNR enhancement brings the most benefit to a higher measurand resolution and an extended sensing range. The measurand resolution could be

Dieses Werk ist copyrightgeschützt und darf in keiner Form vervielfältigt werden noch an Dritte weitergegeben werden.
Es gilt nur für den persönlichen Gebrauch.

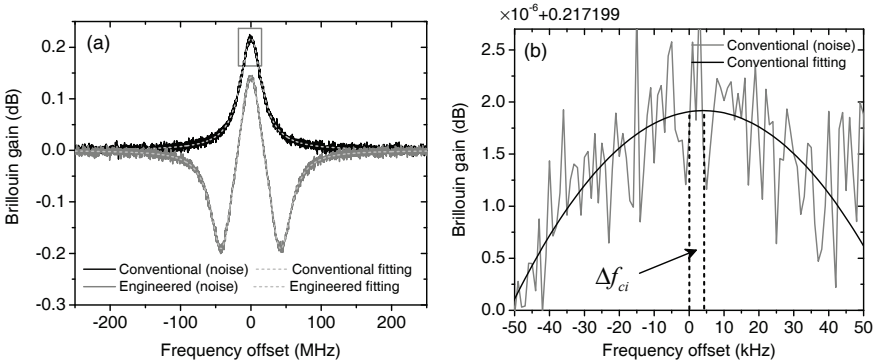

Figure 4.2.1.: (a) Fitting demonstration of a typical conventional (black solid) and engineered (gray solid) simulated BGS; (b) the magnified peak area of the conventional BGS (gray rectangular area in (a)), highlighting the BFS estimation error Δf_{ci} due to the noise in the i^{th} measurement.

characterized as the standard deviation of the BFS at each fiber section with a large number of measurements [62]. Since the BFS estimation error is statistically increasing with the fiber length, the sensing range extension could be quantified under the same requirement of the measurand resolution, *i.e.*, the same tolerance of BFS estimation error. The demonstration of the application of an engineered BGS in a BOTDA setup starts from the simulation.

Simulation Process

As discussed in Sec. 3.5.5, the sensing system noise comes mainly from the detection. Therefore, the noise performance is simulated by additive white Gaussian noise (AWGN) with an uniform frequency distribution. Figure 4.2.1(a) demonstrates the conventional BGS and a typical engineered BGS modeled with 1 kHz granularity (frequency scanning step) by Eq. (2.7.2) at the pump launching end of the fiber. The pump peak power is set at 20 dBm to avoid MI [82] and the pulse width is set to 100 ns. Provided that the probe power is set to −14 dBm to avoid NLE in a conventional setup [88], the thermal noise of the detector dominates the overall noise performance with negligible shot and RIN contributions [108]. Therefore, the simulated noise added on both the conventional and engineered BGS should be of the same level, as depicted in Fig. 4.2.1(a).

For simplicity, the modeled conventional and engineered BGS are originally centered at zero frequency offset (to the BFS). A Voigt function fitting is applied on the conventional and engineered BGS with noise to determine the peak frequency. Due to the influence of the noise,

Dieses Werk ist copyrightgeschützt und darf in keiner Form vervielfältigt werden noch an Dritte weitergegeben werden.
Es gilt nur für den persönlichen Gebrauch.

the estimated BFS is not always at zero frequency offset. As a single fitting result for the conventional BGS in Fig. 4.2.1(b) demonstrates, the offset of the estimated BFS to the precise BFS (zero frequency) is denoted as Δf_{ci} for the conventional BGS in the i^{th} measurement. Similarly, an offset to the zero frequency can be determined for engineered BGS, denoted as Δf_{pi} in the i^{th} measurement. Standard deviations of the BFS determination errors can be calculated when the number of fittings N is sufficiently large. In this simulation, the number of fittings is set to N=500. The advantage of the engineered BGS is quantified by the ratio of the two standard deviations η given by: [36, 124]

$$\eta = \sqrt{\sum_{i=1}^{N} \Delta f_{pi}^2 / \sum_{i=1}^{N} \Delta f_{ci}^2} \tag{4.2.1}$$

It is clearly indicated that the application of the engineered BGS is advantageous regarding the measurand error reduction when η <1.

Simulation Results

The simulation is carried out with d in the range from 0.3 to 3 and m in the range from 0.1 to 2. The ratio of the BFS determination error η is demonstrated as a function of m and d in Fig. 4.2.2(a). As it is clearly indicated, the application of the engineered BGS is showing advantage (η <1) in most of the situations, with the best performance, *i.e.*, lowest η value of 0.282 with m=2 and d=1.78, highlighted as $P4$ in Fig. 4.2.2(a). However, this situation is

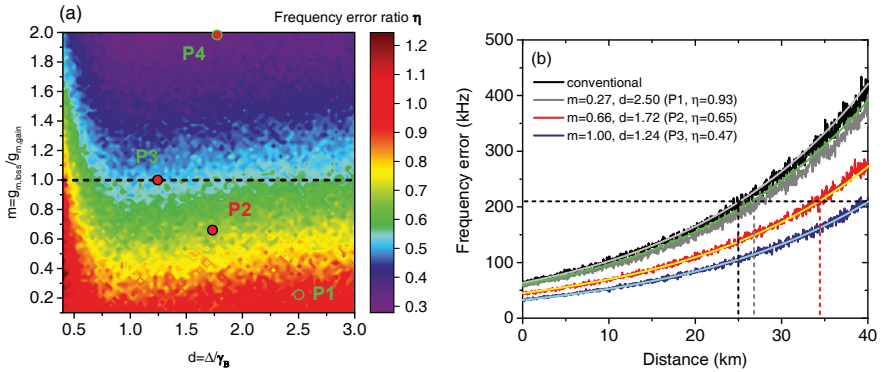

Figure 4.2.2.: Simulation results of: (a) the ratio of the BFS determination error η as a function of m and d; (b) the distribution of the BFS determination error with the conventional and engineered BGS with selected m and d values in (a) marked as P1-3.

Dieses Werk ist copyrightgeschützt und darf in keiner Form vervielfältigt werden noch an Dritte weitergegeben werden.
Es gilt nur für den persönlichen Gebrauch.

impractical. The reason for the impracticability with $m > 1$ will be specifically explained in Sec. 4.3. Within the practical range of $m \leq 1$, the best performance is achieved with m=1 and d=1.24, highlighted as $P3$ in Fig. 4.2.2(a). At this point, the BFS determination error with an engineered BGS is reduced to only 47% of the conventional one.

The distribution of the BFS determination error along the fiber will then be investigated. According to the model introduced in Sec. 3.4, the local conventional Brillouin gain $G(\nu, z)$ at the fiber section z from the pump launching end can be modeled by Eq. (3.4.7). Similarly, the local engineered Brillouin gain at the fiber section z can be calculated by the multiplication of Eq. (2.7.2) by an exponential fiber loss factor. The distribution of the BFS determination error can be statically calculated by repeating the simulation process under the same conditions with a fiber length step of 50 m. Due to the large amount of data, only results with the selected parameters highlighted in Fig. 4.2.2(a) as $P1$-$P3$ are depicted in Fig. 4.2.2(b). Under the same BFS error tolerance of 210 kHz (horizontal dashed line), the sensing range of the conventional BGS is measured to be 25 km. However, with the engineered BGS at $P1$, $P2$ and $P3$, the sensing range is extended to 26.8 km, 34 km, and 40 km, respectively, achieving the maximum sensing range extension of 60% with the best performance. The BFS error reduction and thus the sensing range extension can be physically interpreted as, a higher signal level within a narrow frequency range, *i.e.*, an overall sharper spectrum is more robust to the noise in peak estimation.

4.3. Proposed Implementations

Specifically there are three ways to generate a superimposed engineered BGS, namely the multi-pump wave scheme, multi-probe wave scheme, and post-superposition. In this section, details of all three methods as well as the advantages and disadvantages will be presented.

Multi-pump Scheme

An engineered BGS can be achieved by the simultaneous Brillouin interaction between three pump and a single probe wave. As the scheme in Fig. 4.3.1 illustrates, pump 3 produces a Brillouin gain interaction on the probe wave, while pump 1 and 2 generate the Brillouin loss interactions with an offset. The relative frequencies between the pump and probe waves can be expressed by:

$$f_{RF1} = f_{RF2} + d \cdot \gamma_B = f_{RF3} - d \cdot \gamma_B \tag{4.3.1}$$

The BGS scanning can be carried out by scanning f_{RF1} in the vicinity of the BFS with the simultaneous corresponding scanning of f_{RF2} and f_{RF3} of the Brillouin loss spectra. To

Dieses Werk ist copyrightgeschützt und darf in keiner Form vervielfältigt werden noch an Dritte weitergegeben werden.
Es gilt nur für den persönlichen Gebrauch.

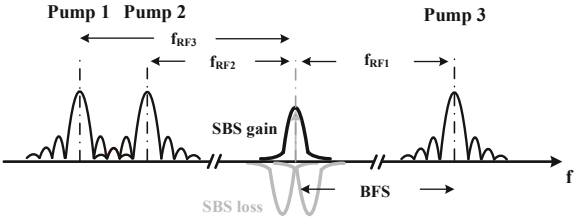

Figure 4.3.1.: Multi-pump wave scheme in frequency domain for engineered BGS implementation

guarantee a stable relative frequency between the pump and probe waves, all the pump and probe waves shall be generated from the same source.

The biggest advantage of this scheme is the full flexibility of both m and d. Specifically d can be changed according to Eq. (4.3.1) while m can be tuned by the pump pulse powers. However, despite the flexibility on m, it is still not practical for m >1. The reason can be explained as follows: the maximum pump power for the gain and loss pulses is defined by the threshold of MI [82]. Therefore, the pump power of the gain must be reduced to achieve m >1. However, this reduces the SNR of the overall spectrum and is detrimental for the sensor performance. Therefore, the practically achievable maximum value of m is 1.

The disadvantage of this scheme comes with the penalty on the SNR due to the FWM induced by the co-propagation of the pump pulses [84]. With the pump power converted to the idler frequencies, the SNR and sensing range are both drastically reduced, losing all the advantages on the measurand resolution to the conventional configuration. Despite the reported possibility to circumvent the FWM via consecutive FBG [84], which provides a group delay on the pulses and enables sequential interactions, a very complicated setup is required with precise control on the group delay and its recovery. Considering the best performance is achieved at m=1, it is not worthwhile to make a large effort to implement the full flexibility.

Multi-probe Scheme

Another method to achieve the engineered BGS is to utilize the simultaneous interaction between three probe waves and a single pump wave. As shown by the scheme in Fig. 4.3.2, one probe wave is located inside the gain spectrum and the other two are within the loss spectrum with an offset. All three probe wave powers will be summed up at the detector to reconstruct the proposed BGS. Due to the low probe powers, the FWM between the probe wave is negligible and the FWM between the pump waves in the multi-pump scheme can be avoided. The relative frequencies of the probe waves to the pump f_{RF1}, f_{RF2} and f_{RF3} still

Dieses Werk ist copyrightgeschützt und darf in keiner Form vervielfältigt werden noch an Dritte weitergegeben werden.
Es gilt nur für den persönlichen Gebrauch.

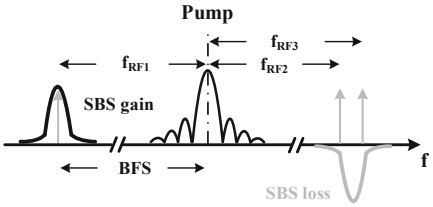

Figure 4.3.2.: Multi-probe wave scheme in frequency domain for engineered BGS implementation

follow Eq. (4.3.1), so that the same precise control over the parameter d can be achieved. The reconstructed BGS via frequency scanning in multi-pump and multi-probe scheme are fully equivalent [36].

The biggest disadvantage of the scheme is the inflexibility on the parameter m. Due to the insensitivity of the Brillouin gain on a small probe power in case of a negligible pump depletion, the multi-probe scheme could only achieve m=1. However, since the best performance is predicted with m=1 in the simulation, the inflexibility on m shall not be a disadvantage. Since the probe waves have to be launched separately, the same complexity of the setup as the multi-pump scheme is required.

Post-superposition

Alternatively, the engineered BGS could also be summed up by post-superposition of the conventional BGS and two conventional Brillouin loss spectra at an offset. The biggest advantage of this scheme is the simplicity of the setup. Only a typical conventional setup such as Fig. 3.3.2 is required with different probe wave frequencies for Brillouin gain and loss interactions. In this scheme, the probe waves are not simultaneously but sequentially launched into the sensing fiber with the acquired BGS and loss spectrum literally superimposed.

The biggest disadvantage of this scheme is the non-equivalence of the gain spectrum post-superposition in the aspect of noise. Practically, the superposition of the gain spectrum is inevitable accompanied by the superposition of noise. Under the assumption of a thermal noise dominant detection, the noise on the gain probe wave is the same on the loss probe waves, *i.e.*, $\sigma_g = \sigma_{l1} = \sigma_{l2} = \sigma_{conv}$, where σ_{conv} represents the noise level of the conventional BGS with the same measurement time. The post-superposition of the time-domain traces leads to the noise level of the engineered BGS as:

$$\sigma_{eng}^2 = \sigma_g^2 + \sigma_{l1}^2 + \sigma_{l2}^2 = 3\sigma_{conv}^2 \tag{4.3.2}$$

Dieses Werk ist copyrightgeschützt und darf in keiner Form vervielfältigt werden noch an Dritte weitergegeben werden.
Es gilt nur für den persönlichen Gebrauch.

indicating a $\sqrt{3}$ times higher noise level than the conventional one.

A further disadvantage lies in the 3 times longer measurement time due to the sequential launched measurements for separate gain and loss interactions. For a fair comparison, the measurement time with the conventional BGS must also be extended by 3 times, leading to a reduction of the noise level from σ_{conv} to $\sigma_{conv}/\sqrt{3}$. Considering the noise increase by the post-superposition, the engineered BGS will suffer from 3 times higher noise than the conventional one, leading to the penalty with a factor of $\sqrt{3}$ on the BFS determination error according to Eq. (3.5.2). However, the best simulation predicted advantage is only 47%, leaving the residual advantage of 47% $\times\sqrt{3}\approx$81.4% on the BFS determination error to the best case.

4.4. Experimental Setup

Based on the tradeoffs of different implementation schemes discussed in Sec. 4.3, the specific experimental setup is illustrated in Fig. 4.4.1. To demonstrate the best performance with the engineered BGS, m=1 and d=1.24 are set according to the simulation prediction in Sec. 4.2.

The output beam from the laser diode is split into four branches with several optical couplers. In the pump branch at the top, the pump wave is shaped into a pulse sequence by a switching type SOA (Thorlabs SOA1013SXS with driving board from Highland Technology T160-9). The pulse width is set to be 100 ns in the pulse generator. This pulse width ensures the conventional Lorentzian BGS without broadening [28], so that the acquired experimental results may have

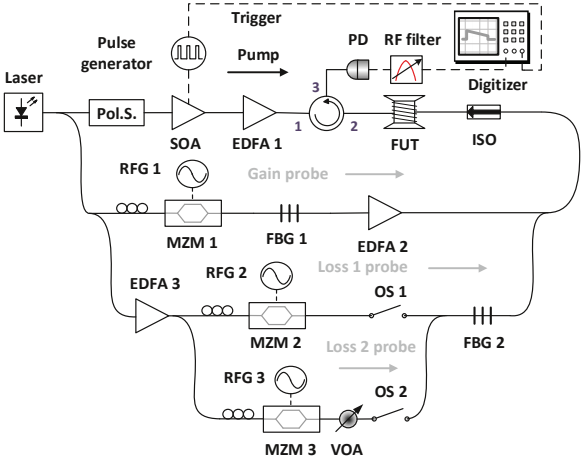

Figure 4.4.1.: Experimental setup. OS: optical switch; ISO: isolator.

Dieses Werk ist copyrightgeschützt und darf in keiner Form vervielfältigt werden noch an Dritte weitergegeben werden.
Es gilt nur für den persönlichen Gebrauch.

a direct comparison with the simulation results. The SOA provides a sufficient high ER of the pump pulse (32 dB calculated by Eq. (3.5.3)) to avoid NLEs [93, 94, 96]. EDFA 1 amplifies the pump pulse peak power to 19 dBm, below the MI threshold [82], before launching the pulse into the 10.6 km FUT via a circulator. The polarization fading is circumvented by the fast polarization scrambling. In the lower branches, the probe wave for the Brillouin gain interaction is generated via a modulation by MZM 1 operated by RFG 1 with the frequency f_{RF1} while the two probe waves for the Brillouin loss interactions are generated by MZM 2 and MZM 3 operated by RFG 2 and RFG 3 with the frequencies f_{RF2} and f_{RF3}, respectively. Here RF frequencies f_{RF1}, f_{RF2} and f_{RF3} follow the relation in Eq. (4.3.1).

To reconstruct the (conventional and engineered) BGS, f_{RF1} is scanned in the vicinity of the BFS. The frequency scanning span and step are set to be 180 MHz and 1 MHz, respectively. Tunable narrowband FBGs (AOS T-FBG) are utilized to block the undesired higher and lower modulation frequency sidebands in the gain and loss probe branches, respectively. The three probe powers are controlled to -15 dBm, below the threshold of NLE [88], and equalized by EDFA 2, EDFA 3 and a variable optical attenuator (VOA) assisted by optical switches (OS) separately via a power meter. An extra 10 MHz low-pass RF filter is utilized after the PD (Finisar XPDV2120R) to block the possible interference signal between the two loss probe waves and reduce the noise [63].

The optical-to-electrical converted signal is eventually processed in a digitizer (Acqiris U5309A) with a sampling rate of 1 GS/s, 8 bit resolution, 4096 times of averaging and triggered by the synchronized inverse pulse signal from the pulse generator. The switching between the proposed and conventional sensing method can be achieved by turning on and off EDFA 3. To ensure a fair comparison, all other components, including the 10 MHz RF filter, remain the same for measurements with conventional and engineered BGS.

4.5. Experimental Validation

The reconstructed conventional and engineered BGS at 10 m is depicted in Fig. 4.5.1(a) with their corresponding Voigt fitting curves for BFS estimations. For the sake of the measurement time, the frequency scanning is carried out with 180 MHz span and 1 MHz step in the experiment. The FWHM of the conventional BGS is measured to be γ_B=54 MHz, showing good consistence with the simulation. Please note that, the Brillouin gain level of the engineered BGS in Fig. 4.5.1(a) is not showing consistence with the simulation results in Fig. 4.2.1(a). This inconsistency is a direct result of the division of sensing response by 3 probe powers in acquiring the Brillouin gain with the engineered BGS, *i.e.*, gain penalty. However, while the gain is suffering from a penalty by a factor of 3, the noise level is also reduced. Whether the

Dieses Werk ist copyrightgeschützt und darf in keiner Form vervielfältigt werden noch an Dritte weitergegeben werden.
Es gilt nur für den persönlichen Gebrauch.

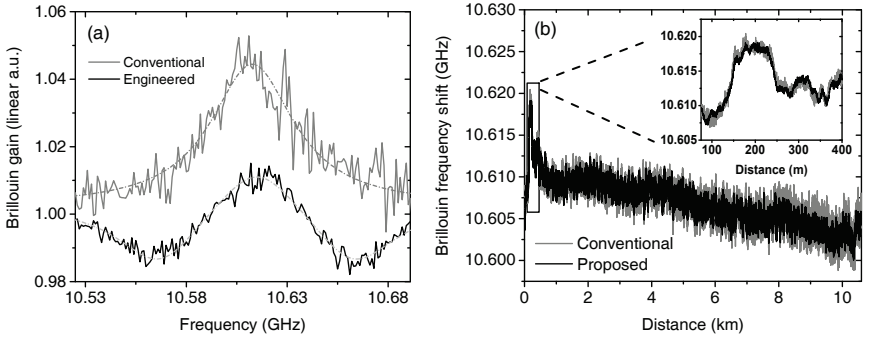

Figure 4.5.1.: The experimental (a) conventional (gray) and engineered (black) BGS at 10 m with the dash dotted curves as the corresponding Vogit function fitting, (b) the determined BFS distribution via the fitting and the detected stretched fiber section (inset).

SNR is eventually changed or not is determined by if the dominant contribution comes from the thermal or shot noise in the detection. A detailed discussion on this point will be given in Sec. 4.6.

Figure 4.5.1(b) illustrates the BFS distribution along the fiber from the curve fitting. It is clearly indicated that, the BFS distribution with the engineered BGS is well overlapped with and clearer than the one acquired with the conventional BGS. In the inset of Fig. 4.5.1(b), a stretched strain spot at around 200 m is successfully detected with both methods, indicating a better sensing functionality with the engineered BGS.

To investigate the enhancement of the BFS determination error, 48 measurements have been carried out consecutively under the same conditions. The BFS error in both cases is represented by the standard deviation (RMS value) of the 48 estimated BFS values from the curve fitting at each fiber section. As depicted in Fig. 4.5.2(a), the BFS error with the engineered BGS sensor is reduced to only 45.7% of the conventional one and more robust to the fiber loss. In Fig. 4.5.2(b), simulated BFS determination errors with the conventional and engineered BGS are demonstrated according to the procedure in Sec. 4.2, but with the experimental conditions (same fiber length, number of measurements, frequency scanning span and step, noise level, etc.). The experimental results show very good agreement with the simulation results demonstrated in Fig. 4.5.2(b). As clearly indicated in both Fig. 4.5.2(a) and (b), the BFS error with the conventional BGS is higher than the one with the engineered BGS at the same fiber section. Therefore, the sensing range could be widely extended under the same measurand error tolerance, showing a success in the application of an engineered BGS in a BOTDA sensor.

Dieses Werk ist copyrightgeschützt und darf in keiner Form vervielfältigt werden noch an Dritte weitergegeben werden.
Es gilt nur für den persönlichen Gebrauch.

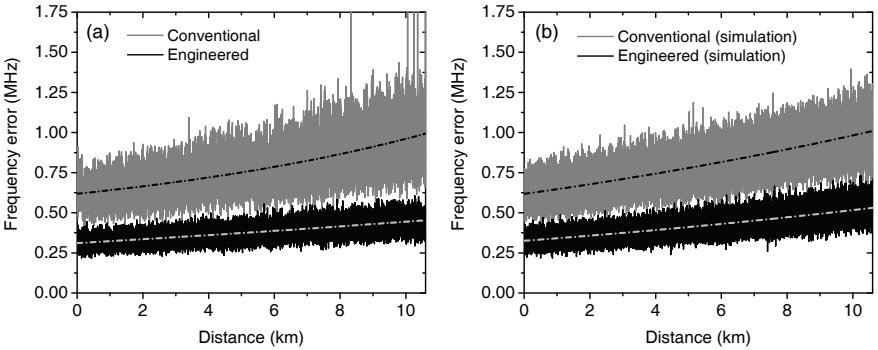

Figure 4.5.2.: Distributions of the BFS determination error after 48 measurements with a conventional (gray) and engineered (black) BGS and their corresponding exponential fitting curves (dash dotted) in the (a) experiment and (b) simulation with the experimental conditions.

4.6. Gain Recovery

The gain penalty mentioned in Sec. 4.5 can be explicitly explained by Eq. (3.4.7). To acquire the local Brillouin gain at each fiber section, a division between the probe wave power with and without the Brillouin interaction is to be carried out. However, instead of a single probe wave power in the baseline of the BOTDA trace with the conventional BGS, the baseline of the BOTDA trace with the engineered BGS is composed of all three probe powers and it could hardly be separated. Provided that the probe waves have the same power level, the division of the baseline value (before the Brillouin interaction) degrades the logarithmic engineered gain by a factor of 3 (see Appendix C for the mathematical justification).

The influence on the noise due to the division of the signal by a factor is more complicated and should be discussed separately. The main noise contributions of a BOTDA sensor can be expressed in Eq. (3.5.9). A thermal noise dominant detection ensures the independence of the noise level of the detected signal on the input probe wave power (or even without input power). This means, the division of the signal by a factor of N will lead to a simultaneously decrease of the noise level also by a factor of N, leading to an eventually unchanged SNR. On the contrary, considering the statistical origin of the shot noise, if the detection is dominated by the shot noise, the division of the signal by a factor of N will result in the noise level reduction only by a factor of $\sqrt{N}$. In this scenario, the overall SNR will suffer from a penalty of $\sqrt{N}$. In the rest of the cases where the contributions from the shot and thermal noise are comparable, the influence on the noise reduction lies between a factor of $\sqrt{N}$ and N.

Based on the above explanation of the origin of the gain penalty, the gain recovery by

Dieses Werk ist copyrightgeschützt und darf in keiner Form vervielfältigt werden noch an Dritte weitergegeben werden.
Es gilt nur für den persönlichen Gebrauch.

the multiplication by a factor of 3 is only justified under the satisfaction of all the following conditions:

- very similar probe powers;
- small gain approximation;
- a thermal noise dominant detection.

The first two conditions are justified in Appendix C based on the experimental conditions.

Thermal Noise Dominant Detection

The thermal noise dominant detection can be justified by the demonstration of the same noise level for various input powers at the detector. Figure 4.6.1 shows the BOTDA trace measured with the conventional (gray) and engineered (black) BGS. Please note that, instead of the Brillouin gain, the vertical axis of Fig. 4.6.1 is the voltage that is proportional to the photocurrent via the impedance of 50 Ohm, so that a direct comparison between the original noise level of the traces can be made. Due to the detection of a summation of three probe powers with the engineered BGS, the photocurrent level of the trace with the engineered BGS is manually down shifted to show a visualized well overlap.

A calculation on the contribution from the thermal noise according to Eq. (3.5.9) could also be carried out to justify the thermal noise dominant. According to the data sheet of the PD, the typical responsivity of 0.65 A/W, output resistance of 50 Ohm, dark current of 200 nA

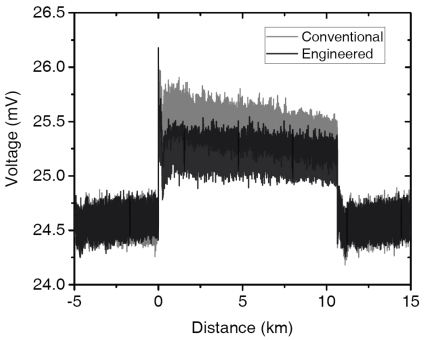

Figure 4.6.1.: Time domain trace measured with conventional (gray) and engineered (black) BGS at a pump-probe frequency offset of 10.605 GHz. The photocurrent level of the trace with the engineered BGS is down shifted for a better visualized comparison of the noise with the conventional one.

Dieses Werk ist copyrightgeschützt und darf in keiner Form vervielfältigt werden noch an Dritte weitergegeben werden.
Es gilt nur für den persönlichen Gebrauch.

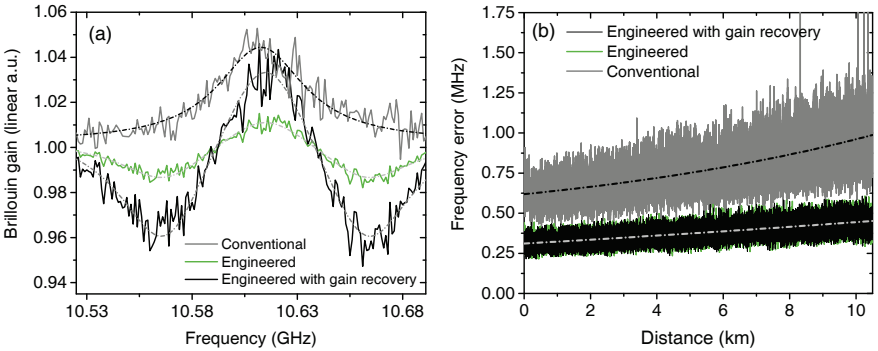

Figure 4.6.2.: The experimental (a) BGS at 10 m with the dash dotted curves as the Vogit function fitting and (b) distributions of the BFS determination error after 48 measurements and their corresponding exponential fitting curves (dash dotted) with the conventional (gray) and engineered method with (black) and without (green) gain recovery.

lead to eventually 18 times higher thermal noise than the shot noise with 3 times −15 dBm probe wave power. This conclusion shows consistence with the visualization in Fig. 4.6.1.

Equivalence with Gain Recovery

The previous subsection justified the full fulfillment of conditions for a gain recovery. In this subsection, the equivalence of gain recovery will be demonstrated. The expressions of the gain recovery in the logarithmic and linear scale are given in Appendix C.

Similar to Fig 4.5.1(a), Fig. 4.6.2(a) depicts an extra engineered BGS with gain recovery at 10 m. In comparison to the simulation results, the gain level of the gain recovered engineered BGS is showing consistence with the one in Fig. 4.2.1(a) and so is the noise level. With the assistance of the Voigt fitting curve (dash dotted), the BFS is re-calculated with the engineered BGS with the gain recovery. As clearly indicated in Fig. 4.6.2(b), the well overlapped distribution of BFS determination error with and without the gain recovery verifies the full equivalence of the gain recovery and an unchanged SNR.

Dieses Werk ist copyrightgeschützt und darf in keiner Form vervielfältigt werden noch an Dritte weitergegeben werden.
Es gilt nur für den persönlichen Gebrauch.

Dieses Werk ist copyrightgeschützt und darf in keiner Form vervielfältigt werden noch an Dritte weitergegeben werden.
Es gilt nur für den persönlichen Gebrauch.

5 Gain Spectrum Engineering in Dynamic BOTDA

Most of the dynamic sensing tasks aim to measure the strain or vibration signals applied on the sensing fiber, such as structural health monitoring of skyscrapers, the turbulence on airplane wings and offshore wind turbines. The main difference between the dynamic and static sensing on the distributed interrogation techniques include: *(a)* a short measurement time in comparison to the measurand variation period and *(b)* a short sensing fiber length, usually in the range of several 100 m. Considering the short length, high pump and probe powers can be launched into the fiber due to weaker nonlinear effects. This reduces drastically the requirement on the number of averaging and thus shortens the measurement time.

In Sec. 3.5.6, three main solutions for dynamic distributed Brillouin sensing, *i.e.*, fast-BOTDA, SF-BOTDA and SA-BOTDA, have been introduced. The fast-BOTDA technique [117] still implements frequency scanning but replaces the slow, synthesizer-based frequency switching by an almost instantaneous one. Despite the optimization, the scanning of fast-BOTDA still takes time. The demonstrated 120 μs measurement time limits the measurand acquisition rate to about $(120\ \mu\text{s})^{-1} \approx 8.33$ kHz and according to the Nyquist–Shannon sampling theorem, the measurement of vibrations should not be faster than 4.16 kHz. Multi-tone interrogation, or SF-BOTDA, has also been suggested [118, 120] where the full BGS is simultaneously measured at the expense of quite a complicated hardware and a few other constraints. Though with some inherent limitations, the fastest Brillouin interrogation techniques increase the gain measurement speed by entirely skipping the frequency scanning process, making SA-BOTDA one of the simplest and currently the most practical dynamic Brillouin sensing techniques.

5.1. Key Performances of SA-BOTDA

The linear conversion between the measurand variation and the BFS shift is ensured by Eq. (3.1.1). Without the direct determination of the BFS shift, SA-BOTDA utilizes a single

Dieses Werk ist copyrightgeschützt und darf in keiner Form vervielfältigt werden noch an Dritte weitergegeben werden.
Es gilt nur für den persönlichen Gebrauch.

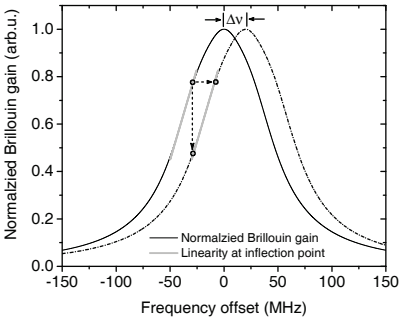

Figure 5.1.1.: Schematic of frequency-to-gain conversion in SA-BOTDA with the conventional BGS excited by a 10 ns pump pulse sequence and linear extension from the inflection point.

frequency, ν_{wp} (*wp* for Working Point), that interrogates the BGS in the vicinity of the middle of its rising/falling slopes [119, 121]. Measurand variations shift the BGS in the frequency domain, resulting in corresponding changes of the Brillouin gain at the interrogating frequency [121], as Fig. 5.1.1 demonstrates. The mathematical expression of the frequency-to-gain conversion can be given by a Taylor expansion with the linear approximation at the working point frequency ν_{wp} and a small variation $\Delta\nu$ as:

$$G(\nu_{wp}+\Delta\nu) \approx G(\nu_{wp}) + \left.\frac{dG}{d\nu}\right|_{\nu_{wp}} \Delta\nu = G(\nu_{wp}) + S(\nu_{wp})\Delta\nu \tag{5.1.1}$$

The BFS shift is then approximated by:

$$\Delta\nu \approx \frac{G(\nu_{wp}+\Delta\nu) - G(\nu_{wp})}{S(\nu_{wp})} \tag{5.1.2}$$

where the sensitivity $S(\nu_{wp})$ is the first order derivative of the BGS at the working point ν_{wp}. The working point was first suggested to be the 3 dB point of the BGS at the first demonstration of SA-BOTDA [119]. However, if a similar Taylor expansion is applied to the sensitivity at the working point as:

$$S(\nu_{wp}+\Delta\nu) \approx S(\nu_{wp}) + \left.\frac{dS}{d\nu}\right|_{\nu_{wp}} \Delta\nu \quad \Longrightarrow \quad \left.\frac{dS}{d\nu}\right|_{\nu_{wp}} = \frac{S(\nu_{wp}+\Delta\nu) - S(\nu_{wp})}{\Delta\nu} \to 0 \tag{5.1.3}$$

it is clearly indicated that, the inflection point of the BGS is the best working point to ensure a higher and more stable sensitivity. Further investigation shows that, working at the inflection

Dieses Werk ist copyrightgeschützt und darf in keiner Form vervielfältigt werden noch an Dritte weitergegeben werden.
Es gilt nur für den persönlichen Gebrauch.

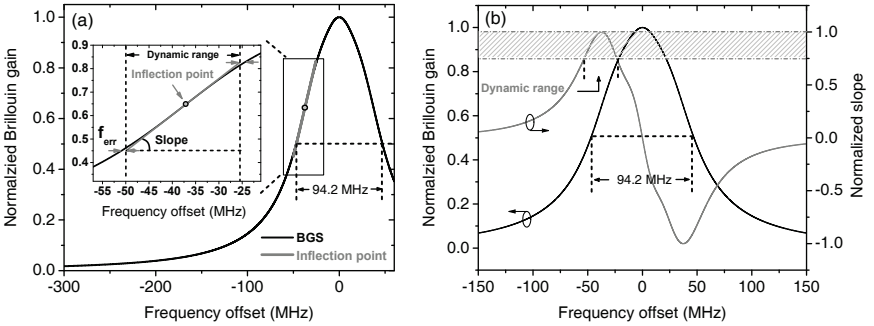

Figure 5.1.2.: Illustration of the sensitivity and dynamic range of the conventional BGS excited by a 10 ns pump pulse sequence based on the definition of (a) frequency error tolerance [125] and (b) slope variation tolerance [127].

point provides also a wider dynamic range, better symmetry at the working point, *i.e.*, better full use of the linear range [125].

The dynamic range and the sensitivity are two important sensing metrics of SA-BOTDA [126]. Currently, there are two different types of quantified definitions on them. Figure 5.1.2(a) depicts the definition based on the frequency error tolerance f_{err} [123], while Fig. 5.1.2(b) illustrate the definition based on the fraction of the slope. Though the two definitions are not quantitatively equivalent, the characteristics of the dynamic range and the sensitivity are the same under both definitions.

Dynamic Range

The dynamic range is featured by the span of the linear range on the edge of the BGS. It determines the maximum measurable strain signal. Under the definition of a frequency error tolerance in Fig. 5.1.2(a), the dynamic range is defined as the frequency span of the linear fit extended from the inflection point with the slope at the inflection point when the frequency error (between the linear fit and the BGS) reaches a certain pre-defined cut-off value f_{err} [123]. In Fig. 5.1.2(a), the situation with f_{err}=2 MHz is demonstrated, corresponding to an error tolerance of 40 $\mu\varepsilon$. Under the definition of slope variation tolerance, the dynamic range is defined as the frequency span, within which the variations of the slope are smaller than a pre-defined fraction to the maximum slope at the inflection point. Figure 5.1.2(b) illustrates the normalized slope (gray) of the normalized BGS (black) excited by 10 ns pump pulse sequence. The shadow region depicts the situation of a flatness tolerance of 25% [127]. The dynamic range in this definition is quantified as the span of the two crossing points of the

Dieses Werk ist copyrightgeschützt und darf in keiner Form vervielfältigt werden noch an Dritte weitergegeben werden.
Es gilt nur für den persönlichen Gebrauch.

shadow region and the normalized slope curve.

Sensitivity

The sensitivity is featured by the slope of the linear range on the edge of BGS. The value of the slope at the working frequency, $\alpha(\nu_{wp}) = \Delta Gain/\Delta BFS$ defines the conversion factor between the BFS shift and the corresponding gain change and governs the minimum detectable strain variance, *i.e.*, the larger α, the higher the measurement sensitivity, so that smaller strain changes can be discerned for a given amount of encountered gain noise. The optimized working point has to be set at the point which the sensitivity is maximized and stabilized.

Previous Investigations on Performance Enhancement

Due to the intrinsic limits on the Lorentzian shape, the dynamic range of the conventional BGS is usually in the same magnitude of its FWHM. The enhancement of the above mentioned two key performances has been under intensive investigations since the first demonstration of SA-BOTDA [119], however, with most of them focusing on the dynamic range extension. The extension of the dynamic range is inevitably associated with the broadening of the BGS and hence the widening of the BGS edge. Currently the most common ways are:

- pump modulation: adds two extra sidebands to the pulsed pump in the frequency domain [127]. With the careful setting of the modulation frequency and depth, the generated sidebands could excite their own Brillouin spectra, leading to an overall broadened BGS with a wider and linear edge, as depicted in Fig. 5.1.3(a).

- multi-tone pumps: the edge of the broadened BGS excited by the multi-tone pump is not widened, but its BPS is [128]. The superimposed BPS excited by each tone pump offers a much wider and linear response to the frequency, as demonstrated in Fig. 5.1.3(b). When this phase response is applied on the sideband of a phase modulated probe wave, the

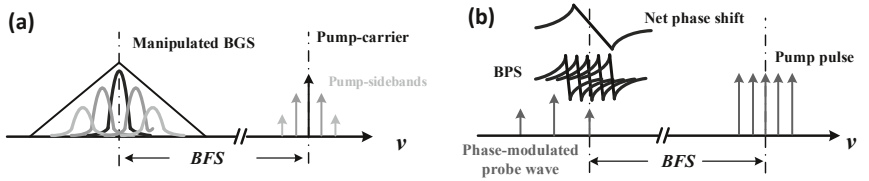

Figure 5.1.3.: Schematic of dynamic range enhancement via (a) pump modulation [127] and (b) multi-tone pump comb [128].

Dieses Werk ist copyrightgeschützt und darf in keiner Form vervielfältigt werden noch an Dritte weitergegeben werden.
Es gilt nur für den persönlichen Gebrauch.

detected RF signal at the modulation frequency would benefit from both the immunity to the pump power fluctuation [123] and a wider dynamic range.

Though successful demonstrations up to several times of extension on the dynamic range with simple configurations, almost all of the techniques suffer from a strong penalty on the sensitivity.

5.2. Schematic Operation Principle

The strong motivation of this investigation is to achieve a dynamic range extension without compromise on the sensitivity in SA-BOTDA. This can be validated by utilizing the superposition of the conventional BGS with a BLS with a frequency offset, as illustrated in Fig. 5.2.1(a).

The mathematical expression of the engineered BGS can be written as:

$$g_s(\nu) = V(\nu) - m \cdot V(\nu + d \cdot \gamma_B) \tag{5.2.1}$$

where $V(\nu)$ is the Voigt profile with the form of Eq. (4.1.1), and m and d have the same definitions as in Eq. (2.7.2). However, different from the spectrum engineering in Sec. 2.7 and Sec. 4.1, only a single loss spectrum is superimposed for circumvention of interference from two loss probe waves and wider extension on the dynamic range. In Fig. 5.2.1(a), the conventional BGS (black) is simulated from the Voigt fitting curve of an experimental conventional BGS excited by a 14 ns pulse with the FWHM slightly broadened to 70 MHz. The engineered BGS is demonstrated with m=0.845 and d=1.337 in Eq. (5.2.1). A visualized extended linear

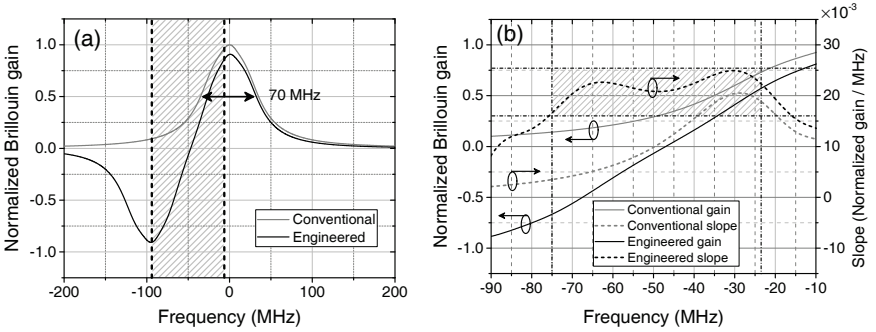

Figure 5.2.1.: Simulation of (a) the conventional (gray) and engineered (black) BGS with the shadowed region zoomed in for (b) their first order derivatives.

Dieses Werk ist copyrightgeschützt und darf in keiner Form vervielfältigt werden noch an Dritte weitergegeben werden.
Es gilt nur für den persönlichen Gebrauch.

range is built between the maximum gain and maximum loss in the frequency domain. The first derivative of the BGS in the shadowed area in Fig. 5.2.1(a) is calculated and depicted in Fig. 5.2.1(b). Compared to the conventional BGS, the flattened shadowed area in Fig. 5.2.1(b) clearly indicates that a well engineered BGS is able to provide an extended linear range with even a steeper slope.

5.3. Theory and Harmonic Analysis

In linear algebra, a function $y(x)$ is defined as linear only if $y(x_1 + x_2) = y(x_1) + y(x_2)$ and $y(ax) = ay(x)$. An important conclusion of these requirements is the absence of harmonics in strictly linear systems: The output of a linear system does not include frequencies beyond those in its input. This feature of linearity is not directly covered by the slope tolerance introduced in Sec. 5.1. In scenarios involving dynamic strains, as for example in the case of vibration monitoring, it is important to ensure that the transduction mechanism represented by SA-BOTDA exhibits minimum harmonic distortion. However, knowing the slope flatness within a given tolerance does not provide information about the magnitude of the corresponding harmonic distortion. Therefore, we propose to characterize the linear range of SA-BOTDA by specifying tolerances for both the slope flatness and the relative magnitude of signal harmonics, quantified here by the ratio of the power of the highest harmonic to that of the signal. In this section, the theory and the simulation results based on this theory will be presented.

Theory

The theory will be presented for a conventional BGS with the Voigt profile described in Eq. (4.1.1). When a dynamic strain signal $s(t)$ is applied to the FUT and induces proportional BFS shifts $\delta\nu_B(t)$, where the conversion factor $C_\varepsilon = \delta\nu_B(t)/s(t)$ is introduced in Eq. (3.1.2) for standard SMF at around 1550 nm, the probe wave at the working point optical frequency ν_{wp} will experience an oscillating gain [121] proportional to $V(\nu_{wp} + \delta\nu_B(t))$. When $s(t)$ and, consequently, $\delta\nu_B(t)$ are sinusoidal, that is:

$$\delta\nu_B(t) = A\sin(\omega t) \tag{5.3.1}$$

with ω being the strain signal angular frequency, the oscillating gain may exhibit harmonics, reducing the measurement fidelity. To study these harmonics, the BGS is extended in a Taylor series in the vicinity of ν_{wp} to:

$$V(\nu_{wp}+\delta\nu_B(t)) = \sum_{n=0}^{\infty} a_n(\nu_{wp})\cdot[\delta\nu_B(t)]^n \approx a_0+a_1\cdot\delta\nu_B(t)+a_2\cdot[\delta\nu_B(t)]^2+a_3\cdot[\delta\nu_B(t)]^3 \tag{5.3.2}$$

Dieses Werk ist copyrightgeschützt und darf in keiner Form vervielfältigt werden noch an Dritte weitergegeben werden.
Es gilt nur für den persönlichen Gebrauch.

where the coefficients a_n are proportional to the corresponding order of derivatives of the function:

$$a_0 = V(\nu_{wp}) \tag{5.3.3a}$$
$$a_1 = V'(\nu_{wp}) \tag{5.3.3b}$$
$$a_2 = \tfrac{1}{2}V''(\nu_{wp}) \tag{5.3.3c}$$
$$a_3 = \tfrac{1}{6}V'''(\nu_{wp}) \tag{5.3.3d}$$

Considering Eq. (5.3.1) and the following trigonometric identities:

$$\sin^2(\omega t) = \frac{1}{2}[1 - \cos(2\omega t)] \tag{5.3.4a}$$
$$\sin^3(\omega t) = \frac{3}{4}\sin(\omega t) - \frac{1}{4}\sin(3\omega t) \tag{5.3.4b}$$

Eq. (5.3.2) can be further expanded as:

$$\begin{aligned} V(\nu_{wp}) =& a_0 + a_1 A\sin(\omega t) + a_2 A^2 \frac{1}{2}[1 - \cos(2\omega t)] + a_3 A^3\left[\frac{3}{4}\sin(\omega t) - \frac{1}{4}\sin(3\omega t)\right] \\ =& a_0 + \frac{1}{2}a_2 A^2 + (a_1 + \frac{3}{4}a_3)A\sin(\omega t) - \frac{1}{2}a_2 A^2\cos(2\omega t) - \frac{1}{4}a_3 A^3\sin(3\omega t) \end{aligned} \tag{5.3.5}$$

The severity of the normally highest harmonics at 2ω and 3ω, namely: the Second and Third Harmonic Distortions (SHD and THD), respectively, are then defined by the power ratios of the signals at frequencies 2ω and 3ω to that of the applied signal at frequency ω. When a fast Fourier transform (FFT) algorithm is applied on Eq. (5.3.5), we may find their expressions as:

$$SHD(\nu_{wp}) \equiv 10\lg\frac{Power(2\omega)}{Power(\omega)} \underset{A\to 0}{=} 20\lg\left|\frac{0.5a_2(\nu_{wp})}{a_1(\nu_{wp}) + 0.75a_3(\nu_{wp})}A\right| \tag{5.3.6a}$$
$$THD(\nu_{wp}) \equiv 10\lg\frac{Power(3\omega)}{Power(\omega)} \underset{A\to 0}{=} 20\lg\left|\frac{0.25a_3(\nu_{wp})}{a_1(\nu_{wp}) + 0.75a_3(\nu_{wp})}A^2\right| \tag{5.3.6b}$$

Taking the expression of Eq. (4.1.1) into consideration, the explicit expressions of a_n, SHD as well as THD can be derived. For the engineered BGS, thanks to the linearity of the algorithm, the corresponding SHD and THD expressions can be derived by replacing the $a_n(\nu_{wp})$ in Eqs. (5.3.6a) and (5.3.6b) with $a_n(\nu_{wp}) - a_n(\nu_{wp} + d\gamma_B)$. Please note that, the expression of Eqs. (5.3.6a) and (5.3.6b) are valid only in the limit of small strain amplitudes so that a_2 and a_3 do not vary too much in the frequency range of $\nu_{wp} \pm A$.

Dieses Werk ist copyrightgeschützt und darf in keiner Form vervielfältigt werden noch an Dritte weitergegeben werden.
Es gilt nur für den persönlichen Gebrauch.

Harmonic Analysis

Simulation results based on the above mentioned model uses the Voigt profile in Fig. 5.2.1 that best fits the experimental measured conventional BGS in Sec. 5.5. For the engineered spectrum, m=0.845 and d=1.337 in Eq. (5.2.1) is applied for an optimized extended linear slope without compromising the slope value.

The studied dynamic strain is a 50 Hz sinusoidal signal. Figure 5.3.1(a) plots the SHD(ν_{wp}) and THD(ν_{wp}) calculated via the analytic expressions of Eqs. (5.3.6a) and (5.3.6b) for both the conventional and engineered Brillouin gain spectra at a strain peak-to-peak amplitude of 280 $\mu\varepsilon$. This value will also be used in the experiment, giving rise to a peak-to-peak BFS variation $\delta\nu_B(t)$ of 5.6 MHz. For a direct comparison, Fig. 5.3.1(b) depicts the numerical calculation results with the same strain signal. As it is clearly indicated, the analytical model at 280 $\mu\varepsilon$ strain amplitude provides a very good approximation. Summarized from Fig. 5.3.1, the proposed engineered spectrum offers a dynamic range larger than that of the conventional BGS. With the cut-off harmonic tolerance of 30 dBc (*e.g.*, 30 dB to the 50 Hz frequency component), the dynamic range is extended more than six times, while for the harmonic tolerance of 25 dBc, four times extension is demonstrated with the dash dotted black line in Fig. 5.3.1. For every doubled strain signal amplitude but still under the limit of small strain amplitude, SHD and THD increase by 3 and 6 dB, respectively, as expected from the expression of SHD and THD, keeping the same spectral shape of the SHD and THD curves as depicted in Fig. 5.3.1.

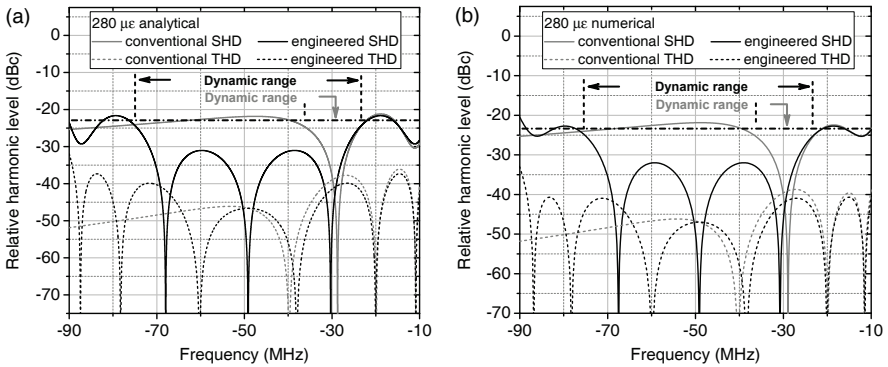

Figure 5.3.1.: The SHD (solid) and THD (dashed) values at different working points of the conventional (gray) and engineered (black) BGS with the dynamic range defined as SHD value above 25 dB (black dash-dotted line) with 280 $\mu\varepsilon$ strain with the (a) analytical and (b) numerical model.

Dieses Werk ist copyrightgeschützt und darf in keiner Form vervielfältigt werden noch an Dritte weitergegeben werden.
Es gilt nur für den persönlichen Gebrauch.

5.4. Experimental Setup

Similar to the setup in Sec. 4.4, the experimental setup as illustrated in Fig. 5.4.1 is configured in a multi-probe scheme depicted in Fig. 5.4.2(a). To avoid any polarization fading, every components in the setup are polarization maintaining. Two 50:50 optical couplers split the laser diode (LD) output at around 1550 nm into three branches. In the upper pump branch, the pump wave is pulsed by an electrical pulse signal via MZM 0. The pulse width and repetition rate originated from a data timing generator (DTG, Tektronix DTG 5534) are set at 14 ns (rise/fall times of few ns) and 50 kHz (20 μs in period), respectively. The value of the repition rate was dictated by hardware limitations rather than by the length of the fiber, which could support a much higher rate. The optical pulse power is controlled by EDFA 0 and VOA 0 to 18 dBm in averaging power before launching into the FUT as the pump wave. In the middle gain probe branch, the optical wave is modulated by MZM 1 working in the carrier suppression regime and driven by the RF signal (f_{RF1} in Fig. 5.4.2(a) from an RFG 1 (Agilent E8267D). The probe wave for the SBS gain interaction is shaped by an optical band-pass filter (O-BPF 1, Yenista XTM-50) by blocking the suppressed carrier, the upper frequency sideband and the ASE noise from EDFA 1. Similarly, in the lower loss probe branch, the optical wave is configured with the suppressed carrier and the lower frequency sideband being blocked by O-BPF 2. Figure 5.4.2(a) depicts the spectrum at the point S in Fig. 5.4.1,

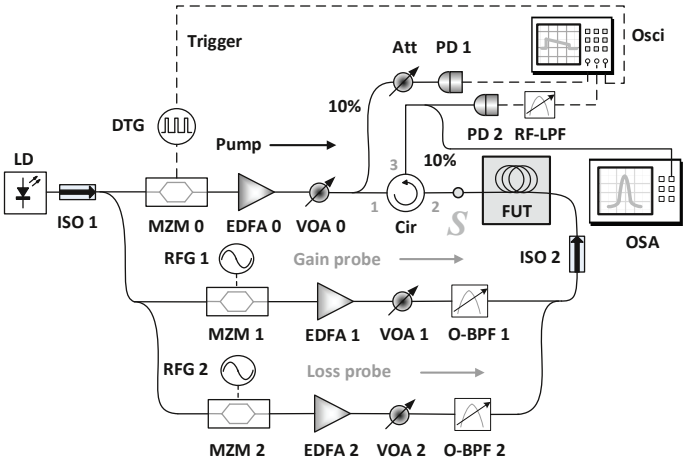

Figure 5.4.1.: Experimental setup. LD: laser diode, DTG: data timing generator, O-BPF: optical band-pass filter, RF-LPF: radio frequency low-pass filter, OSA: optical spectrum analyzer, Osci: oscilloscope, Att: fixed attenuation. [126]

Dieses Werk ist copyrightgeschützt und darf in keiner Form vervielfältigt werden noch an Dritte weitergegeben werden.
Es gilt nur für den persönlichen Gebrauch.

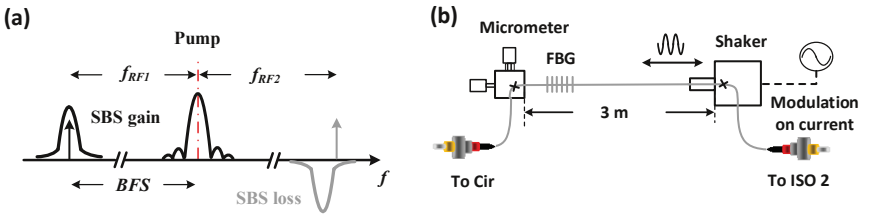

Figure 5.4.2.: (a) Schematic optical spectrum at the point S in Fig. 5.4.1 with CW gain and loss probe waves (solid arrows) and a pulsed pump wave. (b) The specific structure of the FUT in Fig. 5.4.1.

indicating a multi-probe scheme of the experimental implementation. The RF frequencies follow $f_{RF2} = f_{RF1} + d \cdot \gamma_B$, indicated by Eq. (5.2.1). The gain and loss probe wave powers are controlled by the EDFAs and VOAs in the corresponding branches to an almost same power level of −4.1 dBm and −2.7 dBm, respectively. The three MZMs were in good thermal contact with large metal masses and the laboratory environment was air-conditioned. Once properly set, their operating points remained stable during the measurement session. A digital oscilloscope (Keysight DSO-X-91604) records the electrical sensor response from the PD 2 (Newport 1592). A DC–270 MHz RF low-pass filter limits the noise at the input of the digital recording oscilloscope [114], while being wide enough to preserve the spatial resolution offered

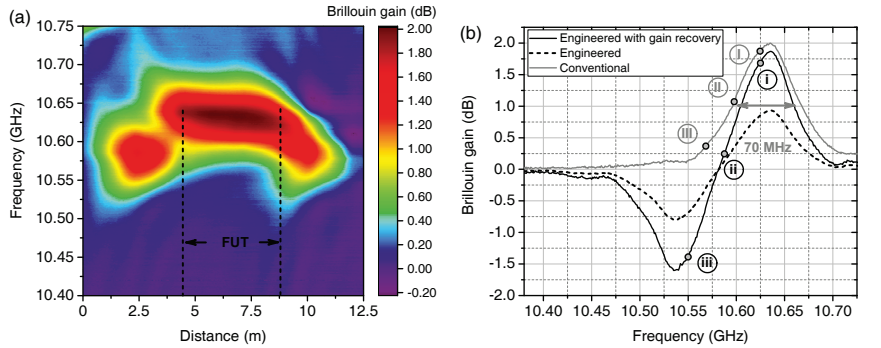

Figure 5.4.3.: (a) The reconstructed BGS with the FUT section; (b) the conventional (gray) and the engineered BGS with (black dashed) and without (black) gain recovery excited by 14 ns pulse measured within the FUT section in static conditions. I-III and i-iii are the selected working points on the conventional and engineered BGS, at which the dynamic sensing is carried out [126].

Dieses Werk ist copyrightgeschützt und darf in keiner Form vervielfältigt werden noch an Dritte weitergegeben werden.
Es gilt nur für den persönlichen Gebrauch.

by the temporal characteristics of the pump pulse [63]. Simultaneous monitoring on the pump pulse is enabled via PD 1 (Newport 1811) with a sufficient power attenuation. Trace recording is triggered by the synchronized electrical pulse sequence signal from the DTG.

The specific structure of the FUT (box with gray background in Fig. 5.4.1) is illustrated in Fig. 5.4.2(b). It consists of a 12 m long polarization maintaining fiber, where a 3 m segment is held between a 2-dimensional micrometer stage (left) and a shaker (right). The motion of the shaker is driven by an audio sinusoidal signal generator, which determines the operating vibration amplitude and frequency. An FBG, having its reflection spectrum centered around 1530 nm, is inscribed on one end of the vibrating segment to allow for an independent monitoring of the vibration amplitude and spectral purity. FBG measurements are performed by disconnecting ports 1 and 3 of the circulator from the Brillouin setup, and connecting them to an LED source and a fast (3 kHz) commercial spectrometer, respectively, which converts the strain induced variations of the FBG peak reflection wavelength to strain. Being practically transparent at the Brillouin operating wavelength of 1550 nm, the FBG does not interfere with the SA-BOTDA experiment.

5.5. Experimental Validation

Static Sensing

Figure 5.4.3(a) shows the reconstructed BGS along the fiber under static conditions with 1 MHz scanning frequency step, 350 MHz span and 32 averages. The BFS ν_B of the FUT is at 10.634 GHz with no ambiguities to the other fiber sections. Figure 5.4.3(b) depicts the experimentally obtained conventional (dark gray) and engineered Brillouin gain spectra (black) with m=0.845 and d=1.337 of the 3 meter FUT section. The FWHM γ_B is broadened to 70 MHz due to the excitation from 14 ns pulse. The gain recovery retrieves the logarithmic gain of the engineered BGS by a multiplication of 2 due to the division of two probe powers (see Appendix C). Three working points on each BGS have been chosen to carry out the slope-assisted dynamic sensing, namely: working points I (10.629 GHz), II (10.597 GHz), III (10.566 GHz) on the conventional BGS and i (10.626 GHz), ii (10.591 GHz), iii (10.551 GHz) on the engineered BGS (with gain recovery). Among them, I, III and i, iii are at the edges of the linear range, while II and ii are in the middle.

Dynamic Sensing

The dynamic signal to be measured is a 50 Hz sinusoidal strain signal. Its peak-to-peak amplitude is set to 280 $\mu\varepsilon$, as independently measured by the FBG. For the dynamic measurement, the oscilloscope works in the segmented mode with 1 GSa/s sampling rate. The trace record

Dieses Werk ist copyrightgeschützt und darf in keiner Form vervielfältigt werden noch an Dritte weitergegeben werden.
Es gilt nur für den persönlichen Gebrauch.

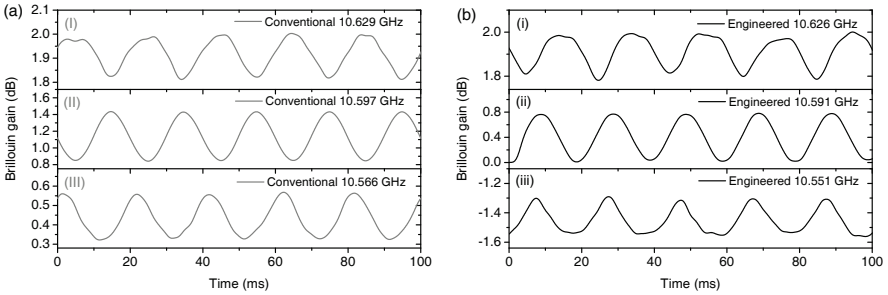

Figure 5.5.1.: Sinusoidal gain signals measured at (a) 10.629 GHz, 10.597 GHz, 10.566 GHz (working points I, II and III in Fig. 5.4.3(b)) on the conventional BGS (dark gray), and (b) 10.626 GHz, 10.591 GHz, 10.551 GHz (working points i, ii and iii in Fig. 5.4.3(b)) on the engineered BGS (black).

is triggered at every 4 pulses. This means, for each sequence of 4 pump pulses, 4 periods of probe output traces are stored in one segment (out of 16,384), and 4 times of averaging can be achieved within these 4 recorded periods to improve the SNR.

The retrieved sinusoidal Brillouin gain responses at the selected working points are illustrated in Fig. 5.5.1. Since the vibration signal amplitude is close to the frequency offset between the working point and the BFS, distortions of the measured gain signals can be observed at the upper edges for the working point I and i on the conventional and engineered BGS, respectively (see Fig. 5.5.1(a-I and b-i)). Therefore, the frequency-to-gain conversion is not linear at these working points. The similar behavior happens for the conventional and engineered BGS at the lower edge with working points III and iii.

To analyze the second harmonic level, an FFT analysis has been carried out at the selected working points with the results presented in Fig. 5.5.2. It can be calculated from the experimental conditions that, the effective vibration signal sampling rate of the proposed sensor is 1 / (4×20 μs) = 12.5 kHz, the number of samples per vibration signal cycle is 12.5 kHz / 50 Hz = 250 and the number of recorded vibration signal cycles is 16,384 / 250 ≈ 65. Sufficient samples per signal cycle and number of recorded cycles ensure an accurate FFT analysis. For the working point with a small frequency offset to the BFS at the edge of the linearity of the conventional BGS (I), where the distortion in the time domain also appears in Fig. 5.5.1, the 2^{nd} harmonic level rises (see Fig. 5.5.2(a-I)). Despite the slightly better situation than the conventional case, the same behavior occurs also for the engineered BGS. The relative 2^{nd} harmonic level at working point i and iii are quite low (see Fig. 5.5.2(b-i) and (b-iii)) while the situation at working point ii is totally different (>40 dBc).

Dieses Werk ist copyrightgeschützt und darf in keiner Form vervielfältigt werden noch an Dritte weitergegeben werden.
Es gilt nur für den persönlichen Gebrauch.

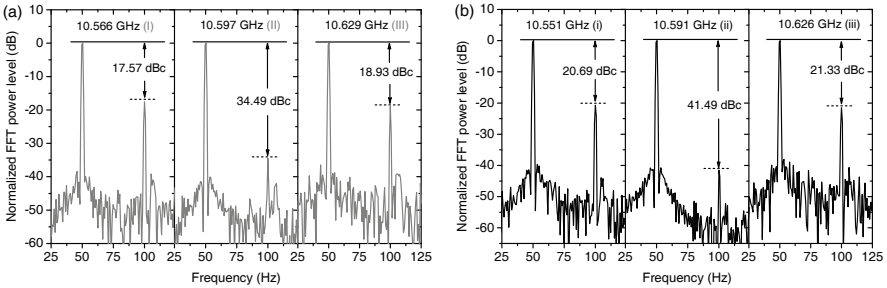

Figure 5.5.2.: FFT spectra of the measured sinusoidal gain signals and their 2^{nd} harmonic level with the (a) conventional (Fig. 5.5.1(a)) and (b) engineered BGS (Fig. 5.5.1(b)).

Systematic dynamic measurements at various working points on both conventional and engineered BGS are carried out. The sensitivities (the slope α) at each working point are analyzed from the retrieved sinusoidal Brillouin gain signals and depicted in Fig. 5.5.3(a). Please note that, different from the simulation results in Fig. 5.2.1(b), the sensitivities in Fig. 5.5.3(a) are not a simple derivative of the static BGS in Fig. 5.4.3(b), but derived from the maximum slope of the retrieved sinusoidal Brillouin gain signals (with necessary fitting curves if severe distortions occur at the edge of the linear range) and converted into the frequency domain under the assumption of a sinusoidal strain signal. The results in Fig. 5.5.3(a) is in good agreement with the simulated one in Fig. 5.2.1(b). An enhancement of the sensitivity by

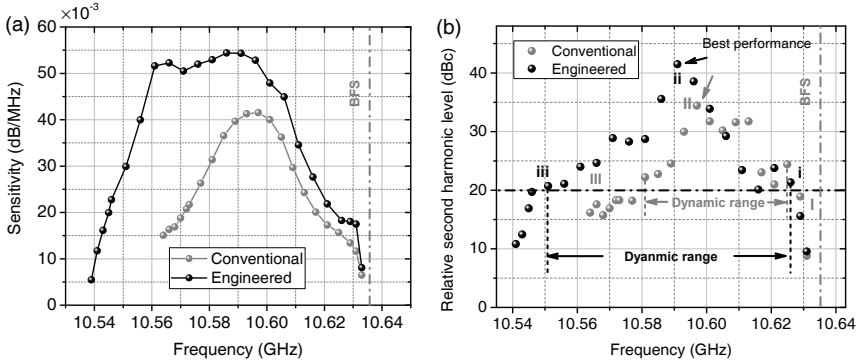

Figure 5.5.3.: (a) Sensitivities measured from the gain signals and (b) the relative 2^{nd} harmonic level at different working points for the conventional (gray) and engineered (black) BGS in the experiment [126].

Dieses Werk ist copyrightgeschützt und darf in keiner Form vervielfältigt werden noch an Dritte weitergegeben werden.
Es gilt nur für den persönlichen Gebrauch.

30% is experimentally demonstrated.

Under the same FFT analysis, the relative harmonic levels are depicted in Fig. 5.5.3(b). The best dynamic sensing performance could be defined at the working point with the highest relative harmonic level (working points with corresponding highlighted arrows in Fig. 5.5.3(b)). The highest relative harmonic level of the engineered BGS is 7 dB higher than the one with conventional BGS, indicating a better dynamic sensing performance. The quantitatively defined dynamic range can be determined with the harmonic level tolerance as shown by the horizontal black dash-dotted line in Fig. 5.5.3(b). According to this definition (relative harmonic level>20 dBc), the dynamic range for the demonstrated conventional and engineered BGS are 44 MHz and 75 MHz, respectively. Thus, an extension of 70.45% has been experimentally demonstrated.

Justification of Gain Recovery

According to the analysis in Sec. 4.6, a thermal noise dominant detection should be justified for a gain recovery. Here the noise level with a single probe input (conventional BGS, gray dots) and two probe inputs (engineered BGS, black dots) are demonstrated in Fig. 5.5.4. The noise level is calculated as the standard deviation of the acquired trace signals in Volt before the Brillouin interaction takes place (before the pulse launches into the fiber). The mean values of the noise level with conventional and engineered BGS are 1.795 mV and 1.802 mV, respectively. These two values show very good agreement with the output noise specification of the photoreceiver (1.8 mV in RMS value). This less than 0.4% error indicates the independence of the noise level on the input power and a thermal noise dominant detection.

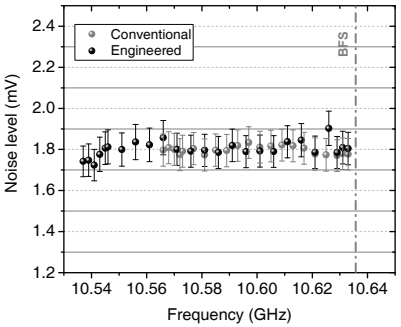

Figure 5.5.4.: The noise level in Volt of the detected trace as a function of working point frequency.

Dieses Werk ist copyrightgeschützt und darf in keiner Form vervielfältigt werden noch an Dritte weitergegeben werden.
Es gilt nur für den persönlichen Gebrauch.

6 Microwave Photonic Filters

Microwave technology is almost everywhere in the daily life today, particularly in the applications such as radar, wireless communications and modern instrumentation. This rises considerably the requirements on the generation, processing, precise control and distribution of microwave and millimeter-wave signals [129]. Conventionally, the generation of microwaves is available from electronic circuits with multiple stages of frequency doubling until a desired frequency is reached. Therefore, such a system is usually complicated, costly and noisy. Not only the generation system, but also the electronic circuits based microwave processing, *i.e.,* filters, and controlling systems are also suffering from the bottleneck problems of the current microwave techniques, namely the frequency (bandwidth) flexibility and tunability.

Microwave photonics studies the interaction between microwave and optical signals, aiming at the photonic generation, processing, controlling and distribution of microwave signals [129]. The microwave signal can be generated in the optical domain via optical heterodyning, circumventing the bandwidth limitation of frequency doubling in circuits and owing striking advantages on the frequency flexibility, low propagation attenuation and electromagnetic immunity. This technique is able to generate RF signals up to the THz band, limited only by the detector bandwidth [129]. Based on the same motivation and closely cooperated with the photonic microwave generation, microwave photonic filtering (MPF) as a typical device of microwave photonic signal processing has been intensively investigated in the past decades. In this chapter, an overview of the MPF performance, and especially the advantages and limitations of the Brillouin based MPF will be presented.

6.1. Key Performances

The discussion about the performance of MPF could follow similar criteria on any traditional microwave filters, as demonstrated in Fig. 6.1.1. Currently, typical consolidated MPF techniques such as FBG, Mach-Zehnder interferometers (MZI), Fabry-Perot interferometers (FPI) and

Dieses Werk ist copyrightgeschützt und darf in keiner Form vervielfältigt werden noch an Dritte weitergegeben werden.
Es gilt nur für den persönlichen Gebrauch.

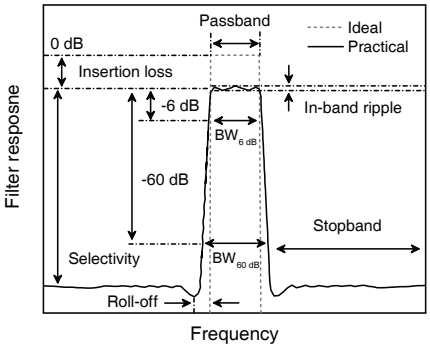

Figure 6.1.1.: An ideal (gray dashed) and practical (black solid) band-pass filter profile with their key specifications.

ring resonators are already available for passive filtering. However, an ideal MPF should have outstanding performances in several aspects, such as flat-top filter response, high selectivity and a wide and independent bandwidth and center frequency tunability [35, 130]. In this regard, the above mentioned MPF techniques have their own pros and contras and could hardly fulfill all the requirements. The description of an ideal MPF performance include:

- Selectivity: symbolizes the rejection of the undesired signals in the stopband and could be quantified as the power difference between the passband and stopband. In some references, the filter selectivity with periodical pass-bands, such as interference based MZI and FPI filters, could be characterized by the quality factor Q as the ratio of the free-spectral range and the FWHM of the single filter response [131]. The selectivity of an ideal MPF should not disturb the original signal in the passband and fully suppress the signal in the stopband.

- Roll-off: is the steepness of the filter profile with frequency. Combined with selectivity, it characterizes the sharpness of the filter profile. The design of a filter seeks to make the roll-off as narrow as possible so that rectangular edges are the case of an ideal MPF profile.

- Flat-top response: symbolizes the response uniformity in the filter passband. It is usually quantified by the in-band ripple, as shown in Fig. 6.1.1.

- Shape factor: is defined as the ratio of the bandwidths of the passband and the stopband. For this figure to have a practical meaning, the attenuation at which the bandwidths of pass- and stopband is measured should also be quoted. As demonstrated in Fig. 6.1.1,

Dieses Werk ist copyrightgeschützt und darf in keiner Form vervielfältigt werden noch an Dritte weitergegeben werden.
Es gilt nur für den persönlichen Gebrauch.

the shape factor can be calculated as: $SF_{6/60dB} = BW_{60dB}/BW_{6dB}$ [35]. For an ideal MPF, $SF_{0/+\infty} = 1$.

- Bandwidth and center frequency tunability: show the advantage of microwave photonics. The center frequency tunability for MPF can usually be achieved by changing the frequency of the optical source. Depending on the specific mechanism of the MPF, there are several solutions to tune the bandwidth. One of the most common ways would be modulation on the optical sources.

In modern RF communication systems, interference mitigation plays also an important role [132, 133], leading to the requirement of another type of filters, *i.e.*, RF notch or bandstop filters. In order to protect sensitive receivers from the high power level undesired interfering signals, RF notch or bandstop filters with high peak absorption, high center frequency accuracy and simultaneously flexible tunability on center frequency and bandwidth are required. Despite the availability of modern RF notch filters with high peak attenuation and high selectivity in low RF frequency range [134–136], a desired high quality RF filter with wide tunable center frequency and bandwidth tuning range in the high RF frequency range is still challenging. Data processing in the optical domain, a branch of microwave photonics, provides a good solution to the bottleneck problem of conventional RF filters. Several techniques have been implemented in realizing microwave photonic notch filters (MPNF). Currently, the consolidated techniques include parallel topology [137], photonic crystal waveguide [138], optical frequency comb [139] and ring resonantor [140].

6.2. Brillouin based MPFs

MPFs based on SBS take the advantage of the Brillouin gain as the filter passband. Unlike FBG and interference based MPFs, Brillouin based MPFs belong to active filters, *i.e.*, the filter works only under the existence of a pump. Out-of-band signals are conventionally not suppressed. Therefore, the selectivity of a conventional Brillouin based MPF equals to the Brillouin gain and is highly dependent on the pump power. Due to the striking advantages of SBS, such as low threshold, high gain and ultra-narrow linewidth, Brillouin based MPFs are usually easy to achieve, and owns a high selectivity and sharp roll-off. Considering the SBS is available all over the telecommunication band, the center frequency tunability of the Brillouin based MPFs is intrinsically ensured. Several solutions for spectrum engineering as mentioned in Sec. 2.7 help to achieve a tunable bandwidth of the Brillouin spectrum. All these factors make the Brillouin based MPFs an attractive application in microwave photonic signal processing.

Dieses Werk ist copyrightgeschützt und darf in keiner Form vervielfältigt werden noch an Dritte weitergegeben werden.
Es gilt nur für den persönlichen Gebrauch.

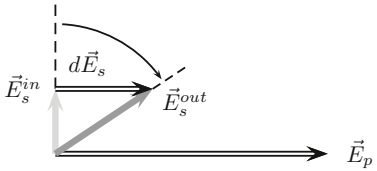

Figure 6.2.1.: The schematic principle of polarization pulling in a field vector point of view [142]. $\vec{E}_s^{in}$ and $\vec{E}_s^{out}$ represent the electric field of in- and output probe wave, respectively, $\vec{E}_p$ is the pump field.

6.2.1. Selectivity Enhancements

The selectivity of the Brillouin based MPF is dependent on the pump wave power. Provided that the input signal is small enough (*e.g.*, < -30 dBm [141]), the Brillouin gain of a monochromatic probe wave could rise up to 30 dB once the pump wave exceeds the threshold, as indicated from the measurement results in Fig. 2.6.1. However, the ASE noise of SBS and the pump depletion restrict the gain from being higher. For a spectrum broadened pump wave, *i.e.*, a wider filter pass-band, the saturation regime will come with a significantly lower gain, since the power is distributed in the spectrum density. To break these limits, the common strategies include:

- Multi-stage amplification: when the pump power exceeds ∼23 dBm, Raman scattering will rise and deplete the Brillouin pump, leading to Brillouin gain saturation [143]. By splitting a very high pump power into several stages of relative lower power amplifications to the probe wave, the Brillouin amplification in every stage would reach its highest efficiency [143] so that Brillouin pump depletion is circumvented.

- Polarization pulling: can be explained as the pulling of the probe wave SOP towards the one of the pump wave due to the energy conversion in the Brillouin interaction, as schematically illustrated in Fig. 6.2.1 [142]. From a field vector point of view, the probe wave SOP is changed by the fraction of the pump field transffered to the probe wave. This gradually dragging effect will eventually align the probe wave SOP with the pump field under a high amplification, leading to an SOP locking even when the input probe wave SOP is random [142]. Different from a traditional mechanical polarization synthesizer, an optical polarization synthesizer can be built based on this principle [144]. The selectivity of the Brillouin based MPFs could be enhanced by utilizing this polarization pulling effect and a polarization beam splitter (PBS). By setting the SOP of probe and pump wave to be orthogonal, the output signal from the same port of the PBS is minimized when the pump wave is off due to the SOP orthogonality, and maximized when the

Dieses Werk ist copyrightgeschützt und darf in keiner Form vervielfältigt werden noch an Dritte weitergegeben werden.
Es gilt nur für den persönlichen Gebrauch.

pump wave is on, due to the parallel SOP [145, 146]. According to the principle of polarization pulling, the selectivity enhancement is mainly attributed to the suppression of the stop-band signal instead of the amplification of the pass-band signal, and the enhancement is more efficient under a high pump power.

6.2.2. Filter Response Engineering

Theoretically, in order to acquire an ideal rectangular SBS gain spectrum, the pump wave spectrum is required to have the same designed shape. This can be achieved preferably by an external modulation with an AWG, as introduced in Sec. 2.7. However, due to the nonlinear response of the electrical and optical components, especially the optical modulator and its driver, the generated optical spectrum is not showing a precise agreement to the electrical modulation signal. As depicted in Fig. 6.2.2, the original flat electrical comb leads to an uneven pump comb and hence the SBS gain. To achieve an agreement between the electrical modulation pattern and gain spectrum, a feedback compensation algorithm is required to continuously modify the amplitude of each electrical comb line according to Gain(dB)$\propto P_p \propto E_p^2$ until a convergence is reached, where P_p is the pump intensity at a specific frequency and E_p is the corresponding electrical amplitude [147]. Cooperated with the feedback compensation, the commonly used modulation pattern for filter response engineering include:

- Electrical comb: with equal channel spacing is usually used for a rectangular spectrum shape. A comb interval smaller than the SBS linewidth is commonly utilized [148]. However, remarkable FWM will be introduced to the adjacent comb lines when the channel spacing becomes small (∼10 MHz), leading to a pump comb with uneven amplitude that could only be partially compensated by a feedback. Furthermore, the FWM converts the energy to out-of-band signals, leading to a decreased pump efficiency, particularly when the pump power is strong and the comb line bandwidth is wide. The solution for this phenomenon is to apply an uneven channel spacing. In this way, the superposition of the intermodulation components on the comb lines can be well

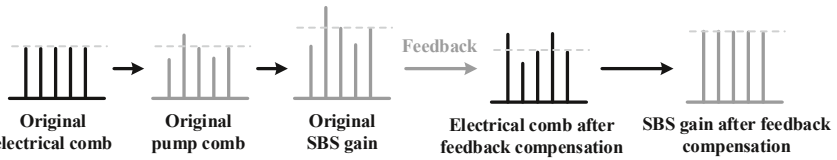

Figure 6.2.2.: The schematic principle of the feedback compensation algorithm with electrical comb as the external modulation pattern [147].

Dieses Werk ist copyrightgeschützt und darf in keiner Form vervielfältigt werden noch an Dritte weitergegeben werden.
Es gilt nur für den persönlichen Gebrauch.

circumvented [148]. However, the competition between the FWM components and comb lines for pump amplification still remains.

- Frequency sweeping: is proposed to overcome the disadvantages of the electrical comb signal [143]. The signal sweeping speed must be carefully determined as one of the important parameters. Too fast sweep in ∼ns period will fail the feedback compensation algorithm, while only an incomplete filter response will be generated if the sweep period is longer than the propagation time of the pump wave [35]. Since the applied fibers are usually long (∼10 km for low threshold), there is usually some space for the sweeping period determination. Currently, the frequency sweeping signal is one of the most favorable choices for Brillouin based MPFs in optical fibers. Just like the case in an ultra-short fiber, different strategies are required to achieve Brillouin based MPFs on chips.

- Direct modulation for arbitrary filter response: can be achieved with the control of the Brillouin gain at a specific frequency in a linear relation given by $G_{SBS}(\nu) \propto S_P(\nu + \nu_B) \propto \Delta t(I_{\nu+\nu_B})$, where $G_{SBS}(\nu)$ is the logarithmic Brillouin gain in the unit of decibels, $S_P(\nu + \nu_B)$ is the pump spectrum, $\Delta t(I_{\nu+\nu_B})$ is the time duration of the current waveform at the corresponding value [41]. With a pre-designed current waveform and an accurate feedback adjustment, arbitrary filter responses, such as rectangular and triangular with a maximized flexibility can be obtained [42].

6.2.3. Brillouin Noise

Just like all the amplification mechanisms, Brillouin interaction provides undesired noise as well. The origin of the Brillouin noise is the random nature of the SpBS [26]. It becomes a severe drawback to Brllouin based applications once the SpBS gets amplified together with the probe signal from the pump energy conversion. The impairment from the Brillouin noise could be significant. Due to the competition of the Brillouin noise and the signal to be amplified for the pump energy, the Brillouin amplification is saturated until a certain level [116]. Similar for the case of Brillouin based MPFs, the selectivity is restricted and saturated [143]. Furthermore, due to the origin of SpBS, the frequency distribution of Brillouin noise is uneven, but densely in the vicinity of BFS with the intensity pump wave (spectrum and power) dependent. Therefore, the probe signal can hardly be separated from the Brillouin noise and several conventional noise reduction methods, such as filtering, are not efficiently working for Brillouin noise reduction [63, 78], making it a bottleneck of almost all Brillouin based applications. In Ch. 7, a typical solution will be proposed to overcome the disadvantage of the Brillouin noise.

Dieses Werk ist copyrightgeschützt und darf in keiner Form vervielfältigt werden noch an Dritte weitergegeben werden.
Es gilt nur für den persönlichen Gebrauch.

7 Transparent Optical Filter

High roll-off, re-configurable bandwidth and independent center frequency tunability make the active Brillouin based optical filter an attractive application in comparison to the traditional passive filters. Conventionally, the gain spectrum of the SBS interaction is served as the filter passband. In Sec. 6.2, an overview about the performance enhancements on this gain based techniques is presented. However, just as for all the gain mechanisms, the Brillouin noise is also introduced in the filter passband, leading to eventually a limit on the selectivity [143]. Since the Brillouin noise is originated from SpBS (ASE noise) and located in the same frequency range of the gain spectrum [26], a circumvention can hardly be achieved. In this chapter, a novel idea on the Brillouin based optical filter is presented providing a Brillouin noise free passband. Based on the suppression of the stop-band signals by the Brillouin loss interactions, the noise-free characteristic of the proposed filter is demonstrated. In principle, all the previous techniques on selectivity enhancement [143, 145] and filter profile engineering [41, 42] can be applied simultaneously to achieve an ideal optical filter free of excess Brillouin noise.

7.1. Schematic Operation Principle

In order to circumvent ASE noise from the Brillouin gain, the proposed optical filter is based on the Brillouin loss interaction. The schematic principle of the proposed filter is illustrated in Fig. 7.1.1(a). The passband of the filter is the transparency region between two broadened losses with an overall frequency bandwidth of 10 GHz. The broadening of the loss spectra can be achieved by a broadened pump wave with either multi-tones [148] or sweeping signals [143] via either direct or external modulation [37]. To avoid FWM due to multi-tone pumps [148], two pump waves (pumps A and B) are generated from the same laser source and broadened by a direct modulation with the same electrical sweeping signal with the sweeping periodicity within the propagation time in the fiber [35].

Dieses Werk ist copyrightgeschützt und darf in keiner Form vervielfältigt werden noch an Dritte weitergegeben werden.
Es gilt nur für den persönlichen Gebrauch.

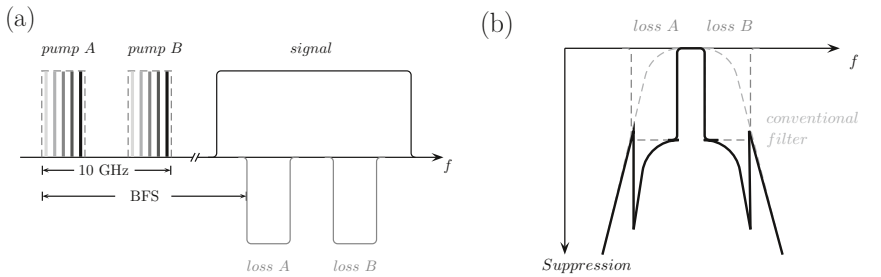

Figure 7.1.1.: (a) Principle of Brillouin loss based filter. Black solid line stands for a broad input signal. (b) Overall filter profile of proposed filter with a conventional optical filter. The light and dark gray dashed line represents the profile of the conventional filter and SBS losses, respectively; the black solid line stands for the overall filter profile [130].

The broad input signal is suppressed symmetrically on both sides by the broadened SBS losses (losses A and B) in the frequency upshifted range to the pump wave by the BFS of the fiber, while the center frequency part stays transparent. All other undesired out-of-range frequency components on both sides of the losses can be suppressed with the assistance of an extra conventional optical filter, as shown with the blue dashed line in Fig. 7.1.1(b). The reason for the proposed filter configuration within 10 GHz is the general accessibility of a commercial optical filter with high performance for this passband range. Since the signal in the proposed filter passband is placed in the maximum transmission of the external filter, it is neither affected by the SBS process nor influenced by the conventional filter, and hence no additional noise is imposed. Considering the Gaussian-shaped filter profile of most of the conventional optical filters with high rejections on both sides and flat-top response in the vicinity of the center frequency, as shown in Fig. 7.1.1(b), the suppression of the spectral components far from the passband center is higher than close to the passband center of the proposed SBS filter.

By carefully controlling the frequency separation between the two pumps and the linewidth of the pump waves, the overall pump range and thereby the loss range can be well manipulated in a frequency range of 10 GHz. In order to eliminate the undesired components from the simultanoues SBS gain interaction in the frequency downshifted range, the assisted conventional optical filter must have a rejection at about 30 GHz. By changing the pump frequency and the amplitude of the sweeping signal, the center frequency and the bandwidth of the filter can be arbitrarily and independently tuned. Due to the transparency in the passband, a flat-top response and low-noise characteristic are easy to achieve.

Dieses Werk ist copyrightgeschützt und darf in keiner Form vervielfältigt werden noch an Dritte weitergegeben werden.
Es gilt nur für den persönlichen Gebrauch.

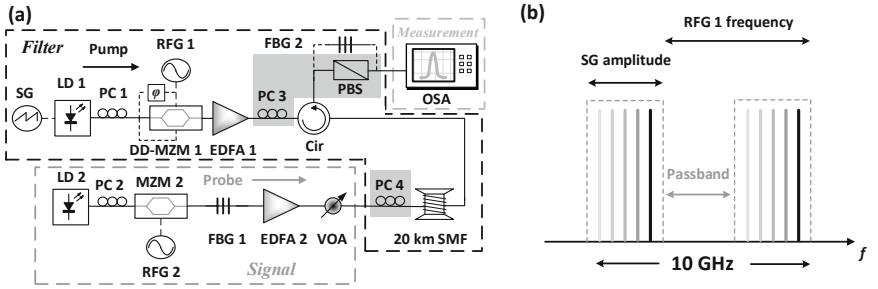

Figure 7.2.1.: (a) Experimental setup. SG: signal generator; DD-MZM, dual-drive MZM. (b) Configuration of the broadened dual pump spectrum.

7.2. Experimental Setup

The experimental setup is illustrated in Fig. 7.2.1(a). The black dashed box depicts the components for the filter, the dark gray dashed box illustrates the generation of the probe signal, and the measurement module is composed of an OSA. The filter profile is generated by a direct modulation of a DFB laser diode (LD 1) centered at 1549.26 nm. The frequency of the direct modulation ramp sweeping signal is 50 kHz, fast enough for the filter generation with a 20 km SMF [35]. The broadened pump linewidth depends on the amplitude of the sweeping signal from the signal generator (SG). The duplication and separation of the pump is achieved by a sinusoidal modulation of a dual-drive MZM (DD-MZM 1). Different from a conventional MZM, DD-MZM provide the possibility to modulate both arms of a MZM with different RF signals. Here an external optical single-sideband (OSSB) modulation is required from DD-MZM 1, so that both arms are modulated by the same RF signal from RFG 1 with an extra phase shifter on one of the arms. With a proper phase shift on one of the arms, one of the modulation sidebands is suppressed. By setting the bias voltage properly, we could achieve the same power of the carrier and another unsuppressed sideband (see Appendix B.2 for the derivation of carrier suppression and OSSB modulation). The modulation frequencies of RFG 1 and the SG are selected so that the broadened carrier, unsuppressed sideband, and the frequency separation between them cover a frequency range of approximately 10 GHz, as schematically depicted in Fig. 7.2.1(b). Please note that, due to the intrinsic narrow Brillouin linewidth, the frequency separation between the unsuppressed sideband and the carrier is equivalent to the passband more than 100 MHz. A high-power EDFA 1 in the pump branch amplifies the pump wave at constant power mode and launches into the 20 km SMF via a circulator. The circulator with dual-isolation offers a directivity of more than 60 dB, blocking efficiently the possible Rayleigh scattering even when the pump power is amplified to a high

Dieses Werk ist copyrightgeschützt und darf in keiner Form vervielfältigt werden noch an Dritte weitergegeben werden.
Es gilt nur für den persönlichen Gebrauch.

level.

The probe signal for measuring the filter response is injected from the other end of the fiber from another LD. The operating frequency of LD 2 is 20 GHz upshift to LD 1. It is modulated by the RF signal from RFG 2 via MZM 2 and works in the carrier suppression regime. The lower frequency sideband from MZM 2 is selected by FBG 1 and utilized as the probe signal. This probe frequency can be scanned in a wide range to cover the total filter bandwidth. Though a higher probe power ensures a higher SNR, the probe power must be below the threshold of any nonlinear effects in the fiber. In the experiment, EDFA 2 and a VOA are utilized to ensure the probe power to be 5 dBm. Since the BFS of the 20 km SMF in the setup is 10.861 GHz, the RF signal from RFG 2 scans from 6 GHz to 20 GHz with 20 MHz steps to get the detailed filter profile with peak detection in the OSA. Please note that, FBG 2 is only connected to the setup during the noise measurement described in Sec. 7.3. The components with gray background are optional for a filter selectivity enhancement via polarization pulling [145], the principle of which has been discussed in Sec. 6.2.1.

7.3. Experimental Validation

Figure 7.3.1 illustrates the pump signal after EDFA 1 measured by a heterodyne detection with a local oscillator (LO, not shown in the setup) in a PD (Finisar XPDV21X0R). With a fixed direct modulation frequency and an increase of the amplitude from the SG, the pump bandwidth from LD 1 increases from 0.25 GHz via 1.45 GHz and 3.15 GHz to 5.48 GHz. The pump powers from the EDFA 1 are 17, 25, 28, and 30 dBm, correspondingly. With a

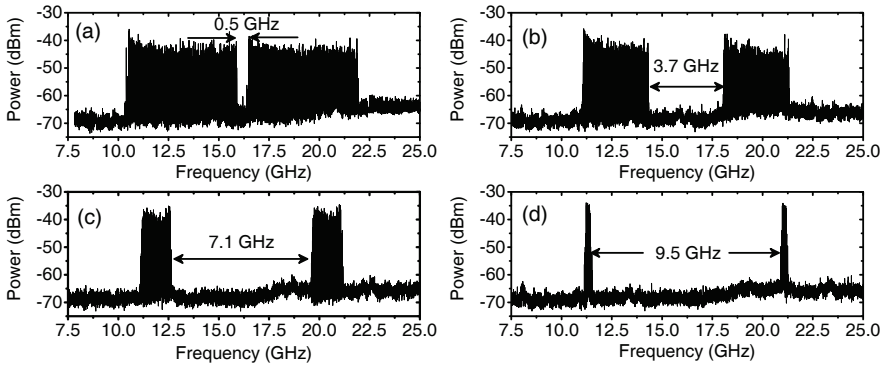

Figure 7.3.1.: Pump spectrum for the filter pass bandwidth of (a) 0.5 GHz, (b) 3.7 GHz, (c) 7.1 GHz and (d) 9.5 GHz.

Dieses Werk ist copyrightgeschützt und darf in keiner Form vervielfältigt werden noch an Dritte weitergegeben werden.
Es gilt nur für den persönlichen Gebrauch.

proper protective attenuation with the VOA before the PD, the detected amplitudes can be manually adjusted to almost the same value, as shown in Fig. 7.3.1. The unflatness of the pump wave is a direct result of the parasitic effect [149]. However, the filter passband is not influenced by this effect. Besides, this effect can also be eliminated with a feedback control on the signal from SG [41]. With these pump configurations, the corresponding targeted filter pass-bandwidth are 9.5 GHz, 7.1 GHz, 3.7 GHz and 0.5 GHz, respectively.

Selectivity Enhancement via Polarization Pulling

As a proof-of-concept of the ability to cooperate with the consolidated performance enhancement techniques, the selectivity enhancement of the proposed filter is demonstrated via polarization pulling [145]. The components required for the polarization pulling are highlighted in Fig. 7.2.1 with gray background. The principle of polarization pulling is introduced in Sec. 6.2.1. Please note that, unlike the scenario of a Brillouin gain based optical filter in Sec. 6.2.1, the SOP of the probe wave in the stop-band here is influenced by the SOP of the pump wave due to the Brillouin interaction. Specifically, the SOP of the probe wave is controlled by a polarization controller (PC 4), so that the output power in the passband through the PBS is maximized. On the other hand, the SOP of the pump wave is controlled

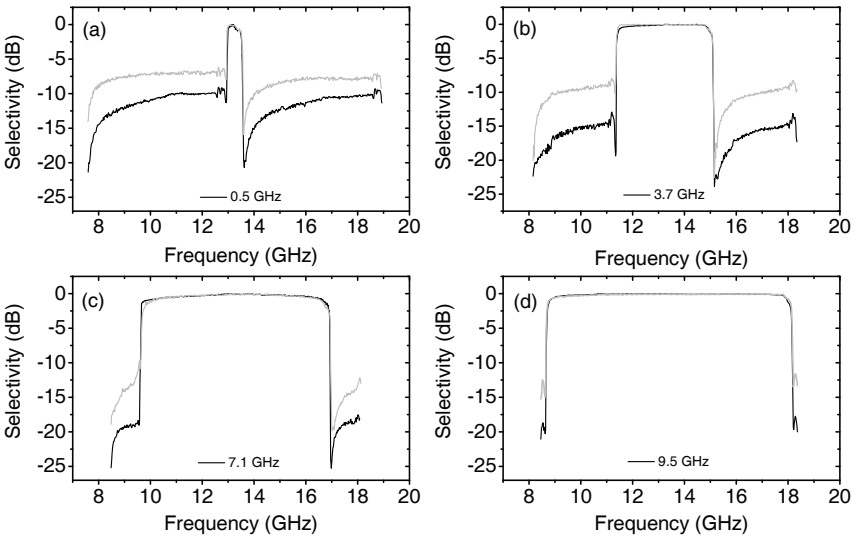

Figure 7.3.2.: The selectivity with (black) and without (gray) polarization pulling with the proposed filter pass bandwidth of (a) 0.5 GHz, (b) 3.7 GHz, (c) 7.1 GHz and (d) 9.5 GHz.

Dieses Werk ist copyrightgeschützt und darf in keiner Form vervielfältigt werden noch an Dritte weitergegeben werden.
Es gilt nur für den persönlichen Gebrauch.

by PC 3, so that the output power in the stop-band through the same port of the PBS is minimized. Considering the output in the stop-band will suffer from not only the attenuation through SBS losses but also an extra polarization suppression, an enhancement of the selectivity can be achieved [85, 145]. Figure 7.3.2 depicts the filter responses with the described pump configurations with (black) and without (gray) the assistance of polarization pulling. Dependent on the bandwidth, an average of 5.5 dB selectivity enhancement has been demonstrated. Despite the limited demonstrated enhancement, the filter selectivity could be further enhanced by a multistage configuration [143] or a phase-modulated probe wave [150], which could also lead to a much sharper edge with much higher roll-off.

Independent Bandwidth and Central Frequency Tunaibility

As demonstrated in Fig. 7.3.3(a), filter pass bandwidths from 9.5 GHz via 7.1 GHz and 3.7 GHz to 500 MHz with the described pump configuration with ripples as low as 0.3 dB are achieved at a fixed center frequency. Since the passband is transparent and SBS interaction free, this ripple might result mainly from the measurement error of the OSA and the output power instability of LD 2. Since the modulation on the pump wave that produces the losses is not perfect, the pump profile is not a perfect rectangle, as shown in Fig. 7.3.1. Thus, at the edges of the filter passbands, the SBS loss interactions have still an influence on the signal. This edge effect leads to a finite roll-off. With a pre-compensation on the LD current of the direct modulation, as demonstrated in Ref. [41], filter bandwidth down to the natural bandwidth of SBS and an edge effect limited to this range can be optimized.

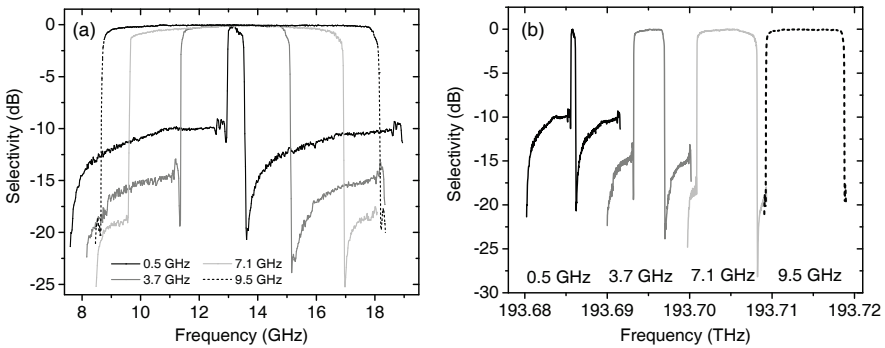

Figure 7.3.3.: Proposed filter profile with (a) fixed and (b) tunable center frequencies and filter pass bandwidth of 0.5 GHz (black solid), 3.7 GHz (dark gray solid), 7.1 GHz (light gray solid), and 9.5 GHz (black dashed)

Dieses Werk ist copyrightgeschützt und darf in keiner Form vervielfältigt werden noch an Dritte weitergegeben werden.
Es gilt nur für den persönlichen Gebrauch.

As it is clearly indicated, although the signal amplitude in the passband is almost independent of the filter bandwidth, the selectivity is bandwidth dependent. Generally, the narrower the pass bandwidth, *i.e.*, the broader the pump linewidth, the more difficult it is to obtain a high selectivity, even under the assistance of polarization pulling. This conclusion shows an agreement with numerous results in gain mechanisms [42, 143, 151, 152] and can be explained as the limited pump power spectral density with the broadened pump linewidth. Specific in the experiment, a selectivity of more than 20 dB is achieved for a bandwidth of 9.5 GHz with polarization pulling for only 17 dBm pump power. In contrast, even with a pump power of up to 30 dBm, a selectivity of only 11 dB can be achieved with polarization pulling for 500 MHz pass bandwidth.

According to the pump spectrum configuration schematically depicted in Fig. 7.2.1(b), the filter center frequency is governed by the pump frequency and further depends on the temperature of LD 1, while the filter bandwidth is governed by the frequency separation between the two pumps, which is further determined by the RF signal frequency from RFG 1 and the amplitude of the direct modulation signal from the SG. Therefore, due to the independence of the above mentioned three parameters, an independent center frequency and bandwidth tuning of the filter can be achieved and demonstrated in Fig. 7.3.3(b). The maximum center frequency tuning range can be as wide as the working frequency range of the LDs in the setup while the minimum and maximum possible bandwidth is limited by the Brillouin linewidth and the available commercial optical filter bandwidth, respectively, as mentioned in Sec. 7.1.

Noise Measurement

Besides the rectangular shape and the narrow bandwidth, the special advantage of the proposed filter is the transparency and additional noise free characteristic in the passband. The noise is measured by a heterodyne detection of the probe signal inside the filter passband with a LO for a Brillouin gain and loss-based filter. The same setup in Fig. 7.2.1 with the frequency of LD 2 downshifted around 20 GHz to LD 1 is used as an SBS gain-based filter. In order to make a fair comparison, the pass bandwidths are set to 2 GHz and the selectivity for both cases are set to be the same, that is, the Brillouin gain and the Brillouin loss are equal to $\approx$ 9 dB, as measured in Fig. 7.3.4(b). To satisfy this condition under the same 17 dBm pump power, a different probe power is applied, *i.e.*, -16 dBm for the gain-based filter, while for the loss case it remains 5 dBm.

Figure 7.3.4(a) depicts the heterodyne signals between the probe signal within the passband of a loss-based filter and a LO are well overlapped when the pump is on and off, *i.e.*,, the filter passband on and off, indicating a full transparency of the filter passband. On the contrary, despite the same SBS gain as depicted in inset (i) of Fig. 7.3.4(b), an obvious pump-spectrum-

Dieses Werk ist copyrightgeschützt und darf in keiner Form vervielfältigt werden noch an Dritte weitergegeben werden.
Es gilt nur für den persönlichen Gebrauch.

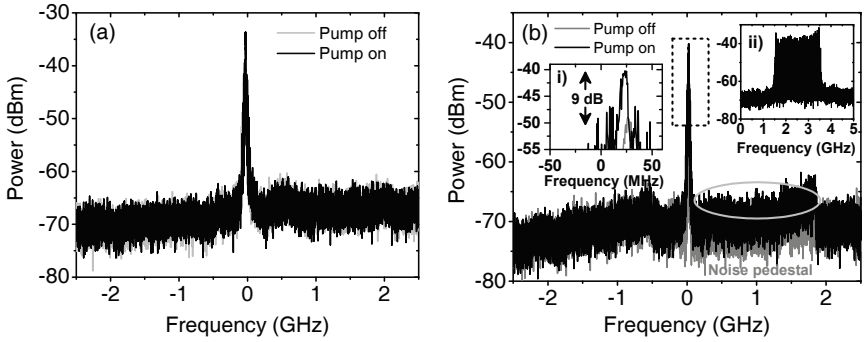

Figure 7.3.4.: Heterodyne detection of the signals in the passband with a local oscillator with (a) the SBS loss-based filter and (b) the SBS gain-based filter. Insets (i) and (ii) show the peak signal and the pump spectrum, respectively.

like noise pedestal as shown in inset (ii) of Fig. 7.3.4(b) with maximum 5 dB difference is detected when the pump is on, indicating an interference from the ASE noise from the Brillouin interaction in the passband. This interference vanishes when the pump is off, which is in good agreement with the noise measurement of a gain-based filter [143]. In order to achieve the same selectivity, the frequency of the probe signal is aligned at the edge of the Brillouin gain, so that the Brillouin noise pedestal is off-center to the right in Fig. 7.3.4(b).

Furthermore, based on the definition of the noise figure as the ratio of input and output SNR of the filter, *i.e.*:

$$F = \frac{SNR_{off}}{SNR_{on}} \tag{7.3.1}$$

where SNR_{off} (SNR_{on}) represents the SNR of the probe signal when pump is off (on), and the data in Fig. 7.3.4, the noise figures of the gain and loss-based filter are calculated to be F_{gain}=2.6904 and F_{loss}=0.9861, respectively. For the calculation of the SNR, we have integrated the noise over the filter bandwidth, as would be done by a broadband receiver. Intuitively, the closer the noise factor is to 1, the less impact the noise is in the passband. The reason for F_{loss} <1 might be a measurement error of the used electrical spectrum analyzer (ESA). As it is clearly indicated, there is no additional noise for the proposed filter, whereas the gain-based system has a noise figure of almost 3. Another disadvantage for a gain-based filter is that, for a multistage gain-based system for selectivity enhancement as in Ref. [143], the noise in each stage is accumulated and amplified in the next. However, this would not be the case for a multistage loss-based system as proposed in this chapter.

Dieses Werk ist copyrightgeschützt und darf in keiner Form vervielfältigt werden noch an Dritte weitergegeben werden.
Es gilt nur für den persönlichen Gebrauch.

8 Dispersion Effect in Microwave Photonic Notch Filters

SBS is one of the most favorable nonlinear effects for the implementation of MPF and MPNF owing to its striking advantages, as discussed in Sec. 6.2. The first demonstration of SBS based MPNF in an optical fiber is reported in [150] with precise sideband-amplitude and -phase control [153]. The key factor of the technique is to set the sidebands after the modulation unbalanced and π phase shifted to each other. Due to the limited degrees of freedom, this cannot be achieved by a phase modulator (PM) or a MZM. A dual-parallel Mach-Zehnder modulator (DPMZM) with a more complicated structure is required.

Despite the nice demonstrations, the drawback of the technique is the sensitivity to the fiber dispersion. The influence of dispersion on microwave photonics has been addressed in several previous works in the context of optical millimeter-wave generation and radio-over-fiber systems [154–157]. Due to the dispersion and dependent on the modulation frequency, each frequency component in the dispersive media will experience a different phase shift. Thus the generated RF signal will suffer from a periodical constructive and destructive interference [154, 155]. In order to avoid the dispersion of a long SMF, either dispersion shifted fibers [158], which introduce almost no dispersion at 1550 nm, or a rather short length of SMF (650 m) have been used [150]. However, the use of a long length of DSF is costly and to use a short length of fiber will increase the SBS threshold and makes the nonlinear interaction more difficult. The problem of the dispersion is circumvented only when this idea was adapted to a chip-based SBS-MPF for a compact integration [159, 160] due to the negligible dispersion in a chip. Nevertheless, this solution cannot be adopted to the fiber based MPNF.

In this chapter, we investigate the influence of the dispersion on the performance of fiber based MPNF. Technical details on the precise control of the sideband-amplitude and phase by the DPMZM will be provided. As will be demonstrated by the theory, simulation and experiment, the dispersion leads to two different detrimental effects on the performance of the SBS based MPNF: *(a)* notch frequency shift; *(b)* drastically reduced notch rejection. A

Dieses Werk ist copyrightgeschützt und darf in keiner Form vervielfältigt werden noch an Dritte weitergegeben werden.
Es gilt nur für den persönlichen Gebrauch.

solution with a tunable dispersion compensation module (TDCM) before detection is proposed to compensate this effect. Thus, even in long standard fibers the excellent performance of this kind of MPNF can be maintained. The criteria for optimizing the filter performance are also discussed in detail.

8.1. Dual Parallel Mach-Zehnder Modulator

Modulator Structure

As depicted in Fig. 8.1.1, the structure of a DPMZM consists of two parallel MZM and an extra PM on one of the arm. The two parallel MZMs, also called *child MZM*, in this structure are usually working in push-pull mode and provide pure intensity modulation (see Appendix B.2 for details). Similarly, the extra PM is called *parent MZM*. RF signals with DC bias voltages can be applied into Ports 1 and 2, while only a DC bias voltage can be applied to the phase shifter from Port 3. For most of the applications, the RF signals to Ports 1 and 2 are in quadrature phase split from the same RF source by a 90 degree hybrid 3 dB coupler.

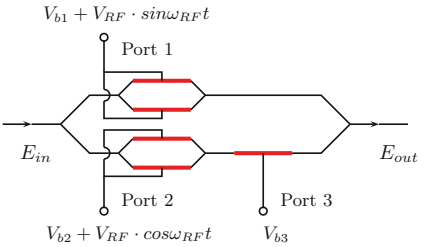

Figure 8.1.1.: Typical structure of a DPMZM with electrodes made of $LiNbO_3$ shown in red.

Modulator Transfer Function

For a CW input into the DPMZM, the complex transfer function is given by: [153]

$$
\begin{aligned}
&E_{out} = \frac{\sqrt{2}}{2} \cdot E_0 \cdot \exp(j\phi) \cdot \\
&\Big\{ J_0(\beta_{RF}) \cdot [(\cos\beta_{b1} + \cos\beta_{b2} \cdot \cos\beta_{b3}) \cdot \cos\omega_0 t + (-\cos\beta_{b2} \cdot \sin\beta_{b3}) \cdot \sin\omega_0 t] \\
&+ J_1(\beta_{RF}) \cdot [(-\sin\beta_{b2} \cdot \cos\beta_{b3}) \cdot \cos(\omega_0 + \omega_{RF})t + (-\sin\beta_{b1} + sin\beta_{b2} \cdot \sin\beta_{b3}) \cdot \sin(\omega_0 + \omega_{RF})t] \\
&+ J_1(\beta_{RF}) \cdot [(-\sin\beta_{b2} \cdot \cos\beta_{b3}) \cdot \cos(\omega_0 - \omega_{RF})t + (\sin\beta_{b1} + sin\beta_{b2} \cdot \sin\beta_{b3}) \cdot \sin(\omega_0 - \omega_{RF})t] \Big\}
\end{aligned}
\tag{8.1.1}
$$

Dieses Werk ist copyrightgeschützt und darf in keiner Form vervielfältigt werden noch an Dritte weitergegeben werden.
Es gilt nur für den persönlichen Gebrauch.

where $E_{in} = E_0 \cdot \exp(j\omega_0 t)$ is the input field with E_0 being the field amplitude and ω_0 being the angular frequency of the optical wave, $\phi = -\omega_0 L n_{eff}/c$ where n_{eff} is the effective refractive index in the waveguide without external voltage, L is the length of the waveguide, the item of $\exp(j\phi)$ represents the phase change due to the propagation distance L in the waveguide without bias voltage, $J_n(z)$ is the n-th Bessel function of the first kind and j is the imaginary unit, β_{bn} and β_{RF} are defined as:

$$\begin{aligned} \beta_{bn} &\equiv \pi V_{bn}/V_\pi \\ \beta_{RF} &\equiv \pi V_{RF}/V_\pi \end{aligned} \tag{8.1.2}$$

whhere V_π is the switching voltage of the modulator and usually assumed to be the same for all ports, V_{bn} is the DC bias voltage applied on the n-th port, V_{RF} and ω_{RF} are the amplitude and the angular frequency of the applied RF signal, respectively.

The output intensity can be calculated from the electric field as $P_{out} = |E_{out}|^2$. By collecting all the items at ω_{RF}, the RF power can be expressed as:

$$\begin{aligned} P_{RF}\Big|_{\omega_{RF}} = -\Re P_{in} \cdot J_0(\beta_{RF}) \cdot J_1(\beta_{RF}) \cdot [&(\cos\beta_{b1} \cdot \sin\beta_{b1} + \sin\beta_{b1} \cdot \cos\beta_{b2} \cdot \cos\beta_{b3}) \cdot \sin\omega_{RF} t \\ &+ (\cos\beta_{b2} \cdot \sin\beta_{b2} + \cos\beta_{b1} \cdot \sin\beta_{b1} \cdot \cos\beta_{b3}) \cdot \cos\omega_{RF} t] \end{aligned} \tag{8.1.3}$$

where $\Re$ is the responsivity of the PD, $P_{in} = |E_{in}|^2$ is the input optical power. As it is clearly indicated, the functionality of the DPMZM could be versatile thanks to the complicated structure and more degrees of freedom on the bias control. The full derivation of the transfer function, Eqs. (8.1.1) and (8.1.3), is demonstrated in Appendix B.3.

I/Q Modulation

In a modern communication system, there are three basic methods to modulate a waveform, namely amplitude modulation (AM), frequency modulation (FM) and phase modulation (PM). Due to the increasing demand on the information capacity, the basic modulation methods can hardly meet the requirement. New modulation methods that are compatible to the digital techniques are developed to increase the modulation efficiency. One of these newly developed modulation methods is called IQ modulation, where I and Q stands for the in-phase and quadrature-phase component of the modulation waveform, respectively. Fig. 8.1.2(a) shows a block diagram of the IQ modulation. Its basic principle is the summation of two signals that are in quadrature phase. In RF systems, this quadrature phase shift of the LO can be achieved by a hybrid 90 degree coupler. Theoretically IQ modulation could generate any type of RF modulation, including AM, FM and PM, within the working frequency range, bandwidth and accuracy capabilities of the modulator device.

Dieses Werk ist copyrightgeschützt und darf in keiner Form vervielfältigt werden noch an Dritte weitergegeben werden.
Es gilt nur für den persönlichen Gebrauch.

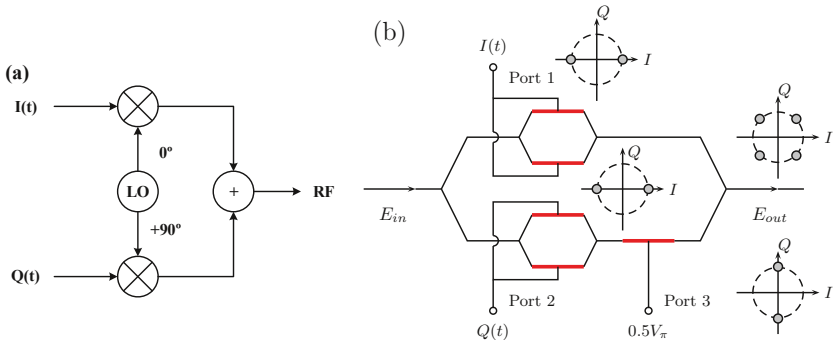

Figure 8.1.2.: (a) IQ modulator block diagram. (b) QPSK modulation process with DPMZM and its constellation diagrams at each stage.

The modulator that enables an IQ modulation is called IQ modulator. In modern optical communication systems, DPMZM are usually used for IQ modulation. The quadrature phase shift of the carrier, as shown in Fig. 8.1.2(a), can be achieved by setting the bias voltage on the parent MZM to half of the switching voltage. The two parallel child MZMs are working in push-pull mode for intensity modulation. Quadrature phase shift keying (QPSK) modulation process with a DPMZM has been schematically demonstrated with its constellation diagrams at each stage in Fig. 8.1.2(b).

8.2. Theory and Schematic Operation Principle

In this section, the theories and operation principles of the SBS based MPNF in the previous investigations [150] and the dispersion effect will be presented.

The operation principle of the SBS based MPNF can be schematically illustrated with Fig. 8.2.1. By utilizing the DPMZM with specific bias voltage and RF signal configuration, the sidebands of a probe wave can be set to be unbalanced while the phases are π shifted to each other. The specific configuration of the DPMZM will be introduced later in this section. In case of an interaction of the SBS gain/loss on one of the sidebands, the amplitudes of the sidebands will be equalized. In principle, the technique is valid for both an equalization on the lower frequency sideband (LSB) and upper frequency sideband (USB) via Brillouin gain and loss interaction. Considering the Brillouin interaction does not provide extra phase shift at the peak gain (or loss) (see Fig. 2.4.1), the sidebands at the peak gain (or loss) remain original out-of-phase, leading to a strong destructive interference at the modulation frequency, similar to the output directly after a PM. Therefore the notch is formed at this specific microwave

Dieses Werk ist copyrightgeschützt und darf in keiner Form vervielfältigt werden noch an Dritte weitergegeben werden.
Es gilt nur für den persönlichen Gebrauch.

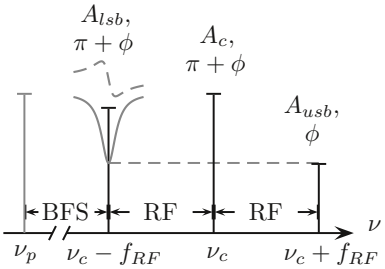

Figure 8.2.1.: Schematic principle of the SBS loss based MPNF: probe wave spectrum after modulation from a DPMZM with unbalanced amplitude and π phase shifted sidebands. The SBS loss interaction from the pump (gray line) takes place on the LSB and equalizes the unbalanced sidebands.

frequency by the signal cancellation at the receiver with the rejection much higher than the conventional SBS gain/loss. For simplicity, the discussion hereafter is carried out based on a higher LSB amplitude of the modulation sideband and an equalization of the sideband via Brillouin loss interaction, as depicted in Fig.8.2.1.

The introduction of the specific configuration of the DPMZM will be divided into two parts: the conditions for the unbalanced and out-of-phase sideband modulation, and the notch formation with this configuration with Brillouin interaction. In the first step, the expressions of the amplitude and phase of the carrier, LSB and USB would be separated. We may denote the electric field of the USB from Eq. (8.1.1) as:

$$\begin{aligned} E_{usb}(t) = &\sqrt{t_{ff}} E_{in} \cdot J_1(\beta_{RF}) \cdot \\ &[(-\sin\beta_{b2} \cdot \cos\beta_{b3}) \cdot \cos(\omega_0 + \omega_{RF})t + (-\sin\beta_{b1} + sin\beta_{b2} \cdot \sin\beta_{b3}) \cdot \sin(\omega_0 + \omega_{RF})t] \\ &\equiv \sqrt{t_{ff}} E_{in} \cdot J_1(\beta_{RF}) \cdot A_{usb} \cdot \sin[(\omega_c + \omega_{RF})t + \phi_{usb}] \end{aligned} \tag{8.2.1}$$

where t_{ff} is the (power) insertion loss including the intrinsic 3 dB loss from the Y-branch of the DPMZM and

$$A_{usb} = J_1(\beta_{RF}) \cdot \sqrt{\sin^2\beta_{b2} \cdot \cos^2\beta_{b3} + (-\sin\beta_{b1} + \sin\beta_{b2} \cdot \sin\beta_{b3})^2} \tag{8.2.2a}$$

$$\sin\phi_{usb} = \frac{-\sin\beta_{b2} \cdot \cos\beta_{b3}}{\sqrt{\sin^2\beta_{b2} \cdot \cos^2\beta_{b3} + (-\sin\beta_{b1} + \sin\beta_{b2} \cdot \sin\beta_{b3})^2}} \tag{8.2.2b}$$

$$\cos\phi_{usb} = \frac{-\sin\beta_{b1} + \sin\beta_{b2} \cdot \sin\beta_{b3}}{\sqrt{\sin^2\beta_{b2} \cdot \cos^2\beta_{b3} + (-\sin\beta_{b1} + \sin\beta_{b2} \cdot \sin\beta_{b3})^2}} \tag{8.2.2c}$$

Dieses Werk ist copyrightgeschützt und darf in keiner Form vervielfältigt werden noch an Dritte weitergegeben werden.
Es gilt nur für den persönlichen Gebrauch.

Similarly we may have the electric field of the LSB as:

$$\begin{aligned} E_{lsb}(t) &= \sqrt{t_{ff}}E_{in}\cdot J_1(\beta_{RF})\cdot \\ &\quad [(-\sin\beta_{b2}\cdot\cos\beta_{b3})\cdot\cos(\omega_0-\omega_{RF})t+(\sin\beta_{b1}+sin\beta_{b2}\cdot\sin\beta_{b3})\cdot\sin(\omega_0-\omega_{RF})t]\Big\} \\ &\equiv \sqrt{t_{ff}}E_{in}\cdot J_1(\beta_{RF})\cdot A_{lsb}\cdot\sin[(\omega_c-\omega_{RF})t+\phi_{lsb}] \end{aligned} \tag{8.2.3}$$

where

$$A_{lsb} = J_1(\beta_{RF})\cdot\sqrt{\sin^2\beta_{b2}\cdot\cos^2\beta_{b3}+(\sin\beta_{b1}+\sin\beta_{b2}\cdot\sin\beta_{b3})^2} \tag{8.2.4a}$$

$$\sin\phi_{lsb} = \frac{-\sin\beta_{b2}\cdot cos\beta_{b3}}{\sqrt{\sin^2\beta_{b2}\cdot\cos^2\beta_{b3}+(\sin\beta_{b1}+\sin\beta_{b2}\cdot\sin\beta_{b3})^2}} \tag{8.2.4b}$$

$$\cos\phi_{lsb} = \frac{\sin\beta_{b1}+\sin\beta_{b2}\cdot\sin\beta_{b3}}{\sqrt{\sin^2\beta_{b2}\cdot\cos^2\beta_{b3}+(\sin\beta_{b1}+\sin\beta_{b2}\cdot\sin\beta_{b3})^2}} \tag{8.2.4c}$$

The expression for the carrier electric field is:

$$\begin{aligned} E_c(t) &= \sqrt{t_{ff}}E_{in}\cdot J_0(\beta_{RF})\cdot[(\cos\beta_{b1}+\cos\beta_{b2}\cdot\cos\beta_{b3})\cdot\cos\omega_0 t+(-\cos\beta_{b2}\cdot\sin\beta_{b3})\cdot\sin\omega_0 t] \\ &\equiv \sqrt{t_{ff}}E_{in}\cdot J_0(\beta_{RF})\cdot A_c\cdot\sin(\omega_c t+\phi_c) \end{aligned} \tag{8.2.5}$$

where

$$A_c = J_0(\beta_{RF})\cdot\sqrt{(\cos\beta_{b1}+\cos\beta_{b2}\cdot\cos\beta_{b3})^2+(-\cos\beta_{b2}\cdot\sin\beta_{b3})^2} \tag{8.2.6a}$$

$$\sin\phi_c = \frac{\cos\beta_{b1}+\cos\beta_{b2}\cdot\cos\beta_{b3}}{\sqrt{(\cos\beta_{b1}+\cos\beta_{b2}\cdot\cos\beta_{b3})^2+(-\cos\beta_{b2}\cdot\sin\beta_{b3})^2}} \tag{8.2.6b}$$

$$\cos\phi_c = \frac{-\cos\beta_{b2}\cdot\sin\beta_{b3}}{\sqrt{(\cos\beta_{b1}+\cos\beta_{b2}\cdot cos\beta_{b3})^2+(-\cos\beta_{b2}\cdot\sin\beta_{b3})^2}} \tag{8.2.6c}$$

8.2.1. Out-of-phase Shifted Sidebands

The π shift of the sideband phase, *i.e.*, $\phi_{lsb}-\phi_{usb}=\pi$ means:

$$\sin\phi_{lsb} = -\sin\phi_{usb} \tag{8.2.7a}$$

$$\cos\phi_{lsb} = -\cos\phi_{usb} \tag{8.2.7b}$$

Besides, the amplitude of the sidebands after the modulation should not be the same, *i.e.*:

$$A_{lsb} \neq A_{usb} \tag{8.2.8}$$

Dieses Werk ist copyrightgeschützt und darf in keiner Form vervielfältigt werden noch an Dritte weitergegeben werden.
Es gilt nur für den persönlichen Gebrauch.

Therefore, Eqs. (8.2.7a), (8.2.7b) and (8.2.8) are the pre-conditions for the π shifted sideband phase.

Considering Eqs. (8.2.2a) and (8.2.4a), Eq. (8.2.8) yields:

$$(\sin\beta_{b1}+\sin\beta_{b2}\cdot\sin\beta_{b3})^2\neq(-\sin\beta_{b1}+\sin\beta_{b2}\cdot\sin\beta_{b3})^2\Longrightarrow\sin\beta_{b1}\cdot\sin\beta_{b2}\cdot\sin\beta_{b3}\neq 0$$

leading to a general solution:

$$\sin\beta_{bn}\neq 0 \tag{8.2.9}$$

Considering Eqs. (8.2.2b), (8.2.4b), (8.2.8) and $\sin\beta_{b2}\neq 0$, the only possible solution to Eq. (8.2.7a) would be:

$$\cos\beta_{b3}=0 \tag{8.2.10}$$

Please note that, Eq. (8.2.10), the solution of Eq. (8.2.7a) does not violate Eq. (8.2.9), the solution to Eq. (8.2.8), since $\sin\beta_{b3}$ meanwhile equals to ±1.

Considering $\cos\beta_{b3}=0$ in Eq. (8.2.7b), we may have:

$$\frac{\sin\beta_{b1}+\sin\beta_{b2}\cdot\sin\beta_{b3}}{|\sin\beta_{b1}+\sin\beta_{b2}\cdot\sin\beta_{b3}|}=-\frac{-\sin\beta_{b1}+\sin\beta_{b2}\cdot\sin\beta_{b3}}{|-\sin\beta_{b1}+\sin\beta_{b2}\cdot\sin\beta_{b3}|} \tag{8.2.11}$$

- $\beta_{b3}=\dfrac{\pi}{2}\Longrightarrow\sin\beta_{b3}=1$, then Eq. (8.2.11) turns into:

$$\frac{\sin\beta_{b1}+\sin\beta_{b2}}{|\sin\beta_{b1}+\sin\beta_{b2}|}=-\frac{-\sin\beta_{b1}+\sin\beta_{b2}}{|-\sin\beta_{b1}+\sin\beta_{b2}|}\Longleftrightarrow(\sin\beta_{b1}+\sin\beta_{b2})\cdot(\sin\beta_{b1}-\sin\beta_{b2})>0$$

- $\beta_{b3}=-\dfrac{\pi}{2}\Longrightarrow\sin\beta_{b3}=-1$, then Eq. (8.2.11) turns into:

$$\frac{\sin\beta_{b1}-\sin\beta_{b2}}{|\sin\beta_{b1}-\sin\beta_{b2}|}=-\frac{-\sin\beta_{b1}-\sin\beta_{b2}}{|-\sin\beta_{b1}-\sin\beta_{b2}|}\Longleftrightarrow(\sin\beta_{b1}-\sin\beta_{b2})\cdot(\sin\beta_{b1}+\sin\beta_{b2})>0$$

  reaching the same equation as the previous case.

In a short summary, in order to make the phase difference between the sidebands π shifted, the bias voltage applied on the parent MZM should follow:

$$\beta_{b3}=\pm\frac{\pi}{2}\quad\Longrightarrow\quad V_{b3}=\pm\frac{V_\pi}{2} \tag{8.2.12}$$

With this condition, the amplitude unbalance can be tuned by V_{b1} and V_{b2}.

Dieses Werk ist copyrightgeschützt und darf in keiner Form vervielfältigt werden noch an Dritte weitergegeben werden.
Es gilt nur für den persönlichen Gebrauch.

8.2.2. Requirements on Carrier Phase

At the first glance, the fulfillment of Eq. (8.2.12) would be sufficient to fulfill the condition for the notch formation. However, this is not necessarily true. Provided that the sidebands phases are π shifted with their initial phase ϕ_s and their amplitudes are also unbalanced, the detected RF power can be expressed as:

$$\Re|A_c \cdot \cos(\omega_c t + \phi_c) + A_{lsb} \cdot \cos[(\omega_c - \omega_{RF}) \cdot t + \pi + \phi_s] + A_{usb} \cdot \cos[(\omega_c + \omega_{RF}) \cdot t + \phi_s]|^2 \quad (8.2.13)$$

where ϕ_c is the carrier phase at the detection. Among the expansion, only two items will contribute to the frequency component with $\omega_{RF}t$, namely:

$$\Re|2A_c \cdot A_{lsb} \cdot \cos(\omega_c t + \phi_c) \cdot \cos[(\omega_c - \omega_{RF}) \cdot t + \phi_s] - 2A_c \cdot A_{usb} \cdot \cos(\omega_c t + \phi_c) \cdot \cos[(\omega_c + \omega_{RF}) \cdot t + \phi_s]| \quad (8.2.14)$$

With further simplification by applying product-to-sum identities and neglecting the $2\omega_{RF}t$ items, we may have:

$$P_{RF}\Big|_{\omega_{RF}} = \Re|A_c \cdot A_{lsb} \cdot \cos(\omega_{RF}t + \phi_c - \phi_s) - A_c \cdot A_{usb} \cdot \cos(\omega_{RF}t - \phi_c + \phi_s)| \quad (8.2.15)$$

As we can see, the result is dependent not only on the sideband amplitude difference $A_{usb} - A_{lsb}$, but also on the phase difference between the sideband and carrier $\phi_c - \phi_s$. This means, an RF power cancellation ($P_{RF} = 0$) cannot be achieved even with a balanced sideband amplitude and a π phase shift between sidebands, if there is phase difference between the sideband and carrier.

One of the typical conditions for the carrier phase is $\phi_c = \phi_s$. We then could re-write the conditions for an out-of-phase cancellation from the DPMZM as:

$$|\phi_{usb} - \phi_{lsb}| = \pi \quad A_{usb} \neq A_{usb} \quad \phi_c = \phi_s \quad (8.2.16)$$

particularly the last requirement on the carrier phase is easy to be neglected. Based on the pump-probe configuration as illustrated in Fig. 8.2.1, we may reach to one of the specific bias voltage configurations as:

$$V_{b1} = 0.5V_\pi \quad 0 < V_{b2} < 0.5V_\pi \quad V_{b3} = 0.5V_\pi \quad (8.2.17)$$

In this scenario, $V_{b3} = 0.5V_\pi$ ensures $\phi_{usb} - \phi_{lsb} = \pi$, $V_{b1} = 0.5V_\pi$ satisfies $\phi_c = \phi_s$, $0 < V_{b2} < 0.5V_\pi$ generates a higher amplitude for the LSB. The specific value of V_{b2} adjusts the amplitude difference between the sidebands. Under the exact bias voltages setting Eq. (8.2.17), the RF

Dieses Werk ist copyrightgeschützt und darf in keiner Form vervielfältigt werden noch an Dritte weitergegeben werden.
Es gilt nur für den persönlichen Gebrauch.

power detected at ω_{RF} could be further derived from Eq. (8.2.15) to

$$\begin{aligned} P_{RF}\Big|_{\omega_{RF}} &= \Re A_c \cdot |A_{lsb} - A_{usb}| \\ &= \Re J_0(\beta_{RF}) \cdot \cos\beta_{b2} \cdot \{J_1(\beta_{RF}) \cdot [1 + \sin(\beta_{b2})] - J_1(\beta_{RF}) \cdot [1 - \sin(\beta_{b2})]\} \\ &= \frac{1}{2}\Re J_0(\beta_{RF}) J_1(\beta_{RF}) \cdot \sin(2\beta_{b2}) \end{aligned} \quad (8.2.18)$$

Considering the case of a total cancellation of the RF power, the minimum P_{RF} is zero with a balanced sideband amplitude. Therefore, to demonstrate a higher notch rejection, the optimal value of β_{b2} and V_{b2} are:

$$\beta_{b2} = \pi/4 \quad \Longrightarrow \quad V_{b2} = 0.25V_{\pi} \quad (8.2.19)$$

8.2.3. Notch Formation via Brillouin Interaction

The notch formation via the Brillouin interaction can be modelled by taking into consideration its simultaneous amplitude (gain or loss) and phase modulation. The detected optical field after the Brillouin loss interaction on the LSB can be re-written as:

$$\Re \cdot |A_c \cdot \cos(\omega_c t + \pi) + G_{SBS} A_{lsb} \cdot \cos[(\omega_c - \omega_{RF}) \cdot t + \pi + \Phi_{SBS}] + A_{usb} \cdot \cos[(\omega_c + \omega_{RF}) \cdot t]|^2 \quad (8.2.20)$$

where G_{SBS} and Φ_{SBS} are the BLS and the corresponding BPS with the negative value of Eqs. (2.4.4) and (2.4.5). By collecting all the components with ω_{RF}, Eq. (8.2.20) can be further simplified to:

$$\Re \cdot A_c \cdot |(G_{SBS} A_{lsb} \cdot \cos\Phi_{SBS} - A_{usb}) \cdot \cos(\omega_{RF} t) + G_{SBS} A_{lsb} \cdot \sin\Phi_{SBS} \cdot \sin(\omega_{RF} t)| \quad (8.2.21)$$

Therefore, the detected RF power is re-written as:

$$P_{RF}\Big|_{\omega_{RF}} = \Re \cdot A_c \cdot \sqrt{(G_{SBS} A_{lsb} \cdot \cos\Phi_{SBS} - A_{usb})^2 + (G_{SBS} A_{lsb} \cdot \sin\Phi_{SBS})^2} \quad (8.2.22)$$

The pump power for a Brillouin loss interaction that well eliminates the sideband unbalance at the maximum loss, as illustrated in Fig. 8.2.1, can be calculated based on Eq. (2.4.4) and the condition of:

$$G_{SBS} A_{lsb} = A_{usb} \quad (8.2.23)$$

with the bias voltage configuration as in Eqs. (8.2.17) and (8.2.19).

Dieses Werk ist copyrightgeschützt und darf in keiner Form vervielfältigt werden noch an Dritte weitergegeben werden.
Es gilt nur für den persönlichen Gebrauch.

8.2.4. Dispersion Effect

In standard SMF, different optical waves with different frequencies have slightly different refractive index and therefore propagate with different phase velocities due to the dispersion [5]. Accordingly, the π phase shift of sidebands directly after the DPMZM with the bias voltage configuration in Eqs. (8.2.17) and (8.2.19) will not be maintained during the propagation through SMF. This dispersion effect will be severe when the length of SMF is typically long. However, contradictorily, longer SMF reduce the SBS threshold and make the Brillouin interaction easier to happen. Owing to the commonly use of short SMF, the dispersion effect has never been mentioned in the previous publications [150]. In this subsection, the theory of the influence of SMF dispersion on the MPNF performance will be investigated.

The detected RF power should be revised when taken the dispersion effect into consideration, *i.e.*, Eq. (8.2.20) should further include the phase items due to dispersion as: [161–163]

$$\Re|A_c\cos(\omega_c t+\pi+\phi_{D,c})+G_{SBS}A_{lsb}\cos[(\omega_c-\omega_{RF})t+\pi+\Phi_{SBS}+\phi_{D,lsb}]+A_{usb}\cos[(\omega_c+\omega_{RF})t+\phi_{D,usb}]|^2 \tag{8.2.24}$$

where the extra phase items $\phi_{D,c}$, $\phi_{D,lsb}$, $\phi_{D,usb}$ stand for the phase changes due to dispersion upon carrier, LSB and USB. By collecting all the components with ω_{RF}, Eq. (8.2.24) can be simplified to:

$$\begin{aligned}\Re A_c|\,&[G_{SBS}A_{lsb}\cdot\cos(\Phi_{SBS}+\phi_{D,lsb}-\phi_{D,c})-A_{usb}\cdot\cos(\phi_{D,usb}-\phi_{D,c})]\cdot\cos(\omega_{RF}t)\\&+[G_{SBS}A_{lsb}\cdot\sin(\Phi_{SBS}+\phi_{D,lsb}-\phi_{D,c})+A_{usb}\cdot\sin(\phi_{D,usb}-\phi_{D,c})]\cdot\sin(\omega_{RF}t)|\end{aligned} \tag{8.2.25}$$

leading to the detected RF power given by:

$$\begin{aligned}P_{RF}\Big|_{\omega_{RF}}=\Re A_c\Big\{&[G_{SBS}A_{lsb}\cdot\cos(\Phi_{SBS}+\phi_{D,lsb}-\phi_{D,c})-A_{usb}\cdot\cos(\phi_{D,usb}-\phi_{D,c})]^2\\&+[G_{SBS}A_{lsb}\cdot\sin(\Phi_{SBS}+\phi_{D,lsb}-\phi_{D,c})+A_{usb}\cdot\sin(\phi_{D,usb}-\phi_{D,c})]^2\Big\}^{1/2}\end{aligned} \tag{8.2.26}$$

According to the Taylor expansion of the propagation constant of carrier β_c and LSB β_{lsb} into the second order at carrier frequency ω_c, the expression of the dispersion related phase items can be written as:

$$\phi_{lsb}-\phi_c=(\beta_{lsb}-\beta_c)\cdot L=\frac{1}{2}\cdot\beta_2(\omega_{lsb}-\omega_c)^2\cdot L=\frac{1}{2}\cdot\beta_2\omega_{RF}^2\cdot L \tag{8.2.27}$$

where β_2 is the second derivative of the propagation constant and symbolizes the chromatic

Dieses Werk ist copyrightgeschützt und darf in keiner Form vervielfältigt werden noch an Dritte weitergegeben werden.
Es gilt nur für den persönlichen Gebrauch.

dispersion. According to the definition of dispersion D: [5]

$$D = -\frac{2\pi c}{\lambda^2}\beta_2 \quad \Longrightarrow \quad \beta_2 L = -\frac{DL\lambda^2}{2\pi c} \tag{8.2.28}$$

Thus, Eq. (8.2.27) can be transferred into: [157]

$$\phi_{D,lsb} - \phi_{D,c} = -\frac{DL\lambda_c^2}{4\pi c} \cdot \omega_{RF}^2 \tag{8.2.29}$$

where for standard SMF, the dispersion $D = 16$ ps/(nm·km). As it is clearly indicated, the phase shift between LSB and carrier is no longer maintained during the propagation in the SMF. Therefore, a proper dispersion compensation D_c is necessary. With the dispersion compensation,

$$\phi_{D,lsb} - \phi_{D,c} = -\frac{\lambda_c^2}{4\pi c} \cdot (DL - D_c) \cdot \omega_{RF}^2 \tag{8.2.30}$$

it is clearly indicated that, when $D_c = D{\cdot}L$, *i.e.*, the dispersion of SMF is properly compensated, the original phase shift will be retrieved. Actually, due to the symmetry, the dispersion compensation module in the setup will compensate the dispersion between the carrier and USB in the same way as, leading to

$$\phi_{D,usb} - \phi_{D,c} = \phi_{D,lsb} - \phi_{D,c} = -\frac{\lambda_c^2}{4\pi c} \cdot (DL - D_c) \cdot \omega_{RF}^2 \tag{8.2.31}$$

8.3. Simulation Prediction

8.3.1. Notch Formation

It can be concluded from Eqs. (8.2.4a) and (8.2.2a) that, the ratio of the sideband (power) between the LSB and USB is a constant, if Eqs. (8.2.17) and (8.2.19) is satisfied. Besides, this ratio is surprisingly independent of the optical input power of the DPMZM. Therefore, it is theoretically possible to find an optimal pump power that generates a suitable SBS loss [22, 23] to eliminate the sideband unbalance of the probe wave, according to Eq. (8.2.23). This optimal pump power P_{pump} can be determined by a feedback shooting method when the unbalance is eliminated within the error tolerance of 0.01% at the maximum loss. The RF frequency and power applied to the DPMZM are set to 6 GHz and 15 dBm, respectively. the length of the SMF is 20 km. We first neglect the dispersion effect. The RF signal and sidebands (power) unbalance, which indicates the Brillouin loss profile, can be calculated according to Eq. (8.2.22). As shown in Fig. 8.3.1(a), the RF spectrum (3 dB) bandwidth is measured to be 19.4 MHz, narrower than the FWHM of the Brillouin loss 37.1 MHz. Besides, due to the out-of-phase

Dieses Werk ist copyrightgeschützt und darf in keiner Form vervielfältigt werden noch an Dritte weitergegeben werden.
Es gilt nur für den persönlichen Gebrauch.

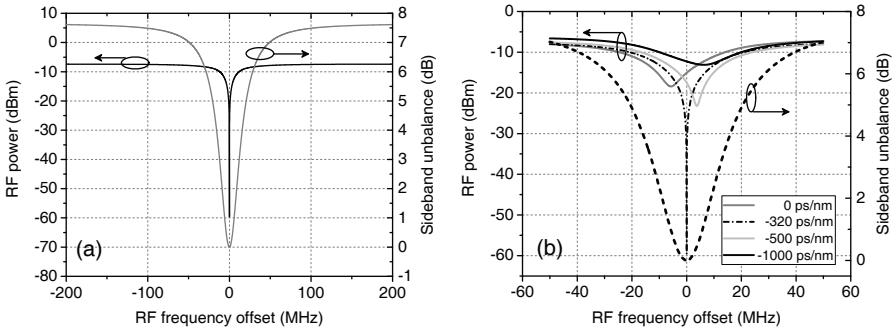

Figure 8.3.1.: (a) The simulated sideband unbalance with SBS loss (optical power, gray) and the RF power at ω_{RF} (black) as a function of RF frequency offset without dispersion taken into consideration. (b) The RF signal under different dispersion compensation values in comparison to the SBS loss (black dashed) [162].

cancellation, the notch depth (52.3 dB) is much deeper than the maximum Brillouin loss of 7.7 dB. These results are in good consistence with the previous reports [150, 158].

8.3.2. Dispersion Effect and Compensation

In order to investigate the dispersion effect, the dispersion items in Eq. (8.2.31) are taken into account. The RF signals are calculated with Eq. (8.2.26). As depicted in Fig. 8.3.1(b), the dispersion influences the performance of the MPNF in two ways, namely:

- notch frequency shift in respect to the Brillouin loss center
- drastic reduction of notch rejection

In Fig. 8.3.2(a), the black curve illustrates how the compensating dispersion (CD) D_c influences the RF notch power. As the CD is approaching the SMF dispersion, the notch power decreases significantly, indicating a more and more efficient out-of-phase cancellation on the RF power at the notch. Considering the simulated SMF length is 20 km, the deepest RF notch is predicted to appear at a compensating dispersion value of -320 ps/nm. Please note that, in the vicinity of -320 ps/nm, the notch power shows strong oscillation. As shown in Fig. 8.3.2(b), the RF notch power oscillates with a period of 3.3 ps/nm, indicating an extreme sensitive dependence of the optical phase on the dispersion value. It is clearly indicated that, only when the dispersion is precisely aligned for the compensation value, the RF notch will be deepened to the most.

Dieses Werk ist copyrightgeschützt und darf in keiner Form vervielfältigt werden noch an Dritte weitergegeben werden.
Es gilt nur für den persönlichen Gebrauch.

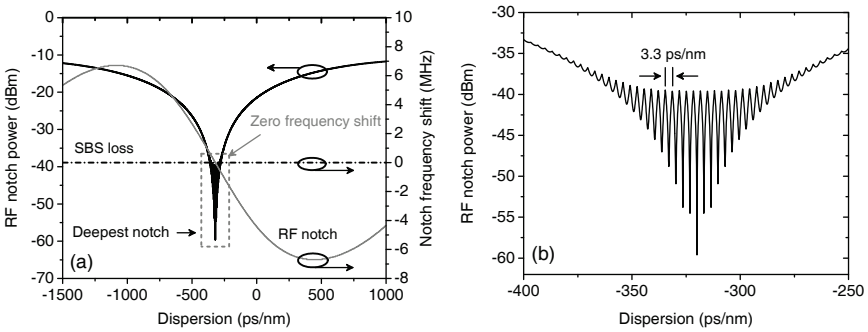

Figure 8.3.2.: (a) The simulated RF notch power (black) and notch frequency shift (gray) for different dispersion compensation values in comparison with the SBS loss (dash dotted). (b) The oscillation of the RF notch power in the vicinity of the proper dispersion compensation value (dashed rectangular in (a)) [162].

The gray curve in Fig. 8.3.2(a) demonstrates the frequency shift of the notch frequency in respect to the Brillouin loss center. This notch frequency offset exists no matter it is over- or less-compensated. This means, unless the system is properly dispersion compensated, the elimination of the sideband unbalance due to the SBS loss will neither lead to the deepest RF notch, nor an overlap of the maximum loss and RF notch.

8.4. Experimental Setup

In order to experimentally validate the theoretical predictions, the setup illustrated in Fig. 8.4.1 is utilized. The LD output is split into two branches. The upper probe branch is modulated by an RF signal from RFG 1 via a DPMZM (Fujitsu, FTM7962EP). The bias voltages are set according to Eqs. (8.2.17) and (8.2.19). The RF frequency and power of RFG 1 are 6 GHz

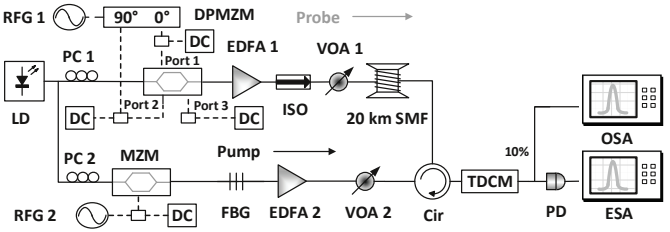

Figure 8.4.1.: Experimental setup. TDCM: tunable dispersion compensation module.

Dieses Werk ist copyrightgeschützt und darf in keiner Form vervielfältigt werden noch an Dritte weitergegeben werden.
Es gilt nur für den persönlichen Gebrauch.

and 15 dBm, respectively, the same as in the simulation. The phases of the RF signals applied on port 1 and 2, *i.e.*, the two parallel child MZMs, are in quadrature shifted through a 90 degrees 3 dB hybrid coupler. The probe wave spectrum with unbalanced amplitude and π phase shifted sidebands is then generated, as illustrated in Fig. 8.2.1. An ISO protects the EDFA 1 from the residual pump wave. EDFA 1 and VOA 1 are used to control the probe power at 5 dBm, closely below the SBS threshold of the 20 km SMF.

In the lower pump branch, the optical wave is modulated by a normal MZM with the RF signal from RFG 2 in carrier suppression mode. The following FBG selects the LSB of this modulation as the pump wave, as illustrated with the gray solid line in Fig. 8.2.1. As indicated by the gray dashed curve in Fig. 8.2.1, the SBS loss generated by the pump wave has an interaction with the LSB of the probe wave. Considering the BFS of the 20 km SMF in the setup is 10.852 GHz at room temperature and the RF frequency upon the probe wave (from RFG 1) is f_{RF}=6 GHz, the RF frequency from RFG 2 should be in the vicinity of 16.852 GHz. The pump power is well controlled by EDFA 2 and VOA 2 before launching into the SMF.

The probe wave after the interaction propagates through a tunable dispersion compensation module (TDCM, TeraXion, TDCMX-C050+0700-0700-D02A). Depending on the dispersion value provided by the TDCM, the SMF dispersion can be partly, fully or over-compensated. 10% of the output power from the TDCM is fed to an OSA, where the (power) sideband unbalance of the probe wave is measured with the peak detection function. The other 90% of the output power are detected by a PD and the RF power at ω_{RF} is measured by an ESA also with the peak detection function. The pump frequency f_p is tuned by RFG 2 in the range of 16.852 GHz $\pm$ 125 MHz with a step size of 0.5 MHz. The pump power is strictly controlled by VOA 2 so that the sidebands balance is achieved at the maximum SBS loss with an error less than 0.2 dB. Due to the wide dispersion tuning range of the TDCM from -740 ps/nm to 740 ps/nm and step size of 20 ps/nm, the complete SBS loss and RF signal under different CD can be simultaneously achieved and recorded by the OSA and ESA, respectively.

8.5. Experimental Validation

8.5.1. Bias Voltages Configuration

The first step of the experimental validation is to characterize the transfer function of the DPMZM. This can be simply implemented by connecting the output from the DPMZM to the 90:10 coupler that links to the OSA, PD and ESA in Fig. 8.4.1. The transfer function is measured without any RF signals. The programmable power supply can arbitrarily control the DC input voltages in all three ports with an accuracy of 0.1 V. By tuning one of the DC port and fixing the other two (at 0 V) and measuring the only peak power (carrier) with the

Dieses Werk ist copyrightgeschützt und darf in keiner Form vervielfältigt werden noch an Dritte weitergegeben werden.
Es gilt nur für den persönlichen Gebrauch.

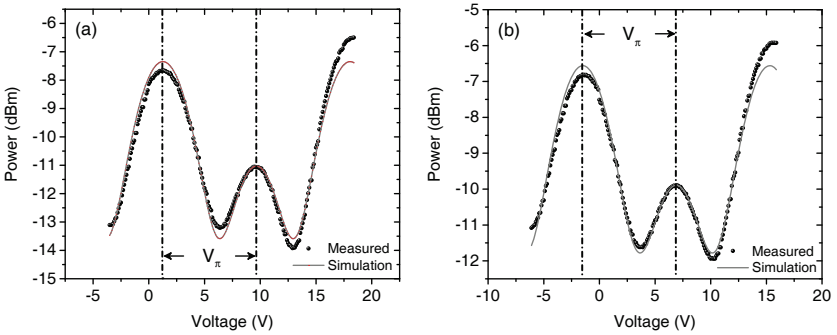

Figure 8.5.1.: Transfer function of MZM (a) child 1 and (b) child 2

OSA, the transfer functions of the DC ports are measured and plotted in Figs. 8.5.1 and 8.5.2. The deviation of the child MZM transfer function from a standard sinusoidal form indicates the existence of the drifting voltages. For a fitting analysis, the square (power) of Eq. (8.2.5) is utilized and the drifting voltages of each port are determined. Considering the structure symmetry, the transfer function of MZM child 1 and child 2 are similar and the measured data (scattered dots) are showing good agreement in a wide range with the simulation results (gray solid line). Please note that, since the MZM parent is not working in push-pull mode, the period of its transfer function is $2V_\pi$ instead of V_π.

The characterization shows that V_{b3} and V_{b1} have positive drifts with $V_{b3,drift} = 4.3$ V and $V_{b1,drift} = 1.2$ V, while V_{b2} has a negative drift with $V_{b2,drift} = -1.5$ V. It is also confirmed by the experiment that the switching voltages of each port are almost the same with $V_\pi = 8.4$ V.

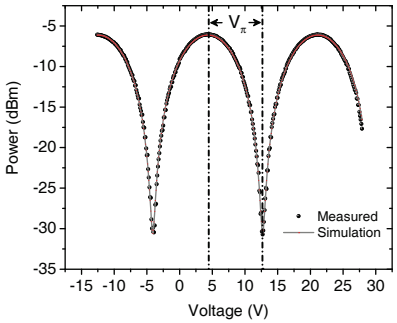

Figure 8.5.2.: Transfer function of MZM parent

Dieses Werk ist copyrightgeschützt und darf in keiner Form vervielfältigt werden noch an Dritte weitergegeben werden.
Es gilt nur für den persönlichen Gebrauch.

With these measured data, the bias voltages configuration for the probe wave can be set according to Eqs. (8.2.17) and (8.2.19).

8.5.2. Dispersion Compensation

In Fig. 8.5.3, typical RF signals under different CDs are illustrated. Please note that, only the fiber dispersion was taken into account for the simulation. However, the measured dispersion is the fiber dispersion plus the dispersion of all other components in the probe branch, which include the EDFA, VOA and so on. From the measurement we have found an additional dispersion of −240 ps/nm. Thus, with the 320 ps/nm from the fiber dispersion, the correct dispersion compensation value would be at −80 ps/nm. As can be seen, the RF notch frequency shifts with the CD. For extreme values such as −580 ps/nm and 640 ps/nm, the RF power at even the notch could also be relatively high, indicating an inefficient RF-cancellation with a dispersion mismatch. The dispersion compensation has almost no influence outside the demonstrated frequency range.

The measured RF signals and optical SBS loss data are further analyzed by applying Lorentzian fittings for minimum value and the corresponding frequency determination. As illustrated in Fig. 8.5.4(a), the center frequency of the SBS loss is dispersion insensitive, while the notch frequency of the RF signal is shifting with a maximum offset of 8.3 MHz in respect to the maximum loss under different compensating dispersion values. The same situation happens also in the analysis of the dispersion induced notch power change. As depicted in Fig. 8.5.4(b), the maximum Brillouin loss remains the same under different dispersion values, while the notch rejection, represented by the notch depth, rises from almost the same magnitude of SBS loss (≈10.7 dB) when the system is less-compensated until the peak of ≈ 33 dB is reached

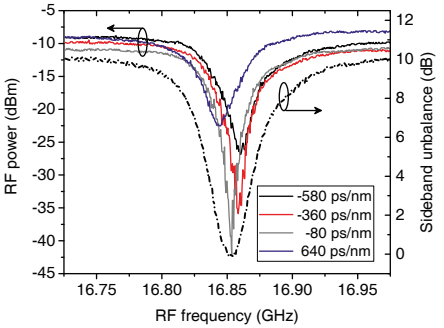

Figure 8.5.3.: The experimental RF signals for different dispersion compensation value in comparison to the dispersion insensitive SBS loss (black dash dotted).

Dieses Werk ist copyrightgeschützt und darf in keiner Form vervielfältigt werden noch an Dritte weitergegeben werden.
Es gilt nur für den persönlichen Gebrauch.

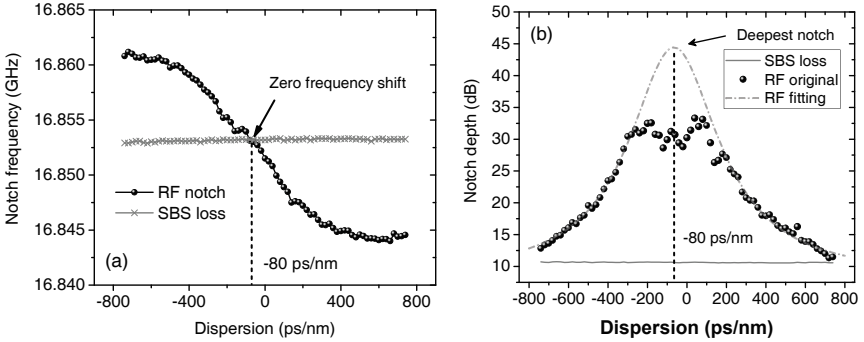

Figure 8.5.4.: The experimental notch (a) frequency and (b) depth of SBS loss and RF signal for different dispersion compensation values. The gray dash dotted curve in (b) is the Lorentzian fitting of the notch depth for the RF signal.

and decreases again in an over-compensated configuration.

A saturation-like behavior in the curve prevents the RF notch depth from further increasing. This can be attributed to the sensitive dependence of the notch depth to the CD in the vicinity of the proper compensation value. For just the fiber in Fig. 8.3.2(b), this proper compensation value is −320 ps/nm, while for the whole setup, this value is −80 ps/nm, as depicted in Fig. 8.5.4(b). Due to the limited tuning resolution of the TDCM, the oscillation structure in the vicinity of the deepest notch cannot be characterized and a more precise dispersion cannot be provided to hit the deepest notch experimentally. Therefore, a saturation instead of an oscillation is measured.

Figure 8.5.4(a) proposes the setup of a dispersion measurement. The gray trace with crosses is the frequency shift of the SBS loss, which remains almost constant due to the dispersion insensitivity, and the black curve is the RF notch frequency shift. The crossing of the two curves is at −80 ps/nm, indicating the dispersion of the setup.

8.6. Discussions

Physical Explanation of the Dispersion Effect

The simulation and the experimental results are in good consistence to each other with respect to the dispersion effects on the notch frequency shift and the notch rejection change. Both behaviors can be well explained by the dispersion induced phase from the setup. Thus, the preconditions for an out-of-phase cancellation directly after the DPMZM is no longer maintained

Dieses Werk ist copyrightgeschützt und darf in keiner Form vervielfältigt werden noch an Dritte weitergegeben werden.
Es gilt nur für den persönlichen Gebrauch.

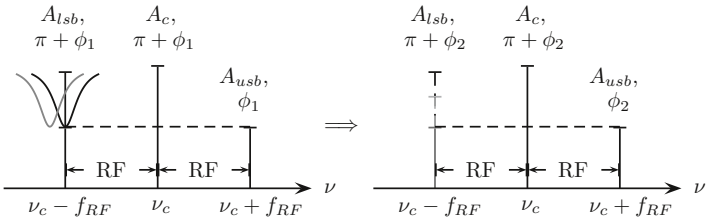

Figure 8.6.1.: The schematic explanation of the dispersion effects. The black curve shows the perfect RF cancellation case, while the gray curve depicts the case of an imperfect RF cancellation.

during the propagation in the setup. Figure 8.6.1 schematically compares two scenarios of the sidebands after the SBS interaction. Originally the sidebands are unbalanced and π shifted in phase, as shown by the black solid line. In both situations the SBS loss eliminates the sidebands unbalance with the maximum loss. However, for the first situation (as indicated by the black dashed curve), the phase of the LSB is well retrieved after the propagation in the SMF with a proper dispersion compensation, so that the phase shift between the LSB and USB is still π at the maximum SBS loss and all the conditions for an out-of-phase cancellation are still satisfied. Considering the SBS interaction does not provide any phase shifts at the gain or loss center, a perfect RF cancellation is formed at the loss center and a deep RF notch can be seen.

In contrast, the other situation is shown with the gray dashed curve. Due to an improper dispersion compensation, the π shift between LSB and USB is retrieved already with a non-zero SBS phase. However, this results in an unbalanced amplitude between the sidebands. Due to the insufficient RF cancellation, only a shallow RF notch signal is generated with a frequency offset to the SBS loss.

For some extreme cases, where the system dispersion is far from the proper dispersion compensation, the retrieving of the π phase shift is no longer possible, even with the help of the SBS phase shift. Under these situations, the RF cancellation will not take place. Due to the linear electro-optic responsivity of the PD, the RF notch in these cases shares the same depth with the optical SBS loss.

Criteria on Pump Power Accuracy

In order to achieve the deepest RF notch of -59.6 dBm according to the simulation in Fig. 8.3.1(a), besides a properly compensated dispersion, the pump power for the Brillouin loss has to be accurately set so that the unbalance between the sidebands would be perfectly

Dieses Werk ist copyrightgeschützt und darf in keiner Form vervielfältigt werden noch an Dritte weitergegeben werden.
Es gilt nur für den persönlichen Gebrauch.

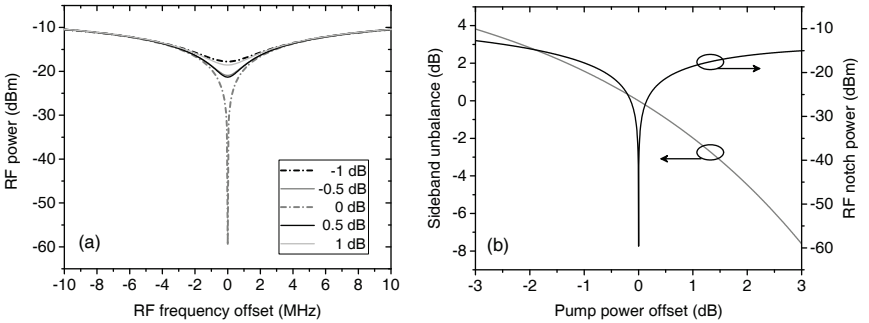

Figure 8.6.2.: (a) The RF signal and (b) RF notch power (black) and probe sidebands unbalance (gray) due to the SBS loss with different power offset to the optimal pump power.

eliminated (with an error tolerance of 0.01%) at the loss center. In this subsection, the sensitivity of the RF notch power will be theoretically investigated under the assumption that the SMF dispersion is always properly compensated but with an offset of the power to the optimal pump power. The RF notch power indicates the rejection ratio of the filter. The only change in the calculation is that, a power offset η from -3 dB to 3 dB is applied on the optimal pump power in calculating the SBS loss with the negative value of Eq. 2.4.1.

Figure 8.6.2(a) demonstrates RF notch spectra with typical pump power offsets. As can be seen, only when the pump power is accurately set (offset to the optimal power less than 0.5 dB), an obvious RF cancellation will take place and the RF notch will be deepened. Furthermore, in comparison with the sensitivity of the SBS loss to the pump power offset, the RF notch power is much more sensitive to the offset, as indicated by Fig. 8.6.2(b). With the same amount of pump power offset (6 dB) the maximum SBS loss has changed by 12 dB and the RF notch rejection has changed by 45 dB. Almost no deep notch will be observed with an offset to the optimal pump power of 3 dB or more. Therefore, in order to get a well performed RF notch filter, the requirement on the accurate setting of the pump power is very high. Therefore, the sidebands unbalance must be equalized at the maximum SBS loss with an error of below 0.2 dB under all dispersion compensation situations in the experiment.

Conclusion

In this chapter, the technical details of the Brillouin based MPNF and the controlling method of the DPMZM were reviewed. The detrimental dispersion effects on the performance of MPNF based on SBS have been investigated. In the experimental demonstration, the fiber dispersion shifts the RF notch frequency by 8.3 MHz in respect to the center of the loss

Dieses Werk ist copyrightgeschützt und darf in keiner Form vervielfältigt werden noch an Dritte weitergegeben werden.
Es gilt nur für den persönlichen Gebrauch.

spectrum. This results in a decrease of the RF notch rejection by up to 21 dB. A physical explanation of this phenomenon by an extra phase shift on the sidebands due to the dispersion of the setup has been proposed. A theoretical model is established upon this explanation. The simulation results show good consistences to the experiment. A solution to this limitation, namely, the dispersion compensation, is also proposed and demonstrated both theoretically and experimentally. Furthermore, the high demand on the pump power setting accuracy in achieving the excellent performance of the SBS based MPNF was discussed.

The presented results would be of great importance for similar microwave photonic applications which rely on the phase difference and phase cancellation of optical waves. Additionally, due to the ultra-sensitive dependence of the RF notch power on the dispersion, these results provide a novel way for dispersion measurement in an optical communication system.

Dieses Werk ist copyrightgeschützt und darf in keiner Form vervielfältigt werden noch an Dritte weitergegeben werden.
Es gilt nur für den persönlichen Gebrauch.

9 Summary and Open Lines

9.1. Summary

In summary, this thesis has introduced the strategies to engineer the conventional Brillouin gain spectrum by involving the Brillouin loss interaction as well as their applications in the filed of distributed Brillouin sensing and optical signal processing. The investigations of this thesis are split into two parts. On the one hand, the motivation of the gain spectrum engineering with the superposition of loss interaction is the ability to further narrow the intrinsic Brillouin gain linewidth. This linewidth narrowing will bring unique benefits to the distributed Brillouin sensing such as SNR enhancement and noise resistance. On the other hand, the Brillouin loss assisted out-of-phase cancellation provides the possibility to enhance the interaction by several magnitudes. This advantage makes the application of the technique extremely attractive in the field of optical and microwave photonic filtering. The four contributed chapters of this thesis have specifically introduced the performance enhancement brought by the gain spectrum engineering.

The first application is focused on the static distributed Brillouin sensing. The benefits from the gain spectrum engineering with the superposition of Brillouin loss spectra include the measurand resolution enhancement and the corresponding sensing range extension. Assisted by the gain spectrum engineering, a solution to the bottleneck problem with the noise dependent measurand resolution is proposed. By the superposition of a gain with two losses, a gain spectrum shape that is sharper and more robust to the inevitable noise is engineered and leads to a less ambiguity in the Brillouin frequency shift estimation. A novel numerical simulation method has been carried out and found the optimized ratios between gain and loss. At the best performance of the proposed sensor, a doubled measurand resolution has been demonstrated in the simulation and an extension of the sensing range up to 60% has been expected. Considering the practical limitations, different experimental implementations and their advantages and

Dieses Werk ist copyrightgeschützt und darf in keiner Form vervielfältigt werden noch an Dritte weitergegeben werden.
Es gilt nur für den persönlichen Gebrauch.

disadvantages have been specifically discussed. The experimental results show good agreement with the simulation results.

The second presented application utilizes the gain spectrum engineering in slope assisted dynamic Brillouin sensing. The investigation proposes a solution to the tradeoff between the two key performances of this technique, namely dynamic range and slope. With the superposition of Brillouin loss spectrum to the conventional gain spectrum, an engineered gain spectrum demonstrates a wider linear range at the edge. Unlike previous works for linear range extension, this technique does not compromise the slope and provides even up to 30% higher slope value. This means that, the proposed sensor could enlarge the maximum measurable strain amplitude without any penalties on the minimum detectable strain signal. A novel quantitative definition of the dynamic range has been proposed with the harmonic distortions of the measured strain signal. Based on this definition, a dynamic range of more than 70% wider than that of a conventional one has been quantified with the proposed method. The simultaneous enhancement of the dynamic range and slope makes the validity of the slope-assisted dynamic Brillouin sensing much more attractive.

Furthermore, the application of an engineered Brillouin spectrum with the loss interaction on optical filtering has been introduced. The motivation of this investigation is to propose a solution to the bottleneck of conventional Brillouin gain based optical filters, namely the amplified spontaneous emission noise introduced by the Brillouin interaction. A novel tunable optical filter based on Brillouin loss interactions with no additional noise has been investigated. With the out-of-band signals being suppressed by two symmetric broadened loss spectra, the pass-bandwidth can be well controlled arbitrarily. An independent tunability of the center frequency and bandwidth ranging from 0.5 GHz to 9.5 GHz is demonstrated. Assisted by the polarization pulling, the maximum selectivity of our proposed filter is enhanced to more than 20 dB. Because the passband is left transparent, the proposed active filter has successfully overcome the noise from the Brillouin interaction as the main disadvantage of well performed Brillouin gain-based filters. Considering the sharp edges, flat-top response, low-noise performance, independent bandwidth, and center frequency tunability, the proposed filter can be used in combination with conventional filters, thus enabling a narrow-bandwidth rectangular filter.

In addition, the microwave photonic notch filter based on Brillouin loss interaction has been investigated. The highlight of this investigation is the precise control of the amplitude and phase of the modulation sidebands with the dual-parallel Mach-Zehnder modulator. Technical details on the manipulation and the characterization of the dual-parallel Mach-Zehnder modulator have been explicitly introduced. Based on the out-of-phase cancellation, a microwave photonic notch filter based on Brillouin interaction is able to provide a notch

Dieses Werk ist copyrightgeschützt und darf in keiner Form vervielfältigt werden noch an Dritte weitergegeben werden.
Es gilt nur für den persönlichen Gebrauch.

rejection much higher than the Brillouin loss itself with narrower linewidth. This investigation aims to solve the detrimental effect from the dispersion on the performance of this Brillouin based microwave photonic notch filter. The investigation shows that the dispersion influences the performance of the notch filter in two ways, namely the notch frequency shift and the notch rejection reduction. Experimentally a notch frequency shift by 8.3 MHz and a notch rejection reduction up to 21 dB have been demonstrated. A theoretical model has been built based on the dispersion induced extra phase shift on the probe waves and the simulation results show good agreement to the experiment. A solution to this impairment, namely the dispersion compensation, is also proposed and demonstrated both theoretically and experimentally. The presented results would be of great importance for other microwave photonic applications that rely on the phase difference of optical waves. Additionally, the investigation results provide also a novel way for dispersion measurement in an optical communication system.

9.2. Open Lines

As analyzed in Sec. 3.2, the performance limit of the BOTDA could be overall attributed to the limited SNR of the sensing system. Currently, the SNR of the (engineered) gain spectrum is highly dependent on the magnitude of the gain (or loss). In this thesis, an ultra high SNR has been demonstrated in the field of microwave photonic filter by exploiting the out-of-phase cancellation, with the SNR much higher than the Brillouin gain (or loss) itself. The following proposal present the open research fields coming from the work performed in this thesis.

Proposal of Out-of-phase Cancellation in BOTDA

As a tentative solution for the restricted SNR in a sensing system, here a simple and feasible SNR enhancement method based on the exploitation of out-of-phase signal cancellation is proposed on SA-BOTDA [119, 121]. Assisted by the destructive interference, a drastically increased sensitivity as well as dynamic range can be expected.

- Principle

The schematic principle of the proposed sensor is depicted in Fig. 9.2.1(a). It is different from the conventional SA-BOTDA in that, the probe wave is phase modulated with a modulation frequency ω_{RF}. Due to destructive interference, no RF frequency component at ω_{RF} will be detected at the PD for a direct detection of the probe wave. However, this scenario will change if a Brillouin interaction is applied on one of the sidebands, for instance, the USB as illustrated in Fig. 9.2.1(a). By scanning the USB through the gain spectrum, it will experience

Dieses Werk ist copyrightgeschützt und darf in keiner Form vervielfältigt werden noch an Dritte weitergegeben werden.
Es gilt nur für den persönlichen Gebrauch.

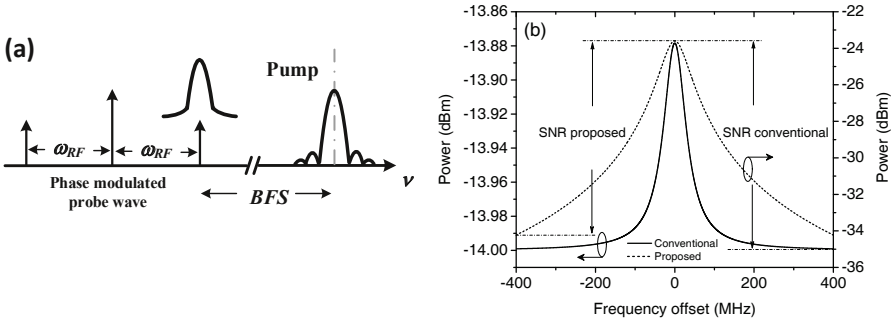

Figure 9.2.1.: a) The schematic principle of the SA-BOTDA based on out-of-phase cancellation, (b) a comparison between the conventional BGS (solid) and RF spectrum from the out-of-phase cancellation (dashed). Please note the different scales of the left and right axes.

both amplitude and phase change. The RF power at ω_{RF} can be expressed as,

$$P_{out}\Big|_{\omega_{RF}} = E_c E_{SB}\sqrt{G_{SBS}^2 + \Phi_{SBS}^2} \tag{9.2.1}$$

where E_c, E_{SB} are the amplitude of the carrier and the sideband, respectively, and governed by the RF power (see Appendix B.1), G_{SBS}, Φ_{SBS} are the SBS amplitude gain and phase response given in Eqs. (2.4.4) and (2.4.5), respectively. Different from the SNR enhancement method mentioned in Chs. 4 and 5, the possible enhancement efficiency by this method is much higher, owing to a much more efficient suppression of the RF power at the modulation frequency from the destructive interference [161, 162].

The expression of Eq. (9.2.1) holds under the small gain approximation, which suits almost all the situations of an SA-BOTDA sensor with short interaction length in dynamic sensing tasks. A comparison of the direct detection of the SBS gain, *i.e.*, conventional BOTDA, and the out-of-phase cancellation is demonstrted with the same pump pulse width of 14 ns, the same pump pulse peak power of 20 dBm and the same probe power of −14 dBm (sideband power for phase modulated probe wave). The RF power and frequency used are 10 dBm and 0.6 GHz, respectively. The spectra of both cases are depicted in Fig.9.2.1(b) with the FWHM of the conventional BGS broadened to 70 MHz. Taking the advantage of the high suppression out of the SBS interaction range and similar to the effect of an SBS based RF notch filter [150, 153], a higher SNR, a sharper spectrum profile and a steeper slope in the linear region of the BGS are achieved.

Dieses Werk ist copyrightgeschützt und darf in keiner Form vervielfältigt werden noch an Dritte weitergegeben werden.
Es gilt nur für den persönlichen Gebrauch.

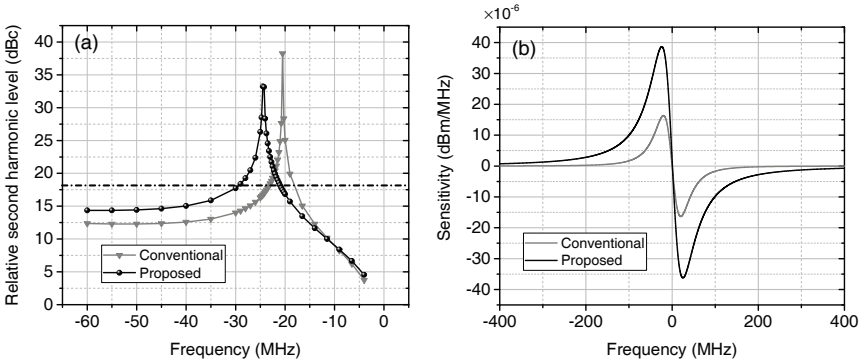

Figure 9.2.2.: The comparison of the (a) dynamic range based on second harmonic level and (b) slope between the out-of-phase cancellation (black) and the conventional BOTDA (gray). The threshold for the dynamic range is set at 18 dB (black dash dotted horizontal line in (a)).

- Advantages on Dynamic BOTDA

The advantage of the proposed out-of-phase cancellation in SA-BOTDA is the simultaneous enhancement of the dynamic range and sensitivity. This advantage is demonstrated with the same numerical method proposed in Ch. 5. The simulated sinusoidal strain signal is 50 Hz in frequency and 280 $\mu\varepsilon$ in peak-to-peak amplitude. The simulated slope assisted strain measurement is carried out in a variety of working points at the spectrum edges.

Similar to the results demonstrated in Sec. 5.5, the relative power of the second harmonic of the Brillouin gain signal is depicted as a function of the working point frequency in Fig. 9.2.2(a). Under the pre-defined threshold of 18 dB, the dynamic range of 8 MHz and 4 MHz are measured for the proposed and conventional sensor, respectively. According to the slope calculation depicted in Fig. 9.2.2(b), more than two times the sensitivity can be achieved by utilizing out-of-phase cancellation. It is clearly indicated that, with the out-of-phase cancellation, both the maximum measurable and minimum detectable strain signal can be enhanced by two times simultaneously.

- Influence of Dispersion

Considering the phase sensitivity in the destructive interference, the influence of the dispersion in this proposed method is investigated. Considering the length of the fiber is only around 100 m in most dynamic sensing tasks, the quantitative characterization of the influence of the dispersion on the out-of-signal cancellation is limited in a small spatial range. Under

Dieses Werk ist copyrightgeschützt und darf in keiner Form vervielfältigt werden noch an Dritte weitergegeben werden.
Es gilt nur für den persönlichen Gebrauch.

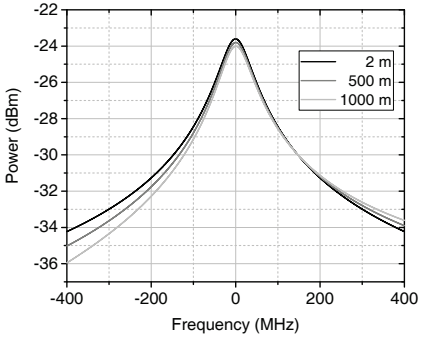

Figure 9.2.3.: RF spectrum of the SBS gain assisted out-of-phase cancellation at 2 m (black), 500 m (dark gray) and 1 km (light gray) with 0.6 GHz modulation frequency.

the consideration of the fiber dispersion, Eq. (9.2.1) can be generalized as,

$$P_{out}\Big|_{\omega_{RF}} = E_c E_{SB}\sqrt{G_{SBS}^2 + 4\sin^2(\frac{1}{2}\beta_2\omega_{RF}^2 z - \frac{1}{2}\Phi_{SBS})\cdot(1+G_{SBS})} \qquad (9.2.2)$$

where β_2 is the 2^{nd} order derivative of the propagation constant at the carrier frequency and symbolizes the chromatic dispersion. The chromatic dispersion in SMF at 1550 nm is $\beta_2 \approx -21.67$ ps^2/km. Please note that, different from Eq. (9.2.1), no small gain approximation is applied in Eq. (9.2.2). It is clearly indicated from Eq. (9.2.2) that, the influence is much more severe for a high modulation frequency. Considering the broadened FWHM of the BGS with short pulse and the possible residual Brillouin interaction on the carrier when ω_{RF} is too low (see Fig. 9.2.1(a)), ω_{RF} is set to be 0.6 GHz in the rest of the simulation for the demontsration of the dispersion effect.

The RF spectra at different fiber sections are illustrated in Fig. 9.2.3. The dispersion influences the gain spectrum mainly by changing the symmetry. Also, as expected that, the dispersion effect is more severe at the far end of the fiber. However, considering the short fiber length and limited asymmetry, it is highly possible to develop a compensation and retrieval algorithm for this effect. Furthermore, the spectrum shape close to the resonance (for instance 3 dB region) is still well maintained, showing an insensitivity to the fiber dispersion. Therefore, a compensation and retrieval algorithm would be only required for the measurements that take place at the working points far from the resonance.

- Possible Experimental Implementation

The possible experimental implementation for the proposed dynamic SA-BOTDA based on

Dieses Werk ist copyrightgeschützt und darf in keiner Form vervielfältigt werden noch an Dritte weitergegeben werden.
Es gilt nur für den persönlichen Gebrauch.

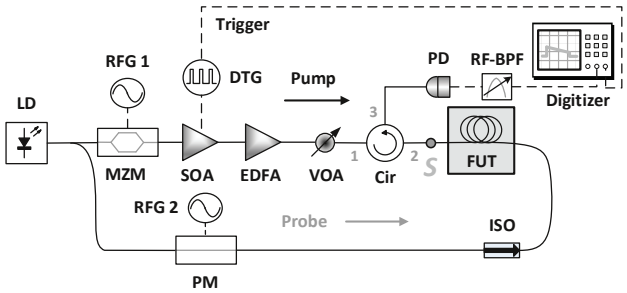

Figure 9.2.4.: Schematic setup of an SA-BOTDA sensor based on out-of-phase cancellation. Schematic spectrum at the spot S is illustrated in Fig. 9.2.1(a)

out-of-phase cancellation is depicted in Fig. 9.2.4. The output from the LD is splitted into two branches via a coupler. In the lower probe branch, the optical wave is modulated by the frequency ω_{RF} from RFG 2 by a PM so that symmetric sidebands with a phase shift of π are generated. In order to build the pump for the probe sideband, the optical wave in the upper pump branch is modulated by the frequency $BFS + \omega_{RF}$ from RFG 1 via a MZM, with the lower frequency sideband and the carrier being blocked by a followed FBG. The DTG pulses the continuous wave into 14 ns via a switching type SOA. After a proper power control via EDFA and VOA, the pump pulse is directed into the FUT for interrogation. A similar structure of FUT in Fig. 5.4.2(b) could be utilized for strain signal implementation.

The RF spectrum is acquired by scanning the RF frequency from the RFG 1 upon the MZM. Considering the response of the PM, the detection module in this scheme must cover the range of ω_{RF} (several 100 MHz). Additionally, the detection module should include an RF-BPF for a better detection of the time evolution of the RF component with only ω_{RF} with a digitizer or oscilloscope.

Dieses Werk ist copyrightgeschützt und darf in keiner Form vervielfältigt werden noch an Dritte weitergegeben werden.
Es gilt nur für den persönlichen Gebrauch.

Dieses Werk ist copyrightgeschützt und darf in keiner Form vervielfältigt werden noch an Dritte weitergegeben werden.
Es gilt nur für den persönlichen Gebrauch.

Appendix

A. Jacobi-Anger Expansion

The Jacobi-Anger expansion is the expression of exponential of trigonometric functions in the basis of their harmonics. It is often used in physics for converting plane waves to cylindrical waves. Its general form is: [164]

$$e^{jzsin\theta} = \sum_{n=-\infty}^{\infty} J_n(z)e^{jn\theta} \tag{A.1}$$

where $J_n(z)$ is the n-th Bessel function of the first kind and j is the imaginary unit with $j^2 = -1$. The substitution of θ with $\frac{\pi}{2} - \theta$ in Eq. (A.1) leads to:

$$e^{jz\cos\theta} = \sum_{n=-\infty}^{\infty} j^n J_n(z)e^{jn\theta} = J_0(z) + 2\sum_{n=1}^{\infty} j^n J_n(z)e^{jn\theta} \tag{A.2}$$

where the later step of Eq. (A.2) has applied the relation:

$$J_{-n}(z) = (-1)^n J_n(z) \tag{A.3}$$

Considering the Euler's formula $e^{j\theta} = \cos\theta + j\sin\theta$, the real-value expression of the expansion can be derived as:

$$\sin(z\sin\theta) = 2\sum_{n=1}^{\infty} J_{2n-1}(z)\sin[(2n-1)\theta] \tag{A.4a}$$

$$\cos(z\sin\theta) = J_0(z) + 2\sum_{n=1}^{\infty}(-1)^n J_{2n}(z)\cos(2n\theta) \tag{A.4b}$$

$$\sin(z\cos\theta) = -2\sum_{n=1}^{\infty}(-1)^n J_{2n-1}(z)\cos[(2n-1)\theta] \tag{A.4c}$$

$$\cos(z\cos\theta) = J_0(z) + 2\sum_{n=1}^{\infty}(-1)^n J_{2n}(z)\cos(2n\theta) \tag{A.4d}$$

Dieses Werk ist copyrightgeschützt und darf in keiner Form vervielfältigt werden noch an Dritte weitergegeben werden.
Es gilt nur für den persönlichen Gebrauch.

B. Transfer Function of the DPMZM

The transfer functions of PM and MZM are the foundations to clarify the transfer function of DPMZM. In this section, the structure of all three modulators and their characteristics will be introduced and derived step by step.

B.1. Phase Modulator

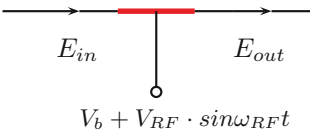

Figure B.1.: Typical structure of a PM with an applied external RF signal and DC bias voltage

The structure of a PM is illustrated in Fig. B.1. In the presence of an external electric field, the electrode made of $LiNbO_3$ (in red in Fig. B.1) changes its refractive index and shifts the phase of the transmitted optical wave in the waveguide according to the Pockels effect, as described in Sec. 1.2. Assume that the length of the waveguide is L, the effective refractive index without external voltage and its change due to the applied voltage are n_{eff} and Δn_{eff}, respectively, the phase shift can be expressed as: [4]

$$\Delta\Phi = \frac{2\pi\Delta n_{eff}L}{\lambda} = \pi\frac{n_{eff}^3\gamma_{33}L}{\lambda}v(t) = \pi\frac{v(t)}{V_\pi} = \pi\frac{V_b + V_{RF}\cdot\sin\omega_{RF}t}{V_\pi} \tag{B.1.1}$$

where $V_\pi = \frac{\lambda}{n_{eff}^3\gamma_{33}L}$ is the switching voltage of the modulator. It symbolizes a π phase shift of the optical wave in the waveguide under this voltage. γ_{33} is the highest electro-optic coefficient of the electro-optic tensor for $LiNbO_3$ crystal substrates, V_b is the DC part of the applied voltage, V_{RF} and ω_{RF} are the amplitude and angular frequency of the applied RF signal.

Let us suppose that the input electric field as:

$$E_{in} = E_0 \cdot \exp(j\omega_0 t) \tag{B.1.2}$$

With E_0 as the field amplitude and ω_0 as the angular frequency of the optical wave, and define:

$$\begin{aligned} \beta_b &\equiv \pi V_b/V_\pi \\ \beta_{RF} &\equiv \pi V_{RF}/V_\pi \end{aligned} \tag{B.1.3}$$

Dieses Werk ist copyrightgeschützt und darf in keiner Form vervielfältigt werden noch an Dritte weitergegeben werden.
Es gilt nur für den persönlichen Gebrauch.

the output electric field can be expressed as:

$$\begin{aligned} E_{out} &= E_{in} \cdot \exp(-j\frac{\omega_0 L n_{eff}}{c}) \cdot \exp(j\Delta\Phi) \\ &= E_0 \cdot \exp(j\omega_0 t) \cdot \exp(j\phi\frac{\omega_0 L n_{eff}}{c}) \cdot \exp(j\pi\frac{V_b}{V_\pi}) \cdot \exp(j\pi\frac{V_{RF}}{V_\pi} \cdot \sin\omega_{RF}t) \\ &= E_0 \cdot \exp(-j\frac{\omega_0 L n_{eff}}{c}) \cdot \exp(j\beta_b) \cdot \exp[j \cdot (\omega_0 t + \beta_{RF} \cdot \sin\omega_{RF}t)] \end{aligned} \tag{B.1.4}$$

For simplifications, the insertion loss of the modulator is neglected here. Due to the only phase change, the averaging output optical power $P_{out} = |E_{out}|^2$ equals to the input optical power $P_{in} = |E_{in}|^2$. Considering the Jacobi-Anger expansion Eq. (A.1) and note that $\phi = -\frac{\omega_0 L n_{eff}}{c}$, Eq. (B.1.4) yields:

$$\begin{aligned} E_{out} &= E_0 \cdot \exp(j\phi) \cdot \exp(j\beta_b) \cdot \Big\{ \sum_{n=-\infty}^{\infty} J_n(\beta_{RF}) \cdot \exp[j(\omega_0 + n\omega_{RF})t] \Big\} \\ &= E_0 \cdot \exp(j\phi) \cdot \exp(j\beta_b) \cdot \Big\{ J_0(\beta_{RF}) \cdot \exp(j\omega_0 t) \\ &+ \sum_{k=1}^{\infty} J_{2k-1}(\beta_{RF}) \cdot \exp\{j[\omega_0 + (2k-1) \cdot \omega_{RF}]t\} + \sum_{k=1}^{\infty} J_{2k}(\beta_{RF}) \cdot \exp\{j(\omega_0 + 2k \cdot \omega_{RF})t\} \\ &- \sum_{k=1}^{\infty} J_{2k-1}(\beta_{RF}) \cdot \exp\Big\{j[\omega_0 - (2k-1) \cdot \omega_{RF}]t\Big\} + \sum_{k=1}^{\infty} J_{2k}(\beta_{RF}) \cdot \exp[j(\omega_0 - 2k \cdot \omega_{RF})t] \Big\} \end{aligned} \tag{B.1.5}$$

As indicated, the output phase shift is composed of several parts. The item $\exp(j\phi)$ represents the intrinsic phase change due to the propagation in the waveguide. The item $\exp(j\beta_b)$ refers to the phase shift due to the DC bias voltage. The output spectrum has symmetric sideband amplitude. The odd-order LSB are π phase shifted to the corresponding USB while the even-order shares the same phase. Due to this characteristic, the RF power calculated by $P_{out} = |E_{out}|^2$ has a missing term at ω_{RF}, leading to a variety of applications in microwave photonics.

B.2. Mach-Zehnder Modulator

The structure of a MZM is depicted in Fig. B.2. It is composed of two parallel PM sandwiched by two Y-shaped branches. Provided that the distance of the waveguide and switching voltage of the two PMs is the same, and the two Y-shaped branches attenuate the input power by ideally 3 dB, then the output electric field can be expressed as the summation of the power at

Dieses Werk ist copyrightgeschützt und darf in keiner Form vervielfältigt werden noch an Dritte weitergegeben werden.
Es gilt nur für den persönlichen Gebrauch.

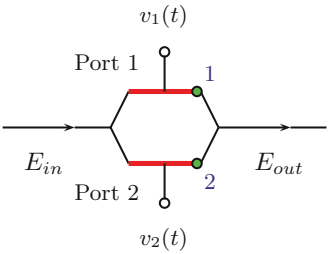

Figure B.2.: Typical structure of a MZM. In general situations, the applied external RF signals on two arms are different.

break point 1 and 2 with the assistance of Eq. (B.1.4):

$$\begin{aligned} E_{out} &= \left[\frac{\sqrt{2}}{2}\cdot E_{in}\cdot\exp(j\Phi_1)+\frac{\sqrt{2}}{2}\cdot E_{in}\cdot\exp(j\Phi_2)\right]\cdot\frac{\sqrt{2}}{2} \\ &= E_{in}\cdot\cos\left(\frac{\Phi_1-\Phi_2}{2}\right)\cdot\exp\left(j\cdot\frac{\Phi_1+\Phi_2}{2}\right) \end{aligned} \tag{B.2.6}$$

where

$$\Phi_n = \phi + \pi\frac{v_n(t)}{V_\pi} \tag{B.2.7}$$

is the phase shift of each branch according to Eq. (B.1.4). Considering $v_n(t)$ contains both the AC and DC part, the output electric field can be further written as:

$$E_{out} = E_{in}\cdot\exp(j\phi)\cdot\cos\left[\pi\frac{v_1(t)-v_2(t)}{2V_\pi}\right]\cdot\exp\left[j\pi\frac{v_1(t)+v_2(t)}{2V_\pi}\right] \tag{B.2.8}$$

Obviously, it is a mix of intensity and phase modulation. Different from the conclusion of PM, the intensity modulation item in Eq. (B.2.8) yields an averaging power loss, leading to a 3 dB power difference between the output and input of an MZM. We may re-write this expression as:

$$E_{out} = \frac{1}{2}E_{in}\cdot\exp(j\phi)\left\{\exp\left[j\pi\frac{v_1(t)}{V_\pi}\right]+\exp\left[j\pi\frac{v_2(t)}{V_\pi}\right]\right\} \tag{B.2.9}$$

If RF signals with the same amplitude but different phase shift are applied on the MZM, *i.e.*:

$$v_1(t) = V_{b1} + V_{RF}\cdot cos\omega_{RF}t \tag{B.2.10a}$$

$$v_2(t) = V_{b2} + V_{RF}\cdot cos(\omega_{RF}t+\theta) \tag{B.2.10b}$$

Dieses Werk ist copyrightgeschützt und darf in keiner Form vervielfältigt werden noch an Dritte weitergegeben werden.
Es gilt nur für den persönlichen Gebrauch.

and take the definition from Eq. (B.1.3), the output electric field can be derived as:

$$E_{out} = \frac{1}{2}E_{in} \cdot \exp(j\phi) \cdot \exp(j\beta_{b2}) \cdot \Big\{ \exp\Big[j\Delta\phi + j\beta_{RF} \cdot \cos\omega_{RF}t\Big] + \exp[j\beta_{RF} \cdot \cos(\omega_{RF}t + \theta)]\Big\} \tag{B.2.11}$$

in which $\Delta\phi = \beta_{b1} - \beta_{b2}$ represents the phase difference of the two branches due to the DC bias voltages. Consider the expansion of Eq. (A.2), the output electric field can be derived as:

$$\begin{aligned} E_{out} &= \frac{1}{2}E_{in} \cdot \exp[j(\phi + \beta_{b2})] \\ &\quad \cdot \Big\{ \exp(j\Delta\phi) \cdot \sum_{n=-\infty}^{\infty} j^n J_n(\beta_{RF}) \exp(jn\omega_{RF}t) + \sum_{n=-\infty}^{\infty} j^n J_n(\beta_{RF}) \exp[jn(\omega_{RF}t + \theta)]\Big\} \\ &= \frac{1}{2}E_{in} \cdot \exp[j(\phi + \beta_{b2})] \cdot \sum_{n=-\infty}^{\infty} j^n J_n(\beta_{RF}) \exp(jn\omega_{RF}t) \cdot \Big\{ \exp(j\Delta\phi) + [\exp(j\theta)]^n\Big\} \end{aligned} \tag{B.2.12}$$

Intensity Modulation

In order to avoid the chirp, an internal circuit is applied to ensure $v_1(t) = -v_2(t)$. Therefore, the MZM is always working in the *push-pull mode* as an intensity modulator. This configuration is valid for most of the commercialized MZM with a chirp-free and amplitude modulated output electric field as:

$$E_{out} = E_{in} \cdot \exp(j\phi) \cos\Big[\pi \frac{v_1(t)}{V_\pi}\Big]. \tag{B.2.13}$$

Now consider a cosinoidal RF signal $v_1(t) = V_b + V_{RF} \cdot \cos\omega_{RF}t$ with the real-value expression of Jacobi-Anger expansion Eqs.(A.4c) and (A.4d), and the definitions in Eq. (B.1.3), the output electric field can be written as:

$$\begin{aligned} &E_{out} = E_{in} \cdot \exp(j\phi) \cdot \cos(\beta_b + \beta_{RF} \cdot \cos\omega_{RF}t) \\ &= E_{in} \cdot \exp(j\phi) \cdot \Big\{ \cos\beta_b \cdot \Big[J_0(\beta_{RF}) + 2\sum_{n=1}^{\infty}(-1)^n J_{2n}(\beta_{RF}) \cos(2n\omega_{RF}t)\Big] \\ &+ 2\sin\beta_b \cdot \sum_{n=1}^{\infty}(-1)^n J_{2n-1}(\beta_{RF}) \cos[(2n-1)\omega_{RF}t]\Big\} \\ &= E_{in} \cdot \exp(j\phi) \cdot \Bigg\{ \Big\{ \cos\beta_b \cdot \Big\{ J_0(\beta_{RF}) + \sum_{n=1}^{\infty}(-1)^n J_{2n}(\beta_{RF}) \Big[\cos(2n\omega_{RF}t) + \cos(-2n\omega_{RF}t)\Big]\Big\}\Big\} \\ &+ \sin\beta_b \cdot \sum_{n=1}^{\infty}(-1)^n J_{2n-1}(\beta_{RF}) \Big\{ \cos[(2n-1)\omega_{RF}t] + \cos[-(2n-1)\omega_{RF}t]\Big\}\Bigg\} \end{aligned} \tag{B.2.14}$$

Dieses Werk ist copyrightgeschützt und darf in keiner Form vervielfältigt werden noch an Dritte weitergegeben werden.
Es gilt nur für den persönlichen Gebrauch.

Therefore, under the condition of small signal modulation, *i.e.*, $\beta_{RF} \ll 1$, there are only first-order sidebands and all the sidebands in the intensity modulation share the same phase with the carrier. The derivation of Eq. (B.2.12) by letting $\theta = \pi$ and $V_b = V_{b1} = -V_{b2}$ will lead to the same conclusion.

Carrier Suppression

Considering the case when

$$\Delta\phi = \pi \quad \text{and} \quad \theta = \pi \tag{B.2.15}$$

every other cases are then periodically the same. Under the push-pull mode, $\theta = \pi$ is automatically achieved. $\Delta\phi = \pi$ can be achieved by setting the bias voltage of $\beta_{b1} = -\beta_{b2} = \pi/2$. In this situation, $\exp(j\Delta\phi) = -1$, $\exp(j\theta) = -1$. Therefore, Eq (B.2.12) can be further simplified as:

$$E_{out} = \frac{1}{2}E_{in} \cdot \exp[j(\phi + \beta_{b2})] \cdot \sum_{n=-\infty}^{\infty} j^n J_n(\beta_{RF}) \exp(jn\omega_{RF}t) \cdot \left[(-1) + (-1)^n\right] \tag{B.2.16}$$

expanding the last item to the first order, we have

$$\begin{aligned} E_{out} &\approx \frac{1}{2}E_{in} \cdot \exp[j(\phi + \beta_{b2})] \cdot [-2j \cdot J_1(\beta_{RF}) \exp(j\omega_{RF}t) + 2j \cdot J_{-1}(\beta_{RF}) \exp(-j\omega_{RF}t)] \\ &= E_{in} \cdot \exp[j(\phi + \beta_{b2})] \cdot [J_1(\beta_{RF}) \exp(\omega_{RF}t - j\frac{\pi}{4}) + J_1(\beta_{RF}) \exp(-j\omega_{RF}t - j\frac{\pi}{4})] \end{aligned} \tag{B.2.17}$$

the item $J_0(\beta_{RF})$ is missing, indicating the carrier with frequency ω_c is suppressed.

Single Sideband Modulation

Considering the case when

$$\Delta\phi = \pm\frac{\pi}{2} \quad \textit{and} \quad \theta = \pm\frac{\pi}{2} \tag{B.2.18}$$

every other cases are then periodically the same. Please note that, the push-pull mode could only provide $\theta = \pi$. This means, single sideband modulation cannot be achieved directly from a push-pull mode MZM. An extra phase shifter on one of the arm is required. The four different scenarios will be discussed as follows:

- $\Delta\phi = \pi/2$, $\theta = \pi/2$

In this situation, $\exp(j\Delta\phi) = j$, $\exp(j\theta) = j$. Therefore, Eq. (B.2.12) can be further

Dieses Werk ist copyrightgeschützt und darf in keiner Form vervielfältigt werden noch an Dritte weitergegeben werden.
Es gilt nur für den persönlichen Gebrauch.

simplified as:

$$E_{out} = \frac{1}{2}E_{in} \cdot \exp[j(\phi + \beta_{b2})] \cdot \sum_{n=-\infty}^{\infty} j^n J_n(\beta_{RF}) \exp(jn\omega_{RF}t) \cdot \left[j + j^n\right] \tag{B.2.19}$$

expand the last item to the first order, we have:

$$\begin{aligned} E_{out} &\approx \frac{1}{2}E_{in} \cdot \exp[j(\phi + \beta_{b2})] \cdot [(1+j)J_0(\beta_{RF}) - 2J_1(\beta_{RF}) \exp(j\omega_{RF}t)] \\ &= E_{in} \cdot \exp[j(\phi + \beta_{b2})] \cdot [J_0(\beta_{RF}) \exp(j\frac{\pi}{4}) - J_1(\beta_{RF}) \exp(j\omega_{RF}t)] \end{aligned} \tag{B.2.20}$$

the item $J_{-1}(\beta_{RF}) \exp(-j\omega_{RF}t)$ is missing, indicating the suppression of LSB with frequency $\omega_c - \omega_{RF}$.

- $\Delta\phi = \pi/2$, $\theta = -\pi/2$

In this situation, $\exp(j\Delta\phi) = j$, $\exp(j\theta) = -j$. Therefore, Eq. (B.2.12) yields:

$$E_{out} = \frac{1}{2}E_{in} \cdot \exp[j(\phi + \beta_{b2})] \cdot \sum_{n=-\infty}^{\infty} j^n J_n(\beta_{RF}) \exp(jn\omega_{RF}t) \cdot \left[j + (-j)^n\right] \tag{B.2.21}$$

expand the last item to the first order, we have

$$\begin{aligned} E_{out} &\approx \frac{1}{2}E_{in} \cdot \exp[j(\phi + \beta_{b2})] \cdot [(1+j)J_0(\beta_{RF}) + 2j \cdot J_{-1}(\beta_{RF}) \exp(-j\omega_{RF}t)] \\ &= E_{in} \cdot \exp[j(\phi + \beta_{b2})] \cdot [J_0(\beta_{RF})exp(j\frac{\pi}{4}) - J_1(\beta_{RF})exp(-j\omega_{RF}t - j\frac{\pi}{2})] \end{aligned} \tag{B.2.22}$$

the item $J_1(\beta_{RF}) \exp(j\omega_{RF}t)$ is missing, indicating the suppression of USB with frequency $\omega_c + \omega_{RF}$.

- $\Delta\phi = -\pi/2$, $\theta = \pi/2$

In this situation, $\exp(j\Delta\phi) = -j$, $\exp(j\theta) = j$. Therefore, Eq. (B.2.12) yields:

$$E_{out} = \frac{1}{2}E_{in} \cdot \exp[j(\phi + \beta_{b2})] \cdot \sum_{n=-\infty}^{\infty} j^n J_n(\beta_{RF}) \exp(jn\omega_{RF}t) \cdot \left[-j + j^n\right] \tag{B.2.23}$$

Dieses Werk ist copyrightgeschützt und darf in keiner Form vervielfältigt werden noch an Dritte weitergegeben werden.
Es gilt nur für den persönlichen Gebrauch.

expand the last item to the first order, we have

$$\begin{aligned} E_{out} &\approx \frac{1}{2}E_{in}\cdot\exp[j(\phi+\beta_{b2})]\cdot[(1-j)J_0(\beta_{RF})+2j\cdot J_{-1}(\beta_{RF})\exp(-j\omega_{RF}t)] \\ &= E_{in}\cdot\exp[j(\phi+\beta_{b2})]\cdot[J_0(\beta_{RF})\exp(-j\frac{\pi}{4})-J_1(\beta_{RF})\exp(-j\omega_{RF}t-j\frac{\pi}{2})] \end{aligned} \tag{B.2.24}$$

the item $J_1(\beta_{RF})\exp(j\omega_{RF}t)$ is missing, indicating the suppression of USB with frequency $\omega_c+\omega_{RF}$.

- $\Delta\phi=-\pi/2$, $\theta=-\pi/2$

In this situation, $\exp(j\Delta\phi)=-j$, $\exp(j\theta)=-j$. Therefore, Eq. (B.2.12) yields:

$$E_{out}=\frac{1}{2}E_{in}\cdot\exp[j(\phi+\beta_{b2})]\cdot\sum_{n=-\infty}^{\infty}j^nJ_n(\beta_{RF})exp(jn\omega_{RF}t)\cdot\left[(-j)+(-j)^n\right] \tag{B.2.25}$$

expand the last item to the first order, we have

$$\begin{aligned} E_{out} &\approx \frac{1}{2}E_{in}\cdot\exp[j(\phi+\beta_{b2})]\cdot[(1-j)J_0(\beta_{RF})+2j\cdot J_1(\beta_{RF})\exp(j\omega_{RF}t)] \\ &= E_{in}\cdot\exp[j(\phi+\beta_{b2})]\cdot[J_0(\beta_{RF})\exp(-j\frac{\pi}{4})+J_1(\beta_{RF})\exp(j\omega_{RF}t+j\frac{\pi}{2})] \end{aligned} \tag{B.2.26}$$

the item $J_{-1}(\beta_{RF})\exp(-j\omega_{RF}t)$ is missing, indicating the suppression of LSB with frequency $\omega_c-\omega_{RF}$.

B.3. Dual-parallel Mach-Zehnder Modulator

The structure of a DPMZM is shown in Fig. B.3. It has a structure of two parallel MZM and one of them is followed with an extra PM. Provided that every MZM in this structure is working in push-pull mode and provide pure intensity modulation, and the RF signals applied into Ports 1 and 2 are in quadrature phase by using a hybrid 3 dB coupler, according to Eqs. (B.2.6) and (B.2.7) and the definitions in Eq. (B.1.3), the output electric field at break point 3 can be expressed as:

$$\begin{aligned} E_3 &= E_{in}\cdot\cos\left\{\frac{1}{2}\Big[(\phi+\beta_{b1}+\beta_{RF}\sin\omega_{RF}t)-(\phi-\beta_{b1}-\beta_{RF}\sin\omega_{RF}t)\Big\}\right. \\ &\quad\cdot\exp\left\{j\cdot\frac{1}{2}\Big[(\phi+\beta_{b1}+\beta_{RF}\sin\omega_{RF}t)+(\phi-\beta_{b1}-\beta_{RF}\sin\omega_{RF}t)\Big\}\right. \\ &= E_{in}\cdot\exp(j\phi)\cdot\cos(\beta_{b1}+\beta_{RF}\sin\omega_{RF}t) \end{aligned} \tag{B.3.27}$$

Dieses Werk ist copyrightgeschützt und darf in keiner Form vervielfältigt werden noch an Dritte weitergegeben werden.
Es gilt nur für den persönlichen Gebrauch.

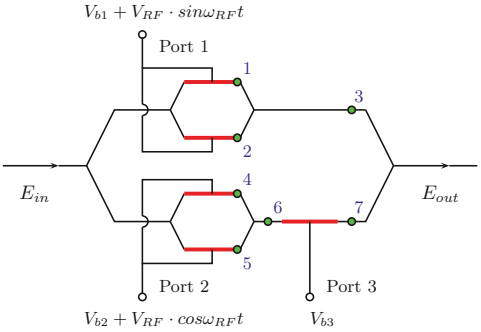

Figure B.3.: Typical structure of a DPMZM with break points for transfer function derivation.

In a similar way, the electric field at break point 6 is given by $E_6 = E_{in} \cdot \exp(j\phi) \cdot \cos(\beta_{b2} + \beta_{RF} \cos\omega_{RF}t)$. After the extra phase from the PM, the electric field at break point 7 is derived as $E_7 = E_6 \cdot \exp(j\beta_{b3}) = E_{in} \cdot \cos(\beta_{b2} + \beta_{RF} \cos\omega_{RF}t) \cdot \exp\Big[j(\phi + \beta_{b3})\Big]$. Providing an ideal 3 dB insertion loss of the Y-shaped branch, $E_{out} = (E_3 + E_7)/\sqrt{2}$ will give:

$$E_{out} = \tfrac{\sqrt{2}}{2} E_{in} \cdot \exp(j\phi) \cdot \Big[\cos(\beta_{b1} + \beta_{RF} \sin\omega_{RF}t) + \cos(\beta_{b2} + \beta_{RF} \cos\omega_{RF}t) \cdot \exp(j\beta_{b3})\Big] \quad \text{(B.3.28)}$$

Considering Eqs.(A.4b) and (A.4d), the expansion of the items in Eq. (B.3.28) yields,

$$\begin{aligned} \cos(\beta_{b1} + \beta_{RF} \sin\omega_{RF}t) &= \cos(\beta_{b1}) \cdot \cos(\beta_{RF} \sin\omega_{RF}t) - \sin(\beta_{b1}) \cdot \sin(\beta_{RF} \sin\omega_{RF}t) \\ &\approx J_0(\beta_{RF}) \cdot \cos(\beta_{b1}) - 2J_1(\beta_{RF}) \cdot \sin\beta_{b1} \cdot \sin\omega_{RF}t \\ \cos(\beta_{b2} + \beta_{RF} \cos\omega_{RF}t) &= \cos(\beta_{b2}) \cdot \cos(\beta_{RF} \sin\omega_{RF}t) - \sin(\beta_{b2}) \cdot \sin(\beta_{RF} \sin\omega_{RF}t) \\ &\approx J_0(\beta_{RF}) \cdot \cos(\beta_{b2}) - 2J_1(\beta_{RF}) \cdot \sin\beta_{b2} \cdot \cos\omega_{RF}t \end{aligned} \quad \text{(B.3.29)}$$

The substitution of $\exp(j\beta_{b3}) = \cos\beta_{b3} + j\sin\beta_{b3}$ and the expression of Eq. (B.1.2) yields:

$$\begin{aligned} E_{out} = &\tfrac{\sqrt{2}}{2} \cdot E_0 \cdot \exp(j\phi) \cdot \\ &\Big\{J_0(\beta_{RF}) \cdot [(\cos\beta_{b1} + \cos\beta_{b2} \cdot \cos\beta_{b3}) \cdot \cos\omega_0 t + (-\cos\beta_{b2} \cdot \sin\beta_{b3}) \cdot \sin\omega_0 t] \\ &+ j \cdot J_0(\beta_{RF})[(\cos\beta_{b2} \cdot \sin\beta_{b3}) \cdot \cos\omega_0 t + (\cos\beta_{b1} + \cos\beta_{b2} \cdot \cos\beta_{b3}) \cdot \sin\omega_0 t] \\ &- 2J_1(\beta_{RF}) \cdot (\cos\omega_0 t \cdot \cos\omega_{RF}t \cdot \sin\beta_{b2} \cdot \cos\beta_{b3} \\ &+ \cos\omega_0 t \cdot \sin\omega_{RF}t \cdot \sin\beta_{b1} - sin\omega_0 t \cdot \cos\omega_{RF}t \cdot \sin\beta_{b2} \cdot \sin\beta_{b3}) \\ &- j \cdot 2J_1(\beta_{RF}) \cdot [\cos\omega_0 t \cdot \cos\omega_{RF}t \cdot \sin\beta_{b2} \cdot \sin\beta_{b3} \\ &+ \sin\omega_0 t \cdot \cos\omega_{RF}t \cdot \sin\beta_{b2} \cdot \cos\beta_{b3} + \sin\omega_0 t \cdot \sin\omega_{RF}t \cdot \sin\beta_{b1}]\Big\} \end{aligned} \quad \text{(B.3.30)}$$

Dieses Werk ist copyrightgeschützt und darf in keiner Form vervielfältigt werden noch an Dritte weitergegeben werden.
Es gilt nur für den persönlichen Gebrauch.

Considering the product-to-sum identities:

$$\begin{aligned}\cos\omega_0 t\cdot\cos\omega_{RF}t &= \frac{1}{2}\cdot[\cos(\omega_0+\omega_{RF})t+\cos(\omega_0-\omega_{RF})t]\\ \cos\omega_0 t\cdot\sin\omega_{RF}t &= \frac{1}{2}\cdot[\sin(\omega_0+\omega_{RF})t-\sin(\omega_0-\omega_{RF})t]\\ -\sin\omega_0 t\cdot\cos\omega_{RF}t &= -\frac{1}{2}\cdot[\cdot[\sin(\omega_0+\omega_{RF})t+\sin(\omega_0-\omega_{RF})t]\end{aligned} \tag{B.3.31}$$

the real part of Eq. (B.3.30) yields:

$$\begin{aligned}&E_{out}=\frac{\sqrt{2}}{2}\cdot E_0\cdot\exp(j\phi)\cdot\\ &\Big\{J_0(\beta_{RF})\cdot[(\cos\beta_{b1}+\cos\beta_{b2}\cdot\cos\beta_{b3})\cdot\cos\omega_0 t+(-\cos\beta_{b2}\cdot\sin\beta_{b3})\cdot\sin\omega_0 t]\\ &+J_1(\beta_{RF})\cdot[(-\sin\beta_{b2}\cdot\cos\beta_{b3})\cdot\cos(\omega_0+\omega_{RF})t+(-\sin\beta_{b1}+sin\beta_{b2}\cdot\sin\beta_{b3})\cdot\sin(\omega_0+\omega_{RF})t]\\ &+J_1(\beta_{RF})\cdot[(-\sin\beta_{b2}\cdot\cos\beta_{b3})\cdot\cos(\omega_0-\omega_{RF})t+(\sin\beta_{b1}+sin\beta_{b2}\cdot\sin\beta_{b3})\cdot\sin(\omega_0-\omega_{RF})t]\Big\}\end{aligned} \tag{B.3.32}$$

The output intensity can be calculated from the electric field as $P_{out}=|E_{out}|^2$. Since the PD is not fast enough to catch optical frequency components, we may safely neglect all components containing ω_0. By collecting all the items at ω_{RF}, the RF power can be expressed as:

$$\begin{aligned}P_{RF}|_{\omega_{RF}} = -P_{in}\cdot J_0(\beta_{RF})\cdot J_1(\beta_{RF})\cdot[&(\cos\beta_{b1}\cdot\sin\beta_{b1}+\sin\beta_{b1}\cdot\cos\beta_{b2}\cdot\cos\beta_{b3})\cdot\sin\omega_{RF}t\\ &+(\cos\beta_{b2}\cdot\sin\beta_{b2}+\cos\beta_{b1}\cdot\sin\beta_{b2}\cdot\cos\beta_{b3})\cdot\cos\omega_{RF}t]\end{aligned} \tag{B.3.33}$$

where $P_{in}=|E_{in}|^2$ is the input optical power. The expressions of Eqs. (B.3.32) and (B.3.33) show very good agreements with Eqs. (1) and (3) in Ref. [153], respectively.

C. Gain Penalty with Multi-probe Waves

In a BOTDA setup with multi-probe waves, the acquired Brillouin gain will suffer from a penalty due to the division of the summation of the multi-probe waves. The number of probe waves is supposed to be N in a multi-probe BOTDA setup as mentioned in Sec. 4.4 and Sec. 5.4. The probe waves have the original input power of P_{si} with i ranging from 1 to N. After their own SBS interactions, the probe powers become $P_{si,SBS}$. In a scenario of sensing with BOTDA, the SBS gain (or loss) of both probe waves are valid for a small gain approximation. Neglecting any cross-interaction between the probe waves, the logarithmic Brillouin gain with

Dieses Werk ist copyrightgeschützt und darf in keiner Form vervielfältigt werden noch an Dritte weitergegeben werden.
Es gilt nur für den persönlichen Gebrauch.

the simultaneous detection of the multiple probe waves is:

$$G_{log} = 10\lg\left(\sum_{i=1}^{N} P_{si,SBS} / \sum_{i=1}^{N} P_{si}\right) \tag{C.1}$$

With an equal probe power, we may denote $P_s = P_{si}$, yielding Eq. (C.1) to,

$$G_{log} = 10\lg\frac{\sum_{i=1}^{N} P_{si,SBS}}{N \cdot P_s} = -10\lg N + 10\lg\left(\sum_{i=1}^{N} G_{i,lin}\right) \tag{C.2}$$

where

$$G_{i,lin} = \frac{P_{si,SBS}}{P_s} = 10^{G_{i,log}/10} \approx 1 + \frac{\ln 10}{10} \cdot G_{i,log} \tag{C.3}$$

is the linear Brillouin gain of corresponding probe wave with the logarithmic Brillouin gain denoted as $G_{i,log}$. In Eq. (C.3), the exponential functions are expanded in a Taylor series with a small offset at zero gain. The substitution of Eq. (C.3) in Eq. (C.2) give rise to:

$$\begin{aligned} G_{log} &= -10\lg N + 10\lg\left\{N\left[1 + \frac{\ln 10}{10N} \cdot \left(\sum_{i=1}^{N} G_{i,log}\right)\right]\right\} \\ &= 10\lg\left[1 + \frac{\ln 10}{10N} \cdot \left(\sum_{i=1}^{N} G_{i,log}\right)\right] \end{aligned} \tag{C.4}$$

Considering the Taylor series of the logarithmic function with a small offset at zero: $\lg(1+x) \approx x/\ln 10$, the expression of G_{log} can be simplified from Eq. (C.4) as

$$G_{log} \approx \frac{1}{N}\left(\sum_{i=1}^{N} G_{i,log}\right) \tag{C.5}$$

indicating a penalty on the logarithmic gain with a factor of N for a simultaneous detection with multi-probe scheme. The equivalent linear expression of Eq. (C.5) is given by,

$$G_{lin} = 10^{G_{log}/10} \approx 10^{\frac{1}{N}\cdot\frac{1}{10}\left(\sum_{i=1}^{N} G_{i,log}\right)} = 10^{\frac{1}{N}\cdot\frac{1}{10}\left(\sum_{i=1}^{N} 10\lg G_{i,lin}\right)} = \prod_{i=1}^{N} G_{i,lin}^{\frac{1}{N}} \tag{C.6}$$

Mathematically, the condition of the approximation of Eqs.(C.5) and (C.6) is $|G_{i,log}/10| \ll 1$ or $|G_{i,lin} - 1| \ll 1$.

Dieses Werk ist copyrightgeschützt und darf in keiner Form vervielfältigt werden noch an Dritte weitergegeben werden.
Es gilt nur für den persönlichen Gebrauch.

Dieses Werk ist copyrightgeschützt und darf in keiner Form vervielfältigt werden noch an Dritte weitergegeben werden.
Es gilt nur für den persönlichen Gebrauch.

References

[1] Agrawal, G. P., [*Nonlinear Fiber Optics*], Academic Press, 5th ed. (2013).

[2] Schneider, T., [*Nonlinear Optics in Telecommunications*], Advanced Texts in Physics, Springer Berlin Heidelberg, Berlin, Heidelberg (2004).

[3] Boyd, R. W., [*Nonlinear Optics*], Academic Press, 3rd ed. (2008).

[4] Courjal, N., Bernal, M.-P., Caspar, A., Ulliac, G., Bassignot, F., Gauthier-Manuel, L., and Suarez, M., "Lithium Niobate Optical Waveguides and Microwaveguides," in [*Emerg. Waveguide Technol.*], IntechOpen (2018).

[5] Agrawal, G. P., [*Fiber-Optic Communication Systems*], Wiley, 4nd ed. (2010).

[6] Feng, C., Zhang, L., Luo, H., Gao, C., He, L., Liu, J., and Zhan, L., "Phase-matched four-wave mixing by the fast light effect in fiber Bragg gratings," in [*14th Int. Conf. Opt. Commun. Networks*], 1–3, IEEE, Nanjing, China (2015).

[7] Feng, C., Zhang, L., Luo, H., Gao, C., He, L., Liu, J., and Zhan, L., "Fast-light-assisted four-wave mixing in the photonic bandgap," *Opt. Lett.* **40**(12), 2790–2793 (2015).

[8] Miya, T., Terunuma, Y., Hosaka, T., and Miyashita, T., "Ultimate low-loss single-mode fibre at 1.55 μm," *Electron. Lett.* **15**(4), 106 (1979).

[9] Fan, X., "Distributed Rayleigh Sensing," in [*Handb. Opt. Fibers*], 1–50, Springer Singapore, Singapore (2018).

[10] Islam, M., "Raman amplifiers for telecommunications," *IEEE J. Sel. Top. Quantum Electron.* **8**(3), 548–559 (2002).

[11] Soto, M. A. and Di Pasquale, F., "Distributed Raman Sensing," in [*Handb. Opt. Fibers*], 1–55, Springer Singapore, Singapore (2018).

[12] Bolognini, G. and Hartog, A., "Raman-based fibre sensors: Trends and applications," *Opt. Fiber Technol.* **19**(6), 678–688 (2013).

[13] Brillouin, L., "Diffusion de la lumière et des rayons X par un corps transparent homogène," *Ann. Phys. (Paris).* **9**(17), 88–122 (1922).

[14] Mandelstam, L. I., "Light scattering by inhomogeneous media," *Zh. Russ. Fiz-Khim. Ova* **58**, 381 (1926).

Dieses Werk ist copyrightgeschützt und darf in keiner Form vervielfältigt werden noch an Dritte weitergegeben werden.
Es gilt nur für den persönlichen Gebrauch.

[15] Gross, E., "Change of Wave-length of Light due to Elastic Heat Waves at Scattering in Liquids," *Nature* **126**(3171), 201–202 (1930).

[16] Chiao, R., Townes, C., and Stoicheff, B., "Stimulated Brillouin scattering and coherent generation of intense hypersonic waves," *Phys. Rev. Lett.* **12**(21), 592–595 (1964).

[17] Ippen, E. P. and Stolen, R. H., "Stimulated Brillouin scattering in optical fibers," *Appl. Phys. Lett.* **21**(11), 539–541 (1972).

[18] Smith, R. G., "Optical Power Handling Capacity of Low Loss Optical Fibers as Determined by Stimulated Raman and Brillouin Scattering," *Appl. Opt.* **12**(3), 82–85 (1972).

[19] Kobyakov, A., Sauer, M., and Chowdhury, D., "Stimulated Brillouin scattering in optical fibers," *Adv. Opt. Photonics* **2**(1), 1–59 (2010).

[20] Hirose, A., Takushima, Y., and Okoshi, T., "Suppression of Stimulated Brillouin Scattering and Brillouin Crosstalk by Frequency-Sweeping Spread-Spectrum Scheme," *J. Opt. Commun.* **12**(3), 82–85 (1991).

[21] Thévenaz, L., "Slow and fast light in optical fibres," *Nat. Photonics* **2**(8), 474–481 (2008).

[22] Zhu, Z., Gauthier, D. J., Okawachi, Y., Sharping, J. E., Gaeta, A. L., Boyd, R. W., and Willner, A. E., "Numerical study of all-optical slow-light delays via stimulated Brillouin scattering in an optical fiber," *J. Opt. Soc. Am. B* **22**(11), 2378–2384 (2005).

[23] Zadok, A., Eyal, A., and Tur, M., "Stimulated Brillouin scattering slow light in optical fibers [Invited]," *Appl. Opt.* **50**(25), E38 (2011).

[24] Al-Taiy, H., Wenzel, N., Preußler, S., Klinger, J., and Schneider, T., "Ultra-narrow linewidth, stable and tunable laser source for optical communication systems and spectroscopy," *Opt. Lett.* **39**(20), 5826–5829 (2014).

[25] Hill, K. O., Kawasaki, B. S., and Johnson, D. C., "cw Brillouin laser," *Appl. Phys. Lett.* **28**(10), 608–609 (1976).

[26] Yeniay, A., Delavaux, J.-M., and Toulouse, J., "Spontaneous and stimulated Brillouin scattering gain spectra in optical fibers," *J. Light. Technol.* **20**(8), 1425–1432 (2002).

[27] Preußler, S., [*Bandwidth Reduction of Stimulated Brillouin Scattering and Applications in Optical Communication*], Cuvillier Verlag (2016).

[28] Motil, A., Bergman, A., and Tur, M., "[INVITED] State of the art of Brillouin fiber-optic distributed sensing," *Opt. Laser Technol.* **78**, 81–103 (2016).

[29] Damzen, M. J., Vlad, V., Mocofanescu, A., and Babin, V., [*Stimulated Brillouin Scattering: Fundamentals and Applications*], CRC Press, Boca Raton (2003).

[30] Horiguchi, T., Shibata, N., Azuma, Y., and Tateda, M., "Brillouin gain variation due to a polarization-state change of the pump or Stokes fields in standard single-mode fibers," *Opt. Lett.* **14**(6), 329–331 (1989).

Dieses Werk ist copyrightgeschützt und darf in keiner Form vervielfältigt werden noch an Dritte weitergegeben werden.
Es gilt nur für den persönlichen Gebrauch.

[31] van Deventer, M. O. and Boot, A. J., "Polarization Properties of Stimulated Brillouin Scattering in Single-Mode Fibers," *J. Light. Technol.* **12**(4), 585–590 (1994).

[32] Billington, R., "Measurement methods for stimulated Raman and Brillouin scattering in optical fibres," tech. rep. (1999).

[33] Bayvel, P. and Radmore, P., "Solutions of the SBS equations in single mode optical fibres and implications for fibre transmission systems," *Electron. Lett.* **26**(7), 434–436 (1990).

[34] Le Floch, S. and Cambon, P., "Theoretical evaluation of the Brillouin threshold and the steady-state Brillouin equations in standard single-mode optical fibers," *J. Opt. Soc. Am. A* **20**(6), 1132–1137 (2003).

[35] Yi, L., Wei, W., Jaouën, Y., Shi, M., Han, B., Morvan, M., and Hu, W., "Polarization-Independent Rectangular Microwave Photonic Filter Based on Stimulated Brillouin Scattering," *J. Light. Technol.* **34**(2), 669–675 (2016).

[36] Feng, C., Lu, X., Preussler, S., and Schneider, T., "Gain Spectrum Engineering in Distributed Brillouin Fiber Sensors," *J. Light. Technol.* **37**(20), 5231–5237 (2019).

[37] Voges, E. and Petermann, K., [*Optische Kommunikationstechnik*], Springer, Berlin, Heidelberg (2002).

[38] Hakki, B. W., "Evaluation of Transmission Characteristics of Chirped DFB Lasers in Dispersive Optical Fiber," *J. Light. Technol.* **10**(7), 964–970 (1992).

[39] Ito, M. and Kimura, T., "Stationary and Transient Thermal Properties of Semiconductor Laser Diodes," *IEEE J. Quantum Electron.* **17**(5), 787–795 (1981).

[40] Zadok, A., Eyal, A., and Tur, M., "Gigahertz-Wide Optically Reconfigurable Filters Using Stimulated Brillouin Scattering," *J. Light. Technol.* **25**(8), 2168–2174 (2007).

[41] Wei, W., Yi, L., Jaouën, Y., and Hu, W., "Arbitrary-shaped Brillouin microwave photonic filter by manipulating a directly modulated pump," *Opt. Lett.* **42**(20), 4083–4086 (2017).

[42] Wei, W., Yi, L., Jaouën, Y., and Hu, W., "Software-defined microwave photonic filter with high reconfigurable resolution," *Sci. Rep.* **6**, 1–10 (2016).

[43] Preussler, S., Wiatrek, A., Jamshidi, K., and Schneider, T., "Brillouin scattering gain bandwidth reduction down to 3.4MHz.," *Opt. Express* **19**(9), 8565–8570 (2011).

[44] Preussler, S., Wiatrek, A., Jamshidi, K., and Schneider, T., "Ultrahigh-resolution spectroscopy based on the bandwidth reduction of stimulated brillouin scattering," *IEEE Photonics Technol. Lett.* **23**(16), 1118–1120 (2011).

[45] Kovalev, V. I. and Harrison, R. G., "Observation of Inhomogeneous Spectral Broadening of Stimulated Brillouin Scattering in an Optical Fiber," *Phys. Rev. Lett.* **85**(9), 1879–1882 (2000).

[46] Juarez, A., *Spectral hole-burning in an inhomogeneous broadened Brillouin resonance*,

Dieses Werk ist copyrightgeschützt und darf in keiner Form vervielfältigt werden noch an Dritte weitergegeben werden.
Es gilt nur für den persönlichen Gebrauch.

PhD thesis, Technische Universität Berlin (2007).

[47] Wiatrek, A., *Untersuchung der Eigenschaften der gesättigten stimulierten Brillouin-Streuung und ihrer Anwendungsmöglichkeiten*, PhD thesis, Brandenburgischen Technischen Universität Cottbus (1976).

[48] Stépien, L., Randoux, S., and Zemmouri, J., "Origin of spectral hole burning in Brillouin fiber amplifiers and generators," *Phys. Rev. A* **65**(5), 053812 (2002).

[49] Wiatrek, A., Preußler, S., Jamshidi, K., and Schneider, T., "Frequency domain aperture for the gain bandwidth reduction of stimulated Brillouin scattering," *Opt. Lett.* **37**(5), 930–932 (2012).

[50] Kersey, A. D., Davis, M. A., Patrick, H. J., LeBlanc, M., Koo, K. P., Askins, C. G., Putnam, M. A., and Friebele, E. J., "Fiber grating sensors," *J. Light. Technol.* **15**(8), 1442–1463 (1997).

[51] Soto, M. A., "Distributed Brillouin Sensing: Time-Domain Techniques," in [*Handb. Opt. Fibers*], 1–91, Springer Singapore, Singapore (2018).

[52] Dakin, J., Pratt, D., Bibby, G., and Ross, J., "Distributed optical fibre Raman temperature sensor using a semiconductor light source and detector," *Electron. Lett.* **21**(13), 569–570 (1985).

[53] Imahama, M., Koyamada, Y., and Hogari, K., "Restorability of Rayleigh Backscatter Traces Measured by Coherent OTDR with Precisely Frequency-Controlled Light Source," *IEICE Trans. Commun.* **E91-B**(4), 1243–1246 (2008).

[54] Kurashima, T., Horiguchi, T., and Tateda, M., "Distributed-temperature sensing using stimulated Brillouin scattering in optical silica fibers," *Opt. Lett.* **15**(18), 1038–1040 (1990).

[55] Horiguchi, T., Kurashima, T., and Tateda, M., "Tensile strain dependence of Brillouin frequency shift in silica optical fibers," *IEEE Photonics Technol. Lett.* **1**(5), 107–108 (1989).

[56] Timoshenko, S. and Goodier, J., [*Theory of Elasticity*], McGraw-Hill, New York (1970).

[57] Galindez-Jamioy, C. A. and López-Higuera, J. M., "Brillouin Distributed Fiber Sensors: An Overview and Applications," *J. Sensors* **2012**, 1–17 (2012).

[58] Zou, W., Long, X., and Chen, J., "Brillouin Scattering in Optical Fibers and Its Application to Distributed Sensors," in [*Adv. Opt. Fiber Technol. Fundam. Opt. Phenom. Appl.*], InTech (2015).

[59] Feng, C., Emad Kadum, J., and Schneider, T., "The State-of-the-Art of Brillouin Distributed Fiber Sensing," in [*Fiber Opt. Sens. - Princ. Meas. Appl.*], IntechOpen (2019).

[60] Haneef, S. M., Yang, Z., Thévenaz, L., Venkitesh, D., and Srinivasan, B., "Performance

Dieses Werk ist copyrightgeschützt und darf in keiner Form vervielfältigt werden noch an Dritte weitergegeben werden.
Es gilt nur für den persönlichen Gebrauch.

analysis of frequency shift estimation techniques in Brillouin distributed fiber sensors," *Opt. Express* **26**(11), 14661–14677 (2018).

[61] Bao, X., Webb, D. J., and Jackson, D. A., "32-km distributed temperature sensor based on Brillouin loss in an optical fiber," *Opt. Lett.* **18**(18), 1561–1563 (1993).

[62] Soto, M. a. and Thévenaz, L., "Modeling and evaluating the performance of Brillouin distributed optical fiber sensors.," *Opt. Express* **21**(25), 31347–31366 (2013).

[63] Feng, C., Preussler, S., Emad Kadum, J., and Schneider, T., "Measurement Accuracy Enhancement via Radio Frequency Filtering in Distributed Brillouin Sensing," *Sensors* **19**(13), 2878 (2019).

[64] Lin, W., Yang, Z., Hong, X., Wang, S., and Wu, J., "Brillouin gain bandwidth reduction in Brillouin optical time domain analyzers," *Opt. Express* **25**(7), 7604–7615 (2017).

[65] Hotate, K. and Hasegawa, T., "Measurement of Brillouin Gain Spectrum Distribution along an Optical Fiber Using a Correlation-Based Technique – Proposal, Experiment and Simulation," *IEICE Trans. Electron.* **E83-C**(3), 405–412 (2000).

[66] Song, K.-Y., He, Z., and Hotate, K., "Distributed Strain Measurement with Millimeter-Order Spatial Resolution Based on Brillouin Optical Correlation Domain Analysis and Beat Lock-in Detection Scheme," in [*Opt. Fiber Sensors*], ThC2 (2006).

[67] Imai, M., Nakano, R., Kono, T., Ichinomiya, T., Miura, S., and Mure, M., "Crack Detection Application for Fiber Reinforced Concrete Using BOCDA-Based Optical Fiber Strain Sensor," *J. Struct. Eng.* **136**(8), 1001–1008 (2010).

[68] Song, K.-Y. and Hotate, K., "Brillouin Optical Correlation Domain Analysis in Linear Configuration," *IEEE Photonics Technol. Lett.* **20**(24), 2150–2152 (2008).

[69] Garus, D., Krebber, K., Schliep, F., and Gogolla, T., "Distributed sensing technique based on Brillouin optical-fiber frequency-domain analysis.," *Opt. Lett.* **21**(17), 1402–1404 (1996).

[70] Bernini, R., Crocco, L., Minardo, A., Soldovieri, F., and Zeni, L., "Frequency-domain approach to distributed fiber-optic Brillouin sensing," *Opt. Lett.* **27**(5), 288–290 (2002).

[71] Xie, S., Pang, M., Bao, X., and Chen, L., "Polarization dependence of Brillouin linewidth and peak frequency due to fiber inhomogeneity in single mode fiber and its impact on distributed fiber Brillouin sensing," *Opt. Express* **20**(6), 6385–6399 (2012).

[72] Foaleng-Mafang, S., Beugnot, J.-C., and Thevenaz, L., "Optical sampling technique applied to high resolution distributed fibre sensors," *20th Int. Conf. Opt. Fibre Sensors* **7503**, 750369 (2009).

[73] Seller, P., "Technology Needs for Modular Pixel Detectors," in [*Solid-State Radiat. Detect. Technol. Appl.*], 125–142, Taylor & Francis Group (2015).

[74] Orwiler, B., [*Oscilloscope vertical amplifiers*], Circuit Concepts, 1st ed. (1969).

Dieses Werk ist copyrightgeschützt und darf in keiner Form vervielfältigt werden noch an Dritte weitergegeben werden.
Es gilt nur für den persönlichen Gebrauch.

[75] Farahani, M. A., Castillo-Guerra, E., and Colpitts, B. G., "Accurate estimation of Brillouin frequency shift in Brillouin optical time domain analysis sensors using cross correlation," *Opt. Lett.* **36**(21), 4275–4277 (2011).

[76] Barnoski, M. K., Rourke, M. D., Jensen, S. M., and Melville, R. T., "Optical time domain reflectometer," *Appl. Opt.* **16**(9), 2375–2379 (1977).

[77] Toshio, K., Tsuneo, H., Hisashi, I., Furukawa, S.-i., and Yahei, K., "Brillouin optical-fiber time domain reflectometry," *IEICE Trans. Commun.* **E76-B**(4), 382–390 (1993).

[78] Feng, C. and Schneider, T., "Optimizing Brillouin Optical Time-Domain Analyzers Based on Gain Spectrum Engineering," *J. Vis. Exp.* (159) (2020).

[79] Van Simaeys, G., Emplit, P., and Haelterman, M., "Experimental Demonstration of the Fermi-Pasta-Ulam Recurrence in a Modulationally Unstable Optical Wave," *Phys. Rev. Lett.* **87**(3), 033902 (2001).

[80] Tai, K., Hasegawa, A., and Tomita, A., "Observation of modulational instability in optical fibers," *Phys. Rev. Lett.* **56**(2), 135–138 (1986).

[81] Fermi, E., Pasta, J., and Ulam, S., "Studies of nonlinear problems," in [*Collect. Pap. Enrico Fermi*], Segre, E., ed., 978–988, The University of Chicago Press (1965).

[82] Alem, M., Soto, M. A., and Thévenaz, L., "Analytical model and experimental verification of the critical power for modulation instability in optical fibers," *Opt. Express* **23**(23), 29514–29532 (2015).

[83] Soto, M. A., Alem, M., Chen, W., and Thévenaz, L., "Mitigating modulation instability in Brillouin distributed fibre sensors," in [*Proc. SPIE 8794, Fifth Eur. Work. Opt. Fibre Sensors*], **8794**, 87943J (2013).

[84] Soto, M. A., Ricchiuti, A. L., Zhang, L., Barrera, D., Sales, S., and Thevenaz, L., "Time and frequency pump-probe multiplexing to enhance the signal response of Brillouin optical time-domain analyzers.," *Opt. Express* **22**(23), 28584–28595 (2014).

[85] Zadok, A., Zilka, E., Eyal, A., Thévenaz, L., and Tur, M., "Vector analysis of stimulated Brillouin scattering amplification in standard single-mode fibers," *Opt. Express* **16**(26), 21692–21707 (2008).

[86] Urricelqui, J., Lopez-Fernandino, F., Sagues, M., and Loayssa, A., "Polarization Diversity Scheme for BOTDA Sensors Based on a Double Orthogonal Pump Interaction," *J. Light. Technol.* **33**(12), 2633–2638 (2015).

[87] VanWiggeren, G. D. and Roy, R., "Transmission of linearly polarized light through a single-mode fiber with random fluctuations of birefringence," *Appl. Opt.* **38**(18), 3888–3892 (1999).

[88] Thévenaz, L., Mafang, S. F., and Lin, J., "Effect of pulse depletion in a Brillouin optical time-domain analysis system," *Opt. Express* **21**(12), 14017–14035 (2013).

Dieses Werk ist copyrightgeschützt und darf in keiner Form vervielfältigt werden noch an Dritte weitergegeben werden.
Es gilt nur für den persönlichen Gebrauch.

[89] Zornoza, A., Minardo, A., Bernini, R., Loayssa, A., and Zeni, L., "Pulsing the probe wave to reduce nonlocal effects in brillouin optical time-domain analysis (BOTDA) sensors," *IEEE Sens. J.* **11**(4), 1067–1068 (2011).

[90] Dominguez-Lopez, A., Angulo-Vinuesa, X., Lopez-Gil, A., Martin-Lopez, S., and Gonzalez-Herraez, M., "Non-local effects in dual-probe-sideband Brillouin optical time domain analysis," *Opt. Express* **23**(8), 10341–10352 (2015).

[91] Bernini, R., Minardo, A., and Zeni, L., "Long-range distributed Brillouin fiber sensors by use of an unbalanced double sideband probe," *Opt. Express* **19**(24), 23845–23856 (2011).

[92] Ruiz-Lombera, R., Urricelqui, J., Sagues, M., Mirapeix, J., Lopez-Higuera, J. M., and Loayssa, A., "Overcoming Nonlocal Effects and Brillouin Threshold Limitations in Brillouin Optical Time-Domain Sensors," *IEEE Photonics J.* **7**(6), 1–9 (2015).

[93] Iribas, H., Urricelqui, J., Mompó, J. J., Mariñelarena, J., and Loayssa, A., "Non-Local Effects in Brillouin Optical Time-Domain Analysis Sensors," *Appl. Sci.* **7**(8), 761 (2017).

[94] Feng, C., Iribas, H., Marinelaerña, J., Schneider, T., and Loayssa, A., "Detrimental Effects in Brillouin Distributed Sensors Caused By EDFA Transient," in [*Conf. Lasers Electro-Optics*], JTu5A.85 (2017).

[95] Iribas, H., Mariñelarena, J., Feng, C., Urricelqui, J., Schneider, T., and Loayssa, A., "Effects of pump pulse extinction ratio in Brillouin optical time-domain analysis sensors," *Opt. Express* **25**(22), 27896–27911 (2017).

[96] Zornoza, A., Olier, D., Sagues, M., and Loayssa, A., "Brillouin distributed sensor using RF shaping of pump pulses," *Meas. Sci. Technol.* **21**(9), 094021 (2010).

[97] Bao, X., Brown, A., DeMerchant, M., and Smith, J., "Characterization of the Brillouin-loss spectrum of single-mode fibers by use of very short (<10-ns) pulses," *Opt. Lett.* **24**(8), 510–512 (1999).

[98] Motil, A., Danon, O., Peled, Y., and Tur, M., "High spatial resolution BOTDA using simultaneously launched gain and loss pump pulses," in [*Fifth Eur. Work. Opt. Fibre Sensors*], 87943L (2013).

[99] Kishida, K. and Li, C.-h., "Pulse pre-pump-BOTDA technology for new generation of distributed strain measuring system," in [*Struct. Heal. Monit. Intell. Infrastruct.*], 471–477, Taylor & Francis Group, London (2006).

[100] Li, W., Bao, X., Li, Y., and Chen, L., "Differential pulse-width pair BOTDA for high spatial resolution sensing," *Opt. Express* **16**(26), 21616–21625 (2008).

[101] Foaleng, S. M., Tur, M., Beugnot, J. C., and Thévenaz, L., "High spatial and spectral resolution long-range sensing using Brillouin echoes," *J. Light. Technol.* **28**(20), 2993–3003 (2010).

Dieses Werk ist copyrightgeschützt und darf in keiner Form vervielfältigt werden noch an Dritte weitergegeben werden.
Es gilt nur für den persönlichen Gebrauch.

[102] Angulo-Vinuesa, X., Dominguez-Lopez, A., Lopez-Gil, A., Ania-Castañón, J. D., Martin-Lopez, S., and Gonzalez-Herraez, M., "Limits of BOTDA Range Extension Techniques," *IEEE Sens. J.* **16**(10), 3387–3395 (2016).

[103] Angulo-Vinuesa, X., Martin-Lopez, S., Corredera, P., and Gonzalez-Herraez, M., "Raman-assisted Brillouin optical time-domain analysis with sub-meter resolution over 100 km," *Opt. Express* **20**(11), 12147–12154 (2012).

[104] Soto, M. A., Bolognini, G., Di Pasquale, F., and Thévenaz, L., "Simplex-coded BOTDA fiber sensor with 1 m spatial resolution over a 50 km range," *Opt. Lett.* **35**(2), 259–261 (2010).

[105] De Souza, K. and Newson, T. P., "Improvement of signal-to-noise capabilities of a distributed temperature sensor using optical preamplification," *Meas. Sci. Technol.* **12**(7), 952–957 (2001).

[106] Liang, H., Li, W., Linze, N., Chen, L., and Bao, X., "High-resolution DPP-BOTDA over 50 km LEAF using return-to-zero coded pulses," *Opt. Lett.* **35**(10), 1503–1505 (2010).

[107] Soto, M. A., Bolognini, G., and Di Pasquale, F., "Long-range simplex-coded BOTDA sensor over 120 km distance employing optical preamplification.," *Opt. Lett.* **36**(2), 232–234 (2011).

[108] Zornoza, A., Sagues, M., and Loayssa, A., "Self-heterodyne detection for SNR improvement and distributed phase-shift measurements in BOTDA," *J. Light. Technol.* **30**(8), 1066–1072 (2012).

[109] Urricelqui, J., Soto, M. A., and Thévenaz, L., "Sources of noise in Brillouin optical time-domain analyzers," in [*24th Int. Conf. Opt. Fibre Sensors*], **9634**, 963434 (2015).

[110] Kadum, J. E., Feng, C., and Schneider, T., "Characterization of the Noise Induced by Stimulated Brillouin Scattering in Distributed Sensing," *Sensors* **20**(15), 4311 (2020).

[111] Jacobs, I., "Dependence of Optical Amplifier Noise Figure on Relative-Intensity-Noise," *J. Light. Technol.* **13**(7), 1461–1465 (1995).

[112] Wang, S., Yang, Z., Soto, M., and Thevenaz, L., "Study on the signal-to-noise ratio of Brillouin optical-time domain analyzers," *Opt. Express* **28**(14), 19864–19876 (2020).

[113] Dominguez-Lopez, A., Lopez-Gil, A., Martin-Lopez, S., and Gonzalez-Herraez, M., "Signal-to-noise ratio improvement in BOTDA using balanced detection," *IEEE Photonics Technol. Lett.* **26**(4), 338–341 (2014).

[114] Kadum, J., Feng, C., Preussler, S., and Schneider, T., "Improvement of the measurement accuracy of distributed Brillouin sensing via radio frequency filtering," in [*Seventh Eur. Work. Opt. Fibre Sensors*], **11199**, 111991R, SPIE (2019).

[115] Soto, M. A., Ramírez, J. A., and Thévenaz, L., "Intensifying the response of distributed optical fibre sensors using 2D and 3D image restoration," *Nat. Commun.* **7**(1), 10870

Dieses Werk ist copyrightgeschützt und darf in keiner Form vervielfältigt werden noch an Dritte weitergegeben werden.
Es gilt nur für den persönlichen Gebrauch.

(2016).

[116] Choi, M., Mayorga, I. C., Preussler, S., and Schneider, T., "Investigation of gain dependent relative intensity noise in fiber brillouin amplification," *J. Light. Technol.* **34**(16), 3930–3936 (2016).

[117] Peled, Y., Motil, A., and Tur, M., "Fast Brillouin optical time domain analysis for dynamic sensing," *Opt. Express* **20**(8), 8584–8591 (2012).

[118] Voskoboinik, A., Wang, J., Shamee, B., Nuccio, S. R., Zhang, L., Chitgarha, M., Willner, A. E., and Tur, M., "SBS-Based Fiber Optical Sensing Using Frequency-Domain Simultaneous Tone Interrogation," *J. Light. Technol.* **29**(11), 1729–1735 (2011).

[119] Bernini, R., Minardo, A., and Zeni, L., "Dynamic strain measurement in optical fibers by stimulated Brillouin scattering.," *Opt. Lett.* **34**(17), 2613–2615 (2009).

[120] Jin, C., Guo, N., Feng, Y., Wang, L., Liang, H., Li, J., Li, Z., Yu, C., and Lu, C., "Scanning-free BOTDA based on ultra-fine digital optical frequency comb," *Opt. Express* **23**(4), 5277–5284 (2015).

[121] Peled, Y., Motil, A., Yaron, L., and Tur, M., "Slope-assisted fast distributed sensing in optical fibers with arbitrary Brillouin profile.," *Opt. Express* **19**(21), 19845–19854 (2011).

[122] Motil, A., Danon, O., Peled, Y., and Tur, M., "Pump-power-independent double slope-assisted distributed and fast Brillouin fiber-optic sensor," *IEEE Photonics Technol. Lett.* **26**(8), 797–800 (2014).

[123] Urricelqui, J., Zornoza, A., Sagues, M., and Loayssa, A., "Dynamic BOTDA measurements based on Brillouin phase-shift and RF demodulation.," *Opt. Express* **20**(24), 26942–26949 (2012).

[124] Feng, C., Lu, X., Preussler, S., and Schneider, T., "Measurement accuracy enhancement of distributed Brillouin sensors based on gain spectrum engineering," in [*Seventh Eur. Work. Opt. Fibre Sensors*], **11199**, 111991S, SPIE (2019).

[125] Feng, C., Mariñelarena, J., and Schneider, T., "Investigation on the working point of slope-assisted dynamic Brillouin distributed fiber sensing," in [*Seventh Eur. Work. Opt. Fibre Sensors*], **11199**, 111991V, SPIE (2019).

[126] Feng, C., Bhatta, H. D., Bohbot, J., Davidi, R., Lu, X., Schneider, T., and Tur, M., "Gain Spectrum Engineering in Slope-Assisted Dynamic Brillouin Optical Time-Domain Analysis," *J. Light. Technol.* **38**(24), 6967–6975 (2020).

[127] Yang, G., Fan, X., Wang, B., and He, Z., "Enhancing strain dynamic range of slope-assisted BOTDA by manipulating Brillouin gain spectrum shape," *Opt. Express* **26**(25), 32599–32607 (2018).

[128] Marinelarena, J., Urricelqui, J., and Loayssa, A., "Enhancement of the Dynamic Range

Dieses Werk ist copyrightgeschützt und darf in keiner Form vervielfältigt werden noch an Dritte weitergegeben werden.
Es gilt nur für den persönlichen Gebrauch.

in Slope-Assisted Coherent Brillouin Optical Time-Domain Analysis Sensors," *IEEE Photonics J.* **9**(3), 1–10 (2017).

[129] Yao, J., "Microwave photonics," *J. Light. Technol.* **27**(3), 314–335 (2009).

[130] Feng, C., Preussler, S., and Schneider, T., "Sharp tunable and additional noise-free optical filter based on Brillouin losses," *Photonics Res.* **6**(2), 132–137 (2018).

[131] Capmany, J., Ortega, B., and Pastor, D., "A tutorial on microwave photonic filters," *J. Light. Technol.* **24**(1), 201–229 (2006).

[132] Cabric, D., O'Donnell, I. D., Chen, M. S. W., and Brodersen, R. W., "Spectrum sharing radios," *IEEE Circuits Syst. Mag.* **6**(2), 30–45 (2006).

[133] Aiello, G. R. and Rogerson, G. D., "Ultra-wideband wireless systems," *IEEE Microw. Mag.* **4**(2), 36–47 (2003).

[134] Kim, B., Lee, J., Lee, J., Jung, B., and Chappell, W. J., "RF CMOS integrated on-chip tunable absorptive bandstop filter using Q-tunable resonators," *IEEE Trans. Electron Devices* **60**(5), 1730–1737 (2013).

[135] Lee, J., Lee, T. C., and Chappell, W. J., "Lumped-element realization of absorptive bandstop filter with anomalously high spectral isolation," *IEEE Trans. Microw. Theory Tech.* **60**(8), 2424–2430 (2012).

[136] Snow, T., Lee, J., and Chappell, W. J., "Tunable high quality-factor absorptive bandstop filter design," in [*2012 IEEE/MTT-S Int. Microw. Symp. Dig.*], 1–3, IEEE (2012).

[137] Minasian, R. A., Alameh, K. E., and Chan, E. H. W., "Photonics-based interference mitigation filters," *IEEE Trans. Microw. Theory Tech.* **49**(10 II), 1894–1899 (2001).

[138] Sancho, J., Bourderionnet, J., Lloret, J., Combrié, S., Gasulla, I., Xavier, S., Sales, S., Colman, P., Lehoucq, G., Dolfi, D., Capmany, J., and De Rossi, A., "Integrable microwave filter based on a photonic crystal delay line," *Nat. Commun.* **3** (2012).

[139] Supradeepa, V. R., Long, C. M., Wu, R., Ferdous, F., Hamidi, E., Leaird, D. E., and Weiner, A. M., "Comb-based radiofrequency photonic filters with rapid tunability and high selectivity," *Nat. Photonics* **6**(3), 186–194 (2012).

[140] Rasras, M. S., Tu, K. Y., Gill, D. M., Chen, Y. K., White, A. E., Patel, S. S., Pomerene, A., Carothers, D., Beattie, J., Beals, M., Michel, J., and Kimerling, L. C., "Demonstration of a tunable microwave-photonic notch filter using low-loss silicon ring resonators," *J. Light. Technol.* **27**(12), 2105–2110 (2009).

[141] Yi, L., Wei, W., Jaouen, Y., and Hu, W., "Ideal Rectangular Microwave Photonic Filter with High Selectivity Based on Stimulated Brillouin Scattering," in [*Opt. Fiber Commun. Conf.*], Tu3F.5, OSA, Washington, D.C. (2015).

[142] Thévenaz, L., Zadok, A., Eyal, A., and Tur, M., "All-Optical Polarization Control Through Brillouin Amplification," in [*OFC/NFOEC 2008 - 2008 Conf. Opt. Fiber*

Dieses Werk ist copyrightgeschützt und darf in keiner Form vervielfältigt werden noch an Dritte weitergegeben werden.
Es gilt nur für den persönlichen Gebrauch.

Commun. Fiber Opt. Eng. Conf.], **2**(1), 1–3, IEEE, San Diego (2008).

[143] Wei, W., Yi, L., Jaouen, Y., Morvan, M., and Hu, W., "Brillouin Rectangular Optical Filter with Improved Selectivity and Noise Performance," *IEEE Photonics Technol. Lett.* **27**(15), 1593–1596 (2015).

[144] Samaniego, D. and Vidal, B., "Brillouin wavelength-selective all-optical polarization conversion," *Photonics Res.* **8**(4), 440–447 (2020).

[145] Wise, A., Tur, M., and Zadok, A., "Sharp tunable optical filters based on the polarization attributes of stimulated Brillouin scattering," *Opt. Express* **19**(22), 21945–21955 (2011).

[146] Stern, Y., Zhong, K., Schneider, T., Zhang, R., Ben-ezra, Y., Tur, M., and Zadok, A., "Tunable sharp and highly selective microwave-photonic band-pass filters based on stimulated Brillouin scattering," *Photonics Res.* **2**(4), 18–25 (2014).

[147] Wei, W., Yi, L., Jaouën, Y., and Hu, W., "Bandwidth-tunable narrowband rectangular optical filter based on stimulated Brillouin scattering in optical fiber," *Opt. Express* **22**(19), 23249–23260 (2014).

[148] Wei, W., Yi, L., Jaouën, Y., Morvan, M., and Hu, W., "Ultra-selective flexible add and drop multiplexer using rectangular optical filters based on stimulated Brillouin scattering," *Opt. Express* **23**(15), 19010–19021 (2015).

[149] Tucker, R. S., "High-speed modulation of semiconductor lasers," *J. Light. Technol.* **3**(6), 1180–1192 (1985).

[150] Marpaung, D., Morrison, B., Pant, R., and Eggleton, B. J., "Frequency agile microwave photonic notch filter with anomalously-high stopband rejection," *Opt. Lett.* **38**(21), 4300–4303 (2013).

[151] Zhu, Z., Dawes, A. M., Gauthier, D. J., Zhang, L., and Willner, A. E., "12-GHz-bandwidth SBS slow light in optical fibers," in [*Opt. Fiber Commun. Conf.*], PDP1, Optical Society of America (2006).

[152] Song, K. Y. and Hotate, K., "25 GHz bandwidth Brillouin slow light in optical fibers," *Opt. Lett.* **32**(3), 217–219 (2007).

[153] Chan, E. H. W., Zhang, W., and Minasian, R. A., "Photonic RF phase shifter based on optical carrier and RF modulation sidebands amplitude and phase control," *J. Light. Technol.* **30**(23), 3672–3678 (2012).

[154] Schmuck, H., "Comparison of optical millimetre-wave system conceptswith regard to chromatic dispersion," *Electron. Lett.* **31**(21), 1848–1849 (1995).

[155] Marti, J., Fuster, J., and Laming, R., "Experimental reduction of chromatic dispersion effects in lightwave microwave/ millimetre-wave transmissions using tapered linearly chirped fibre gratings," *Electron. Lett.* **33**(13), 1170–1171 (1997).

[156] Smith, G., Novak, D., and Ahmed, Z., "Technique for optical SSB generation to overcome

Dieses Werk ist copyrightgeschützt und darf in keiner Form vervielfältigt werden noch an Dritte weitergegeben werden.
Es gilt nur für den persönlichen Gebrauch.

dispersion penalties in fibre-radio systems," *Electron. Lett.* **33**(1), 74–75 (1997).

[157] Meslener, G. J., "Chromatic dispersion induced distortion of modulated monochromatic light employing direct detection," *IEEE J. Quantum Electron.* **20**(10), 1208–1216 (1984).

[158] Zhang, W. and Minasian, R. A., "Ultrawide tunable microwave photonic notch filter based on stimulated brillouin scattering," *IEEE Photonics Technol. Lett.* **24**(14), 1182–1184 (2012).

[159] Choudhary, A., Aryanfar, I., Shahnia, S., Morrison, B., Vu, K., Madden, S., Luther-Davies, B., Marpaung, D., and Eggleton, B. J., "Tailoring of the Brillouin gain for on-chip widely tunable and reconfigurable broadband microwave photonic filters," *Opt. Lett.* **41**(3), 436–439 (2016).

[160] Marpaung, D., Morrison, B., Pagani, M., Pant, R., Choi, D.-Y., Luther-Davies, B., Madden, S. J., and Eggleton, B. J., "Low-power, chip-based stimulated Brillouin scattering microwave photonic filter with ultrahigh selectivity," *Optica* **2**(2), 76–83 (2015).

[161] Feng, C., Preussler, S., and Schneider, T., "Investigation of the Dispersion Effect on Stimulated Brillouin Scattering based Microwave Photonic Notch Filters," in [*2018 Int. Top. Meet. Microw. Photonics*], 1–4, IEEE, Toulouse, France (2018).

[162] Feng, C., Preussler, S., and Schneider, T., "The Influence of Dispersion on Stimulated Brillouin Scattering Based Microwave Photonic Notch Filters," *J. Light. Technol.* **36**(22), 5145–5151 (2018).

[163] Feng, C., Preussler, S., and Schneider, T., "Dispersion measurement via a microwave photonic notch filter based on stimulated Brillouin scattering," in [*Terahertz, RF, Millimeter, Submillimeter-Wave Technol. Appl. XII*], (109171Z), 72, SPIE, San Francisco, USA (2019).

[164] Cuyt, A., Brevik Petersen, V., Verdonk, B., Waadeland, H., and B.Jones, W., [*Handbook of Continued Fractions for Special Functions*], Springer Netherlands, Dordrecht (2008).

Dieses Werk ist copyrightgeschützt und darf in keiner Form vervielfältigt werden noch an Dritte weitergegeben werden.
Es gilt nur für den persönlichen Gebrauch.

List of Publications

Due to the priority reasons, some of the works in this thesis have already been published in peer-reviewed scientific journals as well as on internationally renowned conferences and workshops.

Journal

[1] Iribas, H., Mariñelarena, J., Feng, C., Urricelqui, J., Schneider, T. and Loayssa, A., "Effects of pump pulse extinction ratio in Brillouin optical time-domain analysis sensors," *Opt. Express* **25**(22), 27896–27911 (2017).

[2] Feng, C., Preussler, S. and Schneider, T., "Sharp tunable and additional noise-free optical filter based on Brillouin losses," *Photonics Res.* **6**(2), 132–137 (2018).

[3] Feng, C., Preussler, S. and Schneider, T., "The Influence of Dispersion on Stimulated Brillouin Scattering Based Microwave Photonic Notch Filters," *J. Light. Technol.* **36**(22), 5145–5151 (2018).

[4] Feng, C., Preussler, S., Emad Kadum, J. and Schneider, T., "Measurement Accuracy Enhancement via Radio Frequency Filtering in Distributed Brillouin Sensing," *Sensors* **19**(13), 2878 (2019).

[5] Feng, C., Lu, X., Preussler, S. and Schneider, T., "Gain Spectrum Engineering in Distributed Brillouin Fiber Sensors," *J. Light. Technol.* **37**(20), 5231–5237 (2019).

[6] Feng, C. and Schneider, T., "Optimizing Brillouin Optical Time-Domain Analyzers Based on Gain Spectrum Engineering," *J. Vis. Exp.* (159), (2020).

[7] Emad Kadum, J., Feng, C., and Schneider, T., "Characterization of the Noise Induced by Stimulated Brillouin Scattering in Distributed Sensing," *Sensors* **20**(15), 4311 (2020).

[8] Feng, C., Datta Bhatta, H., Bohbot, J., Davidi, R., Lu, X., Tur, M., and Schneider, T., "Gain Spectrum Engineering in Slope-assisted Dynamic Brillouin Optical Time-Domain Analysis," *J. Light. Technol.* **38**(24), 6967–6975 (2020).

Dieses Werk ist copyrightgeschützt und darf in keiner Form vervielfältigt werden noch an Dritte weitergegeben werden.
Es gilt nur für den persönlichen Gebrauch.

Book Chapter

[1] Feng, C., Emad Kadum, J. and Schneider, T., "The State-of-the-Art of Brillouin Distributed Fiber Sensing,"in *Fiber Optic Sensing - Principle, Measurement and Applications*, IntechOpen, UK (2019).

Conference

[1] Feng, C., Iribas, H., Marinelaerña, J., Schneider, T. and Loayssa, A., "Detrimental Effects in Brillouin Distributed Sensors Caused By EDFA Transient," *Conference on Lasers and Electro-Optics (CLEO)*, paper JTu5A.85, San José, United States, May 14–19, 2017.

[2] Schneider, T., Feng, C. and Preussler, S., "Dispersion engineering with stimulated Brillouin scattering and applications," *Photonics West SPIE, Steep Dispersion Engineering and Opto-Atomic Precision Metrology XI*, 105480U, San Francisco, United States, Jan.27–Feb.1, 2018.

[3] Feng, C., Preussler, S. and Schneider, T., "Investigation of the Dispersion Effect on Stimulated Brillouin Scattering based Microwave Photonic Notch Filters," in *2018 International Topical Meeting on Microwave Photonics (MWP)*, 1–4, Toulouse, France, Oct.22–25, 2018.

[4] Feng, C., Preussler, S. and Schneider, T., "Dispersion measurement via a microwave photonic notch filter based on stimulated Brillouin scattering," in *Photonics West SPIE, Terahertz, RF, Millimeter, and Submillimeter-Wave Technology and Applications XII*, 109171Z, San Fransisco, United States, Feb.2–7, 2019.

[5] Feng, C. and Schneider, T., "Measurement Accuracy Enhancement of Distributed Brillouin Sensors Based on Gain and Losses," in *The 3rd Workshop on OptoMechanics and Brillouin Scattering: Fundamentals, Applications and Technologies (WOMBAT)*, Tel-Aviv, Israel, Mar.26–28, 2019.

[6] Feng, C., Lu, X., Preussler, S. and Schneider, T., "Measurement accuracy enhancement of distributed Brillouin sensors based on gain spectrum engineering," in *Seventh European Workshop on Optical Fibre Sensors (EWOFS)*, 111991S, Limassol, Cyprus, Oct.1–4, 2019.

[7] Feng, C., Mariñelarena, J. and Schneider, T., "Investigation on the working point of slope-assisted dynamic Brillouin distributed fiber sensing," in *Seventh European Workshop on Optical Fibre Sensors (EWOFS)*, 111991V, Limassol, Cyprus, Oct.1–4, 2019.

[8] Emad Kadum, J., Feng, C., Preussler, S. and Schneider, T., "Improvement of the measurement accuracy of distributed Brillouin sensing via radio frequency filtering," in *Seventh European Workshop on Optical Fibre Sensors (EWOFS)*, 111991R, Limassol, Cyprus, Oct.1–4, 2019.

[9] Schneider, T. and Feng, C., "Dispersion engineering in distributed Brillouin dynamic

Dieses Werk ist copyrightgeschützt und darf in keiner Form vervielfältigt werden noch an Dritte weitergegeben werden.
Es gilt nur für den persönlichen Gebrauch.

sensing with spectrum engineering," in *Photonics West SPIE, Optical, Opto-Atomic, and Entanglement-Enhanced Precision Metrology II*, 112962S, San Francisco, United States, Feb.4–6, 2020.

[10] Feng, C., Lu, X. and Schneider, T., "Simultaneous enhancement of dynamic range and sensitivity in slope-assisted Brillouin optical time-domain analyzers via gain spectrum engineering," in *Photonics West SPIE, Optical, Terahertz, RF, Millimeter, and Submillimeter-Wave Technology and Applications XIII*, 112791C, San Francisco, United States, Feb.4–6, 2020.

[11] Emad Kadum, J., Feng, C. and Schneider, T., "Investigation on the excess noise in Brillouin optical time domain analysis due to stimulated Brillouin scattering," in *Photonics West SPIE, Optical, Terahertz, RF, Millimeter, and Submillimeter-Wave Technology and Applications XIII*, 112791W, San Francisco, United States, Feb.4–6, 2020.

[12] Feng, C., Datta Bhatta, H., Davidi, R., Lu, X., Schneider, T and Tur, M., "Dynamic range extension in slope assisted Brillouin optical time-domain analyzers with gain spectrum engineering," in *27th International Conference on Optical Fiber Sensors (OFS)*, Alexandria, United States, Jun.7–11, 2021. (accepted)

[13] Emad Kadum, J., Feng, C., Schneider, T., "Study of stimulated Brillouin scattering-initiated noise in distributed Brillouin sensing," in *27th International Conference on Optical Fiber Sensors (OFS)*, Alexandria, United States, Jun.7–11, 2021. (accepted)

Dieses Werk ist copyrightgeschützt und darf in keiner Form vervielfältigt werden noch an Dritte weitergegeben werden.
Es gilt nur für den persönlichen Gebrauch.

Dieses Werk ist copyrightgeschützt und darf in keiner Form vervielfältigt werden noch an Dritte weitergegeben werden.
Es gilt nur für den persönlichen Gebrauch.

Dieses Werk ist copyrightgeschützt und darf in keiner Form vervielfältigt werden noch an Dritte weitergegeben werden.
Es gilt nur für den persönlichen Gebrauch.

Dieses Werk ist copyrightgeschützt und darf in keiner Form vervielfältigt werden noch an Dritte weitergegeben werden.
Es gilt nur für den persönlichen Gebrauch.